TECHNISCHE UNIVERSITÄT MÜNCHEN

Lehrstuhl für Numerische Mechanik

A dual mortar formulation for finite deformation frictional contact problems including wear and thermal coupling

Markus Gitterle

Vollständiger Abdruck der von der Fakultät für Maschinenwesen der Technischen Universität München zur Erlangung des akademischen Grades eines

Doktor-Ingenieurs (Dr.-Ing.)

genehmigten Dissertation.

Vorsitzender: Univ.-Prof. Dr.-Ing. Wolfram Volk

Prüfer der Dissertation:

1. Univ.-Prof. Dr.-Ing. Wolfgang A. Wall
2. Univ.-Prof. Dr.-Ing. Karl Schweizerhof
   Karlsruher Institut für Technologie
3. Univ.-Prof. Dr.-Ing. Michael W. Gee

Die Dissertation wurde am 25.06.2012 bei der Technischen Universität München eingereicht und durch die Fakultät für Maschinenwesen am 20.11.2012 angenommen.

Abstract

Contact mechanics and friction are fundamental disciplines in engineering and applied science. They describe the potential surface interactions of solids. Closely related to especially frictional contact are effects from wear and thermomechanics. Alone and in combination, they are causal for different kinds of phenomena. Fretting fatigue, a possible damage mechanism in turbine or fan disc to blade joints in aircraft engines, is one of many relevant examples.

This thesis is concerned with the development of a 3D finite deformation frictional contact formulation based on finite elements. It is extended towards the inclusion of wear and towards the multiphysics problem of thermomechanical contact.

The necessary contact surface discretization is realized with the mortar method to overcome problems inherent to node-to-segment approaches. It represents a weak formulation of contact constraints which results in a perfect quality of contact stresses even for non-matching meshes. Contact constraints are enforced with the dual LAGRANGE multiplier method. This necessitates no regularization of contact conditions and allows, due to choosing them from a dual space, for an efficient elimination of these additional unknowns from the global system of equations. The tangential relative velocity, an essential quantity for finite frictional sliding, is formulated in terms of the change of the mortar projection in order to obtain a frame indifferent rate measure. The solution is realized with a semi-smooth NEWTON method. Thus, all nonlinearities are treated within one single iterative scheme which leads to a highly efficient solution algorithm in combination with the consistent linearization that is carried out.

The extension of the developed mortar contact formulation towards wear is performed using both an internal state variable and an Arbitrary LAGRANGEan-EULERian formulation resolved with a fractional-step strategy. The former approach increases the distance between contacting bodies by a so-called wear-gap and is mainly suitable for small amounts of wear. The latter one, which results in a LAGRANGEan step followed by an EULERian one where the mesh is adjusted due to wear, allows for significant wear loss clearly changing the geometry.

The multiphysics problem of 3D thermomechanical contact is obtained by adding the thermal field to the purely mechanical one. It contains coupling effects which are, related to contact, for example the heat conduction over contacting surfaces or heat production from frictional dissipation. For the thermal field, also the mortar method and dual LAGRANGE multipliers are used for contact surface discretization and enforcement of constraints. This transfers the accompanying advantages, which are the correct heat flux transfer over non-matching meshes and the easy elimination of LAGRANGE multipliers. For the solution, both a partitioned and, for frictionless contact, a monolithic scheme are applied. The latter is directly embedded in the semi-smooth NEWTON method and shows, together with a consistent linearization of all contact related terms, an excellent convergence behavior.

Accuracy, efficiency, and robustness of the proposed methods are demonstrated in several numerical examples.

Zusammenfassung

Kontaktmechanik und Reibung sind grundlegende Disziplinen in Wissenschaft und Technik. Sie beschreiben potentielle Oberflächen-Wechselwirkungen von Festkörpern. Eng verknüpft mit solchen Fragestellungen sind, vor allem für den reibungsbehafteten Kontakt, Effekte aus Verschleiß und Thermomechanik. Allein und in Kombination sind sie Ursache für die verschiedensten Phänomene. Reibermüdung (fretting fatigue) als ein möglicher Schädigungsmechanismus in Schaufel-Scheibe-Verbindungen von Flugzeugtriebwerken ist eines von einer Vielzahl von Beispielen.

Die vorliegende Arbeit beschäftigt sich mit der Entwicklung einer 3D reibungsbehafteten Kontaktformulierung für große Deformationen auf Basis der Finite-Element-Methode. Zusätzlich wird sie um die Berücksichtigung von Verschleiß und die Betrachtung von thermomechanischem Kontakt als Mehrfeldproblem erweitert.

Die Diskretisierung der Kontaktoberflächen erfolgt mit der Mortar-Methode, womit Nachteile aus Knoten-Segment-Ansätzen nicht auftreten. Sie besteht aus einer integralen Beschreibung der Kontaktbedingungen und ermöglicht, auch für nicht passende Netze, die Abbildung von Kontaktspannungen in einer sehr guten Qualität. Erzwungen werden die Kontaktbedingungen mit der dualen LAGRANGE-Multiplikatoren-Methode. Diese erfordert keine Regularisierung und erlaubt eine effiziente Beseitigung der damit verbundenen zusätzlichen Unbekannten aus dem globalen Gleichungssystem. Die tangentiale Relativgeschwindigkeit ist eine wesentliche Größe für die Formulierung von reibungsbehaftetem Gleiten bei großen Deformationen. Um ein objektives Maß zu erhalten wird sie mit Hilfe der Änderung der Mortar-Projektion beschrieben. Die Lösung erfolgt mit einem halbglatten NEWTON-Verfahren, womit alle Nichtlinearitäten innerhalb eines einzigen Iterationsschemas behandelt werden. Dies führt, zusammen mit der durchgeführten konsistenten Linearisierung, zu einem sehr effizienten Algorithmus.

Die Erweiterung der entwickelten Mortar-Kontaktformulierung hinsichtlich der Berücksichtigung von Verschleiß erfolgt sowohl mit einer inneren Zustandsvariablen als auch mit einer "Arbitrary LAGRANGEan-EULERian"-Betrachtungsweise, die partitioniert behandelt wird. Der erste Ansatz erhöht den Abstand zwischen kontaktierenden Körpern um die bisher abgeriebene Höhe und ist vor allem für geringe Mengen an Verschleiß geeignet. Der zweite besteht aus einem LAGRANGE-Schritt gefolgt von einem EULER-Schritt, in welchem das Netz entsprechend des Abriebs angepasst wird. Die Methode erlaubt die Abbildung von signifikantem Verschleiß mit deutlichen Geometrieänderungen der kontaktierenden Körper.

Dreidimensionaler thermomechanischer Kontakt gehört zur Gruppe der Mehrfeldprobleme und ergibt sich aus der Hinzunahme des thermischen Feldes zum rein mechanischen Problem. Kopplungsphänomene bezogen auf den Kontakt sind, zum Beispiel, der Wärmeübergang über Kontaktflächen oder die Wärmeerzeugung aus Reibung. Für das thermische Feld werden ebenfalls die Mortar- und die duale LAGRANGE-Multiplikatoren-Methode verwendet. Dies transferiert die entsprechenden Vorteile, die hier die qualitativ hochwertige Abbildung des Wärmestroms über nicht passende Netze und die einfache Elimination der LAGRANGE-Multiplikatoren erlaubt. Die Lösung erfolgt mit einem partitionierten Verfahren und, für reibungsfreien Kontakt, auch mit einem monolithischen Ansatz. Dieser ist direkt in den halbglatten NEWTON-

Algorithmus eingebettet und zeigt, in Kombination mit der konsistenten Linearisierung aller Kontaktbeiträge, ein hervorragendes Konvergenzverhalten.

Genauigkeit, Effizienz, und Robustheit der vorgeschlagenen Methoden werden in mehreren Beispielen demonstriert.

Danksagung

Die vorliegende Arbeit ist in den Jahren 2006 bis 2012 am Lehrstuhl für Numerische Mechanik an der Technischen Universität München entstanden. Finanziell unterstützt wurde sie auch vom Deutschen Wirtschaftsministerium, das eine Zusammenarbeit mit Rolls-Royce Deutschland förderte.

Aufrichtig bedanken möchte ich mich bei meinem Doktorvater Prof. Dr.-Ing. Wolfgang A. Wall. Er hat es mir ermöglicht, in seiner internationalen und vielseitigen Gruppe zu forschen und zu arbeiten. Dank gebührt zudem Prof. Dr.-Ing Michael W. Gee, der einen maßgeblichen Teil meiner Betreuung sowie das dritte Gutachten übernommen hat. Und natürlich den vielen Kollegen für fachliche Diskussionen und die freundschaftliche Arbeitsatmosphäre.

Die Prüfungskommision wurde vervollständigt durch Prof. Dr.-Ing. Wolfram Volk (Vorsitz) und Prof. Dr.-Ing. Karl Schweizerhof (2. Gutachter). Vielen Dank für die sorgfältige Übernahme dieser Ämter.

München, 16. Dezember 2012 Markus Gitterle

Contents

1 Introduction **1**
- 1.1 Motivation . . . 1
- 1.2 Existing methods and objectives . . . 2
  - 1.2.1 Frictional contact problem . . . 2
  - 1.2.2 Frictional contact problem with wear . . . 3
  - 1.2.3 Fully coupled thermomechanical contact problem . . . 5
  - 1.2.4 Summary of objectives . . . 5
- 1.3 Outline . . . 5

2 Frictional contact - problem formulation **7**
- 2.1 Basic continuum mechanics for solids . . . 7
  - 2.1.1 Kinematics . . . 7
  - 2.1.2 Stress concept . . . 11
  - 2.1.3 Balance principles and entropy . . . 12
  - 2.1.4 Constitutive equations . . . 15
- 2.2 Frictional contact related equations . . . 16
  - 2.2.1 Contact kinematics - gap . . . 17
  - 2.2.2 Contact kinematics - tangential relative velocity . . . 18
  - 2.2.3 Contact conditions . . . 21
- 2.3 Boundary value problem of finite deformation frictional contact . . . 23

3 Frictional contact - weak form and finite element discretization **25**
- 3.1 Methods of constraint enforcement . . . 25
  - 3.1.1 LAGRANGE multiplier method . . . 25
  - 3.1.2 Penalty method . . . 26
  - 3.1.3 Augmented LAGRANGE method, USZAWA algorithm . . . 27
- 3.2 Discretization of contact surfaces . . . 28
  - 3.2.1 Node-to-segment approach . . . 28
  - 3.2.2 Segment-to-segment approach, mortar method . . . 29
- 3.3 Weak form . . . 30
  - 3.3.1 Equilibrium equations . . . 30
  - 3.3.2 Contact constraints . . . 32
  - 3.3.3 Summarized weak form . . . 34
- 3.4 Finite element discretization . . . 35
  - 3.4.1 Shape functions . . . 35
  - 3.4.2 Discrete form of contact virtual work . . . 38
  - 3.4.3 Evaluation of mortar surface integrals . . . 39

3.4.4 Discrete form of contact constraints . . . 42
3.4.5 Objectivity of tangential relative velocity . . . 45
3.4.6 Time discretization . . . 47
3.4.7 Quadratic interpolation, different types of interpolation . . . 48
3.4.8 Summarized discrete form . . . 50

4 Frictional contact - solution with semi-smooth NEWTON method 51
4.1 Non-smooth complementarity functions . . . 51
4.1.1 Reformulation of normal contact conditions . . . 51
4.1.2 Reformulation of frictional contact conditions . . . 52
4.2 Semi-smooth NEWTON method . . . 53
4.3 Consistent linearization . . . 55
4.3.1 Force residual . . . 55
4.3.2 Complementarity function - normal direction . . . 55
4.3.3 Complementarity function - tangential direction . . . 56
4.4 Primal-dual active set algorithm . . . 57
4.5 Algebraic representation . . . 58
4.6 Examples . . . 61
4.6.1 HERTZian contact . . . 61
4.6.2 Frictional beam contact problem . . . 65
4.6.3 Two elastic beams . . . 67
4.6.4 Ironing problem . . . 70

5 Frictional contact problem with wear 75
5.1 Overview on wear mechanisms and motivation . . . 75
5.2 ARCHARD's law of wear . . . 78
5.3 Wear with internal state variable approach . . . 80
5.3.1 Boundary value problem of frictional contact with wear . . . 80
5.3.2 Weak form and finite element discretization . . . 80
5.3.3 Solution within the frictional contact framework . . . 82
5.4 Examples . . . 83
5.4.1 HERTZian contact with wear . . . 83
5.4.2 Oscillating beam . . . 84
5.5 Modeling contact surface evolution with ALE approach . . . 86
5.5.1 Idea of using an ALE approach resolved with a fractional-step strategy 86
5.5.2 ALE kinematics . . . 88
5.5.3 Solution algorithm . . . 91
5.5.4 Finite element implementation . . . 92
5.6 Examples . . . 96
5.6.1 Arbitrary mesh movement on rectangle . . . 96
5.6.2 Surface evolution . . . 98
5.6.3 Oscillating block on cylinder . . . 99

6 Fully coupled thermomechanical contact problem 103
6.1 Problem formulation . . . 103
6.1.1 Balance of linear momentum . . . 104
6.1.2 Energy balance, entropy inequality . . . 104
6.1.3 Mechanical contact constraints . . . 104
6.1.4 Laws of thermodynamics at the contact interface . . . 104
6.1.5 Boundary value problem of thermomechanical contact . . . 106
6.2 Weak form . . . 106
6.2.1 Energy balance equations . . . 107
6.2.2 Laws of thermodynamics at the contact interface . . . 108
6.2.3 Summarized weak form . . . 108
6.3 Finite element discretization . . . 109
6.3.1 Shape functions . . . 109
6.3.2 Discrete energy balance equation . . . 111
6.3.3 Discrete thermal contact condition . . . 111
6.3.4 Summarized discrete form . . . 113
6.4 Partitioned solution scheme . . . 113
6.4.1 NEWTON algorithm for thermal field . . . 113
6.4.2 Linearization and algebraic representation . . . 114
6.4.3 Partitioned solution scheme . . . 115
6.5 Outlook to monolithic solution scheme . . . 116
6.5.1 Semi-smooth NEWTON method for fully coupled problem . . . 117
6.5.2 Linearization and algebraic representation . . . 117
6.6 Examples . . . 120
6.6.1 Heat conduction over non matching grids . . . 120
6.6.2 Rotating disc . . . 122
6.6.3 Temperature balancing blocks . . . 124
6.6.4 Block between plates . . . 127

7 Conclusion and outlook 129
7.1 Conclusion . . . 129
7.2 Outlook . . . 130

Glossary

Abbreviations

ALE	Arbitrary LAGRANGEan-EULERian
FEM	finite element method
KKT	KARUSH-KUHN-TUCKER
NTS	node-to-segment
PDASS	primal-dual active set strategy
STS	segment-to-segment

General indices and symbols

$(\cdot)^{(1)}$	associated with slave body
$(\cdot)^{(2)}$	associated with master body
$(\cdot)_c$	associated with contact
$(\cdot)_n$	quantity in normal contact direction
$(\cdot)_\tau$	quantity in tangential contact plane
$(\cdot)^h$	discretized entity
$(\cdot)_{\boldsymbol{\phi}_t}$	associated with material mapping (ALE formulation)
$(\cdot)_{\boldsymbol{\psi}_t}$	associated with spatial mapping (ALE formulation)
$\tilde{(\cdot)}$	associated with alternative (new) mapping (ALE formulation)

Operators

$\frac{\mathrm{d}}{\mathrm{d}t}(\cdot) = \dot{(\cdot)}$	material time derivative
$\mathrm{Grad}\,(\cdot)$	gradient operator, with respect to material configuration
$\mathrm{grad}\,(\cdot)$	gradient operator, with respect to spatial configuration
$\mathrm{Grad}_{\boldsymbol{\mathcal{X}}}(\cdot)$	gradient operator, with respect to reference configuration (ALE formulation)
$\mathcal{L}_v$	LIE-derivative

Nomenclature

t	time
T	total time
Ω_0	domain, material configuration
Ω_t	domain, spatial configuration
γ	boundary, spatial configuration

$\boldsymbol{\varphi}_t$	motion
$\mathbf{X}$	material points / coordinates
$\mathbf{x}$	spatial points / coordinates
$\mathbf{u}$	displacement field
$\mathbf{v}$	velocity field
$\mathbf{a}$	acceleration field
$\mathbf{F}$	material deformation gradient
J	JACOBIan determinant
$\mathbf{E}$	GREEN-LAGRANGE strain tensor
$\mathbf{e}$	EULER-ALMANSI strain tensor
$\mathbf{I}$	identity tensor
$\mathbf{T}$	surface traction vector, material configuration
$\mathbf{t}$	surface traction vector, spatial configuration
$\mathbf{N}$	surface normal, material configuration
$\mathbf{n}$	surface normal, spatial configuration
$\boldsymbol{\sigma}$	CAUCHY stress tensor
$\mathbf{P}$	first PIOLA-KIRCHHOFF stress tensor
$\mathbf{S}$	second PIOLA-KIRCHHOFF stress tensor
m	mass
ρ_0	material density
ρ	spatial density
$\hat{\mathbf{b}}_0$	prescribed body force, material configuration
$\hat{\mathbf{b}}$	prescribed body force, spatial configuration
$\hat{\mathbf{t}}_0$	prescribed surface traction, material configuration
$\hat{\mathbf{t}}$	prescribed surface traction, spatial configuration
e	internal energy per unit mass
$\mathbf{Q}$	heat flux, material configuration
$\mathbf{q}$	heat flux, spatial configuration
$\hat{r}$	prescribed heat source per unit mass
$\boldsymbol{d}$	rate of deformation tensor
η	entropy per unit spatial volume
θ	temperature
$\mathcal{D}_{int}$	internal dissipation per unit mass
ψ	HELMHOLTZ free energy per unit mass
Ψ	HELMHOLTZ free energy per unit material volume
Γ_c	contact boundary, material configuration
γ_c	contact boundary, spatial configuration
Γ_σ	boundary with NEUMANN conditions, material configuration
γ_σ	boundary with NEUMANN conditions, spatial configuration

Γ_u	boundary with DIRICHLET conditions, material configuration
γ_u	boundary with DIRICHLET conditions, spatial configuration
g	normal gap
$\mathbf{g}$	gap vector
P	contact surface mapping
$\hat{\mathbf{X}}^{(2)}$	projection point, material configuration
$\hat{\mathbf{x}}^{(2)}$	projection point, spatial configuration
$\mathcal{A}^{(2)}$	parameter space of master surface
$\mathbf{\Psi}_0^{(2)}$	mapping of master parameter space to material configuration
$\mathbf{\Psi}_t^{(2)}$	mapping of master parameter space to spatial configuration
$\mathbf{T}_\alpha$	slip advected bases, material configuration
$\mathbf{t}_\alpha$	slip advected bases, spatial configuration
$\boldsymbol{V}_{T,rel}$	convective tangential relative velocity, material configuration
$\boldsymbol{v}_{T,rel}$	convective tangential relative velocity, spatial configuration
$\mathbf{v}_{\tau,rel}$	tangential relative velocity
$\boldsymbol{\tau}^\xi$	unit tangent vector, ξ-direction
$\boldsymbol{\tau}^\eta$	unit tangent vector, η-direction
$\mathbf{t}_{c,0}$	contact traction, material configuration
$\mathbf{t}_c$	contact traction, spatial configuration
p_n	contact normal pressure
$\mathbf{t}_\tau$	vector containing tangential components of contact traction
μ	friction coefficient
$\hat{\mathbf{u}}$	prescribed displacement
ϵ_N	penalty parameter, normal direction
ϵ_T	penalty parameter, tangential plane
$\boldsymbol{\lambda}$	LAGRANGE multiplier
G	virtual work
$G^{int,ext}$	virtual work from internal and external forces
G^c	contact virtual work
$\mathbf{w}$	test function for linear momentum equation
$\delta\mathbf{u}$	virtual displacements
$\delta\boldsymbol{\lambda}$	test function for contact conditions
$\mathbf{d}_j$	nodal displacements
$\delta\mathbf{d}_j$	nodal virtual displacements
$\mathbf{z}_j$	nodal LAGRANGE multipliers
$\delta\mathbf{z}_j$	nodal test function values
$\mathbf{d}$	vector of nodal displacements
$\delta\mathbf{d}$	vector of nodal virtual displacements
N	standard shape function

Φ	dual shape function
$\mathbf{z}$	vector of nodal LAGRANGE multipliers
n^{sl}	number of slave nodes
n^{m}	number of master nodes
n^{a}	number of active nodes
n^{stick}	number of stick nodes
n^{slip}	number of slip nodes
$\mathbf{D}$	mortar matrix, related to slave side
$\mathbf{M}$	mortar matrix, related to slave and master side
$\mathcal{N}$	set of remaining nodes
$\mathcal{S}$	set of slave nodes
$\mathcal{M}$	set of master nodes
$\mathcal{I}$	set of inactive nodes
$\mathcal{A}$	set of active nodes
$\mathcal{S}t$	set of stick nodes
$\mathcal{S}l$	set of slip nodes
$\mathbf{f}^{int}$	vector of internal forces
$\mathbf{f}^{ext}$	vector of external forces
$\mathbf{f}^{c}$	vector of contact forces
$\mathbf{n}_j$	nodal outward unit normal vector
$\boldsymbol{\tau}_j^{\xi}$	nodal unit tangent vector, ξ-direction
$\boldsymbol{\tau}_j^{\eta}$	nodal unit tangent vector, η-direction
$\boldsymbol{\tau}_j$	nodal matrix of aggregated tangent vectors
n_{ele}^{j}	number of slave elements adjacent to slave node j
n_{gp}	number of GAUSSian integration points
w_{gp}	GAUSSian integration weights
$\tilde{g}_j$	nodal weighted gap
$\tilde{\mathbf{g}}_j$	nodal weighted gap vector
$\tilde{\mathbf{v}}_{\tau j}$	nodal weighted tangential relative velocity
$\tilde{\mathbf{u}}_{\tau j}$	nodal weighted tangential relative slip increment
Δt	time increment
C_{nj}	complementarity function for normal direction
$\mathbf{C}_{\tau j}$	complementarity function for tangential direction
c_n	parameter for complementarity functions
c_t	parameter for complementarity functions
ϵ_r	NEWTON convergence tolerance of choice
E	YOUNG's modulus
ν	POISSON's ratio
w	accumulated amount of wear

k_w	wear coefficient
Δw	wear increment
Ω	domain, reference configuration (ALE formulation)
$\Omega_{0,t}$	domain, material configuration (ALE formulation)
$\Omega_{t,t}$	domain, spatial configuration (ALE formulation)
$\boldsymbol{\mathcal{X}}$	reference points / coordinates (ALE formulation)
$\boldsymbol{\phi}_t$	material mapping (ALE formulation)
$\boldsymbol{\psi}_t$	spatial mapping (ALE formulation)
$\boldsymbol{\chi}_t$	advection mapping (ALE formulation)
$\Delta\tilde{w}_j$	nodal weighted wear increment
$\tilde{g}_j^w$	nodal weighted gap including wear
Δw_j	nodal wear increment
n_{ele}	number of element nodes
$\boldsymbol{\mathcal{X}}^{ele}$	vector of element reference positions
$\mathbf{X}^{ele}$	vector of element material positions
Γ_q	boundary with thermal NEUMANN conditions, material configuration
γ_q	boundary with thermal NEUMANN conditions, spatial configuration
Γ_θ	boundary with thermal DIRICHLET conditions, material configuration
γ_θ	boundary with thermal DIRICHLET conditions, spatial configuration
c	heat capacity
k_θ	thermal conductivity
$\hat{q}_0$	prescribed heat flux, material configuration
$\hat{\theta}$	prescribed temperature
$q_{c,0}$	heat flux at contact boundary, material configuration
q_c	heat flux at contact boundary, spatial configuration
e_c	surface density of internal energy at contact surface
θ_c	contact interface temperature
α_c	heat transfer parameter
$\bar{\alpha}_c$	original heat transfer parameter
v	test function for energy balance equation
$\delta\theta$	virtual temperature
G_θ	weak energy balance equation
$G_\theta^{int,ext}$	internal and external contributions to weak energy balance equation
G_θ^c	contact contribution to weak energy balance equation
λ_θ	thermal LAGRANGE multiplier
$\delta\lambda_\theta$	test function for thermal contact condition
$\boldsymbol{\theta}$	vector of nodal temperatures
$\delta\boldsymbol{\theta}$	vector of nodal virtual temperatures
$\mathbf{z}_\theta$	vector of nodal thermal LAGRANGE multipliers

$f^D_{m,j}$	nodal mechanical dissipation, master side
$f^D_{s,j}$	nodal mechanical dissipation, slave side
$\mathbf{f}^D$	vector of nodal mechanical dissipations, master side
$\mathbf{f}^{int}_\theta$	vector of internal heat flux
$\mathbf{f}^{ext}_\theta$	vector of external heat flux
$\mathbf{f}^c_\theta$	vector of heat flux at the contact interface
ϵ_u	displacement increment tolerance of choice , partitioned scheme
ϵ_θ	temperature increment tolerance of choice, partitioned scheme
α_T	coefficient of thermal expansion

1 Introduction

This thesis is concerned with frictional contact analysis for finite deformations. It includes the treatment of wear and the extension to the multiphysics problem of thermomechanical contact.

For the numerical solution scheme, nonlinear finite elements are used. Regarding contact, three methods are predominant within this work: The mortar approach is applied for the discretization of contact surfaces and dual LAGRANGE multipliers are used for contact constraint enforcement. To overcome difficulties associated with contact conditions of multivalued character and formulated in terms of inequalities, the semi-smooth NEWTON method is utilized.

This chapter motivates the treatment of contact, wear, and thermomechanical contact in numerical simulations. It contains a review of existing methods and from these, the objectives and classification of the new aspects of the presented work are introduced. Finally, an overview on the structure of this thesis is given.

1.1 Motivation

Contact mechanics and friction are fundamental disciplines in engineering and applied science which describe potential surface interactions of solids. They are of interest in various fields as, for example, crash-tests, metal forming, and machining in mechanical engineering applications or bridge bearings in the area of civil engineering. But also for non-traditional problems, frictional contact is relevant. In biomechanic applications, examples are the clamping of the aorta during cardiopulmonary bypass surgery, the placement of stents in arteries, or the implantation of artificial joint prostheses.

Some of the above mentioned applications are already strongly connected to wear and thermomechanical effects. This is, for example, considering the contact in joint protheses, where wear unavoidably represents a limitation to the lifetime of components, see LONG and RACK [91]. Another example is during metal forming, where temperature can heavily influence the manufacturing process, see NEUGEBAUER et al. [99].

Initially, the damage mechanism of fretting fatigue in turbine or fan disc to blade joints in aircraft engines was the primary motivation for this work. These thermally highly loaded connections rely on frictional contact and are subjected to small-amplitude oscillatory movements. Possible damage can either be wear or, when cracks appear, fretting fatigue, see HILLS and NOWELL [51].

In general, numerical simulations can contribute to the design process and potentially reduce or avoid expensive experiments. As a typical example, the crash-test in the automotive industry is well known. Besides aiding the design process, they are used for interpretation and verification of experimental findings or physical observations. They can also shed light on occurring effects and help to better understanding complex phenomena. This could be, for example, the above mentioned fretting fatigue failure. Numerical analysis can also help to extrapolate known

behavior towards new limits, where experiments are difficult to carry out or data are difficult to obtain. Examples in a large number can be found in the field of biomechanics, as, for instance, the change of blood flow during the above mentioned aorta clamping.

Many of the above given contact examples entail finite deformations. According to demands, these nonlinearities have to be taken into account in numerical contact simulations. Furthermore, coupling effects from the thermal field or wear may also become necessary to consider. Accurate, robust, and highly efficient methods are still matter of current research. This work contributes to this.

1.2 Existing methods and objectives

This thesis is divided into three main parts: The development of a finite deformation frictional contact formulation, its extension to wear and its extension to the fully coupled thermomechanical contact problem. This section gives an overview of existing methods and classifies the new aspects of this work.

1.2.1 Frictional contact problem

The solution of finite deformation contact problems is challenging due to the strong nonlinearities involved. They originate from finite deformations and contact conditions. The latter are non-smooth, of multivalued character, and have to be satisfied on *a priori* unknown contact regions. The inclusion of friction laws, as for example the one of COULOMB, complicates the problem even more. It makes the determination of the frictional traction path dependent and represents a nonsymmetric problem. This aspect stems from the fact that frictional traction is proportional to the contact pressure during sliding. However, the contact pressure is independent of the frictional traction, see COULOMB's law stated in equations (2.63) - (2.66). A comprehensive overview on contact mechanics in general and the related computational methods can be found in, for example, the contributions of LAURSEN [83] and WRIGGERS [144].

Numerical simulation of contact needs two basic ingredients: A technique to discretize the contact surface and a scheme to enforce the contact constraints. For both, several approaches are available in literature. Regarding the first aspect, the most prevalent method is a node-to-segment approach (NTS) which enforces contact conditions at specific collocation points. Due to the well known disadvantages of NTS, segment-to-segment approaches (STS), especially the mortar method, have become very popular in recent years. The mortar method was originally introduced in the context of domain decomposition techniques in BERNARDI et al. [11] and is characterized by the weak formulation of the contact conditions across an interface instead of strong, pointwise constraints. Both methods and their occurrence in literature are explained later within this work. For completeness, a so-called contact domain method as recently presented in HARTMANN et al. [41, 42], OLIVER et al. [102], and WEYLER et al. [137] shall be mentioned. Therein, an intermediate domain of the same dimension as the contacting bodies is utilized.

The second aspect, i.e. the enforcement of contact constraints, is realized mainly by three methods: The penalty approach, the augmented LAGRANGEan method resolved with USZAWA's scheme, and the LAGRANGE multiplier method. Their functioning and occurrence in literature

are explained in detail within the further course of this work. The latter method brings the advantage of an exact fulfillment of contact constraints without regularization as in the first case, or at the extra computational costs required by the second case. However, the drawback is usually an increased system of equations with LAGRANGE multipliers as additional primary unknowns, yielding a saddle point-type problem. This issue can be addressed by using approaches based on the NITSCHE method as presented in HEINTZ and HANSBO [43], where LAGRANGE multipliers can be eliminated. But there again a penalty factor is introduced, which can influence the quality of results. A further possibility is the application of so-called dual LAGRANGE multiplier spaces as originally introduced in WOHLMUTH [140]. These alternative spaces allow for an efficient local elimination of the discrete LAGRANGE multipliers by static condensation and the unknowns of the remaining problem are the displacements only. Throughout this work, the mortar method is applied for contact surface discretization and for contact constraint enforcement, the focus is on using dual LAGRANGE multipliers.

As solution algorithm, the semi-smooth NEWTON method is applied. It can be interpreted as a primal-dual active set strategy, see HINTERMÜLLER et al. [52], and is based on the reformulation of contact conditions in so-called complementarity functions. These are not differentiable in the classical sense, but smooth enough to be treated with NEWTON-type methods. For frictional contact problems, such algorithms were early presented in ALART and CURNIER [2] and in modified form in CHRISTENSEN et al. [16] for small deformations. This was enhanced to elasto-plastic frictional contact problems in CHRISTENSEN [15]. In recent years, such an approach with alternative complementarity functions was proposed in HÜEBER et al. [54, 56, 59] for the two-body frictional contact problem in the context of small deformations. This algorithm was extendend to finite deformations for the 2D and 3D frictionless cases by POPP et al. [110, 111].

This thesis treats the extension of that approach towards 2D and 3D finite deformation frictional contact. To the author's knowledge, it is the first implementation of this problem in the context of the mortar method and dual LAGRANGE multipliers with consistent linearization. For friction, COULOMB's law is applied and the accompanying rate measure, the tangential relative velocity, is formulated in a frame objective way. The new aspects considering the 2D problem have already been published by the author in GITTERLE et al. [35].

The proposed method contains three main advantages: Firstly, there is the excellent convergence behavior of the semi-smooth NEWTON method obtained from the consistent linearization of all deformation and LAGRANGE multiplier dependent terms. Secondly, the additional LAGRANGE multipliers can easily be eliminated from the system of equations since they are chosen from the above mentioned dual spaces. And finally, from the application of a semi-smooth NEWTON method, nonlinearities stemming from contact (search for inactive, stick and slip set) and all other nonlinearities (i.e. geometrical and material ones) are treated in one single iterative scheme. These three advantages ensure that a robust, accurate and highly efficient algorithm for the numerical simulation of three dimensional finite deformation frictional contact problems is obtained.

1.2.2 Frictional contact problem with wear

When considering finite deformation frictional contact problems with wear, besides the governing equations covering contact, a wear evolution law has additionally to be taken into account. For this, often and widely used is the phenomenological law of ARCHARD [4]. Although be-

ing simple, it sufficiently covers the material removal caused from this complex physical phenomenon in a multitude of applications. Wear, even to a small extent, can strongly influence the contact problem. This is because material loss in the contact zone may lead, especially for harder materials, to a significant redistribution of contact tractions. This, in turn, affects the wear evolution. Therefore, these coupling effects have to be considered in numerical simulations.

In literature, there are mainly two approaches that consider wear in finite element analysis: Firstly, the usage of an internal state variable and secondly, the modeling of contact surface evolution. The internal state variable identifies the so far accumulated wear as an additional gap, the so-called wear-gap. It enters the contact conditions by mathematically increasing the distance between the worn bodies. Consequently, wear causes contact to be reached only at a later stage. This approach does not model contact surface changes of participating bodies and is therefore mainly suitable for problems leading to a small amount of wear. It has already been used in STRÖMBERG et al. [131] and has successfully been applied in, for example, AGELET DE SARACIBAR and CHIUMENTI [1], IREMAN et al. [63, 64], SALLES et al. [123], and STRÖMBERG et al. [128, 129, 130] for small and finite deformations.

Modeling of contact surface evolution may become necessary where shape changes due to wear are finite, as for example, contact and wear of rubber like materials. Or for problems, where contact tractions are extremely sensitive to the curvature of contacting surfaces. Such methods have been presented in literature in various forms. There is the contribution of PÕDRA and ANDERSSON [104], which has been improved in ÖQVIST [103], MCCOLL et al. [94], and PAULIN et al. [107]. It consists of a finite element analysis treating frictional contact within a commercial software and a subsequent evaluation of the worn material. With this, the original reference geometry in the input file is changed. In order to overcome problems with degenerated finite elements, the relocation of contact surface nodes has been extended to nodes within so-called wear boxes in the latter work. In MOLINARI et al. [97], the possible distortion of elements due to geometry adaption is solved via a continuous adaptive meshing strategy. Finally, a recent contribution from LENGIEWICZ and STUPKIEWICZ [87] models contact surface evolution with the introduction of three configurations to account for a time dependent material configuration.

The present work extends the above described frictional contact formulation towards wear. It is realized using both the internal state variable approach and a model for contact surface evolution. Here, an Arbitrary LAGRANGEan-EULERian (ALE) formulation resolved with a fractional-step strategy is applied. This is frequently used for finite stain plasticity, see for example ARMERO and LOVE [5] or HUERTA and CASADEI [60], and is firstly transferred to wear problems in this thesis. Within a single time step, it results in a LAGRANGEan step followed by an EULERian one, where the mesh is adjusted due to wear. The second new aspect in this field is, to the author's knowledge, the numerical treatment of wear in the mortar context.

The proposed methods bring clear benefits. Firstly, they allow the treatment of wear with the advantages of the mortar method as well as using dual LAGRANGE multipliers and the semi-smooth NEWTON method as described above. Secondly, for modeling contact surface evolution, the tried and tested structural contact solver can be applied with almost no modifications due to the usage of the fractional-step strategy.

1.2.3 Fully coupled thermomechanical contact problem

Thermomechanical contact represents a multiphysics problem. Additional to the purely mechanical problem, also the thermal field has to be considered in numerical simulations. The problems couple within the bulk equations and at the contact interface. Regarding the latter, this allows heat conduction over contacting surfaces as well as production of heat from frictional dissipation.

In literature, thermomechanical contact problems are treated mainly in the context of node-to-segment approaches for small and finite deformations. Examples are the contributions of LAURSEN [82, 83], OANCEA and LAURSEN [101], SIMO and MIEHE [125], WRIGGERS and MIEHE [146], and ZAVARISE et al. [151]. HÜEBER and WOHLMUTH [56] were the first to treat thermomechanical contact problems with the mortar method in the context of dual LAGRANGE multipliers. This discretization technique is also used in HANSEN [38] and HESCH and BETSCH [46], where in the latter however, it is used for domain decomposition in thermodynamics.

In the last part of the presented work, the finite deformation frictional contact formulation is extended towards thermomechanical contact. It is based on the contribution of HÜEBER and WOHLMUTH [56], where only small deformation problems were considered. Thus, the new aspect here is the first implementation of contact related terms for finite deformations in the frame of the mortar and dual LAGRANGE multiplier method. It contains a consistent linearization for both the partitioned and the initially treated monolithic solution approach.

The advantages resemble those of the purely mechanical contact problem: Firstly, dual LAGRANGE multipliers are also used for the thermal field in order for them to be easily condensated from the system of equations. Secondly, excellent convergence behavior exists for the semi-smooth NEWTON method applied to the monolithic system. It is obtained from consistent linearization.

1.2.4 Summary of objectives

As can be summarized from above sections, the objectives of this thesis are as follows. They are accompanied by the new aspects of this work.

1. Implementation of a finite deformation frictional contact formulation using the mortar method and dual LAGRANGE multipliers with consistent linearization.

2. Inclusion of wear in the frictional contact formulation in 1. using both an internal state variable approach and an ALE description resolved with a fractional-step strategy.

3. Extension of the frictional contact formulation in 1. towards finite deformation thermomechanical contact problems using the mortar method and dual LAGRANGE multipliers.

1.3 Outline

This thesis is organized as follows:

In Chapter 2, the continuous setting of the finite deformation frictional contact problem is presented. It contains a brief overview of nonlinear continuum mechanics for solids and the

introduction of basic equations concerning frictional contact before the actual boundary value problem is given.

Chapter 3 gives an overview of methods of constraint enforcement and contact surface discretization. Committed to the dual LAGRANGE multiplier and mortar approach, the weak form and the finite element discretization are given.

The contact problem is solved with the application of a semi-smooth NEWTON method. This is presented in Chapter 4. It contains the reformulation of contact conditions in complementarity functions, the consistent linearization of contact related terms, and the algebraic representation of the problem. Several numerical examples demonstrate the accuracy, robustness, and efficiency of the proposed method.

In Chapter 5, the developed finite deformation frictional contact formulation is extended towards wear. It contains both the approaches using an internal state variable and an ALE description resolved with a fractional-step strategy. For both methods, appropriate numerical examples are presented for illustration and underlying respective advantages.

In Chapter 6, the developed finite deformation frictional contact formulation is enhanced to the multiphysics problem of thermomechanical contact. It includes the formulation of the fully coupled boundary value problem, its weak form, and finite element discretization. The solution is performed with mainly a partitioned approach, but also a monolithic scheme. Several numerical examples demonstrate the accuracy and efficient of capturing strong coupling effects of the proposed methods.

The scope of Chapter 7 is to summarize the main achievements of this work and to suggest improvements and directions for further work.

2 Frictional contact - problem formulation

Within this chapter, the continuous setting of the finite deformation frictional contact problem is presented. A brief overview on nonlinear continuum mechanics for solids in Section 2.1 and the introduction of basic equations concerning frictional contact related issues in Section 2.2 precede the final description in its strong form in Section 2.3.

2.1 Basic continuum mechanics for solids

This section presents the basic continuum equations for nonlinear solid mechanics. It is not aimed for completeness in every detail, but for an overview on this topic as basis for the contact problem focused on in this work. For a more comprehensive review, the reader is referred, for example, to the books of BELYTSCHKO et al. [9], CRISFIELD [17, 18], HOLZAPFEL [53], or WRIGGERS [145].

2.1.1 Kinematics

Kinematics are used to describe the motion of a body without keeping its cause in mind. In the continuum mechanics framework, the body is assumed to be homogeneous. In general, molecular, grain, or crystal structures are ignored, see BELYTSCHKO et al. [9]. Kinematics encompass the motion and possible deformation.

Motion

Starting from an initial state at time $t = 0$, a body experiences motion with ongoing time $t \in [0, T]$ as shown in Figure 2.1. The domain of the body in its initial state is denoted by $\Omega_0 \subset \mathbb{R}^3$ and called initial configuration. In its current state at time t, it is denoted by $\Omega_t \subset \mathbb{R}^3$ and called current configuration. The motion is described by the unique and continuously differentiable mapping $\boldsymbol{\varphi}_t$, transforming the initial into the current configuration

$$\boldsymbol{\varphi}_t : \Omega_0 \rightarrow \Omega_t \ . \tag{2.1}$$

Consequently, the position vector of material points $\mathbf{X} \in \Omega_0$ of the initial configuration is connected to its position vector $\mathbf{x} \in \Omega_t$ in the current configuration by the mapping $\boldsymbol{\varphi}_t$ at a fixed time t as

$$\mathbf{x} = \boldsymbol{\varphi}_t \left(\mathbf{X}, t \right) \ . \tag{2.2}$$

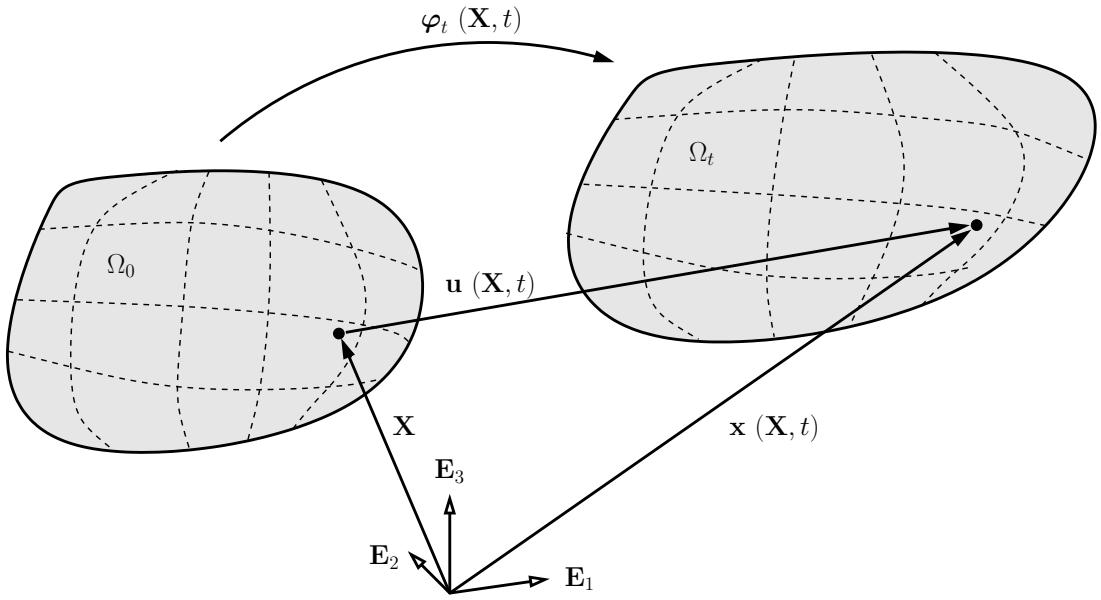

Figure 2.1: Initial (left) and current (right) configuration of a body, LAGRANGEan description.

The displacement $\mathbf{u}$ of a material point $\mathbf{X}$ is the difference between its current and initial position at time t, i.e.

$$\mathbf{u}\,(\mathbf{X},t) = \mathbf{x}\,(\mathbf{X},t) \;-\; \mathbf{X}\;. \tag{2.3}$$

The velocity $\mathbf{v}$ is the temporal change of the material position vector. It is evaluated by the time derivation of the motion $\boldsymbol{\varphi}_t$ for fixed $\mathbf{X}$. Therefore, it is called material time derivative or total derivative and is defined as

$$\mathbf{v}\,(\mathbf{X},t) = \frac{\mathrm{d}\boldsymbol{\varphi}_t\,(\mathbf{X},t)}{\mathrm{d}t} = \frac{\mathrm{d}\mathbf{u}\,(\mathbf{X},t)}{\mathrm{d}t} = \dot{\mathbf{x}}\,(\mathbf{X},t)\;. \tag{2.4}$$

The acceleration $\mathbf{a}$ is the rate of change of the velocity $\mathbf{v}$ of a material point $\mathbf{X}$ and with this, the material derivative of the velocity. It reads

$$\mathbf{a}\,(\mathbf{X},t) = \frac{\mathrm{d}\mathbf{v}\,(\mathbf{X},t)}{\mathrm{d}t} = \frac{\mathrm{d}^2\mathbf{u}\,(\mathbf{X},t)}{\mathrm{d}t} = \dot{\mathbf{v}}\,(\mathbf{X},t)\;. \tag{2.5}$$

It has to be noted that all above expressions, i.e. the motion $\boldsymbol{\varphi}_t\,(\mathbf{X},t)$, the current configuration $\mathbf{x}\,(\mathbf{X},t)$, the displacement $\mathbf{u}\,(\mathbf{X},t)$, the velocity $\mathbf{v}\,(\mathbf{X},t)$, and the acceleration $\mathbf{a}\,(\mathbf{X},t)$, are formulated in terms of the initial coordinates $\mathbf{X}$. With this, they are written in the LAGRANGEan way. More information about the LAGRANGEan formulation and especially its relation to the EULERian one is focused on in the next section.

Nomenclature, LAGRANGEan and EULERian description

The nomenclature used so far contains initial and current configuration. Also the term “material position vector” has been introduced. In this section, denotation is widened and the kinematic

description of the motion of bodies is also regarded from the EULERian point of view. This leads to partly adjusted names.

First of all, material position vectors already introduced above are considered again. They are associated with continuum particles or material points in the initial configuration. Therefore, the initial configuration is often also called material configuration. Unless specified otherwise, the configuration Ω_0 is assumed to be undeformed and stress free, thus a further name is undeformed configuration. The equivalence to this nomenclature in the current configuration Ω_t is spatial and deformed configuration.

In the section above, the motion and all derived quantities are referred to the initial state Ω_0 of the body with its material position vectors $\mathbf{X}$. In that case, the initial configuration acts as reference configuration resulting in the material or LAGRANGEan description. This description implies paying attention to material points $\mathbf{X}$. It is observed what happens to them with ongoing time t starting in the initial configuration $t = 0$.

Alternatively, the motion or any other related quantity can be described with respect to the spatial coordinates $\mathbf{x}$ and time t. This so-called spatial or EULERian form is not based on tracking of material points $\mathbf{X}$ but rather on the inspection of fixed control points $\mathbf{x}$ in space. Essential therein is that these control points are totally independent of material points, whereby motion related quantities are formulated for alternating material points with ongoing time t. Consequently, material or total time derivation leads to the typical convection terms as shown in the following. An exemplary motion is described by means of time dependent velocities at fixed spatial coordinates $\mathbf{x}$ as $\mathbf{v}(\mathbf{x}, t)$. In contrast to the LAGRANGEan way, the reference configuration here coincides with the spatial one. In order to obtain the acceleration field, total time derivation requires the expression of spatial coordinates in $\mathbf{v}(\mathbf{x}, t)$ as a function of material coordinates. The application of the chain rule leads to

$$\mathbf{a}(\mathbf{x}, t) = \frac{\mathrm{d}}{\mathrm{d}t}\mathbf{v}(\mathbf{x}, t) = \frac{\partial \mathbf{v}}{\partial \mathbf{x}} \cdot \frac{\partial \boldsymbol{\varphi}_t(\mathbf{X}, t)}{\partial t} + \frac{\partial \mathbf{v}}{\partial t} = \operatorname{grad} \mathbf{v} \cdot \mathbf{v} + \frac{\partial \mathbf{v}}{\partial t} \,. \tag{2.6}$$

The first term on the right hand side of (2.6) is the convective term, which is often also called transport term. The second one is the spatial time derivative.

In fluid mechanics, the EULERian description is widely used as it is often unnecessary or impossible to describe the motion with respect to an initial configuration. For example, it does not matter where the fluid, which is circulating around a flag, comes from. In solid mechanics in contrast, the stress generally depends on the deformation with what the knowledge of an undeformed or initial state is necessary. Because of this, the LAGRANGEan description is prevalent there. It is also used for the frictional contact formulation with and without thermal effects throughout Chapters 2, 3, 4, and 6.

Besides the LAGRANGEan and EULERian description, there also exists the Arbitrary LAGRANGEan EULERian (ALE) formulation. There, the reference frame is neither the material configuration as in the LAGRANGEan form nor the spatial configuration as in the EULERian form. The motion and all related quantities are referred to, as the name says, an arbitrary frame. In Chapter 5, ALE formulations within a staggered scheme are used to model contact surface evolution due to wear.

Deformation gradient

In general, the motion of a continuum goes along with deformation. For this, the deformation gradient is an essential kinematic quantity. It is defined in its material form as

$$\mathbf{F}\left(\mathbf{X},t\right) := \frac{\partial \boldsymbol{\varphi}_t}{\partial \mathbf{X}} = \frac{\partial \boldsymbol{x}}{\partial \mathbf{X}} = \operatorname{Grad}\mathbf{x}\ . \tag{2.7}$$

By its help, an infinitesimal line element $\mathrm{d}\mathbf{X}$, area element $\mathrm{d}\mathbf{A}$, or volume element $\mathrm{d}V$ can be mapped from the intital configuration to its spatial counterpart. This is given mathematically as

$$\mathrm{d}\mathbf{x} = \mathbf{F}\cdot\mathrm{d}\mathbf{X}\ , \tag{2.8}$$

$$\mathrm{d}\mathbf{a} = J\ \mathbf{F}^{-\mathrm{T}}\cdot\mathrm{d}\mathbf{A}\ , \tag{2.9}$$

$$\mathrm{d}v = J\,\mathrm{d}V\ , \tag{2.10}$$

where $J = \det\mathbf{F} > 0$ is the JACOBIan determinant of the deformation gradient $\mathbf{F}$ and $\mathbf{F}^{-\mathrm{T}}$ is the transpose of the inverse tensor of $\mathbf{F}$. Due to the properties of the mapping $\boldsymbol{\varphi}_t$, the inverse tensor $\mathbf{F}^{-1}$ is well defined as

$$\mathbf{F}^{-1} = \frac{\partial \boldsymbol{X}}{\partial \mathbf{x}} = \operatorname{grad}\mathbf{X}\ . \tag{2.11}$$

The deformation gradient $\mathbf{F}$ describes the deformation containing rigid body rotations and stretch and is used for mapping between the initial and spatial configuration as in (2.8) - (2.10). It is basis for strain measures defined in the next section.

Strain measures

In nonlinear mechanics, there are several ways to describe strains in solids. In the following, the most common definitions are discussed. They differ in the configuration they are referred to and if formulated in rate form or not.

A strain measure completely referred to the undeformed configuration is the GREEN-LAGRANGE strain tensor $\mathbf{E}$. It is defined by

$$\mathrm{d}\mathbf{x}\cdot\mathrm{d}\mathbf{x} - \mathrm{d}\mathbf{X}\cdot\mathrm{d}\mathbf{X} = 2\,\mathrm{d}\mathbf{X}\cdot\mathbf{E}\cdot\mathrm{d}\mathbf{X}\ . \tag{2.12}$$

It gives the change in the square of the length of an infinitesimal line segment $\mathrm{d}\mathbf{X}$ in the reference configuration. Using the deformation gradient $\mathbf{F}$, (2.12) can be rewritten as

$$\mathbf{E} = \frac{1}{2}\left(\mathbf{F}^{\mathrm{T}}\cdot\mathbf{F} - \mathbf{I}\right)\ , \tag{2.13}$$

where $\mathbf{I}$ denotes the identity tensor. In contrast, the EULER-ALMANSI strain tensor $\mathbf{e}$ is a spatial strain measure where the above change of squared lengths is now referred to an infinitesimal line segment $\mathrm{d}\mathbf{x}$ in the current configuration. The underlying definition

$$\mathrm{d}\mathbf{x}\cdot\mathrm{d}\mathbf{x} - \mathrm{d}\mathbf{X}\cdot\mathrm{d}\mathbf{X} = 2\,\mathrm{d}\mathbf{x}\cdot\mathbf{e}\cdot\mathrm{d}\mathbf{x} \tag{2.14}$$

can be resolved as

$$\mathbf{e} = \frac{1}{2}\left(\mathbf{I} - \mathbf{F}^{-\mathrm{T}}\cdot\mathbf{F}^{-\mathbf{1}}\right). \tag{2.15}$$

As the deformation gradient $\mathbf{F}$ relates the material and spatial configuration, it can be employed to transfer the two introduced strain measures into each other. From the material strain measure $\mathbf{E}$ to the spatial strain measure $\mathbf{e}$, this is obtained with a so called push-forward operation. The way back, the transition from $\mathbf{e}$ to $\mathbf{E}$, is based on a pull back operation. More about this can be found, for example, in BELYTSCHKO et al. [9].

Besides, there are also strain measures in rate form. Examples are the material velocity gradient $\dot{\mathbf{F}}$ or the material strain rate $\dot{\mathbf{E}}$ which are defined by total time derivation of the deformation gradient $\mathbf{F}$ in the first case and the GREEN-LAGRANGE strain tensor $\mathbf{E}$ in the second case. An additional measure is the rate of deformation tensor $\boldsymbol{d}$ to be evaluated as

$$\boldsymbol{d} = \frac{1}{2}\left(\operatorname{grad}\mathbf{v} + \operatorname{grad}^{\mathrm{T}}\mathbf{v}\right) . \tag{2.16}$$

It has to be pointed out that the above strain definitions are among the most commonly used measures in nonlinear continuum mechanics. But they do not complete the field of strain and strain rate measures at all, a variety of other definitions have been discussed in literature as, for example, in BELYTSCHKO et al. [9], FRENZEL [33], and HOLZAPFEL [53]. In the present work, the introduced GREEN-LAGRANGE strain tensor $\mathbf{E}$ is used.

2.1.2 Stress concept

Stresses are accompanied by the deformation of bodies. As for the strains, there exist various stress measures in nonlinear continuum mechanics. In this section, three of them are considered.

In order to come closer to the concept of stress, an infinitesimal force resultant vector $\mathrm{d}\mathbf{f}_a$ is defined. It is acting at time t on an infinitesimal surface element $\mathrm{d}\mathbf{a} = \mathrm{d}a\,\mathbf{n}$ with area $\mathrm{d}a$ normal to the vector $\mathbf{n}$ on the boundary of that deformed body Ω_t. The quotient of these quantities, as force per unit surface, defines the traction vector

$$\mathbf{t} = \frac{\mathrm{d}\mathbf{f}_a}{\mathrm{d}a} . \tag{2.17}$$

As the resultant force $\mathrm{d}\mathbf{f}_a$ is acting in the current configuration on a surface element $\mathrm{d}\mathbf{a}$ also defined in the current configuration, $\mathbf{t}$ represents a physical occurring state. With that, it is called the true or CAUCHY traction vector. Accordingly, the CAUCHY stress tensor $\boldsymbol{\sigma}$ accounts for the real internal stresses within a body in its current configuration. It is obtained from CAUCHY's theorem

$$\mathbf{t} = \boldsymbol{\sigma} \cdot \boldsymbol{n} , \tag{2.18}$$

which results from equilibrium evaluations at an infinitesimal tetrahedral element.

As balance equations discussed in Section 2.1.3 are requested for the current configuration, the definition of CAUCHY stresses makes sense. On the other hand, the spatial configurations are unknown *a priori*. Therefore, it can be useful to define stress measures for the known material state. In the derivation above, both the force resultant $\mathrm{d}\mathbf{f}_a$ and the infinitesimal surface element $\mathrm{d}a$ with its related normal vector $\mathbf{n}$ are taken from the current configuration. In order to obtain stress measures connected to the material configuration, either one or both quantities are taken from there.

By taking the quotient of the spatial force vector $\mathrm{d}\mathbf{f}_a$ and the area $\mathrm{d}A$ of the surface element $\mathrm{d}\mathbf{A}$ in the reference configuration, the first PIOLA-KIRCHHOFF traction vector $\mathbf{T}$ is obtained as

$$\mathbf{T} = \frac{\mathrm{d}\mathbf{f}_a}{\mathrm{d}A} = \frac{\mathbf{t}\,\mathrm{d}a}{\mathrm{d}A} \ . \tag{2.19}$$

It has the same direction as the CAUCHY traction vector $\mathbf{t}$, but is of different length. The first PIOLA-KIRCHHOFF stress tensor $\mathbf{P}$ is then defined by

$$\mathbf{T} = \mathbf{P} \cdot \mathbf{N} \ , \tag{2.20}$$

where $\mathbf{N}$ is the unit normal vector of the surface element $\mathrm{d}\mathbf{A}$ within the reference configuration. From (2.18), (2.19), and (2.20), $\mathbf{P}$ can be written in terms of the CAUCHY stress tensor $\boldsymbol{\sigma}$ as

$$\mathbf{P} = J\,\boldsymbol{\sigma} \cdot \mathbf{F}^{-\mathrm{T}} \ . \tag{2.21}$$

Here, the mapping of area elements given in (2.9) is used. The first PIOLA-KIRCHHOFF stress tensor is a two field tensor as it combines the spatial force resultant $\mathrm{d}\mathbf{f}_a$ with the material surface element $\mathrm{d}\mathbf{A}$.

A stress measure completely referred to the material configuration is provided by the second PIOLA-KIRCHHOFF stress tensor $\mathbf{S}$. To obtain this measure, also the spatial force resultant $\mathrm{d}\mathbf{f}_a$ is pulled back into its counterpart $\mathrm{d}\mathbf{F}_a$ in the material configuration as

$$\mathrm{d}\mathbf{F}_A = \mathbf{F}^{-1} \cdot \mathrm{d}\mathbf{f}_a \ , \tag{2.22}$$

and the second PIOLA-KIRCHHOFF stress tensor $\mathbf{S}$ reads

$$\mathbf{S} = \mathbf{F}^{-1} \cdot \mathbf{P} = J\,\mathbf{F}^{-1} \cdot \boldsymbol{\sigma} \cdot \mathbf{F}^{-\mathrm{T}} \ . \tag{2.23}$$

2.1.3 Balance principles and entropy

Fundamental principles in continuum mechanics are the balance equations and the entropy inequality principle. They are presented briefly in the following. Since the work focuses on solid mechanics, they are formulated in a LAGRANGEan way. A more detailled and more general presentation, including for example the EULERian description, can be found in common continuum mechanic literature as for example in BELYTSCHKO et al. [9] or HOLZAPFEL [53].

Conservation of mass

The conservation of mass requires the mass m of any material domain Ω_0 to be constant over time t, i.e.

$$m = \int_{\Omega_0} \rho_0 \,\mathrm{d}\Omega_0 = \int_{\Omega_t} \rho \,\mathrm{d}\Omega_t = \text{const} \ . \tag{2.24}$$

Here, ρ_0 is the density of the material configuration and ρ is the density of the spatial configuration. Transferring the spatial density ρ to the material one ρ_0 and considering an arbitrary portion of the body Ω_0 yields the local form of the mass conservation equation in the LAGRANGEan description:

$$\rho\, J = \rho_0 . \tag{2.25}$$

Balance of linear momentum

The balance of linear momentum, also known as conservation of linear momentum, is equivalent to NEWTON's second law of motion. It is therefore a key equation in nonlinear continuum mechanics. It states that the material time derivative of the linear momentum equals the sum of all applied volume and surface forces

$$\frac{\mathrm{d}}{\mathrm{d}t}\int_{\Omega_t}\rho\,\dot{\mathbf{x}}\,\mathrm{d}\Omega_t = \int_{\Omega_t}\hat{\mathbf{b}}\,\mathrm{d}\Omega_t + \int_{\gamma}\hat{\mathbf{t}}\,\mathrm{d}\gamma\;. \tag{2.26}$$

Here, γ is the boundary of the body in its current configuration and $\hat{\mathbf{b}}$ and $\hat{\mathbf{t}}$ are forces acting on the unit deformed volume $\mathrm{d}v$ and on the unit deformed area $\mathrm{d}a$, respectively. With CAUCHY's law (2.18), the traction $\hat{\mathbf{t}}$ can be reformulated as $\hat{\mathbf{t}} = \boldsymbol{\sigma}\cdot\mathbf{n}$. The application of GAUSS' divergence theorem then allows for the conversion of the boundary integral in (2.26) into a domain integral. Since the equation holds for arbitrary portions of the body, the local form of the balance equation is obtained. Referred to the spatial configuration, it reads

$$\mathrm{div}\boldsymbol{\sigma} + \hat{\mathbf{b}} = \rho\,\ddot{\mathbf{x}} \tag{2.27}$$

and, referred to the material configuration, as

$$\mathrm{Div}\mathbf{P} + \hat{\mathbf{b}}_0 = \rho_0\,\ddot{\mathbf{x}}\;, \tag{2.28}$$

where $\hat{\mathbf{b}}_0$ is the corresponding body force acting on the undeformed configuration.

Balance of angular momentum

The balance of angular momentum states that the sum of all moments resulting from acting volume and surface forces is equal to the material time derivative of the angular momentum with respect to an arbitrary point in space. It is obtained from the cross-product of each term in the corresponding linear momentum principle with the position vector $\bar{\mathbf{x}} \in \Omega_t$ as

$$\frac{\mathrm{d}}{\mathrm{d}t}\int_{\Omega_t}\bar{\mathbf{x}}\times\rho\,\dot{\mathbf{x}}\,\mathrm{d}\Omega_t = \int_{\Omega_t}\bar{\mathbf{x}}\times\hat{\mathbf{b}}\,\mathrm{d}\Omega_t + \int_{\gamma}\bar{\mathbf{x}}\times\hat{\mathbf{t}}\,\mathrm{d}\gamma\;. \tag{2.29}$$

Similar to the balance of linear momentum, CAUCHY's and GAUSS' theorems are applied, which finally lead to the symmetry of the CAUCHY stress tensor

$$\boldsymbol{\sigma}^{\mathrm{T}} = \boldsymbol{\sigma}\;. \tag{2.30}$$

Consequently, also the second PIOLA-KIRCHHOFF stress tensor $\mathbf{S}$ is symmetric whereas the first PIOLA-KIRCHHOFF stress tensor $\mathbf{P}$ is not.

Balance of energy

In thermomechanical systems, the balance of energy states that the rate of change of total energy within a body equals the sum of the power produced by external forces plus and the thermal

energy delivered to the body. It is equivalent to the first law of thermodynamics and can be written as

$$\frac{\mathrm{d}}{\mathrm{d}t}\int_{\Omega_t}\rho\left(e+\frac{1}{2}\dot{\mathbf{x}}\cdot\dot{\mathbf{x}}\right)\mathrm{d}\Omega_t=\int_{\Omega_t}\hat{\mathbf{b}}\cdot\dot{\mathbf{x}}+\rho\,\hat{r}\,\mathrm{d}\Omega_t+\int_{\gamma}\hat{\mathbf{t}}\cdot\dot{\mathbf{x}}-\mathbf{q}\cdot\mathbf{n}\,\mathrm{d}\gamma\,. \tag{2.31}$$

In this equation, e is the internal energy per unit mass, $\hat{r}$ denotes the external heat source per unit mass, and $\mathbf{q}$ is the spatial heat flux. The local form of (2.31) is obtained by application of CAUCHY's law and GAUSS' divergence theorem and considering only a local portion of the body. In spatial description, it results in

$$\rho\,\dot{e}=\boldsymbol{\sigma}:\boldsymbol{d}+\rho\,\hat{r}-\operatorname{div}\mathbf{q}\,. \tag{2.32}$$

The tensor product $\boldsymbol{\sigma}:\boldsymbol{d}$ is called the stress power and denotes the rate of internal mechanical work. Using the equivalent $\mathbf{P}:\dot{\mathbf{F}}$, the material form of (2.32) reads

$$\rho_0\,\dot{e}=\mathbf{P}:\dot{\mathbf{F}}+\rho_0\,\hat{r}-\operatorname{Div}\mathbf{Q}\,. \tag{2.33}$$

In this equation, the vector $\mathbf{Q}$ is the heat flux referred to the material configuration and is obtained from $\mathbf{Q}=J\,\mathbf{F}^{-1}\cdot\mathbf{q}$.

Considering purely mechanical problems and neglecting other forms of energy as for example thermal, electric, or chemical energy, the energy balance is not an additional requirement to be satisfied. It is rather a consequence of the balance of linear momentum. Accordingly, as this work considers purely mechanical problems in Chapters 2 - 5, these terms will not appear until the thermal field is added to the problem in Chapter 6.

Entropy inequality

An additional fundamental law with regards to thermomechanical contact problems discussed in Chapter 6 is the entropy inequality principle. So far, the energy transfer within a thermodynamic process is governed by the balance of energy described above. But laws for the direction of this transfer are still missing. An example is that heat flux always occurs from warmer to colder regions of a body but never the other way round. The entropy inequality, also known as the second law of thermodynamics, closes this gap.

The entropy is a fundamental state variable which can be viewed as a quantitative measure of microscopic randomness and disorder, see BELYTSCHKO et al. [9]. The entropy inequality states that the difference between the rate of entropy possessed by a continuum body and the rate of entropy input into this body is always greater or equal than zero. This input is caused by external heat sources or by heat flux over the surface of the body. The entropy inequality reads

$$\frac{\mathrm{d}}{\mathrm{d}t}\int_{\Omega_t}\rho\,\eta\,\mathrm{d}\Omega_t-\int_{\Omega_t}\frac{\rho\,\hat{r}}{\theta}\,\mathrm{d}\Omega_t-\int_{\gamma}\frac{\mathbf{q}\cdot\mathbf{n}}{\theta}\,\mathrm{d}\gamma\geq\,0. \tag{2.34}$$

The entropy η is defined with respect to the current unit volume and the rate of entropy input in the second and third term is related to the quotient of supplied heat and absolute temperature θ, also known as the entropy flow vector, see BELYTSCHKO et al. [9]. Equation (2.34) is also known as the CLAUSIUS-DUHEM inequality. The local form is obtained by application of

GAUSS' divergence theorem and the consideration of a local portion. In material description, it reads

$$\mathbf{P} : \dot{\mathbf{F}} + \rho_0 \, \theta \, \dot{\eta} - \rho_0 \, \dot{e} - \frac{1}{\theta} \, \mathbf{q} \cdot \operatorname{Grad} \theta \geq 0 \; . \tag{2.35}$$

A stronger form of equation (2.35) is the CLAUSIUS-PLANCK inequality as given by

$$\mathcal{D}_{\text{int}} = \mathbf{P} : \dot{\mathbf{F}} + \rho_0 \, \theta \, \dot{\eta} - \rho_0 \, \dot{e} \geq 0 \; , \tag{2.36}$$

see HOLZAPFEL [53]. Here, $\mathcal{D}_{\text{int}}$ is the internal dissipation per unit mass or local production of entropy. It is zero for reversible and positive for irreversible processes.

2.1.4 Constitutive equations

In addition to the above formulated kinematics, stress concept, and balance and entropy principles, constitutive equations have to be formulated in order to complete the necessary equations for the structural boundary value problem without contact. They characterize the material response by giving the stresses resulting from the deformation. The construction of constitutive equations is conveniently achieved with the help of the CLAUSIUS-PLANCK inequality and the introduction of the HELMHOLTZ free-energy function ψ. It is defined as

$$\psi = e - \theta \, \eta \; . \tag{2.37}$$

With the material time derivative of ψ, the CLAUSIUS-PLANCK inequality (2.36) can be rewritten as

$$\mathcal{D}_{\text{int}} = \mathbf{P} : \dot{\mathbf{F}} - \rho_0 \, \dot{\psi} - \rho_0 \, \eta \, \dot{\theta} \geq 0 \; . \tag{2.38}$$

Elastic materials for purely mechanical theory

Considering frictional contact under purely mechanical theory, thermodynamic variables, such as temperature θ and entropy η, are neglected until Chapter 6. Assuming further only reversible processes within the material and using the equivalent form of the stress power $\mathbf{S} : \dot{\mathbf{E}}$, equation (2.38) reduces to

$$\mathbf{S} : \dot{\mathbf{E}} - \rho_0 \, \dot{\psi} = 0 \; . \tag{2.39}$$

In this case, the HELMHOLTZ free-energy ψ coincides with the internal energy e from (2.37). Defining the HELMHOLTZ free-energy ψ with respect to the reference volume as $\Psi = \rho_0 \, \psi$ with $\dot{\Psi} = \frac{\partial \Psi}{\partial \mathbf{E}} : \dot{\mathbf{E}}$, the desired relationship between stresses and strains results from (2.39) as

$$\mathbf{S} = \frac{\partial \Psi}{\partial \mathbf{E}} \; . \tag{2.40}$$

With the above assumptions covering an isothermal process, the HELMHOLTZ free-energy function Ψ can be identified with the strain-energy function of a material, see BELYTSCHKO et al. [9]. It completely characterizes the hyperelastic material behavior and represents the potential per unit reference volume as a function of the strain measure. In this work, a St. VENANT-KIRCHHOFF and, to take account of geometric nonlinearities in the material, a compressible Neo-HOOKEan behavior as described in the contribution of HOLZAPFEL [53] are used for hyperelastic materials.

Its derivation with respect to the strain measure yields the stresses from which the required relationship between the displacements and the stresses is obtained.

Temperature dependent materials

For treating fully coupled thermomechanical contact problems in Chapter 6, the temperature θ and the entropy η have to be included in the derivation of the constitutive equations. In doing so, the equation (2.39) reads

$$\mathbf{S} : \dot{\mathbf{E}} - \rho_0 \dot{\psi} - \rho_0 \eta \dot{\theta} = 0 \ , \tag{2.41}$$

where again reversible processes are assumed. The free energy function (2.37) depends on the displacement and the temperature. Thus, its time derivation and the insertion into (2.41) now leads to two constitutive relations. These are, assuming constant temperature ($\theta = \text{const}$), the already known equation (2.40) and, assuming a constant deformation $\mathbf{F}$ ($\mathbf{F} = \text{const}$), a connection between entropy and temperature as

$$\eta = -\frac{\partial \Psi}{\partial \theta} \ . \tag{2.42}$$

To sum up, it can be deduced from (2.40) and (2.42) that, for the description of materials in thermomechanical processes, the stress and entropy functions both depend on the deformation gradient and the temperature as

$$\mathbf{S}\left(\mathbf{F}, \theta\right) \ , \qquad \eta\left(\mathbf{F}, \theta\right) \ . \tag{2.43}$$

When deriving the boundary value problem of the coupled thermomechanical problem in Chapter 6, the energy balance (2.32), the entropy inequality in form of the CLAUSIUS-PLANCK inequality (2.36), and the constitutive equations are combined as in the work of SIMO et al. [125] to obtain the temperature evolution equation.

2.2 Frictional contact related equations

The objective of this Chapter 2 is to state the boundary value problem of frictional contact. As the basic equations concerning the structural problem neglecting contact have been presented in Section 2.1, this section now introduces fundamental equations related to frictional contact. These are mainly the definitions of geometric fundamental measures, also known as contact kinematics, in Sections 2.2.1 and 2.2.2 and the formulation of contact conditions in Section 2.2.3. The whole presentation is for three dimensional problems in which also 2D examples are used for illustration.

A three dimensional frictional contact problem with finite deformations and finite sliding is shown in Figure 2.2. In contrast to Figure 2.1, here two elastic bodies are represented by the sets $\Omega_0^{(1)} \subset \mathbb{R}^3$ and $\Omega_0^{(2)} \subset \mathbb{R}^3$ in the reference configuration. With ongoing time $t \in [0, T]$, they experience motions $\varphi_t^{(1)}$ and $\varphi_t^{(2)}$ mapping them into their current configurations $\Omega_t^{(1)}$ and $\Omega_t^{(2)}$. These motions might cause the two bodies to contact and produce interactive forces. The boundaries $\partial\Omega_0^{(i)}$, $i = 1, 2$, include the DIRICHLET boundaries $\Gamma_u^{(i)}$, the NEUMANN boundaries $\Gamma_\sigma^{(i)}$, and the contact boundaries $\Gamma_c^{(i)}$. On the latter, contact constraints will be defined subsequently. The spatial counterparts are denoted as $\gamma_u^{(i)}$, $\gamma_\sigma^{(i)}$, and $\gamma_c^{(i)}$. The three surface sets are assumed to be disjoint, satisfying

$$\partial\Omega_0^{(i)} = \Gamma_u^{(i)} \cup \Gamma_\sigma^{(i)} \cup \Gamma_c^{(i)} \ ,$$

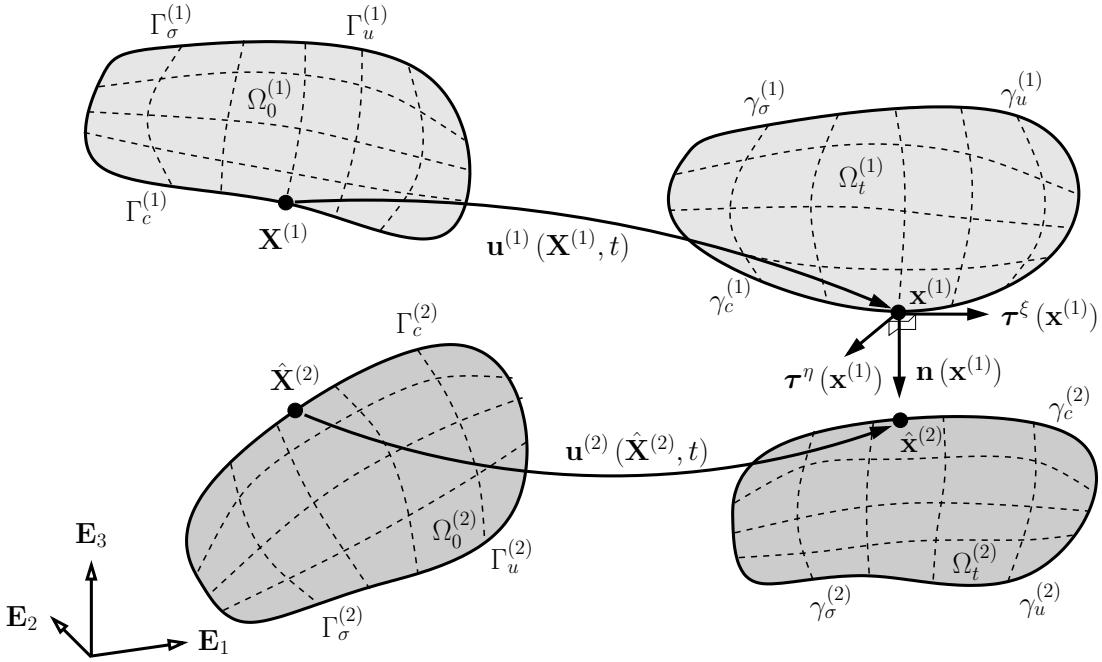

Figure 2.2: Notation for the two body finite deformation contact problem in 3D.

$$\Gamma_u^{(i)} \cap \Gamma_\sigma^{(i)} = \Gamma_u^{(i)} \cap \Gamma_c^{(i)} = \Gamma_\sigma^{(i)} \cap \Gamma_c^{(i)} = \emptyset \, . \tag{2.44}$$

Maintaining a common nomenclature in contact mechanics here, $\Gamma_c^{(1)}$ is the slave surface and $\Gamma_c^{(2)}$ is the master surface, both referred to the reference configuration. Their respective counterparts are denoted as $\gamma_c^{(1)}$ and $\gamma_c^{(2)}$, see for example BENSON et al. [10] or HALLQUIST et al. [37].

In order to formulate the contact conditions, the contact kinematics with the geometric fundamental measures as the gap and the tangential relative velocity will be defined in the following section.

2.2.1 Contact kinematics - gap

The gap function $g(\mathbf{X}^{(1)}, t)$ is defined on the slave contact surface and is a fundamental measure for the distance between the contacting bodies in the current configuration. Its definition is obtained by the following steps and the help of Figure 2.2.

Any point on the reference slave contact surface $\mathbf{X}^{(1)} \in \Gamma_c^{(1)}$ is mapped onto the corresponding spatial point $\mathbf{x}^{(1)} \in \gamma_c^{(1)}$ by $\mathbf{x}^{(1)} = \varphi_t^{(1)}(\mathbf{X}^{(1)})$. For this $\mathbf{x}^{(1)}$, a contact point $\hat{\mathbf{x}}^{(2)} \in \gamma^{(2)}$ on the current master surface is defined via the projection of $\mathbf{x}^{(1)}$ onto $\gamma_c^{(2)}$ along the current outward unit normal vector $\mathbf{n}(\mathbf{x}^{(1)})$ on the slave surface $\gamma_c^{(1)}$. This projection from the slave onto the master contact surface is described by the smooth mapping operator $P : \gamma_c^{(1)} \rightarrow \gamma_c^{(2)}$. The contact point $\hat{\mathbf{x}}^{(2)}$ is, on the other hand, the image of the material point $\hat{\mathbf{X}}^{(2)} \in \Gamma_c^{(2)}$ under the mapping $\varphi_t^{(2)}$. Consequently, both $\hat{\mathbf{x}}^{(2)}$ and $\hat{\mathbf{X}}^{(2)}$ are associated with $\mathbf{X}^{(1)}$ via the described projection. It has to be pointed out that in general, with ongoing time t, the projection changes and thus assigns different material points $\hat{\mathbf{X}}^{(2)} \in \Gamma_c^{(2)}$ with $\mathbf{X}^{(1)} \in \Gamma_c^{(1)}$ for different points in

time. The gap vector $\mathbf{g}\left(\mathbf{X}^{(1)}, t\right)$ is the relative position vector between the corresponding points in the spatial configuration, i.e.

$$\mathbf{g}\left(\mathbf{X}^{(1)}, t\right) = \left[\mathbf{x}^{(1)}\left(\mathbf{X}^{(1)}, t\right) - \hat{\mathbf{x}}^{(2)}\left(\hat{\mathbf{X}}^{(2)}\left(\mathbf{X}^{(1)}, t\right), t\right)\right] . \tag{2.45}$$

The scalar normal gap $g\left(\mathbf{X}^{(1)}, t\right)$ is then defined by the scalar product with the parallel normal vector $\mathbf{n}\left(\mathbf{x}^{(1)}\right)$ as

$$g\left(\mathbf{X}^{(1)}, t\right) = -\mathbf{n}\left(\mathbf{x}^{(1)}\left(\mathbf{X}^{(1)}, t\right)\right) \cdot \mathbf{g}\left(\mathbf{X}^{(1)}, t\right) . \tag{2.46}$$

It is the fundamental quantity needed to formulate the normal contact conditions in Section 2.2.3.

The projection P using the outward unit normal vector $\mathbf{n}\left(\mathbf{x}^{(1)}\right)$ does not correspond with the frequently applied closest point projection, see KONYUKHOV and SCHWEIZERHOF [74] for an extensive treatment. But it avoids the problem of nonunique contact points and is identical to the closest point projection for the normal gap being zero.

2.2.2 Contact kinematics - tangential relative velocity

When treating frictional contact, the tangential relative velocity is the second fundamental measure to be defined in order to formulate the contact conditions in the finite deformation framework. In contrast to the normal gap $g\left(\mathbf{X}^{(1)}, t\right)$, this quantity is a rate measure and depends on former states of the motion. Therefore, it requires the storage of history variables. In this work, two possible definitions of the relative tangential velocity are presented for a better understanding of this quantity and for a classification of traditional and currently used measures in literature. For the further derivation of the discrete frictional contact problem, the second definition will be chosen.

Formulation using slip advected bases

The formulation of frictional kinematics in component form using slip advected bases is presented in LAURSEN [81] as a "natural outcome of the framework under consideration", where it is applied for node-to-segment (NTS) contact. In the NTS context, this formulation is widely used in literature as, for example, in CHAWLA et al. [14], LAURSEN et al. [83, 85], LENGIEWICZ et al. [86], PIETRZAK et al. [108], and WRIGGERS [144, 145]. This form of defining the relative tangential velocity is denoted as "traditional kinematics" in PUSO et al. [118]. A fully covariant description including all linearizations performed in this local coordinate system has firstly been presented in KONYUKHOV and SCHWEIZERHOF [73].

The formulation of the tangential relative velocity consists of the definition of slip advected bases and the formulation of the measure in this coordinate system. Starting point for the definition of slip advected bases is the parametrization of the master contact surface. It is assumed that the mappings $\boldsymbol{\Psi}_0^{(2)}$ and $\boldsymbol{\Psi}_t^{(2)}$ transfer the parameter space $\mathcal{A}^{(2)} \subset \mathbb{R}^2$ into the master contact surface $\Gamma_c^{(2)}$ in the reference configuration and $\gamma_c^{(2)}$ in the current configuration, respectively, as

$$\Gamma_c^{(2)} = \boldsymbol{\Psi}_0^{(2)}\left(\mathcal{A}^{(2)}\right) \quad \text{and} \quad \gamma_c^{(2)} = \boldsymbol{\Psi}_t^{(2)}\left(\mathcal{A}^{(2)}\right) . \tag{2.47}$$

These mappings, visualized in Figure 2.3, are assumed to be smooth. General points of $\mathcal{A}$ are

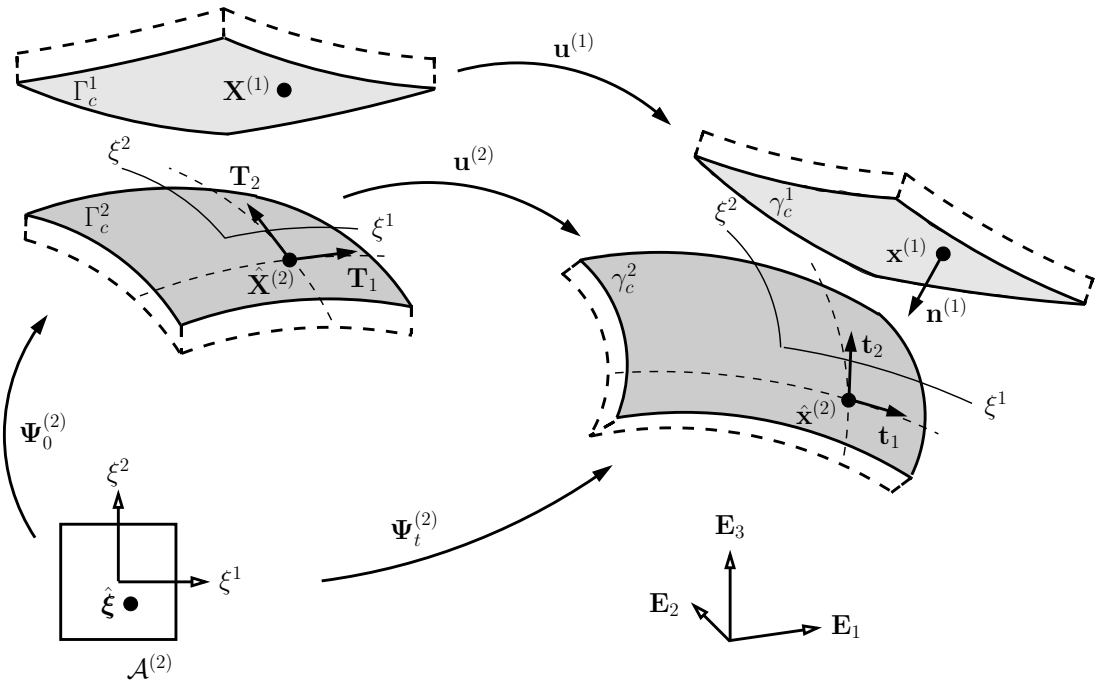

Figure 2.3: Parametrization of master contact surface, coordinate system with origin in projection point and slip advected bases, for current and reference configuration.

denoted as $\boldsymbol{\xi}$, the particular point associated with $\hat{\mathbf{X}}^{(2)}\left(\mathbf{X}^{(1)}, t\right)$ is marked with $\hat{\boldsymbol{\xi}}\left(\mathbf{X}^{(1)}, t\right)$. The slip advected bases now are defined as

$$\mathbf{T}_\alpha := \boldsymbol{\Psi}_0^{(2)}{}_{,\alpha}\left(\hat{\boldsymbol{\xi}}\left(\mathbf{X}^{(1)}, t\right)\right) \quad \text{and} \tag{2.48}$$

$$\mathbf{t}_\alpha := \boldsymbol{\Psi}_t^{(2)}{}_{,\alpha}\left(\hat{\boldsymbol{\xi}}\left(\mathbf{X}^{(1)}, t\right)\right) \ , \ \alpha = 1, 2 \ . \tag{2.49}$$

These definitions (2.48) and (2.49) imply that the advected bases are associated with the same point $\mathbf{X}^{(1)}$ on the slave contact surface for the considered time interval. Origins for the two coordinate systems spanned by these bases are $\hat{\mathbf{X}}^{(2)}$ and $\hat{\mathbf{x}}^{(2)}$. When $\mathbf{x}^{(1)}$ moves over $\gamma_c^{(2)}$, $\mathbf{T}_\alpha$ and $\mathbf{t}_\alpha$ are not fixed on the master surface but move over this surface as the projection point $\hat{\mathbf{x}}^{(2)}$ changes. This motivates the names of these bases.

To formulate the tangential relative velocity, the gap vector $\mathbf{g}\left(\mathbf{X}^{(1)}, t\right)$ as the relative position vector between $\mathbf{x}^{(1)}\left(\mathbf{X}^{(1)}, t\right)$ and $\hat{\mathbf{x}}^{(2)}\left(\mathbf{X}^{(1)}, t\right)$ in (2.45) is considered. During perfect sliding, these two points remain coincident in space which implicates that the gap vector $\mathbf{g}\left(\mathbf{X}^{(1)}, t\right)$ and its total time derivative will remain zero. The latter is considered:

$$\begin{aligned}
\mathbf{0} &= \frac{\mathrm{d}}{\mathrm{d}t}\left[\mathbf{x}^{(1)}\left(\mathbf{X}^{(1)}, t\right) - \hat{\mathbf{x}}^{(2)}\left(\mathbf{X}^{(1)}, t\right)\right] \\
&= \frac{\mathrm{d}}{\mathrm{d}t}\left[\varphi_t^{(1)}\left(\mathbf{X}^{(1)}, t\right) - \varphi_t^{(2)}\left(\hat{\mathbf{X}}^{(2)}\left(\mathbf{X}^{(1)}, t\right), t\right)\right]
\end{aligned}$$

$$= \mathbf{v}^{(1)}\left(\mathbf{X}^{(1)}, t\right) - \mathbf{v}^{(2)}\left(\hat{\mathbf{X}}^{(2)}\left(\mathbf{X}^{(1)}, t\right), t\right) - \mathbf{F}^{(2)}\left(\boldsymbol{\Psi}_0^{(2)}\left(\hat{\boldsymbol{\xi}}\left(\mathbf{X}^{(1)}, t\right)\right)\right) \frac{\mathrm{d}}{\mathrm{d}t}\left[\hat{\mathbf{X}}^{(2)}\left(\mathbf{X}^{(1)}, t\right)\right] \tag{2.50}$$

where $\mathbf{F}^{(2)}$ is the deformation gradient of the master body. The first two terms $\mathbf{v}^{(1)}\left(\mathbf{X}^{(1)}, t\right)$ and $\mathbf{v}^{(2)}\left(\hat{\mathbf{X}}^{(2)}\left(\mathbf{X}^{(1)}, t\right), t\right)$ are the material velocities of the points $\mathbf{x}^{(1)}\left(\mathbf{X}^{(1)}, t\right)$ and $\hat{\mathbf{x}}^{(2)}\left(\mathbf{X}^{(1)}, t\right)$ and are also denoted as $\dot{\mathbf{x}}^{(1)}\left(\mathbf{X}^{(1)}, t\right)$ and $\dot{\hat{\mathbf{x}}}^{(2)}\left(\mathbf{X}^{(1)}, t\right)$ within this work. From (2.50) follows that the desired relative velocity of these two points can also be expressed by the negative third term which emerges the change of contact projection. It can be written in terms of the above derived slip advected bases in its spatial and convective description as

$$\boldsymbol{v}_{T,rel} := \mathbf{F}^{(2)}\left(\boldsymbol{\Psi}_0^{(2)}\left(\hat{\boldsymbol{\xi}}\left(\mathbf{X}^{(1)}, t\right)\right)\right) \frac{\mathrm{d}}{\mathrm{d}t}\left[\hat{\mathbf{X}}^{(2)}\left(\mathbf{X}^{(1)}, t\right)\right] \quad \text{and} \tag{2.51}$$

$$\boldsymbol{V}_{T,rel} := \frac{\mathrm{d}}{\mathrm{d}t}\left[\hat{\mathbf{X}}^{(2)}\left(\mathbf{X}^{(1)}, t\right)\right] = \dot{\hat{\xi}}^{\alpha}\left(\mathbf{X}^{(1)}, t\right) \mathbf{T}_{\alpha} \,. \tag{2.52}$$

From (2.51) and (2.52), it can be seen that $\mathbf{V}_{T,rel}$ represents the pull back of $\boldsymbol{v}_{T,rel}$ by $\varphi_t^{(2)}$. So the spatial relative velocity can also be expressed as

$$\boldsymbol{v}_{T,rel} = \dot{\hat{\xi}}^{\alpha}\left(\mathbf{X}^{(1)}, t\right) \mathbf{t}_{\alpha} \tag{2.53}$$

with

$$\mathbf{t}_{\alpha} = \mathbf{F}^{(2)} \cdot \mathbf{T}_{\alpha} \,. \tag{2.54}$$

In LAURSEN [83], the expressions for the components $\dot{\hat{\xi}}^{\alpha}$ in (2.52) and (2.53) are derived in terms of the slip advected bases and the material velocities. They read

$$\dot{\hat{\xi}}^{\alpha} = \left[\mathbf{v}^{(1)}\left(\mathbf{X}^{(1)}, t\right) - \mathbf{v}^{(2)}\left(\hat{\mathbf{X}}^{(2)}\left(\mathbf{X}^{(1)}, t\right), t\right)\right] \cdot \mathbf{t}^{\alpha} \,, \tag{2.55}$$

where $\mathbf{t}^{\alpha} = m^{\alpha\beta}\, \mathbf{t}_{\beta}$ represents the dual or reciprocal basis to $\mathbf{t}_{\beta}$, $m_{\alpha\beta} = \mathbf{t}_{\alpha} \cdot \mathbf{t}_{\beta}$.

Formulation by difference of material velocities

As a result of equation (2.50), the tangential relative velocity can also be expressed in terms of the material velocities of the opposing points $\mathbf{x}^{(1)}\left(\mathbf{X}^{(1)}, t\right)$ and $\hat{\mathbf{x}}^{(2)}\left(\mathbf{X}^{(1)}, t\right)$ by using the first and second term there. The changeover to the definition on this basis was carried out mainly due to using the mortar method instead of NTS approaches for discretizing the contact surfaces. Examples are KIM et al. [71], LAURSEN et al. [81, 83, 84], MCDEVITT et al. [95], PUSO et al. [116, 117, 118], and YANG et al. [148, 149, 150]. Only the contributions of FISCHER and WRIGGERS [27, 28] or TUR et al. [132] using the mortar method could stay with "traditional kinematics", see PUSO et al. [118]. This is due to the application of an integration scheme where sliding constitutive evaluations are made at quadrature points. This is in stark contrast to the approach applied here and in the literature listed above where frictional sliding is described for nodes of the slave contact surface, see PUSO et al. [118].

From equation (2.50), the relative velocity equally expressed in material velocities reads

$$\boldsymbol{v}_{T,rel} = \mathbf{v}^{(1)}\left(\mathbf{X}^{(1)}, t\right) - \mathbf{v}^{(2)}\left(\hat{\mathbf{X}}^{(2)}\left(\mathbf{X}^{(1)}, t\right), t\right)$$

$$= \dot{\mathbf{x}}^{(1)}\left(\mathbf{X}^{(1)}, t\right) - \dot{\hat{\mathbf{x}}}^{(2)}\left(\hat{\mathbf{X}}^{(2)}\left(\mathbf{X}^{(1)}, t\right), t\right) . \tag{2.56}$$

For the assumption of perfect sliding, it acts in the tangential plane. However, this is not the case if $\dot{\mathbf{g}}\left(\mathbf{X}^{(1)}, t\right)$ is not exactly zero which could happen, for example, for heavily curved contact surfaces. In order to remove a potential normal component, $\boldsymbol{v}_{T,rel}$ in (2.56) is projected into the tangential plane as

$$\mathbf{v}_{\tau,rel}\left(\mathbf{X}^{(1)}, t\right) = \begin{pmatrix} \boldsymbol{\tau}^{\xi}\left(\mathbf{x}^{(1)}\right) \\ \boldsymbol{\tau}^{\eta}\left(\mathbf{x}^{(1)}\right) \end{pmatrix} \cdot \left(\dot{\mathbf{x}}^{(1)}\left(\mathbf{X}^{(1)}, t\right) - \dot{\hat{\mathbf{x}}}^{(2)}\left(\hat{\mathbf{X}}^{(2)}\left(\mathbf{X}^{(1)}, t\right), t\right)\right) . \tag{2.57}$$

Here, the vectors $\boldsymbol{\tau}^{\xi}\left(\mathbf{x}^{(1)}\right)$ and $\boldsymbol{\tau}^{\eta}\left(\mathbf{x}^{(1)}\right)$ are the unit tangent vectors. Together with the outward unit normal $\mathbf{n}\left(\mathbf{x}^{(1)}\right)$, they form an orthonormal basis in $\mathbb{R}^3$ as shown in Figure 2.2. The orientation of the coordinate system regarding the rotation around the $\mathbf{n}\left(\mathbf{x}^{(1)}\right)$-axis therein is arbitrary.

With the definition of the tangential relative velocity $\mathbf{v}_{\tau,rel}\left(\mathbf{X}^{(1)}, t\right)$ as in (2.57), it is a two component vector representing the relative material velocities of opposing points in in $\boldsymbol{\tau}^{\xi}\left(\mathbf{x}^{(1)}\right)$- and $\boldsymbol{\tau}^{\eta}\left(\mathbf{x}^{(1)}\right)$-direction.

For a proper formulation of rate measures as the tangential relative velocity at hand, frame indifference has to be guaranteed. The expressions (2.51) and (2.52) using the slip advected bases above are frame indifferent since the contact projection is unaffected by any rigid body rotation, see LAURSEN [83]. This is an important reason for the application within the node-to-segment approaches listed above. Dealing with the mortar method here, the tangential relative velocity in (2.57) is used for further derivation although this form is not frame indifferent. But this issue is kept in mind and reconsidered within the spatial discretized version in Section 3.4.4. There, the knowledge about the two possibilities to define the tangential relative velocity in the continuum setting comes into play again.

2.2.3 Contact conditions

Besides the geometric fundamental measures defined in Sections 2.2.1 and 2.2.2, also contact tractions at the contact surfaces are required to formulate the contact conditions. On the slave contact surface, they are denoted as $\mathbf{t}_c^{(1)}$ and decomposed into normal and tangential components as

$$\mathbf{t}_c^{(1)} = p_n\,\mathbf{n} + t_\tau^{\xi}\,\boldsymbol{\tau}^{\xi} + t_\tau^{\eta}\,\boldsymbol{\tau}^{\eta} , \quad p_n = \mathbf{t}_c^{(1)} \cdot \mathbf{n} , \quad t_\tau^{\xi} = \mathbf{t}_c^{(1)} \cdot \boldsymbol{\tau}^{\xi} , \quad t_\tau^{\eta} = \mathbf{t}_c^{(1)} \cdot \boldsymbol{\tau}^{\eta} . \tag{2.58}$$

Normal contact condition

The contact conditions are formulated with respect to the current configuration. In normal direction, they are expressed with the classical KARUSH-KUHN-TUCKER (KKT) conditions, which read

$$g\left(\mathbf{X}^{(1)}, t\right) \geq 0 , \tag{2.59}$$

$$p_n \leq 0 , \tag{2.60}$$

$$p_n\, g\left(\mathbf{X}^{(1)}, t\right) = 0 . \tag{2.61}$$

Here, equation (2.59) is the impenetrability condition which does not allow the bodies to penetrate each other. Equation (2.60) implies that no adhesive stresses occur in the contact zone and the complementarity condition (2.61) forces the gap to be closed when non-zero pressure occurs and the pressure to be zero when the gap is open. This set of conditions is also visualized in Figure 2.4.

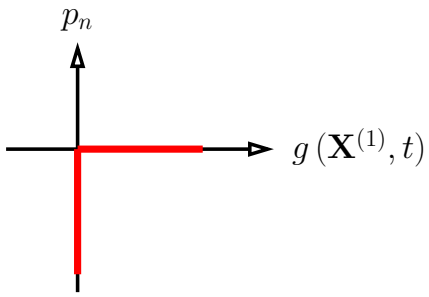

Figure 2.4: Contact conditions in normal direction.

Here, admissible combinations of p_n and $g\,(\mathbf{X}^{(1)}, t)$ are marked red. The normal contact conditions are of multivalued character since they connect the gap at zero $g\,(\mathbf{X}^{(1)}, t) = 0$ with an infinite amount of values for the normal contact traction p_n. Furthermore, they are not differentiable. These reasons and the conditions being formulated in terms of inequalities require a special treatment within the solution process presented in Section 3.1 and Chapter 4.

Tangential contact condition - COULOMB's law

Friction is a very complicated physical phenomenon. It encompasses elastic and plastic deformations at the contact interface, interaction with wear particles, microfractures, excitation of electrons, and a lot more. In continuum mechanics, the most common description is the phenomenological law of COULOMB. It is used throughout this work.

Writing the tangential components t_τ^ξ and t_τ^η of the contact tractions from (2.58) into the two component vector $\mathbf{t}_\tau$ as

$$\mathbf{t}_\tau := \begin{pmatrix} t_\tau^\xi \\ t_\tau^\eta \end{pmatrix} , \tag{2.62}$$

the frictional contact conditions according to COULOMB's law can be written as

$$\psi_c := \|\mathbf{t}_\tau\| - \mu\,|p_n| \leq 0 , \tag{2.63}$$

$$\mathbf{v}_{\tau,rel}(\mathbf{X}^{(1)}, t) + \beta\,\mathbf{t}_\tau = \mathbf{0} , \tag{2.64}$$

$$\beta \geq 0 , \tag{2.65}$$

$$\psi_c\,\beta = 0 , \tag{2.66}$$

where μ is the friction coefficient. Equation (2.63) requires the magnitude of the tangential stress vector to not exceed the product of the coefficient of friction and the normal contact pressure. When the tangential stress is less than the COULOMB limit ($\psi_c < 0$), the continuity equation (2.66) forces β to be zero and, accordingly, the tangential relative velocity to be zero. This is

called the stick state. When the tangential stress is at the COULOMB limit ($\psi_c = 0$), β may be greater than zero in (2.66) and therefore the tangential stress is forced to oppose the relative tangential velocity in (2.64). This is called the slip state. For the two dimensional case, COULOMB's law is visualized in Figure 2.5, where $v_\tau\left(\mathbf{X}^{(1)}, t\right)$ is the only component of the tangential relative velocity.

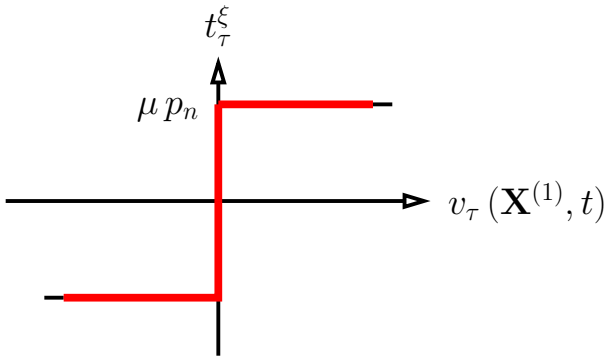

Figure 2.5: Frictional contact conditions in tangential direction, schematic depiction of COULOMB's law in 2D.

The set of equations (2.63) - (2.66) is not the only way of describing COULOMB's law of friction. This can also be achieved equivalently with the structure used, for example, in HÜEBER et al. [54, 56] as

$$\|\mathbf{t}_\tau\| - \mu\,|p_n| \leq 0\,, \tag{2.67}$$

$$\|\mathbf{t}_\tau\| - \mu\,|p_n| < 0 \Rightarrow \mathbf{v}_{\tau,rel}\left(\mathbf{X}^{(1)}, t\right) = \mathbf{0}\,, \tag{2.68}$$

$$\|\mathbf{t}_\tau\| - \mu\,|p_n| = 0 \Rightarrow \exists\,\beta \in \mathbb{R}_0^+ : \mathbf{v}_{\tau,rel}\left(\mathbf{X}^{(1)}, t\right) + \beta\,\mathbf{t}_\tau = 0\,. \tag{2.69}$$

These equivalent expressions are listed here as they will be helpful within the further derivation.

The tangential relative velocity $\mathbf{v}_{\tau,rel}\left(\mathbf{X}^{(1)}, t\right)$ defined above could be used for any other friction model as for example TRESCA's friction law, which is independent of the contact normal pressure. Further, rate, state, or temperature dependent friction laws could easily be included, but are not considered in this work.

As the contact conditions in normal direction, also COULOMB's law is of multivalued character, not differentiable, and given in terms of inequalities. This has to be taken care of within the solution process.

2.3 Boundary value problem of finite deformation frictional contact

With the basic equations of nonlinear continuum mechanics in Section 2.1 and the formulation of contact conditions in Section 2.2 at hand, the finite deformation boundary value problem of frictional contact is presented here. Throughout this work, the discussion limits itself to quasistatic problems as the focus is on frictional contact which is independent of forces of inertia.

However, the tangential relative velocity requires a temporal resolution leading to a quasistatic treatment with pseudo-time steps. This can finally be interpreted as a dynamic process with neglected inertia and viscous terms. Nevertheless, in this work, contact has been implemented in a transient framework and respective examples are presented in Chapters 4, 5, and 6. Well known issues of contact associated with numerical time integration, see for example LAURSEN [83], are not considered within this work. The purely mechanical problem is described whereas thermal effects are not taken into account so far. The notation and the partition of the boundary has been stated in the beginning of Section 2.2.

The boundary value problem of finite deformation frictional contact requires the displacement vectors $\mathbf{u}^{(i)}$ to map the material configuration $\mathbf{X}^{(i)}$ into the spatial configuration $\mathbf{x}^{(i)}$. There, the following equations have to be satisfied:

$$\operatorname{Div} \mathbf{P}^{(i)} + \hat{\mathbf{b}}_0^{(i)} = \mathbf{0} \qquad \text{in } \Omega_0^{(i)} \ , \tag{2.70}$$

$$\mathbf{P}^{(i)} \cdot \mathbf{N}^{(i)} = \hat{\mathbf{t}}_0^{(i)} \quad \text{on } \Gamma_\sigma^{(i)} \ , \tag{2.71}$$

$$\mathbf{P}^{(i)} \cdot \mathbf{N}^{(i)} = \mathbf{t}_{c,0}^{(i)} \quad \text{on } \Gamma_c^{(i)} \ , \tag{2.72}$$

$$\mathbf{u}^{(i)} = \hat{\mathbf{u}}^{(i)} \quad \text{on } \Gamma_u^{(i)} \ , \quad i = 1, 2 \ . \tag{2.73}$$

The first three equations are equilibrium equations. These are the balance of linear momentum within the bodies (2.70), the NEUMANN boundary condition (2.71), and CAUCHY's law for the contact tractions $\mathbf{t}_{c,0}^{(i)}$ acting on the reference configuration (2.72). The fourth equation (2.73) denotes the DIRICHLET boundary condition. The problem (2.70) - (2.73) is constrained by the contact conditions in normal direction (2.59) - (2.61) and in tangential direction (2.63) - (2.66), the problem setup is completed with the definition of a constitutive equation according to (2.40).

It has to be pointed out that equation (2.72) is treated in the same way as the other equations of the boundary value problem. This significance is also visible in CHRISTENSEN [15] and STRÖMBERG et al. [128, 131]. Reason for the equal treatment is the necessity of this term for the derivation of the contact virtual work using integration by parts and GAUSS' divergence theorem presented in Section 3.3.1.

3 Frictional contact - weak form and finite element discretization

The solution of the frictional contact problem requires two basic ingredients. Firstly, the enforcement of contact constraints and secondly, the discretization of the contact surfaces. As they are directly connected with the weak form and finite element discretization, a brief overview on these techniques is given before deriving the weak and discrete form of the problem.

3.1 Methods of constraint enforcement

Historically, the methods of constraint enforcement come from optimization theory as the linear elastic contact problem without friction is similar to constrained minimization problems, see LAURSEN [83]. There are mainly three methods. The penalty method, the augmented LAGRANGE approach in form of USZAWA's algorithm and the LAGRANGE multiplier approach. Besides, there are also methods based on the ideas of NITSCHE [100] as in HEINTZ and HANSBO [43] or WRIGGERS and ZAVARISE [145] and further methods described in WRIGGERS [144] and in ZAVARISE et al. [152].

In general, the methods of constraint enforcement can entirely be obtained from the formulation of the corresponding functionals and its subsequent variation with respect to the unknowns of the problem. This leads to the contact virtual work and, in case of the LAGRANGE multiplier method, also to the contact conditions. For the penalty and the augmented LAGRANGE multiplier approach, the conditions are already contained in the contact virtual work. The derivation of the methods by this way is the most simple for the linear elastic case regarding frictionless contact, see LAURSEN [83]. This is due to the absence of dissipation so that potentials can be formulated. For frictional contact problems in a broader context, this strategy could be pursued by adding pseudo-potentials, see for example ALART and CURNIER [2]. In this work however, the method of weighted residuals, see FINLAYSON [26], is applied in Section 3.3 in order to obtain the weak or also called variational form of the contact problem.

As mentioned, most prevalent are the LAGRANGE multiplier method, the penalty, and the augmented LAGRANGE multiplier approach. Due to the large amount of information available in literature, general characteristics are discussed very briefly in the following. They differ in the way the contact conditions are formulated.

3.1.1 LAGRANGE multiplier method

The LAGRANGE multiplier method uses the contact conditions without modifications. It is characterized by the introduction of additional unknowns, the so-called LAGRANGE multipliers $\boldsymbol{\lambda}$. They are identified as the (negative) contact tractions $\mathbf{t}_c^{(1)}$ and, in general, play the role of forces

that maintain the constraints, see HUGHES [61]. Due to the additional unknowns, the LAGRANGE multiplier method leads to a mixed variational formulation of the problem with saddle point-type characteristics of the system of equations. Because of not modifying the contact conditions, the exact fulfillment of constraints is a significant advantage of this method. For finite deformation contact problems, it is applied for example in FISCHER and WRIGGERS [27] for frictionless or, recently in TUR et al. [132], for frictional contact.

In this work, the so-called dual LAGRANGE multiplier method is used. From there, it is referred to Section 3.3 for the application to the frictional contact problem. This method was originally introduced in WOHLMUTH [140] and can also be found in in GITTERLE et al. [35], HARTMANN et al. [39, 40], HÜEBER et al. [54, 56], POPP et al. [110, 111], or WOHLMUTH [141].

3.1.2 Penalty method

The basis of this method is the modification of contact conditions by regularization. By this, the violation of contact condition is penalized. The method is employed for example in FISCHER and WRIGGERS [28] and YANG et al. [150] for 2D frictional contact or in PUSO et al. [118] for 3D frictional contact using quadratic interpolation. With the help of penalty parameters, the regularization of the multivalued contact conditions is realized as given in the following.

For the normal direction, it is shown in Figure 3.1, where ϵ_N is the respective penalty parameter. It can also be stated in terms of equations as

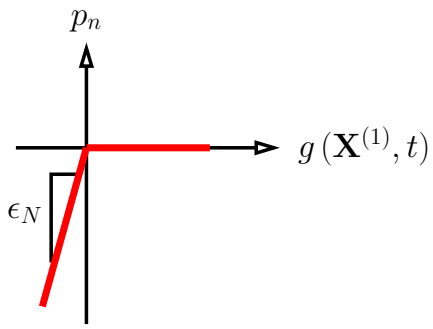

Figure 3.1: Penalty regularization of normal contact conditions.

$$p_n = \begin{cases} 0 & \text{for } g > 0 \quad \text{(no contact)} \\ \epsilon_N\, g & \text{for } g \leq 0 \quad \text{(contact)} \end{cases} . \tag{3.1}$$

The visualization of the regularized version of COULOMB's law is not straightforward as it contains the tangential relative velocity $\mathbf{v}_{\tau,rel}$ as a term in rate form. This requires also the tangential traction $\mathbf{t}_\tau$ as a rate quantity in order to state the penalty regularized form of COULOMB's law as

$$\mathcal{L}_v\, \mathbf{t}_\tau = \epsilon_T \left[\mathbf{v}_{\tau,rel} - \beta \frac{\mathbf{t}_\tau}{\|\mathbf{t}_\tau\|} \right] , \tag{3.2}$$

where $\mathcal{L}_v\, \mathbf{t}_\tau$ is the LIE derivative of the frictional traction and ϵ_T the tangential penalty parameter. It is completed with the remaining equations (2.63), (2.65) and (2.66).

This procedure causes a not exact fulfillment of contact conditions, but leads to a direct connection of the kinematic measures, i.e. the gap and the tangential relative velocity, to the contact tractions. Consequently, the introduction of additional unknowns is not necessary and the problem can be formulated in displacement terms only when, at a later stage, the weak form is derived. The main disadvantage of this method is the violation of contact constraints. This can be minimized with applying high values for the penalty parameters ϵ_N and ϵ_T, but at the drawback of ill conditioned systems of equations.

3.1.3 Augmented LAGRANGE method, USZAWA algorithm

Another method to regularize the normal contact and friction conditions is the augmented LAGRANGE formulation. The main idea is the combination of the penalty method and the LAGRANGE multiplier approach. It is widely used throughout literature, as for example in ALART and CURNIER [2], GEE [34], KIKUCHI and ODEN [70], LAURSEN et al. [84], PIETRZAK and CURNIER [108], PUSO et al. [115, 116, 118], or YANG et al. [148, 149, 150]. One possibility of its numerical treatment is the USZAWA algorithm which is partly used in the contributions given above. It is described in the following.

The normal contact traction is evaluated in terms of the LAGRANGE multiplier λ_n in normal direction and the penalty parameter ϵ_N as

$$p_n = \begin{cases} 0 & \text{for } \lambda_n + \epsilon_N\, g > 0 \quad \text{(no contact)} \\ \lambda_n + \epsilon_n\, g & \text{for } \lambda_n + \epsilon_N\, g \leq 0 \quad \text{(contact)} \end{cases} . \tag{3.3}$$

The tangential contact traction $\mathbf{t}_\tau$ is determined via the relation

$$\mathcal{L}_v\left(\mathbf{t}_\tau - \boldsymbol{\lambda}_\tau\right) = \epsilon_T \left[\mathbf{v}_{\tau,rel} - \beta \frac{\mathbf{t}_\tau}{\|\mathbf{t}_\tau\|}\right] , \tag{3.4}$$

where $\boldsymbol{\lambda}_\tau$ is the tangential LAGRANGE multiplier vector. Together with the remaining equations (2.63), (2.65) and (2.66), the augmented LAGRANGE regularized version of COULOMB's law is complete.

With this and similar to the penalty method, equations (3.3) and (3.4) provide the desired connection between the contact traction $\mathbf{t}_c^{(1)}$ and the geometric fundamental measures as the gap g and the relative tangential velocity $\mathbf{v}_{\tau,rel}$. Using USZAWA's algorithm, the LAGRANGE multiplier $\boldsymbol{\lambda}$ in these equations is resolved via an iterative scheme. Consequently, during an iteration step k, the LAGRANGE multiplier vector $\boldsymbol{\lambda}^k$ is held constant. The contact tractions in turn are expressed in terms of $\boldsymbol{\lambda}^k$ and the displacements. This connection is inserted into the weak form of the problem, derived at a later stage, and is solved towards the unknown displacements. After this, the updated version of the LAGRANGE multiplier $\boldsymbol{\lambda}^{k+1}$ is evaluated from $\boldsymbol{\lambda}^k$ and equations (3.3) and (3.4). The iteration is carried out until the violation of the contact conditions falls below a given measure. In the limit, they are fulfilled exactly and the LAGRANGE multiplier $\boldsymbol{\lambda}$ takes the value of the contact traction $\mathbf{t}_c^{(1)}$. This is an obvious advantage, but at the costs of an additional iteration loop.

For implementation, the LAGRANGE multiplier method, the penalty, and the augmented LAGRANGE multiplier method have been chosen. The further discussion however focuses on the dual LAGRANGE multiplier method as it contains the new aspects of this work.

3.2 Discretization of contact surfaces

The second important ingredient when treating contact problems is the spatial discretization of the contact surfaces carried out in Section 3.4. This is accompanied by the resolution of mutual interactions between the contacting bodies. In general, the finite element nodes of the contact surfaces are not matching and the transfer of contact tractions and the fulfillment of contact constraints is realized mainly with node-to-segment (NTS) or segment-to-segment (STS) approaches.

3.2.1 Node-to-segment approach

The main idea of node-to-segment approaches is that finite element nodes on the slave contact surface are not allowed to penetrate the respective segment on the opposite master surface. Such a situation is shown in Figure 3.2. The gap function and, for the friction law, the tangential relative velocity, are evaluated at the nodes of the slave contact surface $\mathbf{x}^{(1)}$. Instead of using nodes, these considerations could also be made at quadrature points. In either case, the contact conditions are enforced only at a discrete number of points. This corresponds to a variationally inconsistent assumption of contact tractions at the contact interface, see PAPADOPOULOS and TAYLOR [106] and is also denoted as collocation method. Exemplary applications in the finite deformation context can be found in ERHART et al. [24], LAURSEN and SIMO [85], or WRIGGERS et al. [147].

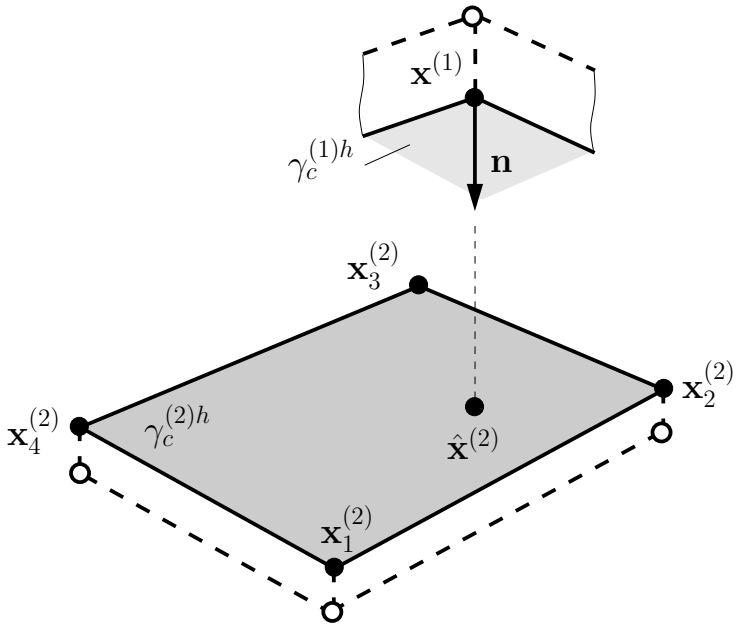

Figure 3.2: Node-to-segment approach for contact surface discretization, fulfillment of contact constraints only for slave nodes.

Although used in many commercial codes, there are well known disadvantages of this approach. Especially for finite deformations, there is the problem of "chattering", see PUSO and

LAURSEN [115]. It occurs where geometry is only approximated very roughly and kinks appear for an originally smooth surface. When a slave node slides over this kink, non-physical jumps in contact forces are typically encountered which can cause serious errors in contact stresses. Similar problems occur for nodes placed near edges when they drop over this edge during the simulation. A further important disadvantage of node-to-segment approaches is that the satisfaction of the patch test is not for sure. This means that it cannot be guaranteed that a constant stress field within two bodies is transferred correctly over a contact surface with non-matching meshes, see HESCH [44] or PAPADOPOULOS and TAYLOR [106].

To overcome the described "chattering" problem, there exist various smoothing techniques in literature. Examples are PADMANABHAN and LAURSEN [105], PUSO and LAURSEN [115] or, towards biomedical applications, KIOUSIS et al. [72]. FRANKE et al. [31, 32] and KONJUKHOV and SCHWEIZERHOF [75] apply higher-order finite elements and DE LORENZIS et al. [20] use NURBS-based isogeometric analysis for enhancing the continuity of the contact surfaces. Additional to these approaches, especially the mortar method explained in the next section, is highly useful to avoid the above mentioned problems.

3.2.2 Segment-to-segment approach, mortar method

A fundamental different approach for discretizing the contact surfaces are segment-to-segment approaches, wherein especially the mortar method has become very popular in recent years. The mortar method has originally been introduced in the context of domain decomposition techniques in BERNARDI et al. [11] and is used since then in a broad field of contact research. It can be found for example in BELGACEM et al. [7, 8], MCDEVITT and LAURSEN [95], and WOHLMUTH [140] for small deformations. For the extension to 3D finite deformation contact with and without friction, contributions are FISCHER and WRIGGERS [27, 28], GITTERLE et al. [35], HESCH and BETSCH [45, 46, 47, 48, 49], POPP et al. [110, 111], PUSO and LAURSEN [116], TUR et al. [132], and YANG et al. [148, 149, 150]. This list here is certainly not exhaustive due to the wide range of activities in this field.

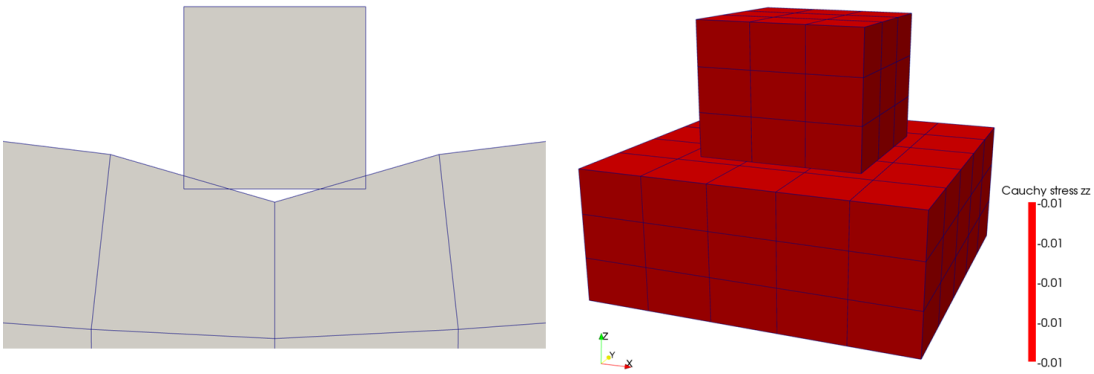

Figure 3.3: Mortar method for contact surface discretization, weak formulation of contact constraints (left) and satisfactory transfer of a constant stress field over surfaces with nonconforming meshes (patch test, right).

The mortar method is characterized by a weak fulfillment of contact constraints which can be clearly seen on the left hand side of Figure 3.3. It shows a coarsely discretized square intruding into a flat surface. This weak enforcement is achieved, in contrast to NTS approaches, with spatially interpolated LAGRANGE multipliers and, corresponding to this, also spatially interpolated test functions for the contact conditions. With this, the mortar method requires the evaluation of the typical mortar coupling surface integrals. They contain the integral product of interpolated quantities which are, in case of the mortar matrix $\mathbf{M}$, even defined on opposing surfaces. The evaluation of these surface integrals can either be realized with a segmentation of the contact surface based on contact segments as in GITTERLE et al. [35], POPP et al. [110, 111], or PUSO et al. [114, 116, 117, 118]. Or it can be performed by an appropriate integration scheme based on not changing slave segments instead of varying contact segments. This is carried out in FISCHER and WRIGGERS [27, 28] and recently in TUR et al. [132].

With the application of the mortar method, the already mentioned patch test can be fulfilled, see Figure 3.3 on the left hand side. "Chattering" and related problems do not occur and optimal spatial convergence rates can be obtained with using this integral representations of the contact constraints, see LAURSEN [83]. Besides these mentioned advantages, the mortar method is, to the author's opinion, the logical consequence for contact surface discretization when using finite elements based on a weak or variational formulation of the problem. It is used throughout this work.

3.3 Weak form

In order to treat the present frictional contact problem with the finite element method, the weak form has to be derived. To obtain this form in general, there is the method of weighted residuals and the variational method as described earlier and in FINLAYSON [26]. The first one works directly with the differential equation and boundary conditions whereas the second one uses a functional related to these items. Here, the method of weighted residuals as a more general principle is applied. It is carried out in Sections 3.3.1 and 3.3.2 to obtain a weak form of the equilibrium equations and contact conditions. Within the considered mortar method, they are enforced in a weak sense, too.

3.3.1 Equilibrium equations

In order to obtain these weak forms, the solution function space $\boldsymbol{\mathcal{U}}^{(i)}$ and weighting function space $\boldsymbol{\mathcal{V}}^{(i)}$ are defined as

$$\boldsymbol{\mathcal{U}}^{(i)} := \left\{ \mathbf{u}^{(i)} \in \left[H^1 \left(\Omega_0^{(i)} \right) \right]^3 \mid \mathbf{u}^{(i)} = \hat{\mathbf{u}}^{(i)} \ \text{ on } \Gamma_u^{(i)} \right\} , \tag{3.5}$$

$$\boldsymbol{\mathcal{V}}^{(i)} := \left\{ \mathbf{w}^{(i)} \in \left[H^1 \left(\Omega_0^{(i)} \right) \right]^3 \mid \mathbf{w}^{(i)} = 0 \ \text{ on } \Gamma_u^{(i)} \right\} . \tag{3.6}$$

Here, $H^1(\Omega_0^{(i)})$ denotes the usual SOBOLEV space of functions whose values and first derivatives are square integrable over the domain. Then, the method of weighted residuals is applied to the equilibrium equations. These are the balance of linear momentum within the bodies (2.70), the

traction boundary condition (2.71), and the balance of linear momentum at the contact interface in equation (2.72). The weak form is obtained by multiplying these equations with the test function $\mathbf{w}^{(i)} \in \boldsymbol{\mathcal{V}}^{(i)}$ and integration for each body i as

$$\int_{\Omega_0^{(i)}} \left[\mathrm{Div}\left(\mathbf{F}^{(i)} \cdot \mathbf{S}^{(i)}\right) + \hat{\mathbf{b}}_0^{(i)} \right] \cdot \mathbf{w}^{(i)} \, \mathrm{d}\Omega_0^{(i)} + \int_{\Gamma_\sigma^{(i)}} \left[\hat{\mathbf{t}}_0^{(i)} - \mathbf{P}^{(i)} \cdot \mathbf{N}^{(i)} \right] \cdot \mathbf{w}^{(i)} \, \mathrm{d}\Gamma_\sigma^{(i)} + \int_{\Gamma_c^{(i)}} \left[\mathbf{t}_{c,0}^{(i)} - \mathbf{P}^{(i)} \cdot \mathbf{N}^{(i)} \right] \cdot \mathbf{w}^{(i)} \, \mathrm{d}\Gamma_c^{(i)} = 0 \, . \tag{3.7}$$

Identifying the arbitrary test functions $\mathbf{w}^{(i)}$ as virtual displacements $\delta\mathbf{u}^{(i)}$, applying integration by parts and subsequently GAUSS' divergence theorem, one obtains the virtual work expression for that body i in material description as

$$\begin{aligned} G^{(i)}(\mathbf{u}^{(i)}, \delta\mathbf{u}^{(i)}) = & \int_{\Omega_0^{(i)}} \mathbf{S}^{(i)} \colon \delta\mathbf{E}^{(i)} \mathrm{d}\Omega_0^{(i)} - \int_{\Omega_0^{(i)}} \hat{\mathbf{b}}_0^{(i)} \cdot \delta\mathbf{u}^{(i)} \mathrm{d}\Omega_0^{(i)} \\ & - \int_{\Gamma_\sigma^{(i)}} \hat{\mathbf{t}}_0^{(i)} \cdot \delta\mathbf{u}^{(i)} \mathrm{d}\Gamma_\sigma^{(i)} \\ & - \int_{\Gamma_c^{(i)}} \mathbf{t}_{c,0}^{(i)} \cdot \delta\mathbf{u}^{(i)} \mathrm{d}\Gamma_c^{(i)} = 0 \quad \forall \, \delta\mathbf{u}^{(i)} \in \boldsymbol{\mathcal{V}}^{(i)} \, . \end{aligned} \tag{3.8}$$

The first three terms are well known and represent the virtual work form internal and external forces $G^{int,ext(i)}$. They are independent of the contact formulation. The last one is the contact virtual work $G^{c(i)}$ resulting from normal and frictional contact traction $\mathbf{t}_{c,0}^{(i)}$ acting on the contact boundary $\Gamma_c^{(i)}$ of the respective body i.

In the following, the focus is on this contact virtual work. Due to implementation reasons, it is written in the current configuration. Furthermore, the formulation is for the entire system as

$$G^c\left(\mathbf{u}^{(i)}, \delta\mathbf{u}^{(i)}\right) = -\sum_{i=1}^{2} \int_{\gamma_c^{(i)}} \mathbf{t}_c^{(i)} \cdot \delta\mathbf{u}^{(i)} \mathrm{d}\gamma \, , \tag{3.9}$$

where $\mathbf{t}_c^{(i)}$ is the contact traction of body i in the current configuration. With the balance of linear momentum across the contact interface as

$$\mathbf{t}_c^{(1)} \mathrm{d}\gamma^{(1)} = -\mathbf{t}_c^{(2)} \mathrm{d}\gamma^{(2)} \, , \tag{3.10}$$

the contact virtual work (3.9) can be rewritten as an integral over the slave surface only

$$G^c\left(\mathbf{u}, \delta\mathbf{u}\right) = -\int_{\gamma_c^{(1)}} \mathbf{t}_c^{(1)} \cdot \left(\delta\mathbf{u}^{(1)} - \left(\delta\mathbf{u}^{(2)} \circ P\right)\right) \mathrm{d}\gamma \, , \tag{3.11}$$

where P is the mapping operator at the contact interface introduced in Section 2.2.1.

At this place, a penalty or augmented LAGRANGE formulation could be obtained by substituting the contact traction $\mathbf{t}_c^{(1)}$ in (3.11) according to equations (3.1) and (3.2) or (3.3) and (3.4), respectively. However, as stated in Section 3.1, the usage of LAGRANGE multipliers for constraint enforcement leading to a mixed variational formulation is aimed for in this work. They

are introduced as additional unknowns on the slave contact surface and are identified as the negative contact traction as

$$\boldsymbol{\lambda} = -\mathbf{t}_c^{(1)}. \tag{3.12}$$

In order to describe the solution function space for them, first, the trace spaces $\boldsymbol{\mathcal{W}}^{(i)} = H^{\frac{1}{2}}(\Gamma_c^{(i)})$ being the restrictions of $\boldsymbol{\mathcal{U}}^{(i)}$ to $\Gamma_c^{(i)}$ are defined. LAGRANGE multipliers simply based on this space will be termed as standard LAGRANGE multipliers in the following. The focus within this work is on dual LAGRANGE multipliers, which are specified to be in the corresponding dual trace space $\boldsymbol{\mathcal{M}} = H^{-\frac{1}{2}}(\Gamma_c^{(1)})$, see WOHLMUTH [140]. They differ in the choice of shape functions in the discrete setting, see Section 3.4.1.

Using LAGRANGE multipliers, the final version of the contact virtual work can be written as

$$G^c(\boldsymbol{\lambda}, \delta\mathbf{u}) = \int_{\gamma_c^{(1)}} \boldsymbol{\lambda} \cdot \left(\delta\mathbf{u}^{(1)} - \left(\delta\mathbf{u}^{(2)} \circ P\right)\right) \mathrm{d}\gamma \,. \tag{3.13}$$

It is pointed out that no further division of the contact virtual work (3.13) into normal and tangentail parts is necessary here. This division is carried out for example in LAURSEN [83] or WRIGGERS [144], where it is useful for the penalty and the augmented LAGRANGE multiplier method.

3.3.2 Contact constraints

Contact constraints as variational inequalities in the continuous setting

The formulation of contact conditions in Section 2.2.3 is not the only possibility within the continuous setting. With regards to deriving the weak form of contact constraints, they are now expressed in a different way. These reformulated conditions are equivalent, they are also used in CHRISTENSEN et al. [15, 16], HÜEBER [54], STRÖMBERG [128], WOHLMUTH [141], and WRIGGERS [144].

Using the introduced LAGRANGE multiplier $\boldsymbol{\lambda}$ in (3.12) and decomposing it into normal and tangential components λ_n and $\boldsymbol{\lambda}_\tau$ similar to (2.58), the normal contact conditions (2.59) - (2.61) are rewritten as

$$\lambda_n \in \mathbb{R}_0^+ : \quad g\,(\delta\lambda_n - \lambda_n) \geq 0 \quad \forall\, \delta\lambda_n \in \mathbb{R}_0^+ \,. \tag{3.14}$$

Here, $\mathbb{R}_0^+$ is the semi-positive real half space and $\delta\lambda_n$ is a "trial" force. The equation (3.14) is classified as a variational inequality, see CHRISTENSEN et al. [16] and HÜEBER [54]. The reformulation of frictional contact constraints (2.63) - (2.66) as a variational inequality reads

$$\boldsymbol{\lambda}_\tau \in \boldsymbol{\mathcal{B}}(\mu\lambda_n) : \quad \mathbf{v}_{\tau,rel} \cdot (\delta\boldsymbol{\lambda}_\tau - \boldsymbol{\lambda}_\tau) \leq 0 \quad \forall\, \delta\boldsymbol{\lambda}_\tau \in \boldsymbol{\mathcal{B}}(\mu\lambda_n) \,, \tag{3.15}$$

where $\boldsymbol{\mathcal{B}}(\mu\lambda_n)$ is a $(n-1)$-dimensional sphere with center $\mathbf{0}$ and radius $\mu\lambda_n$ and $\delta\boldsymbol{\lambda}_\tau$ is a "trial" force in the tangential plane. It is the so-called principle of maximal dissipation representing COULOMB's law of friction, see STRÖMBERG [128].

The equivalence of contact conditions written as variational inequalities (3.14) and (3.15) and their counterparts (2.59) - (2.61) and (2.67) - (2.69) is given in a more descriptive way in the following. The ideas therefore are taken mainly from HÜEBER [54].

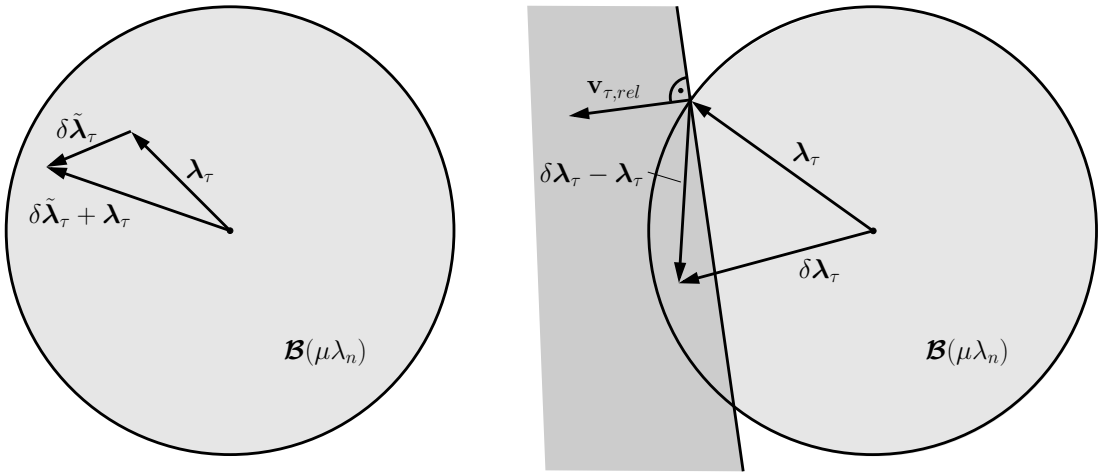

Figure 3.4: Visualization of variational inequality (3.15) representing the tangential contact conditions, stick (left) and slip case (right).

Regarding the conditions in normal direction, (2.60) is directly obtained from the constraint in (3.14) that λ_n has to be within $\mathbb{R}_0^+$. The remaining two equations are derived by choosing the trial or test force $\delta\lambda_n$, which is arbitrary within $\mathbb{R}_0^+$, in a smart and target oriented way. Assuming it to be $\lambda_n + \delta\lambda_n \geq 0$, (3.14) results in

$$g\,\delta\lambda_n \geq 0 \quad \forall\, \delta\lambda_n \in \mathbb{R}_0^+ \,. \tag{3.16}$$

In order to hold this condition for all $\delta\lambda_n \in \mathbb{R}_0^+$, the gap g must always be equal or greater than zero, which is exactly condition (2.59). Let the test force be $\delta\lambda_n = 0 \in \mathbb{R}_0^+$ and $\delta\lambda_n = 2\lambda_n \in \mathbb{R}_0^+$. With this, (3.14) becomes for the individual cases

$$-\,g\,\lambda_n \geq 0 \quad \text{and} \quad g\,\lambda_n \geq 0\,. \tag{3.17}$$

Combining both inequalities leads to $g\,\lambda_n = 0$, which is condition (2.61) and the third desired equation.

For the conditions in tangential direction, the constraint on the absolute value of $\boldsymbol{\lambda}_\tau$ in (2.67) follows directly from (3.15) with the restriction of $\boldsymbol{\lambda}_\tau$ to be within $\boldsymbol{\mathcal{B}}(\mu\lambda_n)$. The further equations are explained with the help of Figure 3.4. Assuming that $||\boldsymbol{\lambda}_\tau|| < \mu\lambda_n$, the stick case is at hand and (3.15) should deliver $\mathbf{v}_{\tau,rel} = \mathbf{0}$ as formulated in (2.68). This can be obtained with having a look at the left plot in Figure 3.4. It shows, as requested for the stick assumption, the tangential traction $\boldsymbol{\lambda}_\tau$ within the sphere $\boldsymbol{\mathcal{B}}(\mu\lambda_n)$. In this case, an arbitrary vector $\delta\tilde{\boldsymbol{\lambda}}_\tau$ can be found and added to $\boldsymbol{\lambda}_\tau$ so that the sum of both vectors $\delta\tilde{\boldsymbol{\lambda}}_\tau + \boldsymbol{\lambda}_\tau$ is within $\boldsymbol{\mathcal{B}}(\mu\lambda_n)$. Vectors within this space can be chosen as trial or test force. Carrying out this allocation $\delta\boldsymbol{\lambda}_\tau = \delta\tilde{\boldsymbol{\lambda}}_\tau + \boldsymbol{\lambda}_\tau$ and inserting $\delta\boldsymbol{\lambda}_\tau$ into (3.15), one obtains

$$\mathbf{v}_{\tau,rel} \cdot \delta\tilde{\boldsymbol{\lambda}}_\tau \leq 0. \tag{3.18}$$

Since the vector $\delta\tilde{\boldsymbol{\lambda}}_\tau$ is arbitrary, the inner product with $\mathbf{v}_{\tau,rel}$ can be positive or negative. Following from this, $\mathbf{v}_{\tau,rel}$ has to be $\mathbf{0}$ in order to fulfill (3.18) and (2.68) is reproduced. Considered

is now the slip case and $||\boldsymbol{\lambda}_\tau|| = \mu\lambda_n$. Here, it has to be shown that $\boldsymbol{\lambda}_\tau = \beta\,\mathbf{v}_{\tau,rel}$ with $\beta > 0$ as given in (2.69) follows from (3.15). This means that the lines of action of these two vectors ($\boldsymbol{\lambda}_\tau$ and $\mathbf{v}_{\tau,rel}$) have to be parallel and both vectors have to act in the same direction. If this is not the case, as illustrated in the right graph of Figure 3.4, an arbitrary trial force $\delta\boldsymbol{\lambda}_\tau$ within $\boldsymbol{\mathcal{B}}(\mu\lambda_n)$ can be found which leads to an acute angle between $\delta\boldsymbol{\lambda}_\tau - \delta\boldsymbol{\lambda}_\tau$ and $\mathbf{v}_{\tau,rel}$. This results in a positive inner product in (3.15) whereby the equation is not fulfilled. Only if $\boldsymbol{\lambda}_\tau = \beta\,\mathbf{v}_{\tau,rel}$ with $\beta > 0$ holds, no trial force leading to a positive inner product can be found from what it is proven that finally (2.69) follows from (3.15), too.

It has been shown that the contact conditions (2.59) - (2.61) and (2.67) - (2.69) in Section 2.2.3 can be derived form the variational inequalities (3.14) and (3.15). Because this is also possible for the other direction as described in HÜEBER [54], both formulations are equivalent. Expressing the contact conditions weakly in the next subsection, the contact conditions written as variational inequalities are used.

Weak form

Applying integration of (3.14) and (3.15) over the slave contact surface, the weak form of both normal and tangential contact conditions is obtained as

$$\boldsymbol{\lambda} \in \boldsymbol{\mathcal{M}}(\boldsymbol{\lambda}): \quad \int_{\gamma_c^{(1)}} g\,(\delta\lambda_n - \lambda_n)\,\mathrm{d}\gamma \geq 0\;, \tag{3.19}$$

$$\int_{\gamma_c^{(1)}} \mathbf{v}_{\tau,rel}\cdot(\delta\boldsymbol{\lambda}_\tau - \boldsymbol{\lambda}_\tau)\,\mathrm{d}\gamma \leq 0 \quad \forall\,\delta\boldsymbol{\lambda} \in \boldsymbol{\mathcal{M}}(\boldsymbol{\lambda})\;. \tag{3.20}$$

Here, $\boldsymbol{\mathcal{M}}(\boldsymbol{\lambda})$ is the admissible solution space for the LAGRANGE multiplier $\boldsymbol{\lambda}$ and the test space for the trial force $\delta\boldsymbol{\lambda}$. It is a convex subset $\boldsymbol{\mathcal{M}}(\boldsymbol{\lambda}) \subset \boldsymbol{\mathcal{M}}$ which accommodates the restrictions of $\boldsymbol{\lambda}$ and $\delta\boldsymbol{\lambda}$ in (3.14) and (3.15). According to HÜEBER [54], this subspace can be written as

$$\boldsymbol{\mathcal{M}}(\boldsymbol{\lambda}) := \{\delta\boldsymbol{\lambda} \in \boldsymbol{\mathcal{M}} : \langle\delta\boldsymbol{\lambda},\boldsymbol{\eta}\rangle \leq \langle\mu\lambda_n, ||\boldsymbol{\eta}_\tau||\rangle, \boldsymbol{\eta} \in \boldsymbol{\mathcal{W}}^{(1)} \;\text{ with }\; \eta_n \leq 0\}\;, \tag{3.21}$$

where $\langle\cdot,\cdot\rangle$ is the duality paring of the spaces $\boldsymbol{\mathcal{M}}$ and $\boldsymbol{\mathcal{V}}^{(1)}$ on $\gamma_c^{(1)}$ given by

$$\langle\delta\boldsymbol{\lambda},\boldsymbol{\eta}\rangle := \int_{\gamma_c^{(1)}} \delta\boldsymbol{\lambda}\,\boldsymbol{\eta}\,\mathrm{d}\gamma\;. \tag{3.22}$$

More detailled information about the construction of the constrained space $\boldsymbol{\mathcal{M}}(\boldsymbol{\lambda})$ can be found in HAGER [36], HÜEBER et al. [54, 55, 57] and WOHLMUTH [141].

3.3.3 Summarized weak form

In Sections 3.3.1 and 3.3.2, the weak form of the frictional contact problem has been derived and is summarized here. Weakly formulated are both balance equations and contact conditions and there are two unknown fields due to the usage of the dual LAGRANGE multiplier method for constraint enforcement. From there, it is called a mixed formulation. Altogether, the mixed weak form of the frictional contact problem looks as follows: Find $\mathbf{u}^{(i)} \in \boldsymbol{\mathcal{U}}^{(i)}$ and $\boldsymbol{\lambda} \in \boldsymbol{\mathcal{M}}(\boldsymbol{\lambda})$, $i = 1, 2$, so that the following three equations are fulfilled for the given possible test functions:

$$G^{int,ext} + \int_{\gamma_c^{(1)}} \boldsymbol{\lambda}\cdot\left(\delta\mathbf{u}^{(1)} - \left(\delta\mathbf{u}^{(2)}\circ P\right)\right)\mathrm{d}\gamma = 0 \quad \forall\,\delta\mathbf{u}^{(i)} \in \boldsymbol{\mathcal{V}}^{(i)}\;, \tag{3.23}$$

$$\int_{\gamma_c^{(1)}} g\,(\delta\lambda_n - \lambda_n)\,\mathrm{d}\gamma \geq 0 \quad \forall\, \delta\boldsymbol{\lambda} \in \boldsymbol{\mathcal{M}}(\boldsymbol{\lambda})\;, \tag{3.24}$$

$$\int_{\gamma_c^{(1)}} \mathbf{v}_{\tau,rel} \cdot (\delta\boldsymbol{\lambda}_\tau - \boldsymbol{\lambda}_\tau)\,\mathrm{d}\gamma \leq 0 \quad \forall\, \delta\boldsymbol{\lambda} \in \boldsymbol{\mathcal{M}}(\boldsymbol{\lambda})\;. \tag{3.25}$$

In order to solve this problem (3.23) - (3.25) by means of the finite element method, it is discretized in time and space in the following.

3.4 Finite element discretization

Generally, the finite element discretization of a problem contains the approximation of the geometry with finite elements and the approximation of the participating continuous solution and weighting functions with ansatz- or shape functions. This section first introduces the shape functions used for interpolation here. Then, with inserting the interpolated fields into the problem equations (3.23) - (3.25), the discrete forms of the contact virtual work and the discrete normal and tangential contact conditions are obtained.

3.4.1 Shape functions

Geometry and displacement fields

Carrying out the approximations for $\Omega_0^{(i)}$, $i = 1, 2$, given above, one has to, besides defining an element size, commit to a finite element type. With this, the discrete solution space as finite dimensional subset $\boldsymbol{\mathcal{U}}^{(i)h} \subset \boldsymbol{\mathcal{U}}^{(i)}$ is defined. Space restrictions of $\boldsymbol{\mathcal{U}}^{(i)h}$ to the slave and master contact surface lead to $\boldsymbol{\mathcal{W}}^{(i)h}$. In this work considering the three-dimensional case, the focus is on linear and trilinear interpolation of LAGRANGEan elements, namely 4-node tetrahedral and 8-node hexahedral elements for the approximation of $\Omega_0^{(i)}$, $i = 1, 2$. From this, the discretization of the contact surfaces follows directly with reduction of the dimension d to $d-1$ leading to 3-node triangular and 4-node quadrilateral elements. Also quadratic interpolation is considered, more about this can be read in Section 3.4.7.

Following the isoparametric concept, the same shape functions are applied for both geometry and field variables. For slave and master surface, the interpolations of the geometry $\mathbf{X}$ and the displacements $\mathbf{u}$ are

$$\mathbf{X}^{(1)h}|_{\Gamma_c^{(1)h}} = \sum_{k=1}^{n_{sl}} N_k^{(1)}(\xi^{(1)}, \eta^{(1)})\,\mathbf{X}_k^{(1)}\;, \tag{3.26}$$

$$\mathbf{X}^{(2)h}|_{\Gamma_c^{(2)h}} = \sum_{l=1}^{n_m} N_l^{(2)}(\xi^{(2)}, \eta^{(2)})\,\mathbf{X}_l^{(2)}\;, \tag{3.27}$$

$$\mathbf{u}^{(1)h}|_{\Gamma_c^{(1)h}} = \sum_{k=1}^{n_{sl}} N_k^{(1)}(\xi^{(1)}, \eta^{(1)})\,\mathbf{d}_k^{(1)}\;, \tag{3.28}$$

$$\mathbf{u}^{(2)h}|_{\Gamma_c^{(2)h}} = \sum_{l=1}^{n_m} N_l^{(2)}(\xi^{(2)}, \eta^{(2)})\,\mathbf{d}_l^{(2)}. \tag{3.29}$$

Here, n_{sl} and n_m represent the total number of slave and master nodes, $N_k^{(1)}$, $N_l^{(2)}$ are the standard shape functions on the respective contact surface defined with respect to the finite element parameter space $\boldsymbol{\xi}^{(i)}(\xi^{(i)}, \eta^{(i)})$, $i = 1, 2$. Finally, $\mathbf{X}_k^{(1)}$, $\mathbf{X}_l^{(2)}$, $\mathbf{d}_k^{(1)}$ and $\mathbf{d}_l^{(2)}$ denote the nodal coordinates and the nodal displacements.

Weighting function for linear momentum equation

The application of the BUBNOV-GALERKIN method goes along with the same interpolation of test function and displacement field. The discrete weighting space is restricted to the finite dimensional subset $\boldsymbol{\mathcal{V}}^{(i)h} \subset \boldsymbol{\mathcal{V}}^{(i)}$ of the continuous one and the interpolation of the weighting function field $\delta\mathbf{u}^{(i)}$ on slave and master surface is written as

$$\delta\mathbf{u}^{(1)h}|_{\Gamma_c^{(1)h}} = \sum_{k=1}^{n_{sl}} N_k^{(1)}(\xi^{(1)}, \eta^{(1)})\, \delta\mathbf{d}_k^{(1)} \ , \tag{3.30}$$

$$\delta\mathbf{u}^{(2)h}|_{\Gamma_c^{(2)h}} = \sum_{l=1}^{n_m} N_l^{(2)}(\xi^{(2)}, \eta^{(2)})\, \delta\mathbf{d}_l^{(2)} \ . \tag{3.31}$$

Here, the shape functions $N_k^{(1)}$ and $N_l^{(2)}$ are the same as in (3.26) - (3.29) and $\delta\mathbf{d}_k^{(1)}$ and $\delta\mathbf{d}_l^{(2)}$ are the discrete nodal weighting values.

LAGRANGE multiplier field and weighting function for contact conditions

A main aspect of the method considered in this work is the interpolation of the LAGRANGE multiplier field $\boldsymbol{\lambda}$ defined on the slave contact surface. It is not carried out with standard shape functions leading to standard LAGRANGE multipliers. Here, so-called dual shape functions proposed by WOHLMUTH [139, 140] are utilized for the discrete form of the LAGRANGE multiplier field $\boldsymbol{\lambda}^h \in \boldsymbol{\mathcal{M}}^h(\boldsymbol{\lambda}^h)$:

$$\boldsymbol{\lambda}^h = \sum_{j=1}^{n_{sl}} \Phi_j(\xi^{(1)}, \eta^{(1)})\, \mathbf{z}_j \ , \tag{3.32}$$

where $\mathbf{z}_j$ are the discrete nodal LAGRANGE multipliers. Dual shape functions Φ_j are constructed such that the so-called biorthogonality condition, see for example HÜEBER [57] or WOHLMUTH [139, 140], holds on the slave side:

$$\int_{\gamma_c^{(1)h}} \Phi_j(\xi^{(1)}, \eta^{(1)}) N_k^{(1)}(\xi^{(1)}, \eta^{(1)})\, \mathrm{d}\gamma = \delta_{jk} \int_{\gamma_c^{(1)h}} N_k^{(1)}(\xi^{(1)}, \eta^{(1)})\, \mathrm{d}\gamma \ , \tag{3.33}$$

where δ_{jk} is the Kronecker delta

$$\delta_{jk} = \begin{cases} 1 & \text{for } j = k \\ 0 & \text{for } j \neq k \ . \end{cases} \tag{3.34}$$

The interpolation of the weighting function field $\delta\boldsymbol{\lambda}$ is carried out with the same dual shape functions Φ_j as used for the LAGRANGE multiplier field:

$$\delta\boldsymbol{\lambda}^h = \sum_{j=1}^{n_{sl}} \Phi_j(\xi^{(1)}, \eta^{(1)})\, \delta\mathbf{z}_j \ , \tag{3.35}$$

where $\delta \mathbf{z}_j$ are the discrete nodal weighting values.

This choice of dual shape functions Φ_j fulfilling the biorthogonality condition (3.33) brings two main aspects for the solution of the contact problem. Firstly, it results in a diagonal mortar matrix $\mathbf{D}$ (see Section 3.4.2) in the contact virtual work expression. This allows for an easy elimination of the discrete LAGRANGE multipliers from the system of equations in Section 4.5. Secondly, the weak contact conditions decouple to nodal ones, see Section 3.4.4.

The construction of dual shape functions Φ_j for each slave node j can be read in FLEMISCH et al. [29], LAMICHHANE et al. [79], or WOHLMUTH [140]. The starting point is to express them as a linear combination of standard shape functions N_k as

$$\Phi_j(\xi,\eta) = a_{jk} N_k(\xi,\eta)\,, \quad \mathbf{A}_e = [a_{jk}] \in \mathbb{R}^{n_{sl}^e \times n_{sl}^e}\,, \tag{3.36}$$

where n_{sl}^e is the number of slave element nodes. The superscript (i) is omitted here. Insertion of (3.36) into equation (3.33) leads to

$$\mathbf{A}_e \mathbf{M}_e = \mathbf{D}_e\,, \tag{3.37}$$

where the matrices $\mathbf{D}_e$ and $\mathbf{M}_e$ are evaluated as

$$\mathbf{D}_e = [d_{e,jk}] \in \mathbb{R}^{n_{sl}^e \times n_{sl}^e}\,, \quad d_{e,jk} = \delta_{jk} \int_{ele} N_k(\xi,\eta)\, J(\xi,\eta)\, \mathrm{d}\xi \mathrm{d}\eta\,, \tag{3.38}$$

$$\mathbf{M}_e = [m_{e,jk}] \in \mathbb{R}^{n_{sl}^e \times n_{sl}^e}\,, \quad m_{e,jk} = \int_{ele} N_j(\xi,\eta)\, N_k(\xi,\eta)\, J(\xi,\eta)\, \mathrm{d}\xi \mathrm{d}\eta\,. \tag{3.39}$$

Here, $J(\xi,\eta)$ is the determinant of the JACOBIan

$$\mathbf{J}(\xi,\eta) = \frac{\partial \boldsymbol{x}^h}{\partial \boldsymbol{\xi}}\,. \tag{3.40}$$

characterizing the mapping between the spatial physical space $\mathbf{x}$ and the finite element parameter space $\boldsymbol{\xi}$ on the slave contact surface. The factors a_{jk} from the matrix $\mathbf{A}_e$ finally can be evaluated as

$$\mathbf{A}_e = \mathbf{D}_e \mathbf{M}_e^{-1}\,. \tag{3.41}$$

Although the contact problem is formulated for 3D throughout this work, as example, the dual shape functions of the linearly interpolated 2D line element are given. This is due to simplicity and clearness. The respective standard shape functions are

$$N_1(\xi) = \frac{1}{2}(1-\xi)\,, \quad N_2(\xi) = \frac{1}{2}(1+\xi)\,, \tag{3.42}$$

where $\xi \in [-1..1]$ as visualized on the left of Figure 3.5. For this case, the determinant J of the JACOBIan $\mathbf{J}$ of the above mapping does not depend on the finite element surface coordinate ξ but is constant over the element size. Accordingly, the dual shape functions can be constructed independently of the deformation in this special case. Following the above given instructions (3.36) - (3.41), one obtains the discontinuous, piecewise linear dual shape functions

$$\Phi_1(\xi) = \frac{1}{2}(1-3\xi)\,, \quad \Phi_2(\xi) = \frac{1}{2}(1+3\xi)\,, \tag{3.43}$$

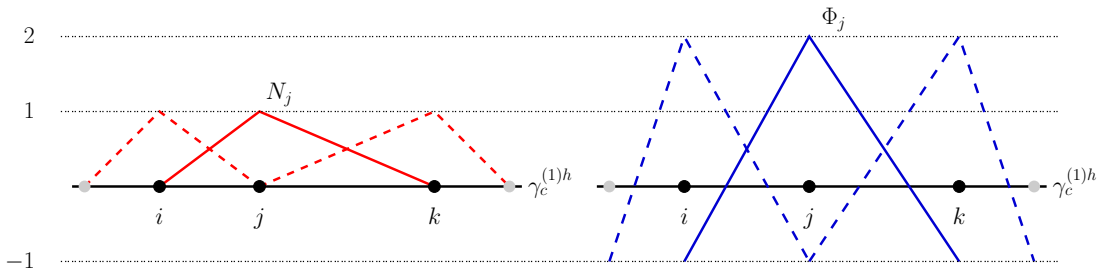

Figure 3.5: Standard (left) and dual (right) shape functions of the linearly interpolated 2D line element.

with $\xi \in [-1..1]$ as visualized on the right of Figure 3.5. In 3D, a constant JACOBIan only exists for triangular elements in the contact surface. From this, the dual shape functions can be expressed directly in the beginning of the analysis without knowing the deformation state. For all other interpolations, such as, for example, 3-node line elements in 2D or 4-node quadrilateral elements in 3D, dual shape functions have to be reconstructed for every deformation state. The construction of dual shape functions is explained and illustrated in more detail in HARTMANN et al. [39, 40], where also an example containing numerical values is presented.

3.4.2 Discrete form of contact virtual work

Substituting both the discrete form of the LAGRANGE multiplier field $\boldsymbol{\lambda}^h$ and the discrete form of the weighting function field $\delta\mathbf{u}^{(i)h}$ into the weak form of the contact virtual work in (3.23), one obtains

$$\begin{aligned} G^c(\mathbf{u},\delta\mathbf{u},\boldsymbol{\lambda}) &\approx G^{c\,h}(\mathbf{u}^h,\delta\mathbf{u}^h,\boldsymbol{\lambda}^h) \\ &= \int_{\gamma_c^{(1)h}} \boldsymbol{\lambda}^h \left(\delta\mathbf{u}^{(1)h} - \left(\delta\mathbf{u}^{(2)h}\circ P^h\right)\right) \mathrm{d}\gamma \\ &= \sum_{j=1}^{n_{sl}} \left[\sum_{k=1}^{n_{sl}} \delta\mathbf{d}_k^{(1)\mathrm{T}} \int_{\gamma_c^{(1)h}} \Phi_j N_k^{(1)} \mathrm{d}\gamma - \sum_{l=1}^{n_m} \delta\mathbf{d}_l^{(2)\mathrm{T}} \int_{\gamma_c^{(1)h}} \Phi_j \left(N_l^{(2)}\circ P^h\right) \mathrm{d}\gamma \right] \mathbf{z}_j \,, \end{aligned} \tag{3.44}$$

where P^h defines the discrete approximation of the contact mapping introduced in Section 2.2.1. The contact virtual work (3.44) contains two different kinds of integrals. There is, on the one hand, the integral of dual shape functions defined on the slave contact surface times standard shape functions, also defined on the slave contact surface. The associated matrix $\mathbf{D} \in \mathbb{R}^{3n_{sl}\times 3n_{sl}}$ is the first of two mortar coupling matrices. In nodal blocks, it is evaluated as

$$\mathbf{D}[j,k] = D_{jk}\,\mathbf{I}_3 = \int_{\gamma_c^{(1)h}} \Phi_j N_k^{(1)} \mathrm{d}\gamma\,\mathbf{I}_3 \,, \quad j = 1,...,n_{sl} \,, \quad k = 1,...,n_{sl} \,, \tag{3.45}$$

where $\mathbf{I}_3$ denotes the identity matrix in $\mathbb{R}^{3\times 3}$. Due to the biorthogonality condition (3.33), equation (3.45) yields the intended diagonal structure of the mortar matrix $\mathbf{D}$ and can therefore also

be evaluated as

$$\mathbf{D}[j,j] = D_{jj}\,\mathbf{I}_3 = \int_{\gamma_c^{(1)^h}} N_j^{(1)} \mathrm{d}\gamma\,\mathbf{I}_3\,, \quad j = 1, ..., n_{sl}\,. \tag{3.46}$$

On the other hand, the contact virtual work also contains the integral of dual shape functions defined on the slave surface times standard shape functions defined on the master surface. The according nodal blocks enter the second mortar coupling matrix $\mathbf{M} \in \mathbb{R}^{3n_{sl}\times 3n_m}$ and are evaluated as

$$\mathbf{M}[j,l] = M_{jl}\,\mathbf{I}_3 = \int_{\gamma_c^{(1)^h}} \Phi_j \left(N_l^{(2)} \circ P^h\right) \mathrm{d}\gamma\,\mathbf{I}_3\,, \quad j = 1, ..., n_{sl}\,, \quad l = 1, ..., n_m\,. \tag{3.47}$$

With these mortar matrices at hand, the discrete form of the contact virtual work can be rewritten as

$$G^{c\,h}(\mathbf{u}^h, \delta\mathbf{u}^h, \boldsymbol{\lambda}^h) = \delta\mathbf{d}^{(1)\mathrm{T}}\,\mathbf{D}^{\mathrm{T}}\,\mathbf{z} - \delta\mathbf{d}^{(2)\mathrm{T}}\,\mathbf{M}^{\mathrm{T}}\,\mathbf{z}\,, \tag{3.48}$$

where $\mathbf{z}$ is the vector of all discrete nodal LAGRANGE multipliers and $\delta\mathbf{d}^{(1)}$ and $\delta\mathbf{d}^{(2)}$ are the vectors of all discrete nodal test function values on the slave and master side. In order to arrange clearly the discrete system of equations with internal, external and contact forces, $\mathbf{f}^{int}$, $\mathbf{f}^{ext}$ and $\mathbf{f}^c$, all finite element nodes of $\Omega_0 = \Omega_0^{(1)} \cup \Omega_0^{(1)}$ are divided into three sets: the set $\mathcal{S}$ containing all n_{sl} potential contact nodes on the slave side, the set $\mathcal{M}$ of all n_m potential contact nodes on the master side and the set $\mathcal{N}$ of all remaining nodes. With this, the global displacement vector is sorted as $\mathbf{d} = (\mathbf{d}_\mathcal{N}, \mathbf{d}_\mathcal{M}, \mathbf{d}_\mathcal{S})^{\mathrm{T}}$. Assuming arbitrary test function values $\delta\mathbf{d}^{(1)}$ and $\delta\mathbf{d}^{(2)}$, the discrete vector of nodal contact forces can be written as

$$\mathbf{f}^c = \begin{bmatrix}\mathbf{0} & -\mathbf{M} & \mathbf{D}\end{bmatrix}^{\mathrm{T}}\,\mathbf{z}\,, \tag{3.49}$$

and thus the discrete version of (3.23), the algebraic form of the force equilibrium, looks like

$$\mathbf{f}^{int}(\mathbf{d}) + \mathbf{f}^c(\mathbf{d}, \mathbf{z}) = \mathbf{f}^{ext}\,. \tag{3.50}$$

Herein, the vectors of internal forces $\mathbf{f}^{int}$ and external forces $\mathbf{f}^{ext}$ are evaluated independently of the contact problem. Of course, $\mathbf{f}^{int}$ contains geometrical and material nonlinearities. The contact forces $\mathbf{f}^c(\mathbf{d}, \mathbf{z})$ are written in terms of the LAGRANGE multipliers $\mathbf{z}$ but also depend on the displacements $\mathbf{d}$. This is due to considering finite deformations throughout this work, where the mortar matrices $\mathbf{D}$ and $\mathbf{M}$ are evaluated with respect to the deformed state. Description and details on the evaluation of these surface integrals can be found in the next Section 3.4.3.

3.4.3 Evaluation of mortar surface integrals

As already mentioned in the beginning of this chapter, the mortar integrals (3.46) and (3.47) can be evaluated with different integration schemes. In this work, so-called contact segments are used as basis for numerical integration. They are defined such that the integrands, represented by the shape functions, are C^1-continuous on these surface subsets. With this, the further numerical integration can be carried out exactly within the limits of the GAUSSian quadrature. In 2D, integration is usually performed on the slave contact surface $\gamma^{(1)h}$, see POPP et al. [110] or YANG

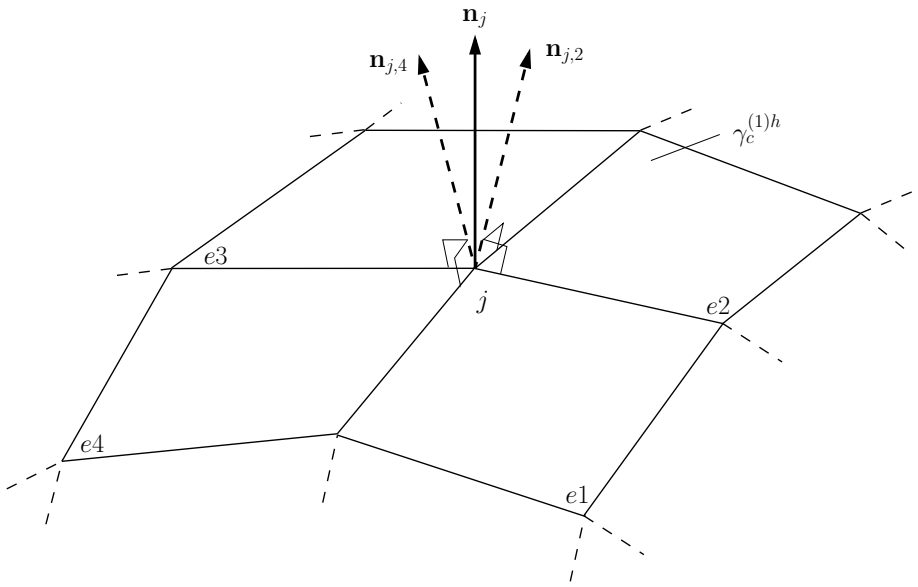

Figure 3.6: Nodally averaged normal vector $\mathbf{n}_j$ at node j. Obtained from element normal vectors $\mathbf{n}_{j,e}$ from adjacent slave elements $e1$ - $e4$ evaluated at j. As examples, the element normal vectors $\mathbf{n}_{j,e}$ are visualized for elements $e2$ and $e4$.

et al. [150]. The extension to 3D is not straightforward as contact segments are arbitrarily shaped polygons in contrast to line segments in 2D. In this work, the mortar coupling algorithm proposed in PUSO et al. [114, 116, 117] is applied. It is also described and used in POPP et al. [111] and consists of the integration on piecewise flat segments which represent the approximated slave contact surface. It is valid for linear shape functions as occurring for 4-node tetrahedrals and 8-node hexahedrals. Quadratic interpolation is discussed in Section 3.4.7, the algorithm is explained in the following.

Basis for the mortar coupling and interface segmentation is the discrete normal field on the slave contact surface. Although already determined in the continuous case in Section 2.2, a repeated definition is required in the discrete setting. This is due to the necessity of a C^1-continuous normal field as kinks in the local basis vectors can adversely affect the robustness of the algorithm, see YANG et al. [150].

The chosen definition of the slave normal field is based on nodal averaging as first suggested in YANG et al. [150]. At each slave node $j \in \mathcal{S}$, the averaged nodal unit normal is evaluated as

$$\mathbf{n}_j = \frac{\sum_{e=1}^{n_{ele}^j} \mathbf{n}_{j,e}}{\left\| \sum_{e=1}^{n_{ele}^j} \mathbf{n}_{j,e} \right\|} , \tag{3.51}$$

where $\mathbf{n}_{j,e}$ is the unit normal vector of the adjacent slave element $e = 1, ..., n_{ele}^j$ evaluated at node j. The number of adjacent slave surface contact elements is represented by n_{ele}^j. The continuous normal field $\mathbf{n}^{(1)h}$ then is set up by the interpolation with standard shape functions $N_j^{(1)}$ on the

slave side as

$$\mathbf{n}^{(1)h}\big|_{\gamma_c^{(1)h}} = \sum_{j=1}^{n_{sl}} N_j^{(1)}(\xi^{(1)}, \eta^{(1)})\, \mathbf{n}_j \ . \tag{3.52}$$

Before going on with the interface segmentation based on the continuous normal field (3.52), also the tangential plane at node j is defined. This is necessary for the discrete frictional conditions acting there, see Section 3.4.4. At each slave node $j \in \mathcal{S}$, two unit tangent vectors $\boldsymbol{\tau}_j^{\xi}$ and $\boldsymbol{\tau}_j^{\eta}$ are constructed from the averaged normal $\mathbf{n}_j$. Together, they give a local, orthonormal basis at node j as

$$\boldsymbol{\tau}_j^{\eta} = \mathbf{n}_j \times \boldsymbol{\tau}_j^{\xi} \ , \quad \mathbf{n}_j \cdot \boldsymbol{\tau}_j^{\xi} = 0 \ , \quad \mathbf{n}_j \cdot \boldsymbol{\tau}_j^{\eta} = 0 \ . \tag{3.53}$$

These equations are not sufficient for a unique determination of $\boldsymbol{\tau}_j^{\xi}$ and $\boldsymbol{\tau}_j^{\eta}$ regarding the rotation around the axis of $\mathbf{n}_j$. Therefore, construction requires an additional condition as for example the adjustment to a global coordinate system. However, this specification is arbitrary as the focus is on the tangential plane in the formulation considered here. For the ease of notation in the further derivation, the tangential basis vectors $\boldsymbol{\tau}_j^{\xi}$ and $\boldsymbol{\tau}_j^{\eta}$ of a node j are aggregated in the matrix $\boldsymbol{\tau}_j \in \mathbb{R}^{3\times 2}$ as

$$\boldsymbol{\tau}_j := \left[\boldsymbol{\tau}_j^{\xi} \ \ \boldsymbol{\tau}_j^{\eta}\right] \ . \tag{3.54}$$

With the continuous normal field at hand, the numerical integration algorithm for the mortar integrals can be carried out. Its description is similar to POPP et al. [111], for details, it is referred to the original work in PUSO et al. [114, 116, 117]. The algorithm is visualized in Figure 3.7 and is described for one pair of slave element s and master element m which are assumed to potentially come into contact.

Algorithm 1

1. Construct an auxiliary plane based on the normal vector $\mathbf{n}_0$ at the slave element center $\mathbf{x}_0^{(1)}$.
2. Project all n_{sl}^e slave element nodes $\mathbf{x}_k^{(1)}$, $k = 1, ..., n_{\text{sl}}^e$ along $\mathbf{n}_0$ onto the auxiliary plane. The projected slave nodes are denoted as $\tilde{\mathbf{x}}_k^{(1)}$. Steps 1 and 2 can be interpreted as a geometrical approximation of the slave surface by removing element warping.
3. Project all n_{m}^e master element nodes $\mathbf{x}_l^{(2)}$, $l = 1, ...n_{\text{m}}^e$ along $\mathbf{n}_0$ onto the auxiliary plane. The projected master nodes are denoted as $\tilde{\mathbf{x}}_l^{(2)}$.
4. Form the clip polygon of projected slave and master element nodes in the auxiliary plane by application of the polygon clipping algorithm, see FOLEY et al. [30] and Figure 3.7.
5. Locate the geometric center of the clip polygon to form n_{cell} triangular integration cells. Each integration cell is parametrized by its three vertices $\tilde{\mathbf{x}}_v^{\text{cell}}$, $v = 1, 2, 3$ and standard shape functions within the integration cell parameter space $\tilde{\boldsymbol{\xi}} = \{(\tilde{\xi}, \tilde{\eta}) | \tilde{\xi} \geq 0, \tilde{\eta} \geq 0, \tilde{\xi} + \tilde{\eta} \leq 1\}$.
6. Find n_{gp} GAUSS integration points with coordinates $\tilde{\boldsymbol{\xi}}_{\text{gp}}$, gp $= 1, ..., n_{\text{gp}}$, on each integration cell and project back along $\mathbf{n}_0$ to the slave and master elements to obtain $\boldsymbol{\xi}_{\text{gp}}^{(1)}$ and $\boldsymbol{\xi}_{\text{gp}}^{(2)}$.
7. Perform GAUSS integration of $D_{jj(s,m)}$ and $M_{jl(s,m)}$, $j = 1, ..., n_{\text{sl}}^e$ and $l = 1, ..., n_{\text{m}}^e$, on all integration cells. Also the weighted gap vector $\tilde{g}_{2,j(s,m)}$ is integrated. Although firstly treated

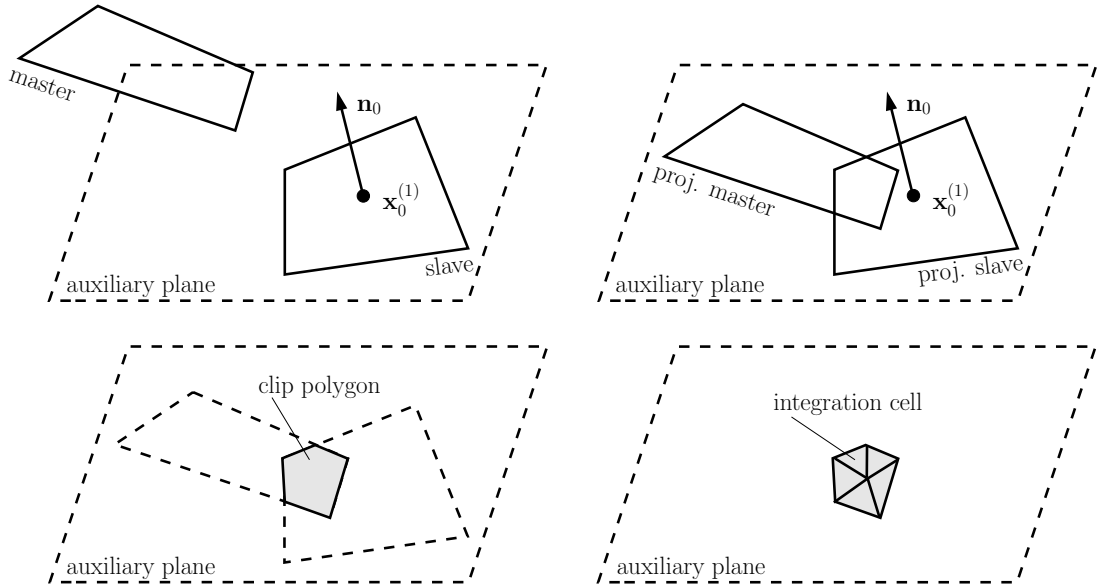

Figure 3.7: Main steps of 3D mortar coupling of one slave and master element pair: Construction of an auxiliary plane (top left), projection of slave and master element onto that auxiliary plane (top right), polygon clipping (bottom left), and division of clip polygon into triangular cells for GAUSS integration (bottom right).

in Section 3.4.4, it is already listed here to avoid unnecessary repetitions. The GAUSS integrations looks as

$$D_{jj(s,m)} = \sum_{\text{cell}=1}^{n_{\text{cell}}} \left(\sum_{\text{gp}=1}^{n_{\text{gp}}} w_{\text{gp}}\, N_j^{(1)} \left(\boldsymbol{\xi}_{\text{gp}}^{(1)} \right) J_{\text{cell}} \right) , \tag{3.55}$$

$$M_{jl(s,m)} = \sum_{\text{cell}=1}^{n_{\text{cell}}} \left(\sum_{\text{gp}=1}^{n_{\text{gp}}} w_{\text{gp}}\, \phi_j^{(1)} \left(\boldsymbol{\xi}_{\text{gp}}^{(1)} \right) N_l^{(2)} \left(\boldsymbol{\xi}_{\text{gp}}^{(2)} \right) J_{\text{cell}} \right) , \tag{3.56}$$

$$\tilde{g}_{2,j(s,m)} = \sum_{\text{cell}=1}^{n_{\text{cell}}} \left(\sum_{\text{gp}=1}^{n_{\text{gp}}} w_{\text{gp}}\, \phi_j^{(1)} \left(\boldsymbol{\xi}_{\text{gp}}^{(1)} \right) g_{\text{gp}}^h \left(\boldsymbol{\xi}_{\text{gp}}^{(1)}, \boldsymbol{\xi}_{\text{gp}}^{(2)} \right) J_{\text{cell}} \right) , \tag{3.57}$$

where w_{gp}, gp $= 1, ..., n_{\text{gp}}$, are the integration weights of the respective GAUSS rule and J_{cell}, cell $= 1, ..., n_{\text{cell}}$, is the integration cell determinant of the JACOBIan.

Expressions (3.55) - (3.57) are the contributions to D_{jj}, M_{jl} and $\tilde{g}_{2,j}$ from one slave and master element pair (s, m). In order to obtain the total quantities, all slave and master element pair contributions have to be summed up.

3.4.4 Discrete form of contact constraints

The discrete form of contact constraints is obtained by substituting the discrete spatial geometry interpolation $\mathbf{x}^{(i)h}$, the LAGRANGE multiplier interpolation $\boldsymbol{\lambda}^h$ and the interpolation of the

weighting function field for the contact constraints $\delta\boldsymbol{\lambda}^h$ into (3.24) and (3.25). In contrast to the contact virtual work (3.23), there is a separation into normal and tangential direction for the contact constraints.

Discrete contact conditions in normal direction

It is started with the contact conditions in normal direction. Applying the above specified substitution for (3.24) yields

$$
\begin{aligned}
&\int_{\gamma_c^{(1)}} g\,(\delta\lambda_n - \lambda_n)\,\mathrm{d}\gamma \approx \int_{\gamma_c^{(1)h}} g^h\,(\delta\lambda_n^h - \lambda_n^h)\,\mathrm{d}\gamma \\
&= -\sum_{j=1}^{n_{sl}} \delta z_{nj} \left[\sum_{k=1}^{n_{sl}} \int_{\gamma_c^{(1)h}} \Phi_j \mathbf{n}_j^{\mathrm{T}} N_k^{(1)} \mathrm{d}\gamma\, \mathbf{x}_k^{(1)} - \sum_{l=1}^{n_m} \int_{\gamma_c^{(1)h}} \Phi_j \mathbf{n}_j^{\mathrm{T}} \left(N_l^{(2)} \circ P^h \right) \mathrm{d}\gamma\, \mathbf{x}_l^{(2)} \right] \\
&\quad + \sum_{j=1}^{n_{sl}} z_{nj} \left[\sum_{k=1}^{n_{sl}} \int_{\gamma_c^{(1)h}} \Phi_j \mathbf{n}_j^{\mathrm{T}} N_k^{(1)} \mathrm{d}\gamma\, \mathbf{x}_k^{(1)} - \sum_{l=1}^{n_m} \int_{\gamma_c^{(1)h}} \Phi_j \mathbf{n}_j^{\mathrm{T}} \left(N_l^{(2)} \circ P^h \right) \mathrm{d}\gamma\, \mathbf{x}_l^{(2)} \right] \\
&= -\sum_{j=1}^{n_{sl}} (\delta z_{nj} - z_{nj}) \left[\sum_{k=1}^{n_{sl}} \int_{\gamma_c^{(1)h}} \Phi_j \mathbf{n}_j^{\mathrm{T}} N_k^{(1)} \mathrm{d}\gamma\, \mathbf{x}_k^{(1)} - \sum_{l=1}^{n_m} \int_{\gamma_c^{(1)h}} \Phi_j \mathbf{n}_j^{\mathrm{T}} \left(N_l^{(2)} \circ P^h \right) \mathrm{d}\gamma\, \mathbf{x}_l^{(2)} \right] \\
&= -\sum_{j=1}^{n_{sl}} (\delta z_{nj} - z_{nj})\, \mathbf{n}_j^{\mathrm{T}} \left[\int_{\gamma_c^{(1)h}} N_j^{(1)} \mathrm{d}\gamma\, \mathbf{x}_j^{(1)} - \sum_{l=1}^{n_m} \int_{\gamma_c^{(1)h}} \Phi_j \left(N_l^{(2)} \circ P^h \right) \mathrm{d}\gamma\, \mathbf{x}_l^{(2)} \right] \\
&\geq 0 \quad \forall\, \delta\boldsymbol{\lambda}^h \in \boldsymbol{\mathcal{M}}^h(\boldsymbol{\lambda}^h)\,.
\end{aligned}
\tag{3.58}
$$

Here, the biorthogonality (3.33) is exploited when going from the fourth to the fifth line. As assumption, the continuous normal field $\mathbf{n}^{(1)h}$ is approximated by the constant vector $\mathbf{n}_j$ within the local support of node j. The scalar values z_{nj} and δz_{nj} are the projections of $\mathbf{z}_j$ and $\delta\mathbf{z}_j$ into the normal direction as

$$
z_{nj} = \mathbf{n}_j^{\mathrm{T}}\, \mathbf{z}_j \quad \text{and} \quad \delta z_{nj} = \mathbf{n}_j^{\mathrm{T}}\, \delta\mathbf{z}_j\,. \tag{3.59}
$$

Defining the nodal weighted gap $\tilde{g}_{1,j}$ in its first variant in terms of the mortar matrices (3.46) and (3.47) as

$$
\tilde{g}_{1,j} = -\mathbf{n}_j^{\mathrm{T}} \left[\mathbf{D}[j,j]\, \mathbf{x}_j^{(1)} + \sum_{l=1}^{n_m} \mathbf{M}[j,l]\, \mathbf{x}_l^{(2)} \right]\,, \tag{3.60}
$$

equation (3.58) can be rewritten as

$$
\sum_{j=1}^{n_{sl}} (\delta z_{nj} - z_{nj})\, \tilde{g}_{1,j} \geq 0 \quad \forall\, \delta\boldsymbol{\lambda}^h \in \boldsymbol{\mathcal{M}}^h(\boldsymbol{\lambda}^h)\,. \tag{3.61}
$$

In order to obtain a nodal form of this above equation for a slave node $j \in \mathcal{S}$, the discrete test function values therein are chosen in an appropriate way. They are assumed to be $\delta z_{nj} \geq 0$ for node j and $z_{nk} \geq 0$ for all other remaining nodes k, whereby the resulting discrete test functions are within the admissible space $\delta\boldsymbol{\lambda}^h \in \boldsymbol{\mathcal{M}}^h(\boldsymbol{\lambda}^h)$. This choice neglects the influence of the remaining nodes k and leads to the uncoupled condition for a slave node j

$$
(\delta z_{nj} - z_{nj})\, \tilde{g}_{1,j} \geq 0 \quad \forall\, \delta z_{nj} \geq 0\,. \tag{3.62}
$$

This nodal equation, containing the restriction $z_{nj} \geq 0$ resulting from the definition of the according admissible space $\boldsymbol{\mathcal{M}}^h(\boldsymbol{\lambda}^h)$, has exactly the same structure as the normal contact constraint written in its strong form as a variational inequality in (3.14). There, it was shown that this variational inequality is equivalent to the conditions written as a complementarity problem (2.59) - (2.61). This equivalence is now transferred to equation (3.62), which is consequently rewritten as

$$\tilde{g}_{1,j} \geq 0 \; , \tag{3.63}$$

$$z_{nj} \geq 0 \; , \tag{3.64}$$

$$z_{nj} \, \tilde{g}_{1,j} = 0 \; . \tag{3.65}$$

It has to be pointed out that the nodal weighted gap can be evaluated differently to (3.60). By knowing the structure of this value from the above derivation, the second variant $\tilde{g}_{2,j}$ is achieved with the direct evaluation of

$$\tilde{g}_{2,j} = \int_{\gamma_c^{(1)h}} \Phi_j \, g^h \, \mathrm{d}\gamma \; . \tag{3.66}$$

The numerical GAUSS integration of this term has already been given in (3.57). The clear advantage of (3.66) is that it does not require the assumption of constant nodal normals as in (3.58). Therefore, for further derivation and implementation, equation (3.66) is used for the definition of the nodal weighted gap $\tilde{g}_j = \tilde{g}_{2,j}$.

Discrete contact conditions in tangential direction

The derivation of the discrete form of the frictional contact constraints is very similar to the normal direction. It is obtained by inserting the discrete form of the material velocity field $\dot{\mathbf{x}}^{(i)h}$, which is interpolated in the same way as the spatial geometry $\mathbf{x}^{(i)h}$, the discrete LAGRANGE multiplier field $\boldsymbol{\lambda}^h$ as well as the discrete weighting function field $\delta\boldsymbol{\lambda}^h$ into (3.25):

$$\begin{aligned}
&\int_{\gamma_c^{(1)}} \mathbf{v}_{\tau,rel} \cdot \left(\delta\boldsymbol{\lambda}_\tau - \boldsymbol{\lambda}_\tau\right) \mathrm{d}\gamma \approx \int_{\gamma_c^{(1)h}} \mathbf{v}_{\tau,rel}^{h\,\mathrm{T}} \left(\delta\boldsymbol{\lambda}_\tau^h - \boldsymbol{\lambda}_\tau^h\right) \mathrm{d}\gamma \\
&= \sum_{j=1}^{n_{sl}} \delta\mathbf{z}_{\tau j}^{\mathrm{T}} \left[\sum_{k=1}^{n_{sl}} \int_{\gamma_c^{(1)h}} \Phi_j \boldsymbol{\tau}_j^{\mathrm{T}} N_k^{(1)} \mathrm{d}\gamma \, \dot{\mathbf{x}}_k^{(1)} - \sum_{l=1}^{n_m} \int_{\gamma_c^{(1)h}} \Phi_j \boldsymbol{\tau}_j^{\mathrm{T}} \left(N_l^{(2)} \circ P^h \right) \mathrm{d}\gamma \, \dot{\mathbf{x}}_k^{(1)} \right] \\
&- \sum_{j=1}^{n_{sl}} \mathbf{z}_{\tau j}^{\mathrm{T}} \left[\sum_{k=1}^{n_{sl}} \int_{\gamma_c^{(1)h}} \Phi_j \boldsymbol{\tau}_j^{\mathrm{T}} N_k^{(1)} \mathrm{d}\gamma \, \dot{\mathbf{x}}_k^{(1)} - \sum_{l=1}^{n_m} \int_{\gamma_c^{(1)h}} \Phi_j \boldsymbol{\tau}_j^{\mathrm{T}} \left(N_l^{(2)} \circ P^h \right) \mathrm{d}\gamma \, \dot{\mathbf{x}}_l^{(2)} \right] \\
&= \sum_{j=1}^{n_{sl}} (\delta\mathbf{z}_{\tau j} - \mathbf{z}_{\tau j})^{\mathrm{T}} \left[\sum_{k=1}^{n_{sl}} \int_{\gamma_c^{(1)h}} \Phi_j \boldsymbol{\tau}_j^{\mathrm{T}} N_k^{(1)} \mathrm{d}\gamma \, \dot{\mathbf{x}}_k^{(1)} - \sum_{l=1}^{n_m} \int_{\gamma_c^{(1)h}} \Phi_j \boldsymbol{\tau}_j^{\mathrm{T}} \left(N_l^{(2)} \circ P^h \right) \mathrm{d}\gamma \, \dot{\mathbf{x}}_l^{(2)} \right] \\
&= \sum_{j=1}^{n_{sl}} (\delta\mathbf{z}_{\tau j} - \mathbf{z}_{\tau j})^{\mathrm{T}} \, \boldsymbol{\tau}_j^{\mathrm{T}} \left[\int_{\gamma_c^{(1)h}} N_j^{(1)} \mathrm{d}\gamma \, \dot{\mathbf{x}}_j^{(1)} - \sum_{l=1}^{n_m} \int_{\gamma_c^{(1)h}} \Phi_j \left(N_l^{(2)} \circ P^h \right) \mathrm{d}\gamma \, \dot{\mathbf{x}}_l^{(2)} \right] \\
&\geq 0 \quad \forall \, \delta\boldsymbol{\lambda}^h \in \boldsymbol{\mathcal{M}}^h(\boldsymbol{\lambda}^h) \; .
\end{aligned} \tag{3.67}$$

The biorthogonality (3.33) again is used stepping from the fourth to the fifth line. Expressions $\mathbf{z}_{\tau j} \in \mathbb{R}^2$ and $\delta\mathbf{z}_{\tau j} \in \mathbb{R}^2$ denote the projection of the vectors $\mathbf{z}_j$ and $\delta\mathbf{z}_j$ into the tangent plane $\boldsymbol{\tau}_j \in \mathbb{R}^{3\times 2}$ defined in (3.54) as

$$\mathbf{z}_{\tau_j} = \boldsymbol{\tau}_j^{\mathrm{T}}\,\mathbf{z}_j \quad \text{and} \quad \delta\mathbf{z}_{\tau_j} = \boldsymbol{\tau}_j^{\mathrm{T}}\,\delta\mathbf{z}_j \;. \tag{3.68}$$

In (3.67), as approximation, the nodal tangent matrix $\boldsymbol{\tau}_j$ is held constant over the local support of a node. Defining the weighted tangential relative velocity $\tilde{\mathbf{v}}_{\tau j}$ of a node $j \in \mathcal{S}$ as

$$\tilde{\mathbf{v}}_{\tau j} = \boldsymbol{\tau}_j^{\mathrm{T}} \left[\mathbf{D}[j,j]\,\dot{\mathbf{x}}_j^{(1)} + \sum_{l=1}^{n_m} \mathbf{M}[j,l]\,\dot{\mathbf{x}}_l^{(2)} \right] \;, \tag{3.69}$$

(3.67) can be rewritten as

$$\sum_{j=1}^{n_{sl}} (\delta\mathbf{z}_{\tau j} - \mathbf{z}_{\tau j})^{\mathrm{T}}\,\tilde{\mathbf{v}}_{\tau j} \geq 0 \quad \forall\, \delta\boldsymbol{\lambda}^h \in \boldsymbol{\mathcal{M}}^h(\boldsymbol{\lambda}^h) \;. \tag{3.70}$$

The nodal form of the above equation results from assuming the discrete test function vector to be $\delta\mathbf{z}_j$ with $\|\delta\mathbf{z}_{\tau j}\| \leq \mu\, z_{nj}$ for the node j and $\mathbf{z}_k$ with $\|\mathbf{z}_{\tau k}\| \leq \mu\, z_{nk}$ for all other remaining nodes k. With the listed restrictions, the discrete test functions are in the admissible space $\delta\boldsymbol{\lambda}^h \in \boldsymbol{\mathcal{M}}^h(\boldsymbol{\lambda}^h)$ and the nodal condition is obtained

$$(\delta\mathbf{z}_{\tau j} - \mathbf{z}_{\tau j})\,\tilde{\mathbf{v}}_{\tau j} \geq 0 \quad \forall\, \delta\mathbf{z}_{\tau j} \quad \text{with} \quad \|\delta\mathbf{z}_{\tau j}\| \leq \mu\, z_{nj} \;, \tag{3.71}$$

where $\mathbf{z}_{\tau j}$ is constrained as $\|\mathbf{z}_{\tau j}\| \leq \mu\, z_{nj}$. Analogous to the strong form of the tangential conditions in Section 3.3.2, this variational inequality is transformed to the equivalent set of equations

$$\psi_c := \|\mathbf{z}_{\tau j}\| - \mu\,|z_{nj}| \leq 0 \;, \tag{3.72}$$

$$\tilde{\mathbf{v}}_{\tau j} + \beta\,\mathbf{z}_{\tau j} = 0 \;, \tag{3.73}$$

$$\beta \geq 0 \;, \tag{3.74}$$

$$\psi_c\,\beta = 0 \;. \tag{3.75}$$

With equations (3.63) - (3.65) and (3.72) - (3.75), one has arrived at the discrete form of normal and tangential contact constraints. Although they are formulated in an integral manner in (3.24) and (3.25), they are now available as decoupled nodal equations for each slave node $j \in \mathcal{S}$ having the same structure as their continuous counterparts (2.59) - (2.61) and (2.63) - (2.66). The integral formulation is present in the geometric measures as in the weighted gap $\tilde{g}_j$ and the weighted tangential relative velocity $\tilde{\mathbf{v}}_{\tau j}$.

3.4.5 Objectivity of tangential relative velocity

An important aspect of a proper formulation of frictional laws in the finite sliding context is frame indifference of the rate measures involved. This affects the tangential relative velocity of the contacting bodies $\tilde{\mathbf{v}}_{\tau,rel}$ in the considered case of frictional contact. Frame indifference, alternatively referred to as objectivity, assures that this quantity is unaffected by any rigid body motion which the two contacting bodies might experience at the instant of question. Mathematically, this can be tested with formulating the tangential relative velocity $\tilde{\mathbf{v}}_{\tau,rel}$ in an alternative reference frame. If frame indifferent, it should be exactly the same there.

Examination of objectivity

In the continuous setting, the tangential relative velocity $\mathbf{v}_{\tau,rel}$ in Expression (2.57) has been chosen for further derivation because of integration reasons. But already in its strong form, this measure is not frame indifferent. This can be proven or looked up in a large amount of publications, treated comprehensively for example in the work of LAURSEN [81, 83]. So it is no surprise that also the weak form derived from this, Expression (3.69), is not frame indifferent:

To show this, first, an alternative frame is introduced. It is denoted in the following by superscripts $(\cdot)^*$ and can be related to the original frame via a rigid body translation $\mathbf{c}(\mathbf{t})$ and a rotation $\mathbf{Q}(\mathbf{t})$:

$$\mathbf{x}^* = \mathbf{c}(t) + \mathbf{Q}(t)\,\mathbf{x}\,, \tag{3.76}$$

where $\mathbf{Q}$ is a 3 x 3 rotation matrix with $\mathbf{Q}^T\,\mathbf{Q} = \mathbf{I}_3$. Then, the weighted tangential relative velocity (3.69), as quantity to be examined, is expressed in this alternative frame

$$\begin{aligned}
\tilde{\mathbf{v}}^*_{\tau j} &= (\mathbf{Q}\,\boldsymbol{\tau}_j)^{\mathrm{T}}\;\mathbf{Q}\left(\mathbf{D}[j,j]\,\dot{\mathbf{x}}^{(1)}_j - \sum_{l=1}^{n_m}\mathbf{M}[j,l]\,\dot{\mathbf{x}}^{(2)}_l\right)\\
&\quad + (\mathbf{Q}\,\boldsymbol{\tau}_j)^{\mathrm{T}}\;\dot{\mathbf{Q}}\left(\mathbf{D}[j,j]\,\mathbf{x}^{(1)}_j - \sum_{l=1}^{n_m}\mathbf{M}[j,l]\,\mathbf{x}^{(2)}_l\right)\\
&= \boldsymbol{\tau}_j^{\mathrm{T}}\,\mathbf{I}_3\left(\mathbf{D}[j,j]\,\dot{\mathbf{x}}^{(1)}_j - \sum_{l=1}^{n_m}\mathbf{M}[j,l]\,\dot{\mathbf{x}}^{(2)}_l\right)\\
&\quad + \boldsymbol{\tau}_j^{\mathrm{T}}\,\mathbf{Q}^{\mathrm{T}}\,\dot{\mathbf{Q}}\left(\mathbf{D}[j,j]\,\mathbf{x}^{(1)}_j - \sum_{l=1}^{n_m}\mathbf{M}[j,l]\,\mathbf{x}^{(2)}_l\right)\\
&= \tilde{\mathbf{v}}_{\tau j} + \boldsymbol{\tau}_j^{\mathrm{T}}\,\mathbf{Q}^{\mathrm{T}}\,\dot{\mathbf{Q}}\left(\mathbf{D}[j,j]\,\mathbf{x}^{(1)}_j - \sum_{l=1}^{n_m}\mathbf{M}[j,l]\,\mathbf{x}^{(2)}_l\right)\,.
\end{aligned} \tag{3.77}$$

In order to obtain objectivity from (3.77), the tangential components of the weighted relative velocity must be the same in both the transformed and the original frame, $\tilde{\mathbf{v}}^*_{\tau j} = \tilde{\mathbf{v}}_{\tau j}$. This is only the case for the term in brackets being zero. This term is the nodal weighted gap vector $\tilde{\mathbf{g}}_j$ defined as

$$\tilde{\mathbf{g}}_j = \mathbf{D}[j,j]\;\mathbf{x}^{(1)}_j - \sum_{l=1}^{n_m}\mathbf{M}[j,l]\;\mathbf{x}^{(2)}_l\,, \tag{3.78}$$

which can be obtained from

$$\tilde{\mathbf{g}}_j = \int_{\gamma_c^{(1)h}} \phi_j\,\mathbf{g}^h\,\mathrm{d}\gamma\,, \tag{3.79}$$

where $\mathbf{g}^h$ is the discrete version of the gap vector defined in (2.45). With this, the vector $\tilde{\mathbf{g}}_j$ has the same characteristic as the scalar values $\tilde{g}_j$ in (3.66) and $\tilde{\mathbf{v}}_{\tau j}$ in (3.69), but contains no projection into normal direction as in the first case or no projection into the tangential plane together with a time derivation as in the second case.

The normal contact conditions only enforce the normal projection of $\tilde{\mathbf{g}}_j$, namely $\tilde{g}_j$ to be zero, but not the vector itself, see also PUSO et al. [116] and YANG et al. [150]. In the case of curved

surfaces discretized with the mortar method, $\tilde{\mathbf{g}}_j$ can vary from zero, so that frame indifference of the weighted tangential relative velocity $\tilde{\mathbf{v}}_{\tau j}$ as derived above cannot be guaranteed in these cases. Therefore, an alternative measure for finite deformation frictional contact is chosen and presented in the next section.

Frame indifferent measure

Discretizing the contact surfaces with the standard, not with the dual mortar method, an alternative objective tangential relative velocity has originally been introduced in PUSO et al. [116] and, since then, applied in LAURSEN et al. [84], PUSO et al. [118], and YANG et al. [148, 149, 150]. The derivation in PUSO et al. [116] is kept very short and repeated here. Starting point is the definition of the relative tangential velocity in the continuous setting in Section 2.2.2. There, two possibilities of evaluation are discussed. Firstly, formulating it in the slip advected bases as in equations (2.51) and (2.52) and secondly, evaluating it from the relative velocity of opposed material points as in equation (2.57). Both formulations are obtained by total time derivation of the relative position vector $\mathbf{g}$ between $\mathbf{x}^{(1)}$ and $\hat{\mathbf{x}}^{(2)}$ which has to be zero, see (2.50).

In the spatially discretized setting, having a non-objective measure for the weighted tangential relative velocity $\tilde{\mathbf{v}}_{\tau j}$ at hand, the above derivation is applied again. The discrete counterpart of the relative position vector $\mathbf{g}$ in the continuous setting is $\tilde{\mathbf{g}}_j$ which is already known from (3.78). As in Section 2.2.2, total time derivation is applied:

$$\begin{aligned}\frac{\mathrm{d}}{\mathrm{d}t}\left(\tilde{\mathbf{g}}_j\right) = \dot{\tilde{\mathbf{g}}}_j = &\left(\mathbf{D}[j,j]\,\dot{\mathbf{x}}_j^{(1)} - \sum_{l=1}^{n_m} \mathbf{M}[j,l]\,\dot{\mathbf{x}}_l^{(2)}\right) \\ &+ \left(\dot{\mathbf{D}}[j,j]\,\mathbf{x}_j^{(1)} - \sum_{l=1}^{n_m} \dot{\mathbf{M}}[j,l]\,\mathbf{x}_l^{(2)}\right) \approx \mathbf{0}\,. \end{aligned} \tag{3.80}$$

Since the vector $\tilde{\mathbf{g}}_j$, as explained before, might not be exactly zero, also its time derivation can vary from this value. Projecting the first term in brackets into the nodal tangential plane $\boldsymbol{\tau}_j$, one obtains exactly the non-objective measure for the relative velocity in (3.69). Now the second term in brackets is considered. It is the discrete equivalent of the right hand side of equation (2.50) in the continuous setting. As the time derivatives $\dot{\mathbf{D}}$ and $\dot{\mathbf{M}}$ are zero during rigid body rotations, it is frame indifferent like its continuous counterpart. It is chosen to construct an objective measure for the weighted tangential relative velocity by changing the sign and projection into the tangent plane as

$$\hat{\mathbf{v}}_{\tau j} = -\boldsymbol{\tau}_j^{\mathrm{T}} \left[\dot{\mathbf{D}}[j,j]\,\mathbf{x}_j^{(1)} + \sum_{l=1}^{n_m} \dot{\mathbf{M}}[j,l]\,\mathbf{x}_l^{(2)}\right]\,. \tag{3.81}$$

3.4.6 Time discretization

Besides the spatial approximation with finite elements discussed above, time dependent terms have to be discretized temporally. As quasi-static problems are treated here, they do not appear in the balance equation (3.50), but in the contact constraints with the tangential relative velocity

(3.81). Choosing a Backward Euler scheme as time discretization

$$\frac{\mathrm{d}(\cdot)}{\mathrm{d}t} \approx \frac{(\cdot)(t) - (\cdot)(t_{n-1})}{\Delta t} \,, \tag{3.82}$$

one obtains the spatially and temporally discretized, tangential relative velocity $\hat{\mathbf{v}}_{\tau j}$ of a slave node j

$$\begin{aligned} \tilde{\mathbf{v}}_{\tau j} = &- \boldsymbol{\tau}_j^{\mathrm{T}}(t_n) \left(\frac{\mathbf{D}[j,j](t_n) - \mathbf{D}[j,j](t_{n-1})}{\Delta t} \, \mathbf{x}_j^{(1)}(t_n) \right) \\ &+ \boldsymbol{\tau}_j^{\mathrm{T}}(t_n) \left(\sum_{l=1}^{n_m} \frac{(\mathbf{M}[j,l](t_n) - \mathbf{M}[j,l](t_{n-1}))}{\Delta t} \, \mathbf{x}_l^{(2)}(t_n) \right) \,. \end{aligned} \tag{3.83}$$

Multiplication with Δt leads from the discretized velocity $\hat{\mathbf{v}}_{\tau_j}$ to the nodal slip increment $\tilde{\mathbf{u}}_{\tau j}$

$$\begin{aligned} \tilde{\mathbf{u}}_{\tau j} = &- \boldsymbol{\tau}_j^{\mathrm{T}}(t_n) \, (\mathbf{D}[j,j](t_n) - \mathbf{D}[j,j](t_{n-1})) \, \mathbf{x}_j^{(1)}(t_n) \\ &+ \boldsymbol{\tau}_j^{\mathrm{T}}(t_n) \sum_{l=1}^{n_m} (\mathbf{M}[j,l](t_n) - \mathbf{M}[j,l](t_{n-1})) \, \mathbf{x}_l^{(2)}(t_n) \end{aligned} \tag{3.84}$$

and the discrete nodal tangential contact conditions can be summarized as

$$\psi_{cj} = \|\mathbf{z}_{\tau j}\| - \mu \, z_{nj} \leq 0 \,, \tag{3.85}$$

$$\tilde{\mathbf{u}}_{\tau j} - \tilde{\beta}_j \, \mathbf{z}_{\tau j} = \mathbf{0} \,, \tag{3.86}$$

$$\tilde{\beta}_j \geq 0 \,, \tag{3.87}$$

$$\psi_{cj} \, \tilde{\beta}_j = 0 \,, \tag{3.88}$$

with $\tilde{\beta}_j = \beta_j \, \Delta t$.

It has to be stressed that the slip increment (3.84) varies from the slip increment applied in LAURSEN et al. [84], PUSO et al. [116, 118] and YANG et al. [148, 149, 150]. This is because the mortar matrices look different there due to the usage of the standard LAGRANGE multiplier interpolation. In addition, the entering spatial configuration coordinates there are from the last point of time $\mathbf{x}^{(1)}(t_{n-1})$ and $\mathbf{x}^{(2)}(t_{n-1})$ and not from the current one $\mathbf{x}^{(1)}(t_n)$ and $\mathbf{x}^{(2)}(t_n)$ as in (3.84). Here, this results from the consistent application of the implicit Backward Euler integration scheme which leads to very good results for $\tilde{\mathbf{u}}_{\tau j}$, even for large rotations during a time step.

3.4.7 Quadratic interpolation, different types of interpolation

Before summarizing the discrete form of contact constraints, further types of interpolation for displacements and LAGRANGE multipliers considered so far are discussed. This is firstly the quadratic interpolation and secondly, the discretization of LAGRANGE multipliers with standard instead of dual shape functions. Although these discretizations have been implemented as extension from normal to frictional contact within this work, they are only addressed very briefly because of not being in the focus here.

Quadratic interpolation

So far, only linear and trilinear interpolation in three dimensions has been considered. This is at hand for hex8 and tet4 discretizations leading to 4-node quadrilateral and 3-node triangular contact surface elements. This determination came into play for both the construction of dual shape functions (section 3.4.1) fulfilling the biorthogonality condition and the evaluation of the mortar surface integrals (section 3.4.3). In this section now, quadratic interpolation as a form of higher-order interpolation is discussed for both issues. Concretely, this is for 9-node quadrilateral, 8-node quadrilateral and 6-node triangular contact surface elements resulting from hex27, hex20 and tet10 discretizations.

Firstly, the extension of the segmentation and integration algorithm for the evaluation of the mortar surface integrals to second-order (quadratic) interpolation is considered. This extension has originally been performed by PUSO et al. [118] and is also employed here. The basic idea here is to subdivide the quadratic surface elements into linearly interpolated subsegments. This leads to the following cases: The 9-node quadrilateral element is split into four 4-node quadrilateral subsegments, the 8-node quadrilateral element into one 4-node quadrilateral and four 3-node triangular subsegments and the 6-node triangular element into four 3-node triangular subsegments. A more descriptive illustration can be found in PUSO et al. [118]. This measure allows for the application of the described algorithm for linearly interpolated elements in Section 3.4.3 with almost no modification. For sure, the subdivision contains a geometrical approximation as it is no longer able to reflect the underlying quadratic surfaces correctly. This affects the integration domain, see POPP et al. [111]. However, by establishing mappings from parent element spaces to subsegment spaces and vice versa, the higher-order shape function products in (3.55) - (3.57) can still be evaluated properly.

The second issue when treating second-order interpolation is the definition of suitable dual LAGRANGE multiplier spaces. For 3-node line elements in 2D and 9-node quadrilateral elements in 3D, quadratic shape functions for the LAGRANGE multipliers are obtained from the biorthogonality condition (3.33) with the application of (3.36) and (3.37) as demonstrated in HARTMANN et al. [40] or POPP et al. [110, 111]. The construction of dual shape functions for 8-node quadrilateral and 6-node triangular contact elements is not straightforward. This is because already the standard shape functions of these elements do not satisfy the integral positivity which can lead to unphysical, negative weighted nodal gaps $\tilde{g}_j$ although the unweighted physical gap at the node j is positive. The solution is addressed for finite deformation frictional contact using standard shape functions for LAGRANGE multiplier interpolation in PUSO et al. [118]. The construction of dual LAGRANGE multiplier shape function for quadratic interpolation requires, of course, the fulfillment of the biorthogonality condition (3.33), but also the fulfillment of the integral positivity as briefly explained above. This is a non-trivial task for 8-node quadrilateral and 6-node triangular contact elements. It has recently been solved on the basis of the work of LAMICHHANE et al. [78, 80] in POPP et al. [112] and WOHLMUTH et al. [143] for finite deformation contact. There, a basis transformation procedure is applied.

Standard shape functions for LAGRANGE multipliers

The interpolation of LAGRANGE multipliers and respective weighting functions for the contact conditions is realized throughout this work mainly with dual shape functions. This brings the

clear advantage of leading to a diagonal structure of the mortar matrix $\mathbf{D}$. It allows, as explained, for an efficient elimination of the discrete LAGRANGE multipliers from the system of equations which will be shown when treating the algebraic representation of the problem in Section 4.5. Besides, the discrete contact conditions for a slave node $j \in \mathcal{S}$ are unaffected from adjacent slave nodes $k \in \mathcal{S}$ yielding point-wise decoupled constraints, see Section 3.4.4.

At first, the more obvious interpolation of LAGRANGE multipliers and weighting functions for the conditions is the interpolation with standard shape functions. They are used successfully for example in DICKOPF and KRAUSE [22], FISCHER and WRIGGERS [27], PUSO et al. [116, 118] or YANG et al. [150]. The application of the LAGRANGE multiplier method with keeping the additional unknowns leads to a saddle point-type problem similar to the dual case shown in Section 4.5. However, the possibility of efficient elimination gets lost so that the saddle point-type system of equations has to be solved within the Newton iteration. Besides, the contact constraints are not point-wise decoupled when using standard instead of dual shape functions. It already requires additional mathematical consideration when deriving the discrete form of the contact constraints, see Section 3.4.4 and HÜEBER [54] and WOHLMUTH [141]. And, to the author's experience, the convergence of the active, stick and slip set in frictional contact simulations is less for not having point-wise decoupled constraints.

3.4.8 Summarized discrete form

Since the derivation of the spatially and temporally discretized form of the 3D finite deformation frictional contact problem extends over several pages, it is summarized shortly here. In order to be able to apply the finite element method as spatial discretization scheme, a weak form of the contact problem including balance equation and contact constraints is obtained with equations (3.23), (3.24) and (3.25). The problem is formulated with LAGRANGE multipliers as method to enforce the contact constraints. Their interpolation and the interpolation of according test functions is realized with continuous shape functions leading to the mortar method which is characterized by a weak formulation of contact constraints. The dual shape functions fulfill the biorthogonality condition (3.33) leading to a diagonal structure of the mortar matrix $\mathbf{D}$. The fully, also temporally discretized 3D frictional contact problem is finally made up of the balance equation (3.50) and the contact constraints (3.63) - (3.65) and (3.72) - (3.75). Although enforced weakly, they are available as nodal and decoupled conditions. Being still formulated as inequalities, the constraints require the treatment with a suitable active set strategy presented in the next chapter. The whole formulation is valid for finite deformations. This requires a consistent linearization of all displacement and LAGRANGE multiplier dependent terms.

4 Frictional contact - solution with semi-smooth NEWTON method

This chapter describes the applied solution algorithm for the discretized finite deformation frictional contact problem in equations (3.50), (3.63) - (3.65) and (3.72) - (3.75). It is the semi-smooth NEWTON method which allows for the treatment of all nonlinearities, including the search for the active, stick and slip set, in one single iterative scheme. For this, contact conditions are reformulated in so-called complementarity functions (section 4.1) leading to the equality instead of inequality constraints. The semi-smooth NEWTON method is equivalent to the well known primal-dual active set strategy (PDASS) as demonstrated in CHRISTENSEN et al. [16], HINTERMÜLLER et al. [52], or QI and SUN [119]. It has successfully been used for small deformation contact problems in ALART and CURNIER [2], CHRISTENSEN et al. [16], HÜEBER et al. [56, 57], and WOHLMUTH [141] and has been extended to finite deformations in GITTERLE et al. [35] and POPP et al. [110, 111, 112]. The chapter describes the algorithm, presents the consistent linearization and the algebraic representation of the problem. It will conclude with several 2D and 3D examples to validate the approach and demonstrate its numerical efficiency.

4.1 Non-smooth complementarity functions

In order to apply the semi-smooth NEWTON method, contact conditions are reformulated in so-called complementarity functions which express them equivalently. They are constructed "smooth enough to use NEWTON like solution methods", as literally described in ALART and CURNIER [2] concerning the construction of frictional contact operators.

4.1.1 Reformulation of normal contact conditions

As given and discussed in detail in, for example, HÜEBER et al. [54, 56] and POPP et al. [110, 111], the complementarity function for the normal direction is defined for each slave node $j \in \mathcal{S}$ as

$$C_{nj}\left(\mathbf{z}_j, \mathbf{d}\right) = \left(z_{nj} - \max\left(0, z_{nj} - c_n \tilde{g}_j\right)\right) \ , \quad c_n > 0 \ . \tag{4.1}$$

It is equivalent to the normal contact conditions (3.63) - (3.65) when

$$C_{nj}\left(\mathbf{z}_j, \mathbf{d}\right) = 0 \ , \tag{4.2}$$

independently of the choice of the parameter c_n. This parameter does not influence the accuracy of results, but can influence the convergence behavior of the semi-smooth NEWTON method. A study concerning this topic will follow in Section 4.6. The equivalence of the normal contact conditions (3.63) - (3.65) with the active and inactive branch and the complementarity function being zero in (4.2) is visualized in Figure 4.1.

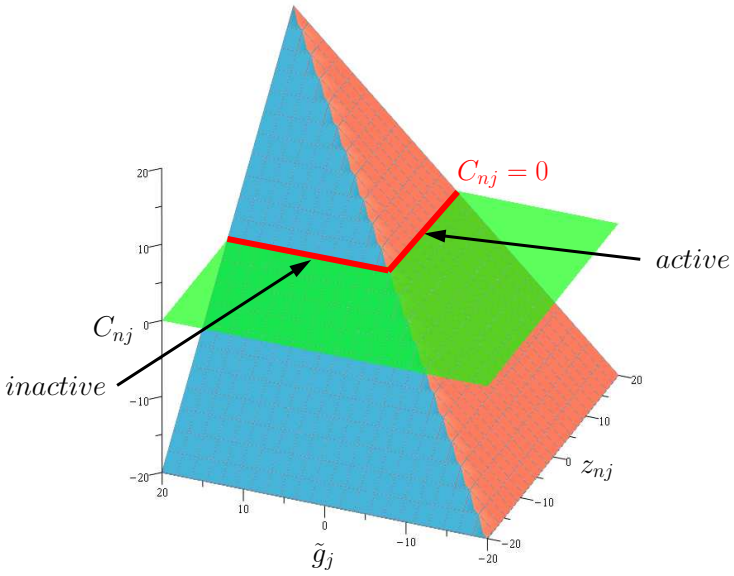

Figure 4.1: Nodal complementarity function C_{nj} for normal direction, $c_n = 1$, equivalent to normal contact conditions for $C_{nj} = 0$.

4.1.2 Reformulation of frictional contact conditions

The reformulation of frictional contact conditions is similar. One possible complementarity function is defined in HÜEBER et al. [54, 56] and used in GITTERLE et al. [35] in the context of 2D finite deformation frictional contact. It takes the form of a two component vector equation and is written as

$$\begin{aligned}\mathbf{C}_{\tau j}\left(\mathbf{z}_j, \mathbf{d}\right) = &\max\left(\mu\left(z_{nj} - c_n\,\tilde{g}_j\right), \left\|\mathbf{z}_{\tau j} + c_t\tilde{\mathbf{u}}_{\tau j}\right\|\right)\mathbf{z}_{\tau j} \\ &- \mu\max\left(0, z_{nj} - c_n\,\tilde{g}_j\right)\left(\mathbf{z}_{\tau j} + c_t\tilde{\mathbf{u}}_{\tau j}\right), \quad c_n > 0, c_t > 0\,. \end{aligned} \tag{4.3}$$

It can be shown that COULOMB's friction law (3.85) - (3.88) is equivalently expressed when

$$\boldsymbol{C}_{\tau j}\left(\mathbf{z}_j, \mathbf{d}\right) = \mathbf{0}\,, \quad c_n,\, c_t > 0 \tag{4.4}$$

for any choice of the parameters c_n and c_t. As valid for c_n, also c_t does not influence the accuracy of results but can influence convergence behavior. Again, the reader is referred to Section 4.6 for more information about this parameter. In Figure 4.2, the complementarity function in tangential direction (4.3) is visualized for 2D and a constant value of $\mu\, z_{nj}$. The intersection with the horizontal plane $C_{\tau j} = 0$ leads to conditions (3.85) - (3.88) with their characteristic stick and slip branches.

It has to be pointed out that (4.3) is not the only possible complementarity function to express COULOMB's friction law. Different ones are used for example in ALART and CURNIER [2] and CHRISTENSEN et al. [16]. In HÜEBER et al. [56], also an additional complementarity function is mentioned. But it is not preferred there because of less robustness compared to the algorithm

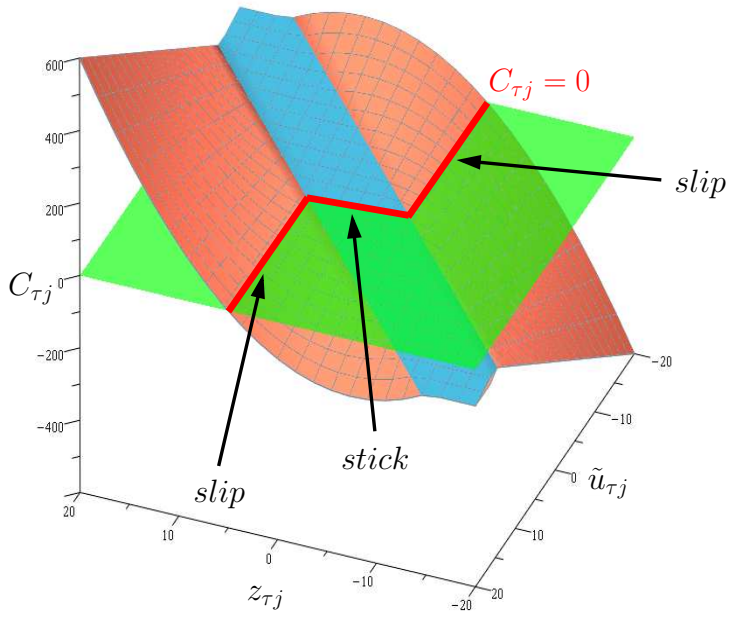

Figure 4.2: Nodal complementarity function $C_{\tau j}$ for tangential direction, visualized for 2D, $\mu\, z_{nj} = 5$, $c_t = 1$, equivalent to frictional contact conditions for $C_{\tau j} = 0$.

based on (4.3). This statement has been confirmed in BUCHNER [13], where extensive convergence studies addressing the robustness of algorithms with different complementarity functions have been carried out.

4.2 Semi-smooth NEWTON method

From now on, the contact conditions (3.63) - (3.65) and (3.85) - (3.88) are replaced by (4.2) and (4.4). In combination with the force equilibrium (3.23), the following nonlinear system of equation is obtained. It represents the spatially and temporally discretized frictional contact problem and is written in residual form:

$$\begin{aligned} \mathbf{r} = \mathbf{f}^{int}(\mathbf{d}) + \mathbf{f}^{c}(\mathbf{d},\mathbf{z}) - \mathbf{f}^{ext} &= \mathbf{0}\,, \\ C_{nj}\left(\mathbf{z}_j, \mathbf{d}\right) &= 0 \qquad \forall\, j \in \mathcal{S}\,, \\ \mathbf{C}_{\tau j}\left(\mathbf{z}_j, \mathbf{d}\right) &= \mathbf{0} \qquad \forall\, j \in \mathcal{S}\,. \end{aligned} \tag{4.5}$$

To this set of equations, the semi-smooth NEWTON method as a NEWTON type algorithm is applied. It is justified as the used complementarity functions contain the max-function and the EUCLIDean norm, which is why they are are semi-smooth. This is known from mathematical contributions in HINTERMÜLLER et al. [52] or QI and SUN [119]) treating optimization and in HÜEBER et al. [56] or KOZIARA and BICANCIC [76] treating contact problems. For more prerequisites and details concerning semi-smooth NEWTON methods, for example for the concise

proof of superlinear convergence, the reader is referred to HINTERMÜLLER et al. [52] and QI and SUN [119].

The solution of the frictional contact problem is possibly made up of active and inactive regions, whereas the active regions are further divided into sticking and slipping areas. As commonly known, the correct determination of these regions can turn out to be difficult. For resolving these contact nonlinearities, the complementarity functions are helpful. Through using the max-function and the EUCLIDean norm, they contain the different branches of the respective conditions. These are, for the normal direction, the active and the inactive branch and, for the tangential direction, the stick and the two slip branches. Besides being able to treat these functions within a NEWTON type scheme as given above, C_{nj} and $\mathbf{C}_{\tau j}$ supply tangent information about the correct contact sets of the solution. With this, the contact nonlinearities can be treated, together with possible geometric or material nonlinearities, in one single iterative scheme. This leads to an excellent convergence behavior. As is going to be demonstrated in Section 4.6, the algorithm only requires a few NEWTON steps in order to find the correct active, inactive, stick and slip sets. Then, when the sets remain constant, the residual is reduced quadratically due to the consistent linearization presented.

The application of a semi-smooth NEWTON method gives an iterative process. The current iteration step k for solving for the primal-dual pair $(\mathbf{d}^{k+1}, \mathbf{z}^{k+1})$ requires at first the consistent linearization of all nonlinear equations in (4.5) at $(\mathbf{d}^k, \mathbf{z}^k)$ as

$$\Delta \mathbf{r}\left(\mathbf{d}^k, \mathbf{z}^k\right) = -\mathbf{r}^k \,, \tag{4.6}$$

$$\Delta C_{nj}\left(\mathbf{d}^k, \mathbf{z}_j^k\right) = -C_{nj}^k \qquad \forall\, j \in \mathcal{S} \,, \tag{4.7}$$

$$\Delta \mathbf{C}_{\tau j}\left(\mathbf{d}^k, \mathbf{z}_j^k\right) = -\mathbf{C}_{\tau j}^k \qquad \forall\, j \in \mathcal{S} \,. \tag{4.8}$$

Here, the quantities $\Delta(\cdot)$ denote the directional derivatives given by

$$\Delta\left(\cdot\right) = \frac{\partial\left(\cdot\right)}{\partial \mathbf{d}} \Delta \mathbf{d} + \frac{\partial\left(\cdot\right)}{\partial \mathbf{z}} \Delta \mathbf{z} \,, \tag{4.9}$$

which are also called "linearizations" for ease of use in the following. Then, the linear system of equations (4.6) - (4.8) is solved towards the solution increments $(\Delta \mathbf{d}^k, \Delta \mathbf{z}^k)$ and the update for the new iterate $\left(\mathbf{d}^{k+1}, \mathbf{z}^{k+1}\right)$ is

$$\left(\mathbf{d}^{k+1}, \mathbf{z}^{k+1}\right) = \left(\mathbf{d}^k, \mathbf{z}^k\right) + \left(\Delta \mathbf{d}^k, \Delta \mathbf{z}^k\right) \,. \tag{4.10}$$

These steps are repeated until convergence is achieved.

Remark: Semi-smooth NEWTON method and augmented LAGRANGE strategy

Within this section, the semi-smooth NEWTON method derived above is classified with regards to the augmented LAGRANGE strategy. It contributes to the clarification of possibly existing misunderstandings concerning the names of these methods.

In the early work of ALART and CURNIER [2], a mixed penalty-duality approach for treating small deformation contact problems is proposed. It is obtained from the formulation of an augmented Lagrangian functional initially introduced by HESTENES [50] and POWELL [113] for the solution of nonlinear programming problems with equality constraints. Evaluation of the directional derivatives towards the unknown displacements and the LAGRANGE multipliers leads

to two governing equations: The equilibrium equation and, as it is denoted there, the contact equation. They are solved with either a modified NEWTON method or the generalized NEWTON method. These strategies are also applied in, for example, CHRISTENSEN et al. [16] or IREMAN et al. [63].

The complementarity function for the normal direction here is, except from discretization and finite deformation formulation, identical to the one obtained from the augmented Lagrangian functional in ALART and CURNIER [2]. This is not the case for the frictional one as already stated in HÜEBER et al. [56], but they have the same structure. From there, the semi-smooth NEWTON method could also be interpreted as an augmented LAGRANGE strategy and resembles the generalized NEWTON method from above. The approach here however at first handles the non-smoothness and multivalued character of contact conditions with their reformulation in complementarity functions. This is in contrast to ALART and CURNIER [2], where this is already done for the formulation of the functional. In LAURSEN [83], the augmented LAGRANGE strategy is derived from the same functional. There, the numerical treatment however is realized with the sequential treatment of variables in USZAWA's algorithm. This resembles the modified NEWTON method from above.

4.3 Consistent linearization

Being a new and important aspect of the formulation considered here, the consistent linearization of the force residual and the two complementarity functions is addressed in the following.

4.3.1 Force residual

The evaluation of $\Delta\mathbf{r}$ requires the linearizations of the internal force vector $\mathbf{f}^{int}(\mathbf{d})$ and the contact force vector $\mathbf{f}^{c}(\mathbf{d},\mathbf{z})$. The vector $\mathbf{f}^{int}(\mathbf{d})$ is not addressed here at all as it results from well-known finite element technology leading to a standard tangential stiffness matrix $\mathbf{K}$. It is completely independent of contact. The linearization of the contact force vector $\mathbf{f}^{c}(\mathbf{d},\mathbf{z})$ can be expressed as

$$\Delta\mathbf{f}^{c,k} = \begin{pmatrix} \mathbf{0} \\ -\Delta\mathbf{M}^{\mathrm{T}}\,\mathbf{z}^{k} - \mathbf{M}^{\mathrm{T}}\,\Delta\mathbf{z}^{k} \\ \Delta\mathbf{D}^{\mathrm{T}}\,\mathbf{z}^{k} + \mathbf{D}^{\mathrm{T}}\,\Delta\mathbf{z}^{k} \end{pmatrix} \tag{4.11}$$

It requires the consistent determination of the directional derivatives of the mortar matrices $\mathbf{D}$ and $\mathbf{M}$. This can be found in POPP et al. [110, 111]. For the further treatment of this equation, the LAGRANGE multiplier increment $\Delta\mathbf{z}^{k}$ is replaced by $\mathbf{z}^{k+1} - \mathbf{z}^{k}$.

4.3.2 Complementarity function - normal direction

Containing the max-function as discussed above, the complementarity function for the normal direction is not differentiable in the classical sense. For its linearization, a generalized derivative has to be defined. It consists of the distinction of cases as

$$f(x) = \max(a,x) \longrightarrow \Delta f(x) = \begin{cases} 0 & \text{if } x \leq a \\ 1 & \text{if } x > a \end{cases} . \tag{4.12}$$

Then, when evaluating the directional derivative of the complementarity function C_{nj} at the current iterate k, this yields the separation of the slave node set $\mathcal{S}$ into the inactive node set $\mathcal{I}_k$ and the active node set $\mathcal{A}_k$. Furthermore, the respective solution branches are separated, too. In compact form, all equations resulting from the linearized complementarity function C_{nj} are given in the following. The sets are divided by

$$\mathcal{I}_k := \{j \in \mathcal{S} \,|\, z_{nj}^k - c_n \tilde{g}_j^k \leq 0\} \,, \tag{4.13}$$

$$\mathcal{A}_k := \{j \in \mathcal{S} \,|\, z_{nj}^k - c_n \tilde{g}_j^k > 0\} \,, \tag{4.14}$$

which is tantamount to an update formula to be applied after each semi-smooth NEWTON step in order to obtain $\mathcal{I}_k$ and $\mathcal{A}_k$. And the accompanying nodal equations result in

$$z_{nj}^{k+1} = 0 \qquad \forall\, j \in \mathcal{I}_k \,, \tag{4.15}$$

$$\Delta \tilde{g}_j^k = -g_j^k \qquad \forall\, j \in \mathcal{A}_k \,. \tag{4.16}$$

They are written to this certain level. For ongoing consistent linearizations, like the evaluation of $\Delta \tilde{g}_j^k$, the reader is referred to POPP et al. [110, 111].

4.3.3 Complementarity function - tangential direction

As discussed, the complementarity function representing the frictional conditions $\mathbf{C}_{\tau j}$ contains the max-function and the EUCLIDean norm. Concerning differentiation, the EUCLIDean norm in (4.3) appears for nonzero arguments only. This results from the straightforward calculation of (4.3), see also HÜEBER et al. [56]. With this, the only non-differentiability that matters is again the max-function. It is treated in the same manner as in Section 4.3.2 .

At a current iterate k, $\mathbf{C}_{\tau j}$ contains the separation of the slave node set $\mathcal{S}$ into the inactive node set $\mathcal{I}_k$ and the active node set $\mathcal{A}_k$. It is independent of the division resulting from the complementarity function for the normal direction C_{nj}, but leads to identical sets. In addition, the active set $\mathcal{A}_k$ is further split into the stick node set $\mathcal{S}t_k$ and the slip node set $\mathcal{S}l_k$. The respective equations are

$$\mathcal{I}_k := \left\{j \in \mathcal{S} \,|\, z_{nj}^k - c_n \tilde{g}_j^k \leq 0\right\} \,, \tag{4.17}$$

$$\mathcal{S}t_k := \left\{j \in \mathcal{A}_k \,|\, \|\mathbf{z}_{\tau j}^k + c_t \tilde{\mathbf{u}}_{\tau j}^k\| - \mu(z_{nj}^k - c_n \tilde{g}_j^k) < 0\right\} \,, \tag{4.18}$$

$$\mathcal{S}l_k := \left\{j \in \mathcal{A}_k \,|\, \|\mathbf{z}_{\tau j}^k + c_t \tilde{\mathbf{u}}_{\tau j}^k\| - \mu(z_{nj}^k - c_n \tilde{g}_j^k) \geq 0\right\} \,, \tag{4.19}$$

and for $\mathcal{I}_k$, $\mathcal{S}t_k$ and $\mathcal{S}l_k$, equation (4.7) yields the following notation

$$\mathbf{z}_{\tau j}^{k+1} = \mathbf{0} \qquad \forall\, j \in \mathcal{I}_k \,, \tag{4.20}$$

$$\begin{aligned} \Delta \mathbf{C}_{\tau j, \mathcal{S}t} =& -\mu \left(z_{nj}^k - c_n \tilde{g}_j^k\right) c_t \Delta \tilde{\mathbf{u}}_{\tau j}^k \\ & -\mu \left(\Delta z_{nj}^k - c_n \Delta \tilde{g}_j^k\right) c_t \tilde{\mathbf{u}}_{\tau j}^k \\ =& \mu \left(z_{nj}^k - c_n \tilde{g}_j^k\right) c_t \tilde{\mathbf{u}}_{\tau j}^k \\ =& -\mathbf{C}_{\tau j, \mathcal{S}t}^k \qquad \forall\, j \in \mathcal{S}t_k \,, \end{aligned} \tag{4.21}$$

$$
\begin{aligned}
\Delta \mathbf{C}_{\tau j,\mathcal{S}l} = & \left\| \mathbf{z}_{\tau j}^k + c_t \tilde{\mathbf{u}}_{\tau j}^k \right\| \Delta \mathbf{z}_{\tau j}^k \\
& + \frac{\left(\mathbf{z}_{\tau j}^k + c_t \tilde{\mathbf{u}}_{\tau j}^k \right)}{\left\| \mathbf{z}_{\tau j}^k + c_t \tilde{\mathbf{u}}_{\tau j}^k \right\|} \mathbf{z}_{\tau j}^k \left(\Delta \mathbf{z}_{\tau j}^k + c_t \Delta \tilde{\mathbf{u}}_{\tau j}^k \right) \\
& - \mu \left(z_{nj}^k - c_n \tilde{g}_j^k \right) \left(\Delta \mathbf{z}_{\tau j}^k + c_t \Delta \tilde{\mathbf{u}}_{\tau j}^k \right) \\
& - \mu \left(\Delta z_{nj}^k - c_n \Delta \tilde{g}_j^k \right) \left(\mathbf{z}_{\tau j}^k + c_t \tilde{\mathbf{u}}_{\tau j}^k \right) \\
= & - \left\| \mathbf{z}_{\tau j}^k + c_t \tilde{\mathbf{u}}_{\tau j}^k \right\| \mathbf{z}_{\tau j}^k + \mu \left(z_{nj}^k - c_n \tilde{g}_j^k \right) \left(\mathbf{z}_{\tau j}^k + c_t \tilde{\mathbf{u}}_{\tau j}^k \right) \\
= & - \mathbf{C}_{\tau j,\mathcal{S}l}^k \qquad \forall \; j \in \mathcal{S}l_k \; . \qquad (4.22)
\end{aligned}
$$

Concerning COULOMB's friction law for the tangential direction, the expressions $\Delta \mathbf{z}_{\tau j}^k$ and $\Delta \tilde{\mathbf{u}}_{\tau j}^k$ still depend nonlinearly on the displacements $\mathbf{d}^k$ and the nodal LAGRANGE multiplier vector $\mathbf{z}_j^k$. According to GITTERLE et al. [35], ongoing consistent linearization of these contributions towards the primary unknowns reads

$$
\Delta \mathbf{z}_{\tau j}^k = \boldsymbol{\tau}_j^k \, \Delta \mathbf{z}_j^k + \Delta \boldsymbol{\tau}_j^k \, \mathbf{z}_j^k \qquad (4.23)
$$

and

$$
\begin{aligned}
\Delta \tilde{\mathbf{u}}_{\tau j}^k = & - \boldsymbol{\tau}_j^k \left(\mathbf{D}[j,j]^k - \mathbf{D}_{(n-1)}[j,j] \right) \, \Delta \mathbf{d}_j^{(1)\,k} \\
& + \boldsymbol{\tau}_j^k \sum_{l=1}^{n_m} \left(\mathbf{M}[j,l]^k - \mathbf{M}_{(n-1)}[j,l] \right) \, \Delta \mathbf{d}_l^{(2)\,k} \\
& - \Delta \boldsymbol{\tau}_j^k \left(\mathbf{D}[j,j]^k - \mathbf{D}_{(n-1)}[j,j] \right) \, \mathbf{x}_j^{(1)\,k} \\
& + \Delta \boldsymbol{\tau}_j^k \sum_{l=1}^{n_m} \left(\mathbf{M}[j,l]^k - \mathbf{M}_{(n-1)}[j,l] \right) \, \mathbf{x}_l^{(2)\,k} \\
& - \boldsymbol{\tau}_j^k \, \Delta \mathbf{D}[j,j]^k \, \mathbf{x}_j^{(1)\,k} + \boldsymbol{\tau}_j^k \sum_{l=1}^{n_m} \Delta \mathbf{M}[j,l]^k \, \mathbf{x}_l^{(2)\,k} \; . \qquad (4.24)
\end{aligned}
$$

For the further derivation of $\Delta \boldsymbol{\tau}_j^k$, $\Delta \mathbf{D}[j,j]^k$ and $\Delta \mathbf{M}[j,l]^k$, the reader is referred to POPP et al. [110, 111], where these linearizations are carried out for the frictionless case.

4.4 Primal-dual active set algorithm

The semi-smooth NEWTON algorithm within one increment is summarized in this section. As the complementarity functions implicitly contain the distinction of all potential contact nodes into nodes not in contact, nodes in contact and sticking and nodes in contact and slipping, it shows the form of a primal dual active set strategy. It is arranged as follows:

Algorithm 2

1. Set $k = 0$ and initialize the solution $(\mathbf{d}^0, \mathbf{z}^0)$

2. Initialize $\mathcal{I}_0$, $\mathcal{S}t_0$ and $\mathcal{S}l_0$ such that $\mathcal{I}_0 \cup \mathcal{S}_0 \cup \mathcal{S}l_0 = \mathcal{S}$, $\mathcal{I}_0 \cap \mathcal{S}t_0 = \mathcal{I}_0 \cap \mathcal{S}l_0 = \mathcal{S}t_0 \cap \mathcal{S}l_0 = \emptyset$, and $\mathcal{S}t_0 \cup \mathcal{S}l_0 = \mathcal{A}_0$

3. Find $\Delta\mathbf{d}^k, \mathbf{z}^{k+1}$ by solving

$$\Delta\mathbf{r}\left(\mathbf{d}^k, \mathbf{z}^k\right) = -\mathbf{r}^k \,, \tag{4.25}$$
$$\mathbf{z}_j^{k+1} = \mathbf{0} \qquad \forall\, j \in \mathcal{I}_k \,, \tag{4.26}$$
$$\Delta\tilde{g}_j^k = -\tilde{g}_j^k \qquad \forall\, j \in \mathcal{A}_k \,, \tag{4.27}$$
$$\Delta\mathbf{C}_{\tau j,\mathcal{S}t}^k = -\mathbf{C}_{\tau j,\mathcal{S}t}^k \quad \forall\, j \in \mathcal{S}t_k \,, \tag{4.28}$$
$$\Delta\mathbf{C}_{\tau j,\mathcal{S}l}^k = -\mathbf{C}_{\tau j,\mathcal{S}l}^k \quad \forall\, j \in \mathcal{S}l_k \,. \tag{4.29}$$

4. Update $\mathbf{d}^{k+1} = \mathbf{d}^k + \Delta\mathbf{d}^k$

5. Set $\mathcal{I}_{k+1}$, $\mathcal{S}t_{k+1}$ and $\mathcal{S}l_{k+1}$ to

$$\mathcal{I}_{k+1} := \left\{ j \in \mathcal{S} \,|\, z_{nj}^{k+1} - c_n\tilde{g}_j^{k+1} \leq 0 \right\} \,,\, \mathcal{A}_{k+1} = \mathcal{S} \setminus \mathcal{I}_{k+1} \,, \tag{4.30}$$
$$\mathcal{S}t_{k+1} := \left\{ j \in \mathcal{A}_{k+1} \,|\, \|\mathbf{z}_{\tau j}^{k+1} + c_t\tilde{\mathbf{u}}_{\tau j}^{k+1}\| - \mu(z_{nj}^{k+1} - c_n\tilde{g}_j^{k+1}) < 0 \right\} \,, \tag{4.31}$$
$$\mathcal{S}l_{k+1} := \left\{ j \in \mathcal{A}_{k+1} \,|\, \|\mathbf{z}_{\tau j}^{k+1} + c_t\tilde{\mathbf{u}}_{\tau j}^{k+1}\| - \mu(z_{nj}^{k+1} - c_n\tilde{g}_j^{k+1}) \geq 0 \right\} \,, \tag{4.32}$$

6. If $\mathcal{I}_{k+1} = \mathcal{I}_k$, $\mathcal{S}t_{k+1} = \mathcal{S}t_k$, $\mathcal{S}l_{k+1} = \mathcal{S}l_k$ and $\|\mathbf{r}_{abs}\| \leq \epsilon_r$, then stop,
else set $k := k + 1$ and repeat from 3.

Here, ϵ_r denotes an absolute NEWTON convergence tolerance of choice. The algorithm shows that the contact nonlinearities and all other types of nonlinearities are resolved within one single NEWTON iteration. This necessitates an update of the inactive, stick and slip set after each semi-smooth NEWTON step. The absolute residual vector $\mathbf{r}_{abs}$ not only contains the force residual $\mathbf{r}$ but also the residual of the contact constraints (4.26) - (4.29).

4.5 Algebraic representation

In this chapter, the algebraic representation of the linear system to be solved in each semi-smooth NEWTON step is derived. The assembly of the global matrices representing the directional derivatives in (4.25) - (4.28) is straightforward. It is provided in compact form in the following.

From (4.11), the directional derivatives of the contact force vector $\mathbf{f}^c$ in (4.25) towards the displacements can be expressed as

$$\left(\mathbf{0},\ -\Delta\mathbf{M}^{\mathrm{T}}\,\mathbf{z}^k,\ \Delta\mathbf{D}^{\mathrm{T}}\,\mathbf{z}^k\right)^{\mathrm{T}} = \tilde{\mathbf{C}}\Delta\mathbf{d}_{\mathcal{SM}}^k. \tag{4.33}$$

Here, the matrix $\tilde{\mathbf{C}} \in \mathbb{R}^{(3n_{sl}+3n_m)\times(3n_{sl}+3n_m)}$ contains the directional derivatives of both mortar matrices $\mathbf{D}$ and $\mathbf{M}$ together with the current LAGRANGE multiplier vector $\mathbf{z}^k$. The vector $\Delta\mathbf{d}_{\mathcal{SM}}^k$ is a subset of the global displacement vector containing the entries from slave and master nodes $\mathcal{S}$ and $\mathcal{M}$, their numbers are denoted by n^{sl} and n^m.

Linearization of the normal constraint for all active nodes $j \in \mathcal{A}$ in (4.27) yields

$$\mathop{\mathsf{A}}_{j=1}^{n^a} \left(\Delta \tilde{g}_j^k\right) \;=\; \tilde{\mathbf{S}}_{\mathcal{A}_k} \Delta \mathbf{d}_{\mathcal{S}}^k + \tilde{\mathbf{M}}_{\mathcal{A}_k} \Delta \mathbf{d}_{\mathcal{M}}^k \;, \tag{4.34}$$

where matrices $\tilde{\mathbf{S}}_{\mathcal{A}_k} \in \mathbb{R}^{n^a \times 3n^{sl}}$ and $\tilde{\mathbf{M}}_{\mathcal{A}_k} \in \mathbb{R}^{n^a \times 3n^m}$ completely represent the assembly of all linearizations of $\Delta \tilde{g}_j$, where A is the standard finite element assembly operator and n^a the number of active slave nodes.

The following notation expresses the assembled form of equation (4.28) for all stick nodes $j \in \mathcal{S}t_k$:

$$\mathop{\mathsf{A}}_{j=1}^{n^{stick}} \left(\Delta \mathbf{C}_{\tau j,\mathcal{S}t}^k + \mathbf{C}_{\tau j,\mathcal{S}t}^k\right) \;=\; \mathbf{F}_{\mathcal{S}t_k} \Delta \mathbf{d}_{\mathcal{S}}^k + \mathbf{H}_{\mathcal{S}t_k} \Delta \mathbf{d}_{\mathcal{M}}^k + \mathbf{P}_{\mathcal{S}t_k} \mathbf{z}_{\mathcal{S}t}^{k+1} + \mathbf{C}_{\tau,\mathcal{S}t} \;. \tag{4.35}$$

Here, n^{stick} is the number of stick nodes. The matrices $\mathbf{F}_{\mathcal{S}t_k} \in \mathbb{R}^{n^{stick} \times 3n^{sl}}$, $\mathbf{H}_{\mathcal{S}t_k} \in \mathbb{R}^{n^{stick} \times 3n^m}$ and $\mathbf{P}_{\mathcal{S}t_k} \in \mathbb{R}^{n^{stick} \times 3n^{stick}}$ represent the assembly of all linearizations with respect to displacements $\mathbf{d}^k$ and LAGRANGE multipliers $\mathbf{z}^k$. The vector $\mathbf{C}_{\tau,\mathcal{S}t} \in \mathbb{R}^{n^{stick}}$ contains the entries of the right hand side.

The algebraic formulation for the linearized slip constraint (4.29) for all slip nodes $j \in \mathcal{S}l$ is derived in analogue form and yields

$$\mathop{\mathsf{A}}_{j=1}^{n^{slip}} \left(\Delta \mathbf{C}_{\tau j,\mathcal{S}l}^k + \mathbf{C}_{\tau j,\mathcal{S}l}^k\right) \;=\; \mathbf{G}_{\mathcal{S}l_k} \Delta \mathbf{d}_{\mathcal{S}}^k + \mathbf{J}_{\mathcal{S}l_k} \Delta \mathbf{d}_{\mathcal{M}}^k + \mathbf{L}_{\mathcal{S}l_k} \mathbf{z}_{\mathcal{S}l}^{k+1} + \mathbf{C}_{\tau,\mathcal{S}l} \;, \tag{4.36}$$

where n^{slip} is the number of all slip nodes and the matrices $\mathbf{G}_{\mathcal{S}l_k} \in \mathbb{R}^{n^{slip} \times 3n^{sl}}$, $\mathbf{J}_{\mathcal{S}l_k} \in \mathbb{R}^{n^{slip} \times 3n^m}$ and $\mathbf{L}_{\mathcal{S}l_k} \in \mathbb{R}^{n^{slip} \times 3n^{slip}}$ being the assembled form of all directional derivatives and the vector $\mathbf{C}_{\tau,\mathcal{S}l} \in \mathbb{R}^{n^{slip}}$ represents the right hand side. The transpose of the global mortar matrices, the diagonal matrix $\mathbf{D}$ and the non-diagonal matrix $\mathbf{M}$, are split with the respect to the inactive set $\mathcal{I}$, stick set $\mathcal{S}t$ and slip set $\mathcal{S}l$ as

$$\mathbf{D}^{\mathrm{T}} = \begin{bmatrix} \mathbf{D}_{\mathcal{I}_k}^{\mathrm{T}} & \mathbf{0} & \mathbf{0} \\ \mathbf{0} & \mathbf{D}_{\mathcal{S}t_k}^{\mathrm{T}} & \mathbf{0} \\ \mathbf{0} & \mathbf{0} & \mathbf{D}_{\mathcal{S}l_k}^{\mathrm{T}} \end{bmatrix} \tag{4.37}$$

and

$$\mathbf{M}^{\mathrm{T}} = \begin{bmatrix} \mathbf{M}_{\mathcal{I}_k}^{\mathrm{T}} & \mathbf{M}_{\mathcal{S}t_k}^{\mathrm{T}} & \mathbf{M}_{\mathcal{S}l_k}^{\mathrm{T}} \end{bmatrix} \;. \tag{4.38}$$

Finally, with the assembled sub-matrices above, the algebraic representation of the linear system (4.25) - (4.29) to be solved in each semi-smooth NEWTON step can be written. It shows saddle point problem characteristics due to the fact that both displacements and LAGRANGE multipliers as primary unknowns. The index for the current iteration k is dropped here for the

ease of notation:

$$\begin{bmatrix} \mathbf{K}_{\mathcal{NN}} & \mathbf{K}_{\mathcal{NM}} & \mathbf{K}_{\mathcal{NI}} & \mathbf{K}_{\mathcal{NS}t} & \mathbf{K}_{\mathcal{NS}l} & \mathbf{0} & \mathbf{0} & \mathbf{0} \\ \mathbf{K}_{\mathcal{MN}} & \tilde{\mathbf{K}}_{\mathcal{MM}} & \tilde{\mathbf{K}}_{\mathcal{MI}} & \tilde{\mathbf{K}}_{\mathcal{MS}t} & \tilde{\mathbf{K}}_{\mathcal{MS}l} & -\mathbf{M}_{\mathcal{I}}^{\mathrm{T}} & -\mathbf{M}_{\mathcal{S}t}^{\mathrm{T}} & -\mathbf{M}_{\mathcal{S}l}^{\mathrm{T}} \\ \mathbf{K}_{\mathcal{IN}} & \tilde{\mathbf{K}}_{\mathcal{IM}} & \tilde{\mathbf{K}}_{\mathcal{II}} & \tilde{\mathbf{K}}_{\mathcal{IS}t} & \tilde{\mathbf{K}}_{\mathcal{IS}l} & \mathbf{D}_{\mathcal{I}}^{\mathrm{T}} & \mathbf{0} & \mathbf{0} \\ \mathbf{K}_{\mathcal{S}t\mathcal{N}} & \tilde{\mathbf{K}}_{\mathcal{S}t\mathcal{M}} & \tilde{\mathbf{K}}_{\mathcal{S}t\mathcal{I}} & \tilde{\mathbf{K}}_{\mathcal{S}t\mathcal{S}t} & \tilde{\mathbf{K}}_{\mathcal{S}t\mathcal{S}l} & \mathbf{0} & \mathbf{D}_{\mathcal{S}t}^{\mathrm{T}} & \mathbf{0} \\ \mathbf{K}_{\mathcal{S}l\mathcal{N}} & \tilde{\mathbf{K}}_{\mathcal{S}l\mathcal{M}} & \tilde{\mathbf{K}}_{\mathcal{S}l\mathcal{I}} & \tilde{\mathbf{K}}_{\mathcal{S}l\mathcal{S}t} & \tilde{\mathbf{K}}_{\mathcal{S}l\mathcal{S}l} & \mathbf{0} & \mathbf{0} & \mathbf{D}_{\mathcal{S}t}^{\mathrm{T}} \\ \mathbf{0} & \mathbf{0} & \mathbf{0} & \mathbf{0} & \mathbf{0} & \mathbf{I}_{\mathcal{I}} & \mathbf{0} & \mathbf{0} \\ \mathbf{0} & \tilde{\mathbf{M}}_{\mathcal{A}} & \tilde{\mathbf{S}}_{\mathcal{AI}} & \tilde{\mathbf{S}}_{\mathcal{AS}t} & \tilde{\mathbf{S}}_{\mathcal{AS}l} & \mathbf{0} & \mathbf{0} & \mathbf{0} \\ \mathbf{0} & \mathbf{H}_{\mathcal{S}t} & \mathbf{F}_{\mathcal{S}t\mathcal{I}} & \mathbf{F}_{\mathcal{S}t\mathcal{S}t} & \mathbf{F}_{\mathcal{S}t\mathcal{S}l} & \mathbf{0} & \mathbf{P}_{\mathcal{S}t} & \mathbf{0} \\ \mathbf{0} & \mathbf{J}_{\mathcal{S}l} & \mathbf{G}_{\mathcal{S}l\mathcal{I}} & \mathbf{G}_{\mathcal{S}l\mathcal{S}t} & \mathbf{G}_{\mathcal{S}l\mathcal{S}l} & \mathbf{0} & \mathbf{0} & \mathbf{L}_{\mathcal{S}l} \end{bmatrix} \cdot \begin{bmatrix} \Delta\mathbf{d}_{\mathcal{N}} \\ \Delta\mathbf{d}_{\mathcal{M}} \\ \Delta\mathbf{d}_{\mathcal{I}} \\ \Delta\mathbf{d}_{\mathcal{S}t} \\ \Delta\mathbf{d}_{\mathcal{S}l} \\ \mathbf{z}_{\mathcal{I}} \\ \mathbf{z}_{\mathcal{S}t} \\ \mathbf{z}_{\mathcal{S}l} \end{bmatrix} = - \begin{bmatrix} \mathbf{r}_{\mathcal{N}} \\ \mathbf{r}_{\mathcal{M}} \\ \mathbf{r}_{\mathcal{I}} \\ \mathbf{r}_{\mathcal{S}t} \\ \mathbf{r}_{\mathcal{S}l} \\ \mathbf{0} \\ \tilde{\mathbf{g}}_{\mathcal{A}} \\ \mathbf{C}_{\tau,\mathcal{S}t} \\ \mathbf{C}_{\tau,\mathcal{S}l} \end{bmatrix} \tag{4.39}$$

The first five rows represent the linearized equilibrium equation (4.25). The 16 blocks marked with the tilde symbol $\tilde{\mathbf{K}}$ imply the summation of the standard tangential stiffness matrix and linearization entries from the contact force vector in (4.33) as for example $\tilde{\mathbf{K}}_{\mathcal{MM}} = \mathbf{K}_{\mathcal{MM}} + \tilde{\mathbf{C}}_{\mathcal{MM}}$. The sixth row trivially is the contact constraint for nodes of the inactive set $\mathcal{I}$ in (4.26), with $\mathbf{I}_{\mathcal{I}} \in \mathbb{R}^{|\mathcal{I}|\times|\mathcal{I}|}$ as identity matrix. Normal contact constraints for nodes of the active set $\mathcal{A}$ in (4.27) are placed in the seventh row. And, for friction, the tangential conditions for the active nodes are divided in those for stick nodes $j \in \mathcal{S}t$ in (4.28) in row eight and slip nodes $j \in \mathcal{S}l$ in (4.29) in row nine.

The saddle point-type system (4.39) contains displacement degrees of freedom $\Delta\mathbf{d}^k$ and LAGRANGE multipliers $\mathbf{z}^{k+1}$ and therefore is of increased size. Due to using dual shape functions leading to a diagonal matrix $\mathbf{D}$, the discrete LAGRANGE multipliers can easily be eliminated from the global system of equation. For this, they are expressed in terms of displacements as

$$\mathbf{z} = \mathbf{D}^{-\mathrm{T}} \left(-\mathbf{r}_{\mathcal{S}} - \mathbf{K}_{\mathcal{SN}}\Delta\mathbf{d}_{\mathcal{N}} - \tilde{\mathbf{K}}_{\mathcal{SM}}\Delta\mathbf{d}_{\mathcal{M}} - \tilde{\mathbf{K}}_{\mathcal{SS}}\Delta\mathbf{d}_{\mathcal{S}} \right) . \tag{4.40}$$

It requires the inversion of the mortar matrix $\mathbf{D}$ which is, due to its diagonality, of minor computational costs. Equation (4.40) is written in general form valid for all slave nodes $j \in \mathcal{S}$. For condensation, it is applied to rows four and five. With eliminating the sixth row and column of (4.39), substitution of (4.40) into (4.39) leads to the reduced system with displacement degrees of freedom only:

$$\begin{bmatrix} \mathbf{K}_{\mathcal{NN}} & \mathbf{K}_{\mathcal{NM}} & \mathbf{K}_{\mathcal{NI}} & \mathbf{K}_{\mathcal{NS}t} & \mathbf{K}_{\mathcal{NS}l} \\ \begin{pmatrix} \mathbf{K}_{\mathcal{MN}} + \\ \hat{\mathbf{M}}_{\mathcal{A}}^{T}\mathbf{K}_{\mathcal{AN}} \end{pmatrix} & \begin{pmatrix} \tilde{\mathbf{K}}_{\mathcal{MM}} + \\ \hat{\mathbf{M}}_{\mathcal{A}}^{T}\tilde{\mathbf{K}}_{\mathcal{AM}} \end{pmatrix} & \begin{pmatrix} \tilde{\mathbf{K}}_{\mathcal{MI}} + \\ \hat{\mathbf{M}}_{\mathcal{A}}^{T}\tilde{\mathbf{K}}_{\mathcal{AI}} \end{pmatrix} & \begin{pmatrix} \tilde{\mathbf{K}}_{\mathcal{MS}t} + \\ \hat{\mathbf{M}}_{\mathcal{A}}^{T}\tilde{\mathbf{K}}_{\mathcal{AS}t} \end{pmatrix} & \begin{pmatrix} \tilde{\mathbf{K}}_{\mathcal{MS}l} + \\ \hat{\mathbf{M}}_{\mathcal{A}}^{T}\tilde{\mathbf{K}}_{\mathcal{AS}l} \end{pmatrix} \\ \mathbf{K}_{\mathcal{IN}} & \tilde{\mathbf{K}}_{\mathcal{IM}} & \tilde{\mathbf{K}}_{\mathcal{II}} & \tilde{\mathbf{K}}_{\mathcal{IS}t} & \tilde{\mathbf{K}}_{\mathcal{IS}l} \\ \mathbf{0} & \tilde{\mathbf{M}}_{\mathcal{A}} & \tilde{\mathbf{S}}_{\mathcal{AI}} & \tilde{\mathbf{S}}_{\mathcal{AS}t} & \tilde{\mathbf{S}}_{\mathcal{AS}l} \\ \mathbf{P}_{\mathcal{S}t}\mathbf{D}_{\mathcal{S}t}^{-\mathrm{T}}\mathbf{K}_{\mathcal{S}t\mathcal{N}} & \begin{pmatrix} \mathbf{P}_{\mathcal{S}t}\mathbf{D}_{\mathcal{S}t}^{-\mathrm{T}}\tilde{\mathbf{K}}_{\mathcal{S}t\mathcal{M}} - \\ \mathbf{H}_{\mathcal{S}t} \end{pmatrix} & \begin{pmatrix} \mathbf{P}_{\mathcal{S}t}\mathbf{D}_{\mathcal{S}t}^{-\mathrm{T}}\tilde{\mathbf{K}}_{\mathcal{S}t\mathcal{I}} - \\ \mathbf{F}_{\mathcal{S}t\mathcal{I}} \end{pmatrix} & \begin{pmatrix} \mathbf{P}_{\mathcal{S}t}\mathbf{D}_{\mathcal{S}t}^{-\mathrm{T}}\tilde{\mathbf{K}}_{\mathcal{S}t\mathcal{S}t} - \\ \mathbf{F}_{\mathcal{S}t\mathcal{S}t} \end{pmatrix} & \begin{pmatrix} \mathbf{P}_{\mathcal{S}t}\mathbf{D}_{\mathcal{S}t}^{-\mathrm{T}}\tilde{\mathbf{K}}_{\mathcal{S}t\mathcal{S}l} - \\ \mathbf{F}_{\mathcal{S}t\mathcal{S}l} \end{pmatrix} \\ \mathbf{L}_{\mathcal{S}l}\mathbf{D}_{\mathcal{S}l}^{-\mathrm{T}}\mathbf{K}_{\mathcal{S}l\mathcal{N}} & \begin{pmatrix} \mathbf{L}_{\mathcal{S}l}\mathbf{D}_{\mathcal{S}l}^{-\mathrm{T}}\tilde{\mathbf{K}}_{\mathcal{S}l\mathcal{M}} - \\ \mathbf{J}_{\mathcal{S}l} \end{pmatrix} & \begin{pmatrix} \mathbf{L}_{\mathcal{S}l}\mathbf{D}_{\mathcal{S}l}^{-\mathrm{T}}\tilde{\mathbf{K}}_{\mathcal{S}l\mathcal{I}} - \\ \mathbf{G}_{\mathcal{S}l\mathcal{I}} \end{pmatrix} & \begin{pmatrix} \mathbf{L}_{\mathcal{S}l}\mathbf{D}_{\mathcal{S}l}^{-\mathrm{T}}\tilde{\mathbf{K}}_{\mathcal{S}l\mathcal{S}t} - \\ \mathbf{G}_{\mathcal{S}l\mathcal{S}t} \end{pmatrix} & \begin{pmatrix} \mathbf{L}_{\mathcal{S}l}\mathbf{D}_{\mathcal{S}l}^{-\mathrm{T}}\tilde{\mathbf{K}}_{\mathcal{S}l\mathcal{S}l} - \\ \mathbf{G}_{\mathcal{S}l\mathcal{S}l} \end{pmatrix} \end{bmatrix}$$

$$\cdot \begin{bmatrix} \Delta\mathbf{d}_{\mathcal{N}} \\ \Delta\mathbf{d}_{\mathcal{M}} \\ \Delta\mathbf{d}_{\mathcal{I}} \\ \Delta\mathbf{d}_{\mathcal{S}t} \\ \Delta\mathbf{d}_{\mathcal{S}l} \end{bmatrix} = - \begin{bmatrix} \mathbf{r}_{\mathcal{N}} \\ \mathbf{r}_{\mathcal{M}} + \hat{\mathbf{M}}_{\mathcal{A}}^{T}\mathbf{r}_{\mathcal{A}} \\ \mathbf{r}_{\mathcal{I}} \\ \tilde{\mathbf{g}}_{\mathcal{A}} \\ \mathbf{P}_{\mathcal{S}t}\mathbf{D}_{\mathcal{S}t}^{-\mathrm{T}}\mathbf{r}_{\mathcal{S}t} - \mathbf{C}_{\tau,\mathcal{S}t} \\ \mathbf{L}_{\mathcal{S}l}\mathbf{D}_{\mathcal{S}l}^{-\mathrm{T}}\mathbf{r}_{\mathcal{S}l} - \mathbf{C}_{\tau,\mathcal{S}l} \end{bmatrix}, \tag{4.41}$$

where the abbreviation

$$\hat{\mathbf{M}} = \mathbf{D}^{-\mathrm{T}}\mathbf{M} \tag{4.42}$$

is used. In the presented condensation process, the saddle point-type structure of the final linear system has been removed. It allows for the favorable application of state-of-the-art iterative solvers and preconditioners, such as algebraic multigrid techniques in BRUNSSEN et al. [12] and WOHLMUTH and KRAUSE [142]. Subsequently, the condensed LAGRANGE multipliers are recovered according to (4.40).

4.6 Examples

Four numerical examples in 2D and 3D are chosen to demonstrate the accuracy, robustness and efficiency of the proposed method for finite deformation frictional contact. The 2D examples have already been published in GITTERLE et al. [35].

All simulations are performed using a parallel implementation of the described algorithms in the in-house research code BACI of the Institute for Computational Mechanics, Technische Universität München, see WALL and GEE [135]. If not specified otherwise, a compressible Neo-HOOKEan constitutive law is applied as material. It is determined by YOUNG's modulus E and POISSON's ratio ν. As friction model, COULOMB's law is used and in 2D, plane strain conditions are assumed. Convergence of the NEWTON iterative scheme is measured in terms of the absolute residual norm as mentioned in Section 4.4, with the absolute convergence tolerance ϵ_r set to 10^{-9}. The algorithmic parameter c_n and c_t are both assumed to be 100 when nothing different is mentioned but are further studied in the second example.

4.6.1 HERTZian contact

To investigate the accuracy of the formulation, first the well known cylinder on cylinder frictional contact problem is presented. It is predestined for this as the analytical solution is available under the assumption of infinitesimally small deformation, see JOHNSON [68]. Therefore, the load has been chosen very small. The problem setup is shown in Figure 4.3. The cylinders are modelled with a geometrically linear element formulation with St. VENANT-KIRCHHOFF's material law ($E = 200$, $\nu = 0.3$) and the COULOMB coefficient of friction is 0.2. In a first step, the cylinders are subject to a distributed constant pressure $p = 0.625$. In a second step, holding the vertical pressure constant, a distributed load $q = 0.05851$ is applied horizontally. This induces frictional contact forces in the contact zone. The analytical solution brings, according to JOHNSON [68], the following quantities: The width b of half of the contact zone is evaluated as

$$b = 2\sqrt{\frac{2\,R^2\,p\,(1-\nu^2)}{E\,\pi}} \tag{4.43}$$

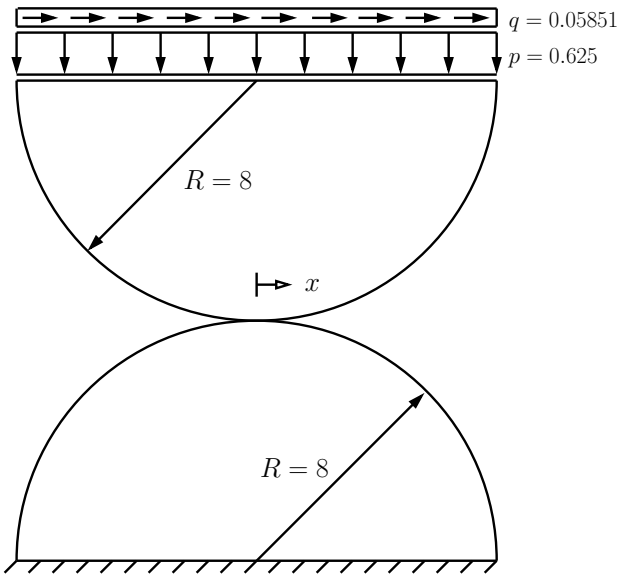

Figure 4.3: Frictional cylinder on cylinder HERTZian contact problem.

and the distribution for the normal contact traction p_n is given as

$$p_n = \frac{4\,R\,p}{\pi\,b^2}\sqrt{b^2 - x^2}\;, \tag{4.44}$$

where R is the radius of the two cylinders. The contact zone b is divided into a stick zone in the central area $|x| \leq c$ and two peripheral slip regions $c < |x| \leq b$ with characteristic parameter c

$$c = b\,\sqrt{1 - \frac{q}{\mu\,p}}\;. \tag{4.45}$$

The frictional tangential traction p_t is

$$\begin{aligned} p_t &= \mu\frac{4\,R\,p}{\pi\,b^2}\left(\sqrt{b^2 - x^2} - \sqrt{c^2 - x^2}\right) \qquad \text{if } \; |x| \leq c\;, \\ p_t &= \mu\frac{4\,R\,p}{\pi\,b^2}\left(\sqrt{b^2 - x^2}\right) \qquad\qquad\qquad\quad \text{if } \; c < |x| \leq b\;. \end{aligned} \tag{4.46}$$

With $R = 8$ and the given set of parameters, we obtain $b = 0.6808$ and $c = 0.4965$. Quasistatic simulations are performed with a coarse mesh with about 12 linearly interpolated elements in the potential contact zone shown in Figure 4.4, with the same mesh but quadratically interpolated elements and a finer mesh with about 80 linear interpolated elements in the contact zone (not shown). The vertical compression is realized within 10 load steps. Then, the horizontal load is applied within 10 load steps.

The numerical results plotted in Figure 4.5 show that already for the coarse mesh frictional contact tractions represent the analytical solution very well. This is improved by quadratic interpolation (Figure 4.6) and when applying mesh refinement, where also the change from the stick to the slip region can be identified very precisely (Figure 4.7). The small discrepancy in the outermost part of the contact zone, most notably for the coarse mesh, is due to the end of the contact zone not coinciding with a finite element node and decreases with mesh refinement, compare Figures 4.5 and 4.7 respectively.

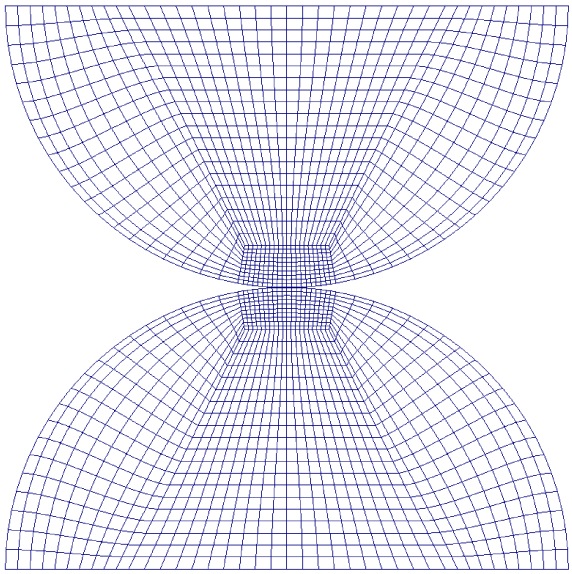

Figure 4.4: Coarse mesh for frictional cylinder on cylinder HERTZian contact problem.

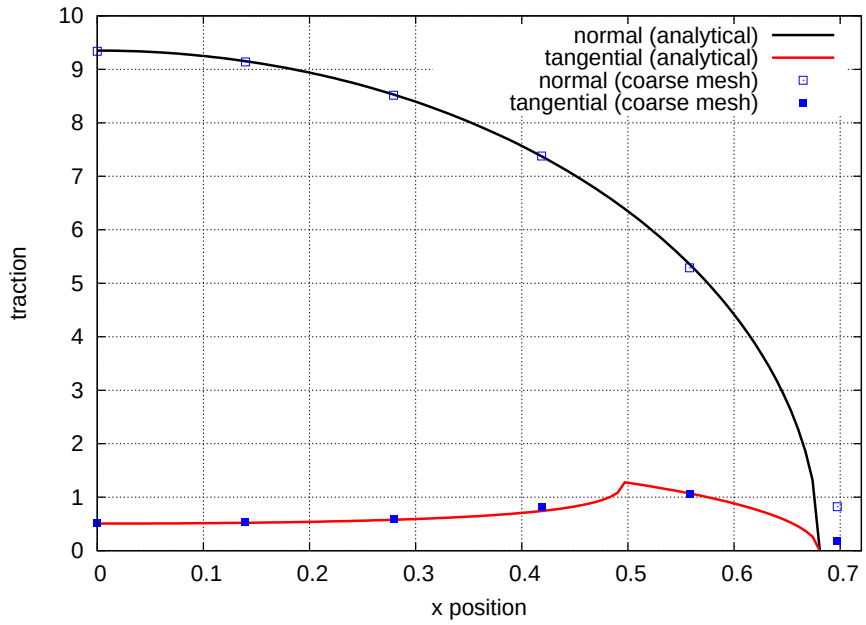

Figure 4.5: Contact traction for frictional cylinder on cylinder contact problem - coarse mesh.

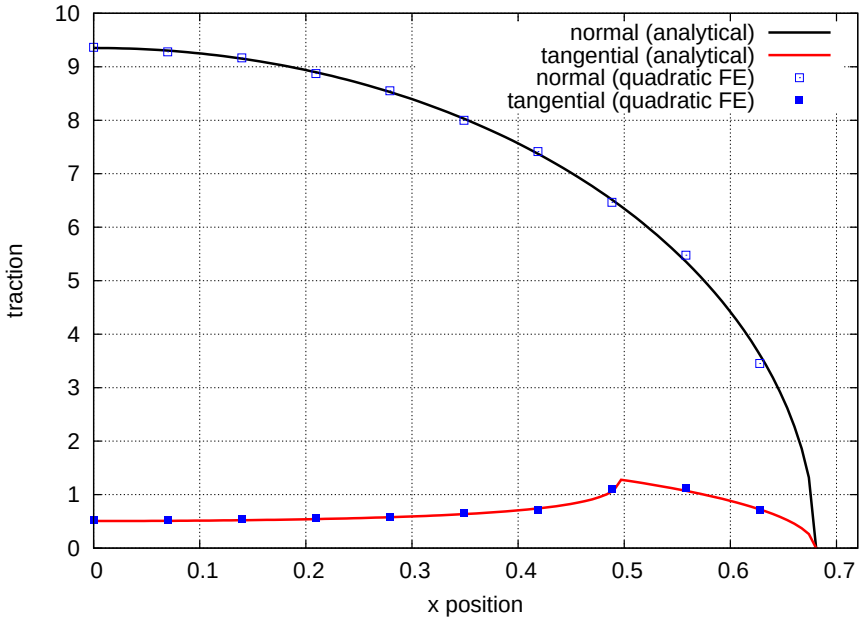

Figure 4.6: Contact traction for frictional cylinder on cylinder contact problem - quadratic interpolation.

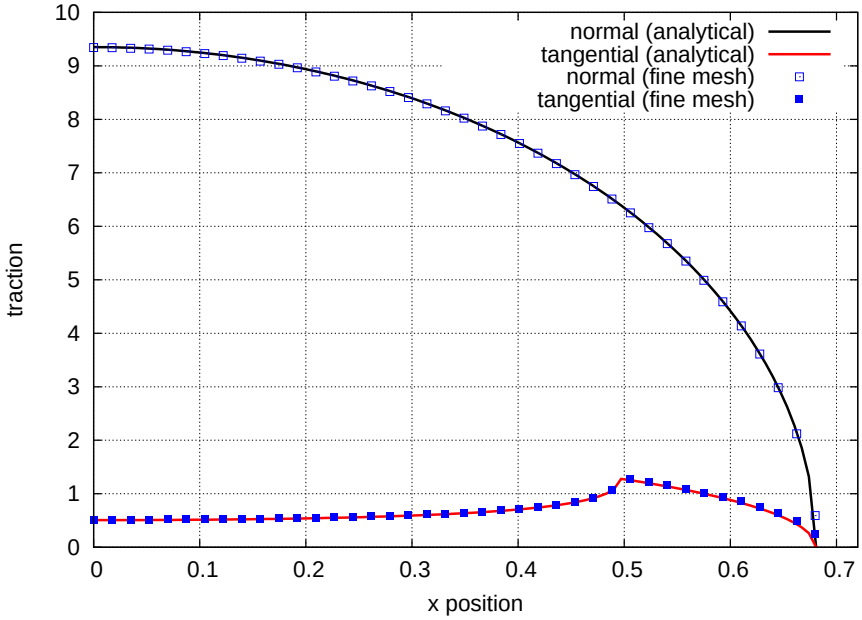

Figure 4.7: Contact traction for frictional cylinder on cylinder contact problem - fine mesh.

4.6.2 Frictional beam contact problem

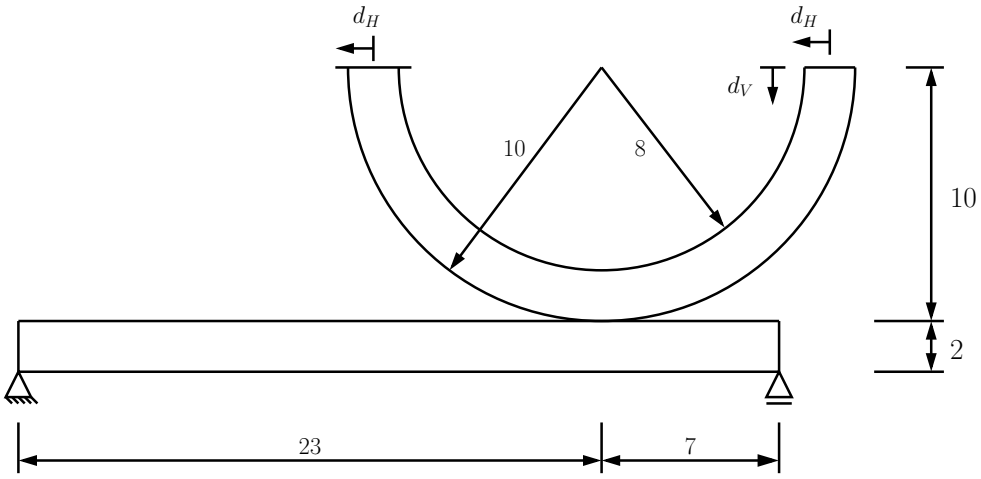

Figure 4.8: Frictional beam contact problem.

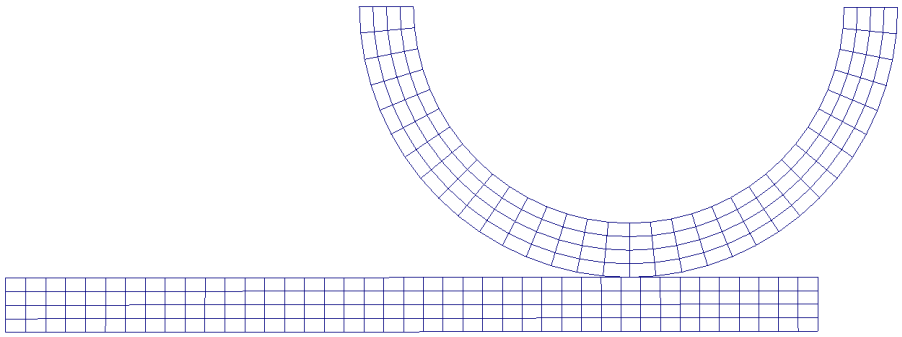

Figure 4.9: Discretization of the frictional beam contact problem.

With this example, the robustness of the formulation in the context of large deformations with finite sliding is demonstrated. Additionally, the accuracy of the method is shown by comparing to results in [150], from where the problem setup is taken. It consists of a curved beam ($E = 2250$, $\nu = 0.125$) and a straight beam ($E = 2700$, $\nu = 0.35$) as shown in Figure 4.8. The loading is realized with Dirichlet conditions: The straight beam is fixed in vertical direction at both ends and in horizontal direction at the left hand side. The curved beam is subjected to a horizontal displacement $d_H = 2.0\,t$ at both ends and to a vertical displacement $d_V = 1.2\,t$ at the right hand side. At time $t_{\max} = 8$, the maximum prescribed displacements are $d_{H\max} = 16$ and $d_{V\max} = 9.6$. Between the two beams, frictional contact takes place, where COULOMB friction with a frictional coefficient $\mu = 0.5$ is considered. The discretization of the problem is shown in Figure 4.9, the quasistatic simulation uses 320 pseudo-time increments with $\Delta t = 0.025$. In Figure 4.10, the

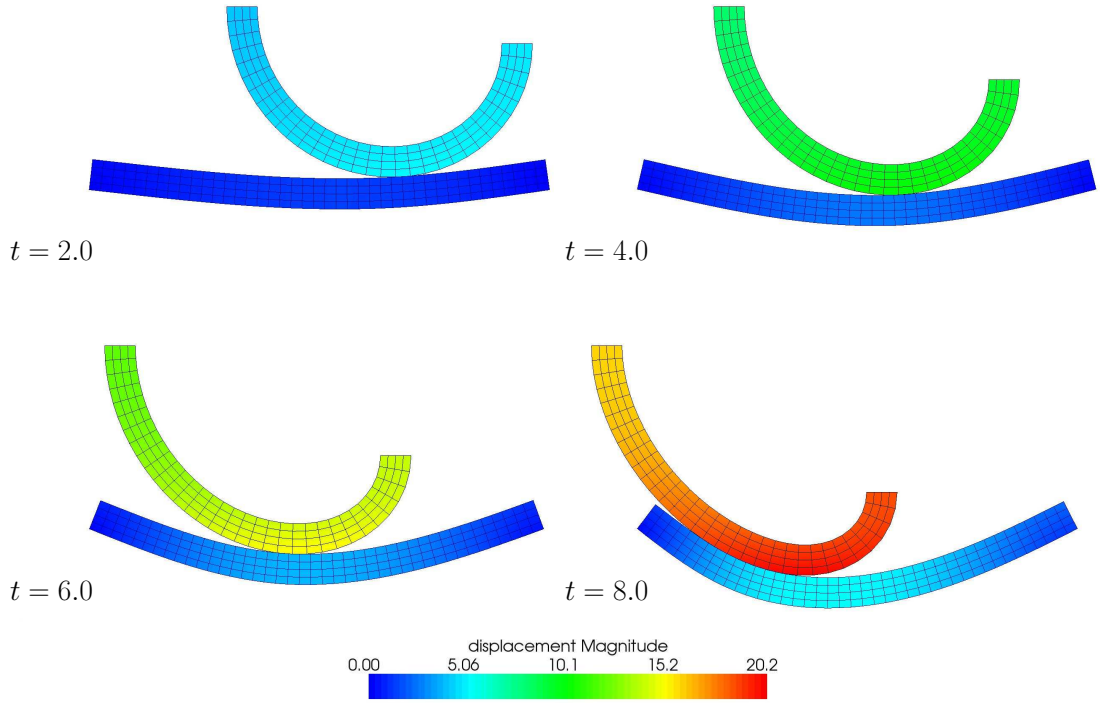

Figure 4.10: Deformed configurations for frictional beam contact problem.

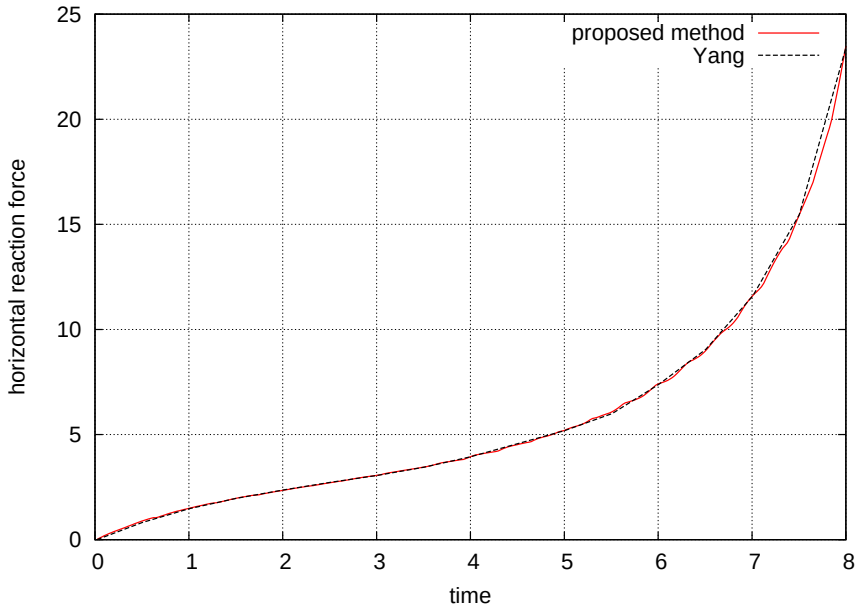

Figure 4.11: Reaction force at the left support of the straight beam; Comparison with results from YANG et al. [150].

c_n \ c_t	10^{-1}	10^{0}	10^{1}	10^{2}	10^{3}	10^{4}	10^{5}	10^{6}
10^{-1}	4	4	4	4	4	4	4	-
10^{0}	4	4	4	4	4	4	4	-
10^{1}	6	4	4	4	4	4	6	-
10^{2}	-	5	4	4	4	4	4	-
10^{3}	-	-	5	4	4	5	5	-
10^{4}	-	-	7	4	5	5	5	-
10^{5}	-	-	10*	7*	6*	8*	-	-
10^{6}	-	-	-	8*	-	-	-	-

(*) = more than one change in active and/or slip set.

Table 4.1: Number of NEWTON steps as function of parameters c_n and c_t for a representative step starting from $t = 0.325$.

evolution of the deformations is exemplarily shown at times $t = 2.0,\ 4.0,\ 6.0$ and 8.0. Figure 4.11 supplies the horizontal reaction force at the left support of the straight beam compared to original results obtained in YANG et al. [150], thus demonstrating very good agreement.

Moreover with this example, the influence of the parameters c_n and c_t introduced with the complementarity functions in Section 4.1 is commented. It is worth mentioning that the conditions in tangential direction are also influenced by the parameter c_n, which is a result of the applied COULOMB friction law. Examining the update formulas (4.31) and (4.32) it seems advantageous to choose c_t such that the different scales of $\tilde{\mathbf{u}}_{\tau j}$ and $\mathbf{z}_{\tau j}$ are balanced. Due to this consideration c_t and c_n are suggested to reflect the material parameters of the contacting bodies in HÜEBER et al. [56]. Another assumption is that c_t should be in the range of the quotient of the absolute values of $\mathbf{z}_{\tau j}$ and $\tilde{\mathbf{u}}_{\tau j}$. With this, the two summands in equations (4.31) and (4.32) are of the same order of magnitude.

Table 4.1 illustrates convergence behavior for different values of c_n and c_t. A representative step, including changes in the active and slip set, is investigated listing the number of NEWTON steps needed to reach convergence. It can be seen that there exists a very broad spectrum for c_t and c_n without any deterioration of convergence. With increasing c_n, also c_t has to be increased in order to obtain a robust algorithm. Choosing c_n and c_t in the range of material parameters results in very satisfactory performance. At the end of the considered time step, one slipping node is in contact. Its quotient of $|z_{\tau j}|$ and $|\tilde{u}_{\tau j}|$ in the 2D example is about 20. With this, also the orientation at this factor for the choice of c_t can be recommended.

It is emphasized that, according to Section 4.2, c_n and c_t can be interpreted as penalty parameters. But they do not influence the accuracy of results within an augmented Lagrangian scheme which is similar to the semi-smooth NEWTON applied here, see Section 4.2.

4.6.3 Two elastic beams

The problem setup shown in Figure 4.12 is chosen according to YANG et al. [150], yet we assume hyperelastic material behavior and a friction coefficient of $\mu = 0.8$. The two curved beams ($E = 689.56$, $\nu = 0.32$) come into frictional contact (COULOMB's law) due to the upper

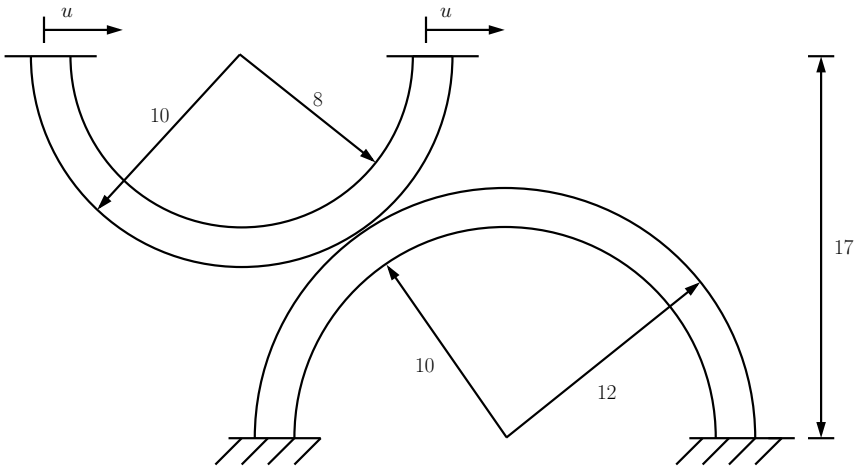

Figure 4.12: Two elastic beams contact problem.

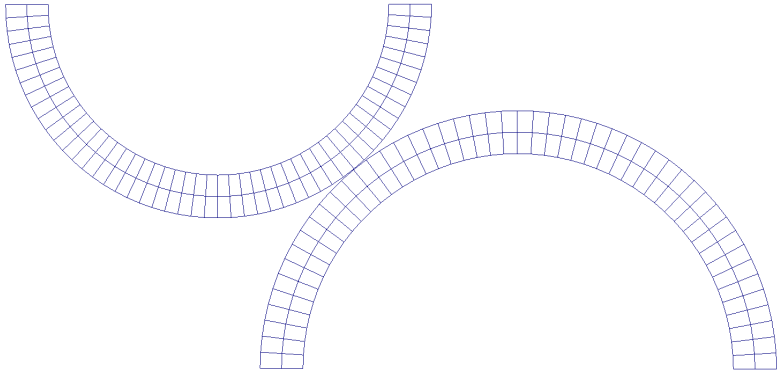

Figure 4.13: Discretization of the two elastic beams contact problem.

beam being subjected to a horizontal displacement u. The discretization given in Figure 4.13 with linear shape as well as quadratic shape functions (not shown) are used. The parameters c_n and c_t are assumed to be 10.

The simulation is quasistatic leading to a snapthrough behavior towards the end of the analysis. In Figure 4.14, the evolution of deformation is shown at different stages. The simulation is driven with a displacement increment $\Delta u = 0.5$. In order to demonstrate the performance and the robustness of the proposed algorithm, a large time step of $\Delta u = 2.5$ has been applied. It is starting form $u = 5$ as it is performed in YANG et al. [150] for the penalty regularized approach. The full deformation of this large step is given in Figure 4.15 and the evolution of the absolute residual is supplied in Table 4.2. Both changes in the active set as well as in the slip set occur. The fully linearized, semi-smooth NEWTON approach exhibits excellent convergence behavior with seven iterations (column 1 of Table 4.2) for linear shape functions and 12 iterations for quadratic shape functions (column 2 of Table 4.2). Omitting linearizations of mortar matrices and normal and tangential vectors leads to a significant larger number of iterations with associated high computational costs. This is also the case for fixed point type methods, where comparisons have already been demonstrated in POPP et al. [110].

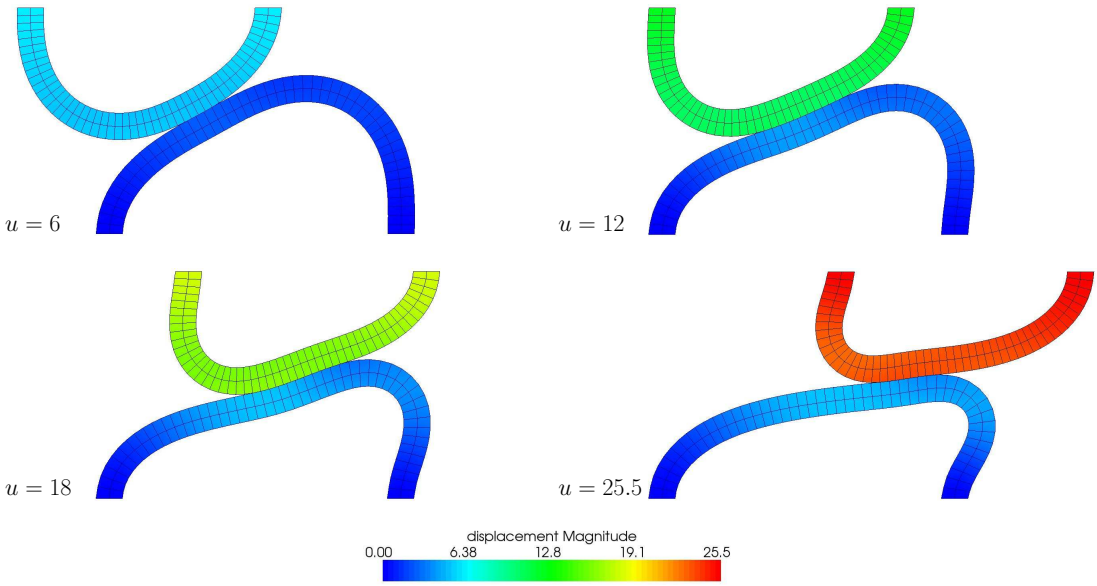

Figure 4.14: Deformed configurations for the two elastic beams contact problem.

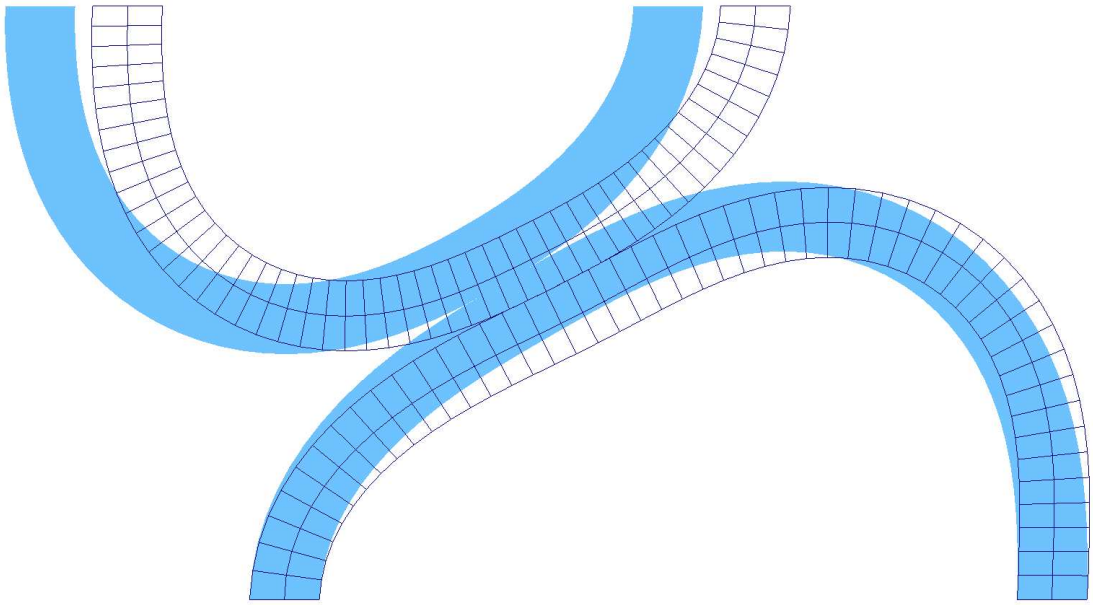

Figure 4.15: Deformation for a large step $\Delta u = 2.5$ starting form $u = 5$.

	linear shape functions	quadratic shape functions
1	8.55e+02 (*)	1.00e+04(*)
2	3.14e+02 (*)	4.09e+03(*)
3	8.91e+01 (*)	1.92e+03(*)
4	1.30e+01	1.48e+03(*)
5	3.41e−01	7.44e+02(*)
6	2.40e−04	2.50e+02(*)
7	1.28e−10	3.90e+02(*)
8		1.57e+02(*)
9		2.52e+01(*)
10		5.35e−01
11		5.34e−04
12		4.93e−10
Σ	7	12

(*) = change in active and/or slip set

Table 4.2: Convergence behavior of the fully linearized, semi-smooth NEWTON method in terms of the absolute residual norm for the large step $\Delta u = 2.5$ starting from $u = 5$ for linear and quadratic shape functions.

4.6.4 Ironing problem

The setup of the frictional ironing problem is shown in Figure 4.16. It is the frictional extension of the one presented in POPP et al. [111] and is similar to PUSO and LAURSEN [117]. Finite deformation contact results from a cylindrical die ($E = 1000, \nu = 0.3$) intruded into an elastic block ($E = 1, \nu = 0.3$). For the contact interface, the friction coefficient is assumed to be $\mu = 0.2$. The die is first pressed into the block by prescribing a vertical displacement of $w = 1.4$ in negative z-direction at the upper end of it. Then, holding the vertical displacement constant, the die slides along by a prescribed horizontal displacement in x-direction up to a value of $u = 4.0$. The problem is discretized with 8-node hexahedrals as also given in Figure 4.16. The analysis is run quasistatically with the vertical intrusion phase being realized with 10 pseudo-time steps. For the horizontal movement, additional 65 steps are applied.

Deformed configurations at different stages are shown in Figure 4.17. The accompanying frictional tractions can be found in Figure 4.18. With the help of both of them, the different phases of sticking and sliding can easily be identified: First, the die is pressed into the block which deforms strongly. Basically sticking occurs, frictional contact tractions appear also pointing into the y-direction caused from 3D effects. The respective stages are placed on the top left and top right. Then, when the die experiences the prescribed horizontal displacement, the die takes along the block due to mainly sticking and the frictional contact tractions align themselves in the opposite direction of the movement (bottom left). When the COULOMB limit is reached at every point in the contact zone, finite sliding occurs (bottom right).

With the ironing problem, the excellent convergence behavior of the semi-smooth NEWTON method in three dimensions is demonstrated. The evolution of the absolute residual norm is

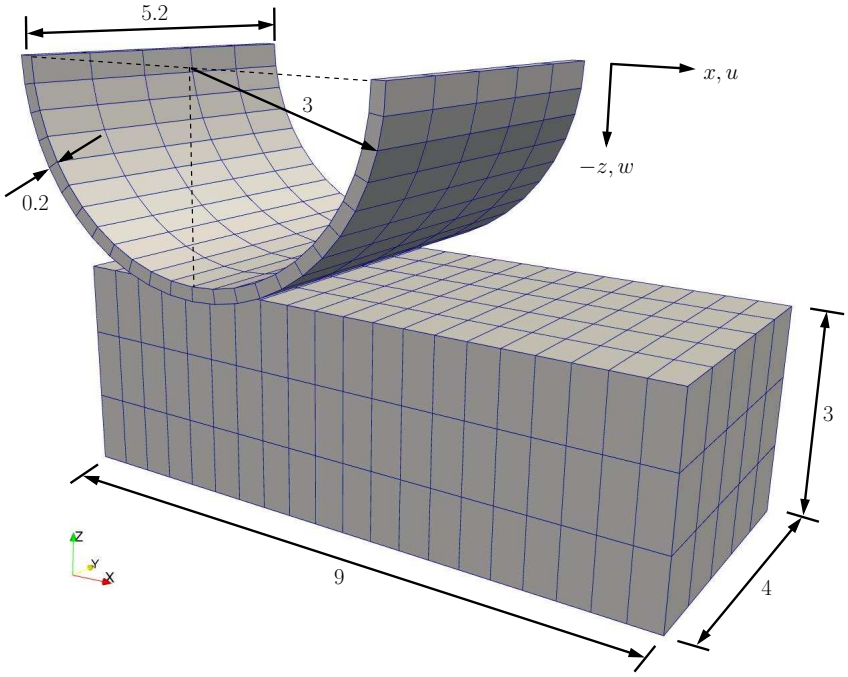

Figure 4.16: Ironing example, problem setup and finite element discretization.

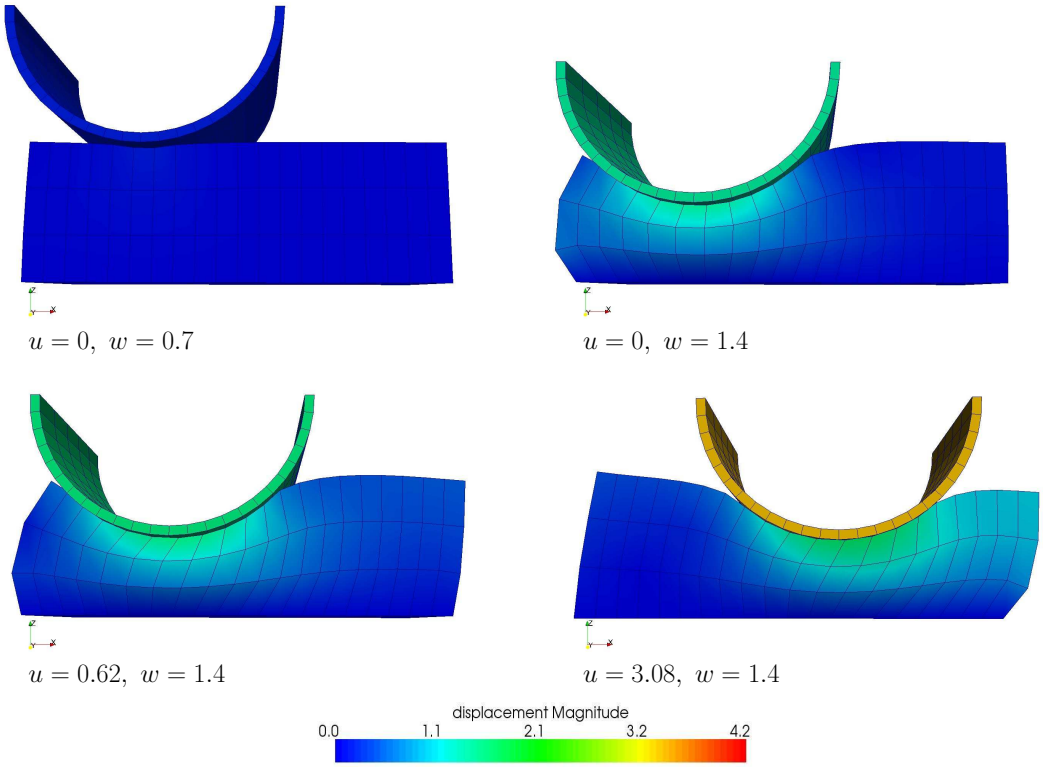

Figure 4.17: Deformed configurations for the ironing example, stages during intrusion (top left, top right) and prescribed horizontal displacement (bottom left, bottom right).

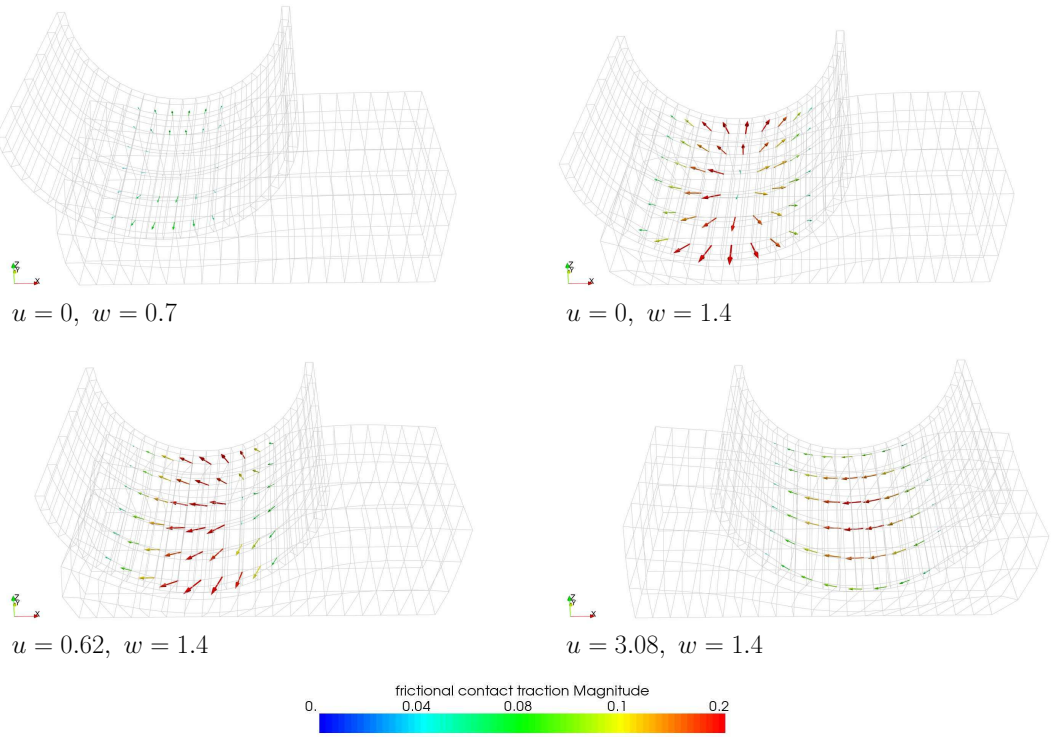

Figure 4.18: Frictional contact tractions for the ironing example, stages during intrusion (top left, top right) and prescribed horizontal displacement (bottom left, bottom right).

	intrusion phase	sliding phase
1	6.53e+03 (*)	4.36e+02
2	2.49e+03 (*)	5.05e+01
3	8.27e+02 (*)	1.03e+00
4	1.80e+02 (*)	5.98e−04
5	1.40e+01 (*)	2.62e−10
6	1.14e−01	
7	8.74e−06	
8	3.52e−12	
Σ	8	5

(*) = change in active and/or slip set

Table 4.3: Convergence behavior of the semi-smooth NEWTON method for the ironing example. Evolution of the absolute residual norm for a time step of the intrusion phase (increment in displacement $\Delta w = 0.14$) and a time step of the sliding phase (increment in displacement $\Delta u = 0.06$).

shown in Table 4.3 for a significant time step in the intrusion phase (increment in displacement $\Delta w = 0.14$) in column 1 and in the sliding phase (increment in displacement $\Delta u = 0.06$) in column 2. For the time step in the intrusion phase, additional nodes come into contact, which

is why it contains a few changes in the active and in the slip set. This does not appear for the sliding phase as the surface of the die is chosen as the slave contact surface. Once the sets remain constant, the residual decreases quadratically due to the linearization, which has been carried out consistently also for the 3D case. In total, only eight and five iterations are necessary to bring the residual below the given limit.

5 Frictional contact problem with wear

This chapter treats the extension of the developed finite deformation frictional contact formulation towards wear. After giving a short overview on wear mechanisms and a motivation for their consideration in numerical simulations in Section 5.1, ARCHARD's law of wear is presented in Section 5.2. It enters the problem formulation with two different strategies: Firstly, the treatment of wear with an internal state variable approach in Section 5.3 and, secondly, the modeling of contact surface evolution with an ALE formulation in Section 5.5. The respective examples are presented in Sections 5.4 and 5.6.

5.1 Overview on wear mechanisms and motivation

Wear is a complex physical phenomenon. It is characterized by the loss of material at the surface of a body during contact with another surface. It is one of the main causes for component damage and subsequent failure of machines and devices with what it is of high economic importance, see POPOV [109]. It also plays a big role in biomechanic applications as, for example, in the field of joint prostheses, see JOURDAN [69] or LONG and RACK [91]. Wear is closely related to friction and can be divided according to its physical mechanisms. The main wear types from the classifications in POPOV [109] and RABINOWICZ [120] are briefly summarized in the following.

Abrasive wear

Abrasive wear occurs if the contacting bodies are of different hardness. Here, the harder material penetrates and cuts off the softer material as visualized in Figure 5.1 on the left. The wear debris depends, among other things, on the normal contact force and the sliding length.

Adhesive wear

Another fundamental type of wear is the adhesive wear. It plays a primary role if the frictional partners are of equal or similar hardness. Its mechanism can be imagined as the welding together of rough surfaces noticeable on the microscopic level. This grows to wear particles which are removed from the contact surfaces as given in Figure 5.1 on the right. Prerequisite for this type of wear is the plastic deformation of metallic materials when reaching a certain stress level. Similar to abrasive wear, the volume of wear depends on the normal contact force and the sliding length.

Corrosive wear

This type of wear occurs when sliding takes place in a corrosive environment. In the absence of sliding, products of corrosion form a film on the contact surfaces from chemical modifications.

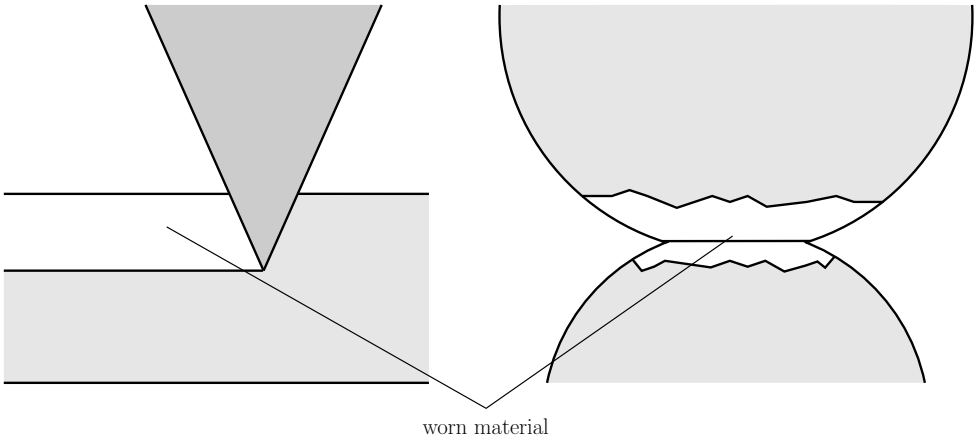

Figure 5.1: Abrasive (left) and adhesive wear (right).

With ongoing time, this progress tends to slow down or even arrest the corrosion. Frictional sliding wears this layer away and the corrosive attack continues.

Fretting wear, fretting fatigue

Fretting occurs whenever contacting bodies are subjected to small-amplitude oscillatory movements between contacting bodies. The resulting damage can either be wear, which is denoted as fretting wear, or fatigue. There, cracks appear and the phenomenon is known as fretting fatigue. Fretting arises in flexible couplings, splines, and jointed structures as for example turbine or fan disc to blade joints in aircraft engines.

The description of the wear mechanisms above is kept very short. For more detailled information, the reader is referred to, for example, POPOV [109] and RABINOWICZ [120], and, especially for fretting wear and fretting fatigue, to ALDHAM et al. [3], HILLS and NOWELL [51], HURRICKS [62], and WATERHOUSE [136] within the vast amount of literature concerning this topic.

Motivation - prediction of fretting fatigue life

Besides the above motivated, very general necessities of modeling wear in numerical simulations, a more specific area is described here. It addresses the prediction of fretting fatigue life of the already mentioned jointed structures in aircraft engines. For those, fatigue equations are developed with experimental fretting fatigue tests, where a typical abstract test setup from JIN and MALL [65, 66] is shown in Figure 5.2 on the left hand side. It is a “flat on punch“ experimental rig, where a pair of cylindrical fretting pads is held in contact with a flat specimen. First, the vertical force P is applied and then, the specimen is loaded with the cyclic loads $\sigma(t)$ and $Q(t)$ leading to slip amplitudes of different lengths in the contact zone. The test stops when fatigue failure occurs. A fundamental outcome of these tests is that fatigue life strongly depends on the occurring slip amplitude. In general, it is reduced markedly for partial slip, i.e. a state where portions of the contact zone remain sticking whereas others undergo slip. In contrast, gross sliding with high wear volumes tends to infinite or, at least, long fatigue life, see Figure 5.2 on the left

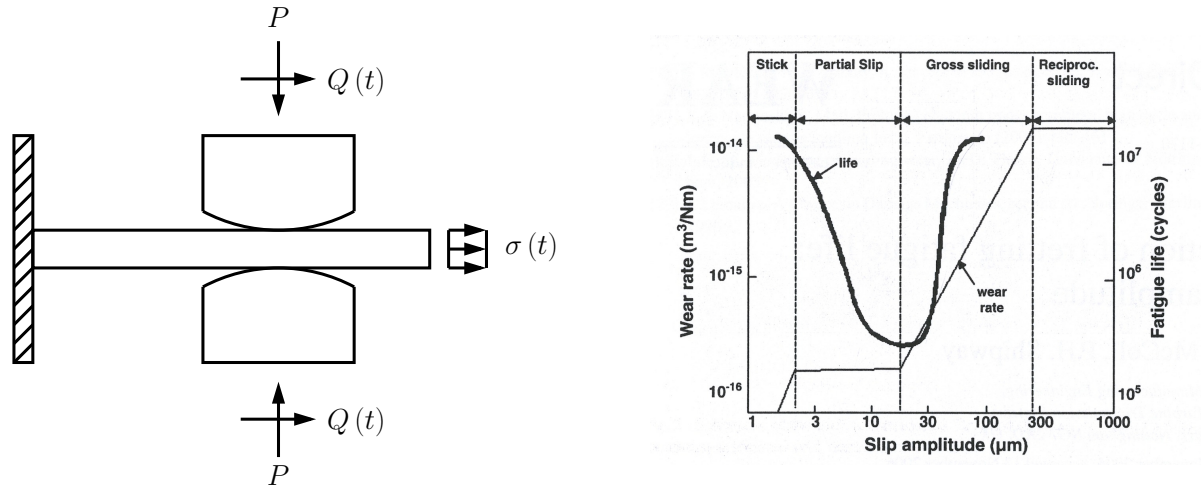

Figure 5.2: Schematic fretting fatigue test setup according to JIN and MALL [65, 66] (left) and the effect of slip amplitude on fretting fatigue life and wear rate (right). The diagram is taken from MADGE et al. [92], where it is further referred to the work of VINGSBO and SÖDERBERG [133].

hand side. More information about fretting fatigue tests, rig setups, and results can be found, for example, in HILLS and NOWELL [51] and JIN and MALL [65, 66].

In literature, suggestions for the described dependence of slip amplitude and fatigue life can be found, for example, in JIN and MALL [66] and VINGSBO and SÖDERBERG [133]. They suspect that the reason for the connection of long fatigue life and large slip amplitudes is some kind of ”rubbing out” effect. Due to gross sliding, the appearing cracks are immediately worn away with what they cannot nucleate to larger ones that may lead to component failure. Furthermore, the modeling of wear in contact analysis as in DING et al. [23], MADGE et al. [92, 93], and MCCOLL et al. [94] contributed to this topic. They implemented a contact model considering wear and validated the predicted wear scars against experimental wear test data. The numerical simulations shed a light on geometry evolution and contact pressure distribution with ongoing number of loading cycles as the components experience wear. A key observation is, that for gross sliding, a widening of the contact area takes place. It is associated with a drop in the peak of the contact pressure. In contrast, partial slip showed an increase of contact pressure in the stick-slip zone. This is due to wear and material removal in the slip area and a redistribution of contact stresses towards the stick region.

Fatigue equations, as for example the one from SMITH-WATSON-TOPPER (SWT) in SMITH et al. [127] applied to fretting fatigue, have the potential to predict the position of cracks, their orientations, and fatigue life of components in multiaxial stress states, see MADGE et al. [92]. The essential input in this model is, besides material parameters and others, the peak normal stress. The authors from above, DING et al. [23], MADGE et al. [92, 93], and MCCOLL et al. [94], obtained a very good agreement of predicted fatigue failure and observed behavior in experimental fretting fatigue tests. This also included capturing the dependency of fatigue life upon slip amplitude, as discussed above. However, this was only possible by considering wear within

the finite element analysis leading to a change in contact geometry and a redistribution of conact stresses in the contact zone. It is fundamental for the prediction of fatigue life.

To sum up, the accurate and efficient solution of wear problems is indispensable for the precise prediction of fatigue life. As above mentioned numerical solution approaches, as for example in DING et al. [23], are dealing with modifications of the contact geometry to obtain matching meshes, the developed contact formulation based on the mortar method is extended towards wear within this work.

5.2 ARCHARD's law of wear

Due to being a complex phenomenon, MENG and LUDEMA [96] found about 180 wear laws within their comprehensive literature review. Nevertheless, commonly the phenomenological ARCHARD's wear law [4] is applied to quantify sliding wear damage.

Basic equations

As explained, for abrasive wear, the harder material cuts out the softer one. Here, ARCHARD's wear law states the following dependencies: The worn volume loss V is proportional to the normal force P and the sliding length S and inversely proportional to the hardness H of the softer material as

$$V = K\frac{P\,S}{H}\,, \tag{5.1}$$

where K is the dimensionless wear coefficient. From MRÓZ and STUPKIEWICZ [98] and STRÖMBERG et al. [131], the rate of wear debris is also proportional to the rate of frictional dissipation. This is also valid, for example, for adhesive wear, with what ARCHARD's law, equivalently expressed in these terms, can be applied there, too. It is a "general" wear law for even more types of wear, see POPOV [109], which is clearly the reason for its frequent use. It is applied also for fretting wear in MCCOLL et al. [94] or SALLES et al. [123] and throughout this work.

For treating wear with finite elements, ARCHARD's wear law in equation (5.1) is expressed in its local form. This is achieved by referring it to a unit surface area as carried out for example in DHIA and TORKHANI [21], LENGIEWICZ and STUPKIEWICZ [87], MCCOLL et al. [94], MOLINARI et al. [97], SALLES et al. [123], and STRÖMBERG [128]. It is then written in terms of the wear rate $\dot{w}$ as height loss per unit time and reads

$$\dot{w} = k_w\,|p_n|\,\|\mathbf{v}_{\tau,rel}\|. \tag{5.2}$$

Here, it is referred to the spatial configuration with $\dot{w}$ yields the reduction of height of the current bodies. The quantities $\mathbf{v}_{\tau,rel}$ and p_n are the previously introduced tangential relative velocity and the spatial normal contact pressure from the frictional contact formulation. The factor k_w is the local wear coefficient, which can be determined from K in equation (5.1) and the penetration hardness of the material according to STRÖMBERG [128]. The formulation accounts for finite deformations and has originally been proposed in DHIA and TORKHANI [21] and recently also applied in LENGIEWICZ and STUPKIEWICZ [87].

Referred to the reference configuration, the local form of ARCHARD's wear law quantifies the height loss of the undeformed configuration. The accompanying wear coefficient is different and

can be obtained from the spatial k_w via the JACOBIan determinant of the respective mapping. However, the question arises for which wear law the wear coefficient obtained from experiments should be used. As there are no observations that would justify the choice of the material or the spatial form, see LENGIEWICZ and STUPKIEWICZ [87], it is used for ARCHARD's wear law in its spatial form in (5.2) here.

For completeness, it is mentioned that ARCHARD's wear law can also be obtained from the model described by STRÖMBERG et al. [128, 131]. Starting from a variational formulation in continuum thermodynamics, the formalism introduces a free energy and a pseudopotential from which a standard model for contact, friction, and wear is derived. It is in the framework of small displacements and small sliding. The interested reader is referred to these contributions for details.

Explicit wear algorithm

With equation (5.2), the available wear law is of evolutionary type. It requires, similar to the frictional conditions, an incremental time strategy which has to be at least a quasistatic analysis. In order to obtain the wear height w, more or less simplified incremental formulations have been developed, see DHIA and TORKHANI [21]. Within this work, an explicit wear algorithm is applied.

Considering a time increment Δt stepping from t_{n-1} to t_n, it is assumed that the displacements $\mathbf{u}\left(t_{n-1}\right)$, the LAGRANGE multipliers $\boldsymbol{\lambda}\left(t_{n-1}\right)$, and the so far accumulated wear $w\left(t_{n-1}\right)$ at t_{n-1} are known. Using the explicit algorithm, the wear problem is at first treated keeping the wear state $w\left(t_{n-1}\right)$ constant. It is solved towards $\mathbf{u}\left(t_n\right)$ and $\boldsymbol{\lambda}\left(t_n\right)$ at t_n with the approach proposed in Section 5.3 or 5.5. Once this is obtained, wear is updated as

$$w\left(t_n\right) = w\left(t_{n-1}\right) + \Delta w \ , \tag{5.3}$$

where Δw being the additional wear height within the current time increment Δt. It is evaluated according to ARCHARD's law (5.2) with the solution variables at t_n and reads

$$\Delta w = k_w \left| p_n\left(t_n\right)\right| \left\| \mathbf{v}_{\tau,rel}\left(t_n\right)\right\| \Delta t \ . \tag{5.4}$$

This means that the displacement and LAGRANGE multiplier solution of the frictional contact problem at time t_n only depends on the accumulated wear $w\left(t_{n-1}\right)$. It is not influenced by the additional wear height Δw within the time step itself. Only when the solution is found, the accumulated wear $w\left(t_n\right)$ is dated up in a postprocessing calculation. This value then enters the problem of the next time increment.

Using an explicit time integration scheme for the wear law, its linearization within the later applied NEWTON algorithm is avoided. It would become very strenuous due its structure at hand. However, this is not the reason for using an explicit time integration scheme, it is rather chosen due to the different time scales at hand. As the wear process is usually very slow in comparison with the finite deformation problem, the rate of wear is negligible within a single time step. Only the accumulation of wear over a longer period of time influences the results and has to be taken into account. An explicit time integration scheme exactly covers these considerations. However, it could lead to numerical instabilities if the change of wear within one time step is too large, see MCCOLL et al. [94]. But, as explained, this classical limitation of explicit schemes will not occur

in most applications treating wear. Therefore, it is frequently used in literature as for example in MCCOLL et al. [94], ÖQVIST [103], PÕDRA and ANDERSSON [104], PAULIN et al. [107], and within this work.

5.3 Wear with internal state variable approach

Within this section, the frictional contact problem including wear is treated by the use of an internal state variable approach. Here, the accumulated wear w is identified as an additional gap along the outward normal vector between two bodies. By using this method, wear does neither change the geometry of the body nor the shape of the contact surfaces. For this reason, the method is mainly suitable for problems leading to very small amounts of wear. It has been early used in STRÖMBERG et al. [131] and is successfully applied in, for example, IREMAN et al. [64], SALLES et al. [123], and STRÖMBERG et al. [128, 129, 130]. Wear leading to finite surface changes is introduced in Section 5.5.

5.3.1 Boundary value problem of frictional contact with wear

The boundary value problem of the finite deformation frictional contact problem with wear, treated with an internal state variable approach, looks like given in the following. It is similar to the formulation in Section 2.3, except for the normal contact conditions. They do not only depend on the gap $g\left(\mathbf{X}^{(1)}, t\right)$ and the normal contact traction p_n, but also contain wear in form of the internal state variable $w\left(\mathbf{X}^{(1)}, t\right)$ defined on the slave side. They are written as

$$g\left(\mathbf{X}^{(1)}, t\right) + w\left(\mathbf{X}^{(1)}, t\right) \geq 0 \,, \tag{5.5}$$

$$p_n \leq 0 \,, \tag{5.6}$$

$$p_n \left(g\left(\mathbf{X}^{(1)}, t\right) + w\left(\mathbf{X}^{(1)}, t\right) \right) = 0 \,, \tag{5.7}$$

where the internal state variable w is evaluated from the already temporally discretized equation (5.3). Similar to Chapter 3, this set of equations is equally expressed as a variational inequality given as

$$\lambda_n \in \mathbb{R}_0^+ : \quad (g + w)\,(\delta\lambda_n - \lambda_n) \geq 0 \quad \forall\, \delta\lambda_n \in \mathbb{R}_0^+ \,. \tag{5.8}$$

Here, the contact normal traction p_n is already identified as the negative LAGRANGE multiplier in normal direction λ_n.

5.3.2 Weak form and finite element discretization

This section treats the discrete form of the finite deformation frictional contact problem with wear. As the entering equilibrium equations to the balance of linear momentum are exactly those of the frictional contact without wear, it results in the already well known equations (3.23) and, discretized in space, (3.50). It is not discussed further here.

The same is valid for the tangential contact conditions. Following the derivation in STRÖMBERG et al. [131], the change of wear $\dot{w}$ is included in the variational formulation of the frictional contact condition. However, as the influence of $\dot{w}$ on the solution within one time step is neglected

in the explicit approach, the discrete frictional conditions remain unchanged. They are used as stated in equations (3.85) - (3.88).

Normal contact conditions

Only the normal contact conditions (5.8) are different to the case without wear. In integral form, they read

$$\boldsymbol{\lambda} \in \boldsymbol{\mathcal{M}}(\boldsymbol{\lambda}): \quad \int_{\gamma_c^{(1)}} (g+w)\,(\delta\lambda_n - \lambda_n)\,\mathrm{d}\gamma \geq 0 \quad \forall\, \delta\boldsymbol{\lambda} \in \boldsymbol{\mathcal{M}}(\boldsymbol{\lambda})\,, \tag{5.9}$$

see also STRÖMBERG [128]. The integral is split as

$$\boldsymbol{\lambda} \in \boldsymbol{\mathcal{M}}(\boldsymbol{\lambda}): \quad \int_{\gamma_c^{(1)}} g\,(\delta\lambda_n - \lambda_n)\,\mathrm{d}\gamma + \int_{\gamma_c^{(1)}} w\,(\delta\lambda_n - \lambda_n)\,\mathrm{d}\gamma \geq 0 \quad \forall\, \delta\boldsymbol{\lambda} \in \boldsymbol{\mathcal{M}}(\boldsymbol{\lambda})\,, \tag{5.10}$$

where the first integral is well known from the contact problem without wear and not considered further. The second one contains a weak formulation of the internal state variable w representing the accumulated wear. It may be regarded as an additional gap or wear-gap and is therefore treated in the same manner as the normal gap g. Referring to the formalism in Section 3.4.4 and applying spatial and temporal discretization, the second integral in (5.10) results in the nodal weighted wear increment $\Delta\tilde{w}_j$ for a node $j \in \mathcal{S}$ stepping from t_{n-1} to t_n. It reads

$$\Delta\tilde{w}_j = k_w \int_{\gamma_c^{(1)h}} \Phi_j^{(1)} \left(\lambda_n^h(t_n)\,\|\mathbf{u}_{\tau,rel}^h(t_n)\|\right)\,\mathrm{d}\gamma\,, \tag{5.11}$$

where $\mathbf{u}_{\tau,rel}^h$ is the tangential relative slip increment resulting from $\mathbf{v}_{\tau,rel}\,\Delta t$. The update of the nodal weighted wear $\tilde{w}_j$ after each time step takes place as

$$\tilde{w}_j(t_n) = \tilde{w}_j\,(t_{n-1}) + \Delta\tilde{w}_j\,. \tag{5.12}$$

The increment $\Delta\tilde{w}_j$ in equation (5.11) is obtained with GAUSS integration within the numerical scheme given in Algorithm 1. Similar to the mortar matrices and the nodal weighted gap, the contribution of one slave and master element pair (s,m) is evaluated as

$$\Delta\tilde{w}_{j(s,m)} = k_w \sum_{\text{cell}=1}^{n_{\text{cell}}} \left(\sum_{\text{gp}=1}^{n_{\text{gp}}} w_{\text{gp}}\,\Phi_j^{(1)}\left(\boldsymbol{\xi}_{\text{gp}}^{(1)}\right)\,\lambda_n^h\left(\boldsymbol{\xi}_{\text{gp}}^{(1)}\right) \left\|\mathbf{u}_{\tau,rel\,\text{gp}}^h\left(\boldsymbol{\xi}_{\text{gp}}^{(1)},\boldsymbol{\xi}_{\text{gp}}^{(2)}\right)\right\| J_{\text{cell}} \right)\,, \tag{5.13}$$

where $\mathbf{u}_{\tau,rel\,\text{gp}}^h\left(\boldsymbol{\xi}_{\text{gp}}^{(1)},\boldsymbol{\xi}_{\text{gp}}^{(2)}\right)$ is defined as

$$\begin{aligned}\mathbf{u}_{\tau,rel\,\text{gp}}^h = &\left(\mathbf{I} - \mathbf{n}^{(1)h}\left(\boldsymbol{\xi}_{\text{gp}}^{(1)}\right) \otimes \mathbf{n}^{(1)h}\left(\boldsymbol{\xi}_{\text{gp}}^{(1)}\right)\right) \cdot \\ &\left(\mathbf{x}_{gp}^{(1)h}\left(\boldsymbol{\xi}_{\text{gp}}^{(1)}\right) - \mathbf{x}_{gp}^{(1)h}(t_{n-1})\left(\boldsymbol{\xi}_{\text{gp}}^{(1)}\right) - \left(\mathbf{x}_{gp}^{(2)h}\left(\boldsymbol{\xi}_{\text{gp}}^{(2)}\right) - \mathbf{x}_{gp}^{(2)h}(t_{n-1})\left(\boldsymbol{\xi}_{\text{gp}}^{(2)}\right)\right)\right)\,.\end{aligned} \tag{5.14}$$

It has to be pointed out that the tangential plane in (5.14) is resolved with the interpolated normal field $\mathbf{n}^{(1)h}$. This is due to the fact that interpolated values at GAUSSian points are used instead

of nodal ones. As the definition of nodal tangent vectors in (3.53) is not unique, they may jump from node to node and consequently cause wrong interpolated quantities. This is prevented by using the interpolated normal field. It results in a three component vector $\mathbf{u}^h_{\tau,rel\,\mathrm{gp}} \in \mathbb{R}^3$ in the tangential plane, of which the absolute value is used for the determination of the weighted nodal slip increment in (5.13). However, for formulating frictional equations in terms of nodal quantities as in Chapters 3 - 4, this problem does not arise.

The evaluation of the nodal weighted wear increment $\Delta\tilde{w}_j$ in (5.11) is based on equation (2.57). However, preferable would be the usage of the nodal weighted tangential relative slip increment $\tilde{\mathbf{u}}_{\tau j}$ defined in equation (3.84), which is applied as frame indifferent quantity for the solution of the frictional contact problem throughout Chapter 4.

In doing so, an alternative nodal weighted wear increment, expressed in nodal quantities only, is evaluated as

$$\Delta\tilde{w}_{2,j} = k_w\, z_{nj}\,(t_n) \|\tilde{\mathbf{u}}_{\tau j}\,(t_n)\|. \tag{5.15}$$

It has to be pointed out that this measure is not a direct consequence of (5.11). This derivation requires, as approximation, keeping the LAGRANGE multiplier in normal direction λ^h_n constant over the local support of a node. However, it contains the desired reformulation of the discrete relative tangential velocity in Section 3.4.5 to obtain objectivity. Due to the above specified approximation, so far, the weighted nodal wear increment is evaluated according to (5.11).

Finally, for the internal state variable approach with $\tilde{w}_j$ at hand, the discrete normal contact conditions for each slave node $j \in \mathcal{S}$ read

$$\tilde{g}_j + \tilde{w}_j \geq 0\,, \tag{5.16}$$

$$z_{nj} \geq 0\,, \tag{5.17}$$

$$z_{nj}\;(\tilde{g}_j + \tilde{w}_j) = 0\,. \tag{5.18}$$

5.3.3 Solution within the frictional contact framework

Treating wear with the internal state variable approach as described above, the structural differences between the problems with and without wear are very small. For this reason, the solution procedure from Chapter 4 can be taken with almost no modifications. The slightly changed counterpart to Algorithm 2 within one time increment stepping from t_{n-1} to t_n is given in the following:

Algorithm 3

1. Perform a LAGRANGEan step to solve the frictional contact problem as described in steps 1. - 6. of Algorithm 2. Within this time step, the accumulated nodal weighted wear $\tilde{w}_j$ is kept constant. Wear is taken into account with substituting the nodal weighted gap $\tilde{g}_j$ by the nodal weighted gap including wear $\tilde{g}^w_j$ in all equations of Chapter 4. For the current NEWTON iterate k, it is evaluated as

$$\tilde{g}^{w,k}_j\,(t_n) = \tilde{g}^k_j\,(t_n) + \tilde{w}_j\,(t_{n-1})\,. \tag{5.19}$$

   The directional derivatives in Section 4.3 are not influenced by this substitution as $\tilde{w}_j\,(t_{n-1})$ does not depend on current displacements or LAGRANGE multipliers.

2. Evaluate the nodal weighted wear increments $\Delta\tilde{w}_j$, $j \in \mathcal{S}$, and the updates $\tilde{w}_j(t_n)$, $j \in \mathcal{S}$, according to equations (5.11) and (5.12). Then, the time step is adjusted as $t_{n-1} := t_n$ and the evaluation continues from 1.

One more comment on the treatment of wear with the internal state variable approach is given. It is embedded consistently within the mortar discretization scheme. Similar to the weighted nodal gap, the weighted nodal wear increment does not represent the physical height loss per time step, but is an integral value over the local support of a node.

5.4 Examples

Considering wear with the internal state variable approach, two numerical examples are presented. Simulations are carried out in BACI and, if not specified otherwise, the same assumptions are made as in Section 4.6.

5.4.1 HERTZian contact with wear

The accuracy of results treating frictional contact problems has already been demonstrated with the HERTZian contact example in Section 4.6.1. A similar problem considering a cylinder on flat problem setup is now presented in the context of wear. It shall show qualitatively the change of contact traction distribution due to gross and partial sliding conditions. As already mentioned, the correct capturing of these rearrangements is essential for lifetime prediction models.

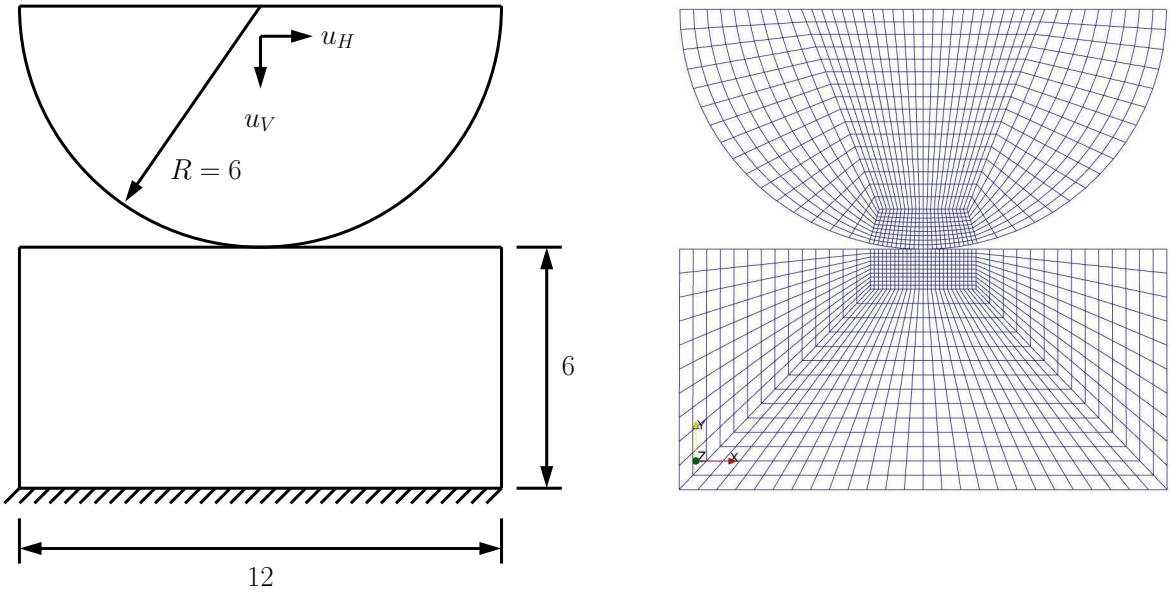

Figure 5.3: HERTZian contact with wear, problem setup and finite element discretization.

The 2D problem setup is given in Figure 5.3 and is similar to the one in DING et al. [23] and MCCOLL et al. [94]. The cylinder and the block are both modelled with St. VENANT-KIRCHHOFF's material law ($E = 200000, \nu = 0.3$). The upper line of the cylinder is subjected

to the DIRICHLET conditions u_V and u_H. For $0 \leq t \leq 1$, the cylinder is pressed onto the block with $u_V = 0.04$. Then, holding u_V constant, a prescribed sinusoidal horizontal displacement u_H is applied for $1 \leq t \leq 301$. Within this time, 300 cycles are performed. The maximum value is determined to $u_{H\max} = 0.02$ and to $u_{H\max} = 0.01$ in the first and the second case. This leads, with assuming the friction coefficient to be $\mu = 0.2$, to two different friction states, respectively. This is on the one hand gross sliding, where the whole contact zone reaches the COULOMB limit and comes into sliding. On the other hand, this is partial sliding. Here, the prescribed horizontal displacement $u_{H\max}$ is not large enough to obtain gross sliding. Only the outer parts of the contact zone experience tangential movements whereas the inner part remains sticking. As wear model, ARCHARD's law of wear is applied, the wear coefficient is assumed to be $k_w = 1.0 \cdot 10^{-6}$.

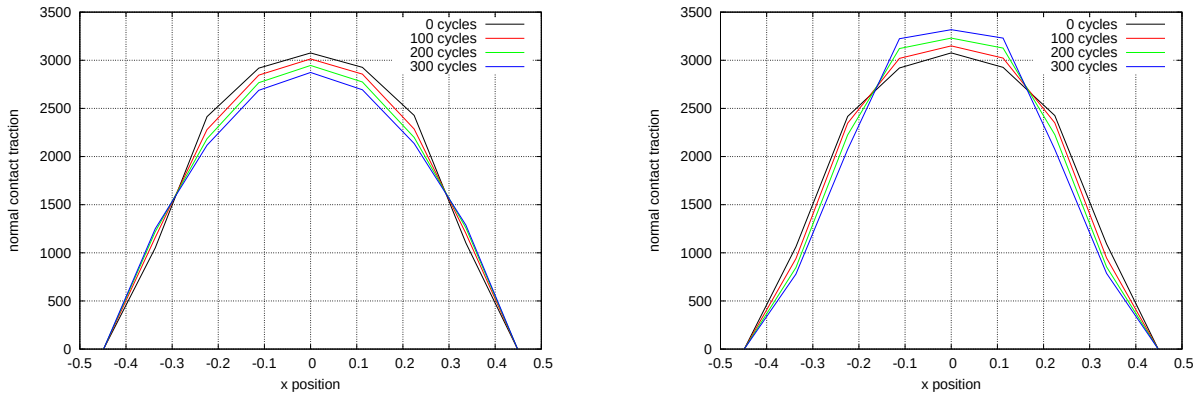

Figure 5.4: HERTZian contact with wear, evolution of normal contact traction for gross sliding (left) and partial sliding (right).

The discretization with 4-node quadrilateral elements is shown on the right of Figure 5.3, the simulation is run quasistatically with 3010 pseudo-time increments of $\Delta t = 0.1$.

As result, the evolution of the normal contact traction in the contact zone is shown in Figure 5.4. It is plotted for 0, 100, 200, and 300 cycles for the gross sliding case (left) and the partial sliding case (right). For the gross sliding case, the maximum value in the center of the contact zone decreases with ongoing number of wear cycles and the profile flattens out. It is because of high normal contact tractions result in high wear rates, too. This leads to a redistribution of contact tractions towards the outer contact zones. In contrast, for the partial sliding case, the maximal contact traction increases. Wear only occurs in the outer sliding zones which therefore escape from loading. It is shifted towards the center sticking zone.

The developed contact formulation with wear using an internal state variable approach captures the wanted redistribution of contact stresses in the contact zone. A qualitatively good agreement with the results in DING et al. [23] is obtained. There, a modification of the contact geometry within the solution algorithm is performed to obtain matching meshes. Of course, this in not necessary due to the usage of the mortar method here.

5.4.2 Oscillating beam

This 2D example demonstrates that the proposed approach also captures the change of normal contact tractions due to wear quantitatively in a a good way. As analytical solutions are difficult

to receive, a setup from STRÖMBERG [128] is taken and numerical results here are compared to those obtained there.

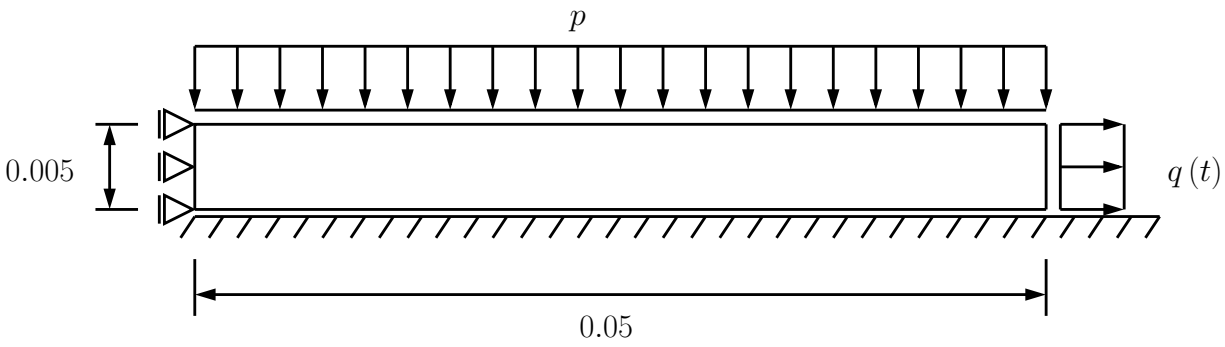

Figure 5.5: Oscillating beam, problem setup.

The beam presented in Figure 5.5 is modelled with St. VENANT-KIRCHHOFF's material law ($E = 210000$, $\nu = 0.3$). It is subjected to a constant vertical load $p = 50$ and a horizontal load $q\,(t) = 50\,sin(2\pi t)$. In the contact zone, the friction and wear coefficients are assumed to be $\mu = 0.2$ and $k_w = 1 \cdot 10^{-5}$.

A quasistatic simulation with a time step size of $\Delta t = 0.0125$ is carried out. Accordingly, 80 steps are necessary for one cycle. Within this work, in total, 3000 cycles are performed. The beam is discretized with 4-node quadrilateral elements as presented in Figure 5.6, see also WICHMANN [138].

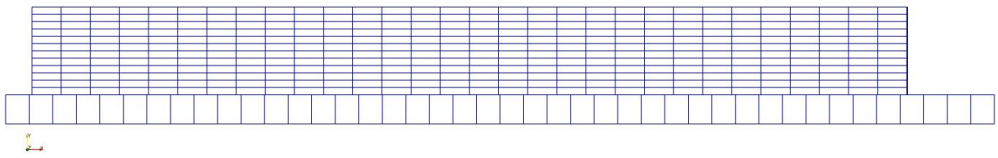

Figure 5.6: Oscillating beam, finite element discretization.

The analysis shows that the oscillating horizontal load leads to a back- and forward sliding of about the right half of the beam whereas the left half of the beam remains sticking. Due to wear, the distribution of normal tractions in the contact zone changes. This is presented in Figure 5.7, where results are compared to those obtained from STRÖMBERG [128]. A good quantitative agreement can be observed. The comparison with higher numbers of load cycles would require a finer mesh due to increasing gradients of wear and normal contact tractions and is not part of this study.

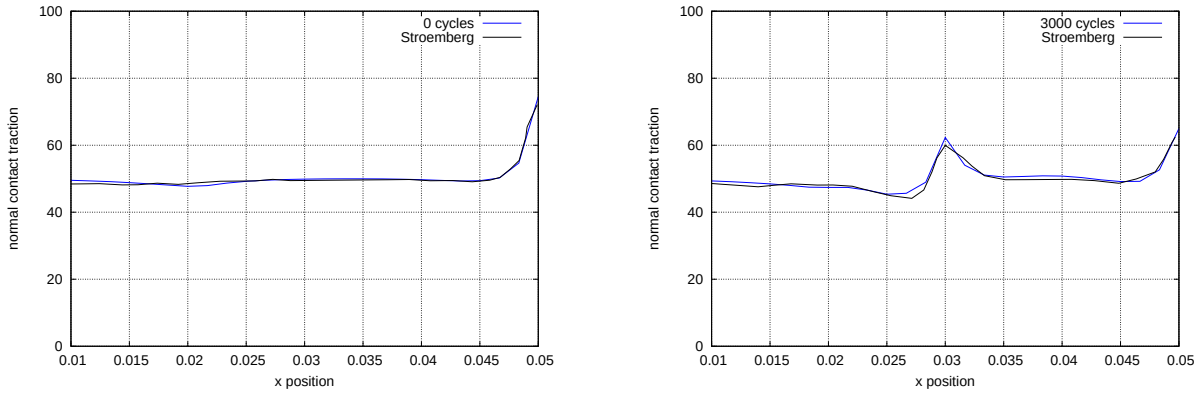

Figure 5.7: Normal contact traction in the contact zone for 0 cycles (left) and 3000 cycles (right). Comparison with the results of STRÖMBERG [128].

5.5 Modeling contact surface evolution with ALE approach

A fundamental different approach to treat wear in finite element contact simulations is presented here. With the internal state variable method above, wear is considered only by the modification of the gap vector as a geometric measure between the contacting bodies. The physical process of wear changing participating bodies is not modeled directly. In this work, an Arbitrary LAGRANGEan-EULERian (ALE) approach allows the domains of the contacting bodies to reduce as material is worn away from them. This brings a time dependent material configuration as visualized in Figure 5.8 for the slave domain. It is denoted as $\Omega_{0,t}^{(1)}$ and its spatial counterpart as $\Omega_{t,t}^{(1)}$. These described items make the method suitable for problems where shape changes due to wear are finite as for example contact and wear of rubber like materials. Or problems with the contact tractions being extremely sensitive also to the curvature of contacting surfaces. The presented formulation is restricted to abrasive wear with material being solely worn from the slave contact surface.

5.5.1 Idea of using an ALE approach resolved with a fractional-step strategy

In this section, the idea of using an Arbitrary LAGRANGEan-EULERian (ALE) approach resolved with a fractional-step strategy to treat contact surface evolution due to wear is presented. In general, the characteristic of this solution strategy is to perform both a LAGRANGEan and an EULERian step within a time increment. So for the problem at hand here, the course of action could be as follows: Within the LAGRANGEan step, the frictional contact problem is solved. It is followed by the evaluation of the amount of wear and, in a subsequent EULERian phase, by the relocation of finite element nodes due to wear. The mesh is moved from the contact surface towards the inside of the slave body in order to model material loss. Subsequently, the analysis continues with the LAGRANGEan step of the next time increment. This approach within a time increment is visualized schematically in Figure 5.9.

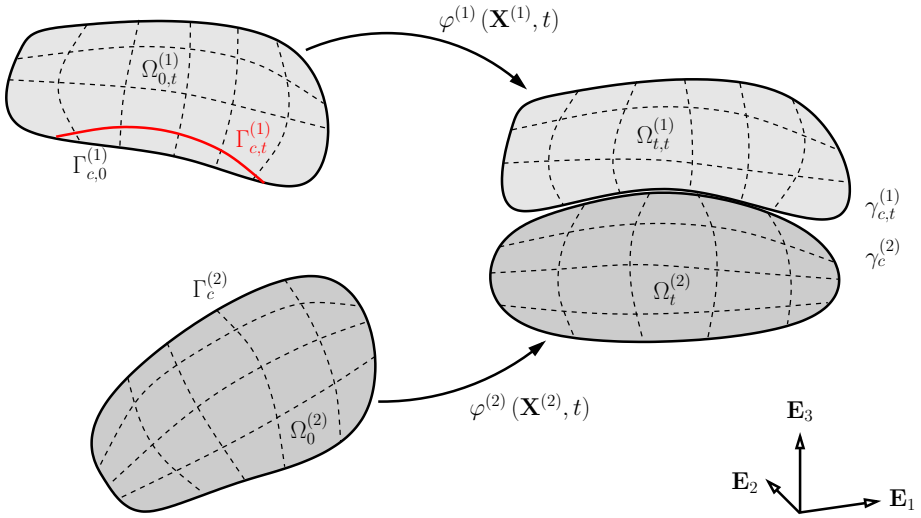

Figure 5.8: Two body contact problem with wear. Time dependent reference configuration of the slave body $\Omega^{(1)}_{0,t}$ from contact surface evolution due to abrasive wear.

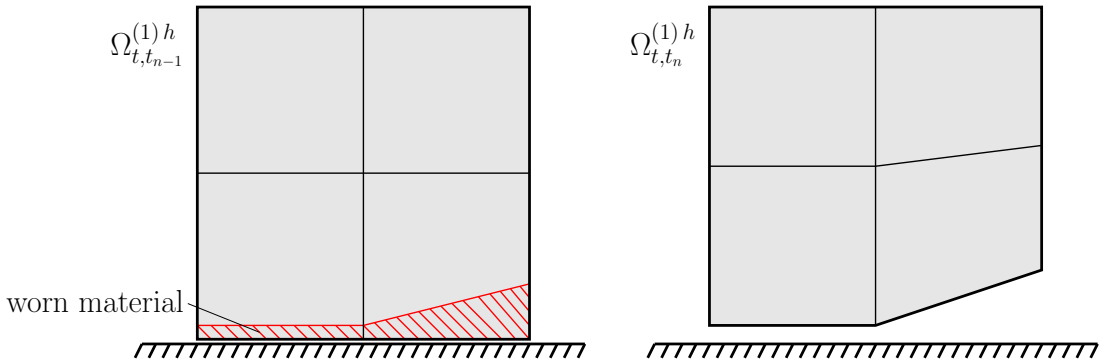

Figure 5.9: Arbitrary LAGRANGEan-EULERian formulation resolved with a fractional-step strategy: Deformed configuration with evaluated amount of wear after LAGRANGEan step (left) and changed deformed configuration due to wear after EULERian step (right).

The described procedure above can be attributed to an Arbitrary LAGRANGEan-EULERian formulation. Here, in general, the motion and related quantities are neither referred to the material configuration, as in the LAGRANGEan formulation, nor to the spatial configuration, as in the EULERian formulation. They are described with respect to an arbitrary domain in terms of spatial and material mappings, see Section 5.5.2. This concerns the whole problem formulation and already the fundamental principles, which can be read, for example, in the contributions of BELYTSCHKO [9], LINDER [89], HUERTA and CASADEI [60], and WALL [134]. An ALE formulation also contains governing equations for the parametrizations of the domains. The solution towards the unknown material and spatial displacements can occur simultaneously, or the probably complex problem is split into a several less complex problems with what the solution strategies are denoted as operator split- or fractional-step methods, see WALL [134]. The sep-

aration may result into a pure LAGRANGEan step and a pure EULERian step. This is applied here.

In literature, ALE formulations resolved with a fractional-step strategy are frequently used in the context of finite strain plasticity. There, the LAGRANGEan description may lead to heavily distorted meshes which have to be repaired from time to time. This is achieved with subsequent EULERian steps, where the deformation is held constant and finite element nodes are rearranged according to certain mesh smoothing algorithms. Examples in this field are the contributions of ARMERO and LOVE [5], HUERTA and CASADEI [60], LINDER [89], and RODRÍGUEZ-FERRAN et al. [121, 122].

Treating wear in numerical simulations, the amount of additional wear within a time step is usually very small. Therefore, it is neglected within this work for the solution of a current time step with the application of an explicit time integration scheme. As the governing equation in a fully coupled ALE description would also be from additional wear within a time step, such a formulation would be unnecessary anyway. Hence, the fractional-step method is the appropriate approach. Therefore, in the following, solely the essential components for the application of a LAGRANGEan step followed by an EULERian step to consider wear are presented.

5.5.2 ALE kinematics

The basic equations of the frictional contact problem in Chapter 2 are expressed within the LAGRANGEan framework. The underlying deformation mapping from the initial to the current configuration is denoted as $\boldsymbol{\varphi}_t(\mathbf{X}, t)$. More freedom is obtained by using an ALE description. Here, this physical deformation mapping $\boldsymbol{\varphi}_t(\mathbf{X}, t)$ can be reparametrized in terms of two independent mappings. This brings the possibility of a mesh motion completely free from the actual physical motion.

Related to the description in ARMERO and LOVE [5], the ALE kinematics are presented in this section. At first, it is kept general without considering wear leading to changing surfaces and domains. This is then treated within a second step.

Material and spatial maps

Considered more closely is the physical motion $\boldsymbol{\varphi}_t(\mathbf{X}, t)$ between the initial or material configuration $\Omega_{0,t}$ and the current or spatial configuration $\Omega_{t,t}$. The objective is to describe it with respect to a fixed reference domain $\Omega \subset \mathbb{R}^3$ in time and the mappings

$$\boldsymbol{\phi}_t : \Omega \to \Omega_{0,t} \quad \text{and} \quad \boldsymbol{\psi}_t : \Omega \to \Omega_{t,t} \tag{5.20}$$

relating both the material and spatial configuration to the reference domain as visualized in Figure 5.10. From this, $\boldsymbol{\phi}_t(\boldsymbol{\mathcal{X}}, t)$ is denoted as material motion and $\boldsymbol{\psi}_t(\boldsymbol{\mathcal{X}}, t)$ as spatial motion. It should be noted that, by the introduction of the material mapping $\boldsymbol{\phi}_t$, the parametrization of the material configuration becomes time dependent. By construction, the physical motion at a fixed time t now can be expressed as

$$\boldsymbol{\varphi}_t = \boldsymbol{\psi}_t \circ \boldsymbol{\phi}_t^{-1} \,. \tag{5.21}$$

The mappings $\boldsymbol{\phi}_t$ and $\boldsymbol{\psi}_t$ represent the parametrization of the material and the spatial configuration. However, main interest is still on the physical motion $\boldsymbol{\varphi}_t$. By the introduction of two

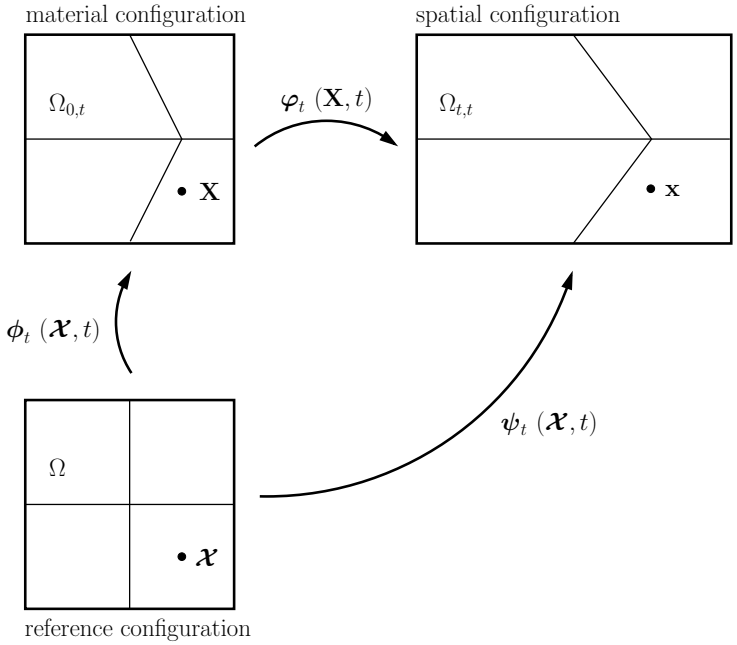

Figure 5.10: The physical motion $\boldsymbol{\varphi}_t\,(\mathbf{X},t)$ is decomposed into the material motion $\boldsymbol{\phi}_t\,(\boldsymbol{\mathcal{X}},t)$ and the spatial motion $\boldsymbol{\psi}_t\,(\boldsymbol{\mathcal{X}},t)$ as $\boldsymbol{\varphi}_t = \boldsymbol{\psi}_t \circ \boldsymbol{\phi}_t^{-1}$. They are expressed with respect to the reference configuration Ω fixed in time and allow a parametrization of material and spatial configuration independent of the physical motion.

independent mappings (5.20) and the expression of $\boldsymbol{\varphi}_t$ as a linear combination of $\boldsymbol{\psi}_t$ and $\boldsymbol{\phi}_t^{-1}$ in (5.21), one of these mappings can be chosen arbitrarily. The other one, of course, has to be adapted consistently. Consequently, an ALE formulation allows to parametrize the material or spatial configuration completely independent of the physical motion. This might be a clear advantage in comparison with a pure LAGRANGEan formulation, where this possibility does not exist.

The above mappings are accompanied by the material and spatial displacement fields. They are defined as

$$\mathbf{u}_{\boldsymbol{\phi}}\,(\boldsymbol{\mathcal{X}},t) := \boldsymbol{\phi}_t\,(\boldsymbol{\mathcal{X}},t) - \boldsymbol{\mathcal{X}} \quad \text{and} \tag{5.22}$$

$$\mathbf{u}_{\boldsymbol{\psi}}\,(\boldsymbol{\mathcal{X}},t) := \boldsymbol{\psi}_t\,(\boldsymbol{\mathcal{X}},t) - \boldsymbol{\mathcal{X}}\ . \tag{5.23}$$

In addition to the well known deformation gradient $\mathbf{F}$ of the physical motion $\boldsymbol{\varphi}_t$ in (2.7), there are now those of the newly introduced material and spatial mappings, too. They are defined as

$$\mathbf{F}_{\boldsymbol{\phi}}\,(\boldsymbol{\mathcal{X}},t) := \frac{\partial \boldsymbol{\phi}_t}{\partial \boldsymbol{\mathcal{X}}} = \frac{\partial \mathbf{X}}{\partial \boldsymbol{\mathcal{X}}} = \mathrm{Grad}_{\boldsymbol{\mathcal{X}}}\,\mathbf{X} \quad \text{and} \tag{5.24}$$

$$\mathbf{F}_{\boldsymbol{\psi}}\,(\boldsymbol{\mathcal{X}},t) := \frac{\partial \boldsymbol{\psi}_t}{\partial \boldsymbol{\mathcal{X}}} = \frac{\partial \mathbf{x}}{\partial \boldsymbol{\mathcal{X}}} = \mathrm{Grad}_{\boldsymbol{\mathcal{X}}}\,\mathbf{x}\ , \tag{5.25}$$

where $\mathrm{Grad}_{\boldsymbol{\mathcal{X}}}$ being the gradient operator with respect to $\boldsymbol{\mathcal{X}}$. Equivalent to the connection of the involved mappings in (5.21), the physical deformation gradient $\mathbf{F}$ can be expressed as

$$\mathbf{F} = \mathbf{F}_{\boldsymbol{\psi}} \cdot \mathbf{F}_{\boldsymbol{\phi}}^{-1}. \tag{5.26}$$

The advection map

As discussed above, for a given deformation state $\boldsymbol{\varphi}_t$, the parametrization of the material $\boldsymbol{\phi}_t$ or the spatial configuration $\boldsymbol{\psi}_t$ can be changed arbitrarily. The respective counterpart has to be adapted consistently. The advection map considers this connection, it is presented in the following.

At a fixed time t, the physical motion $\boldsymbol{\varphi}_t$ is considered. It is described by the material and the spatial map, $\boldsymbol{\phi}_t$ and $\boldsymbol{\psi}_t$, as given in equation (5.21). The same physical motion can be expressed alternatively by a different set of material and spatial motion, for example $\tilde{\boldsymbol{\phi}}_t$ and $\tilde{\boldsymbol{\psi}}_t$. In the following, they are also denoted as "new" motions. It is stated as

$$\boldsymbol{\varphi}_t = \boldsymbol{\psi}_t \circ \boldsymbol{\phi}_t^{-1} = \tilde{\boldsymbol{\psi}}_t \circ \tilde{\boldsymbol{\phi}}_t^{\,-1} \,. \tag{5.27}$$

Considered is a general reference point $\boldsymbol{\mathcal{X}}$. At time t, it is connected with the material point $\mathbf{X}$ and its spatial position $\mathbf{x}$ as

$$\mathbf{X} = \boldsymbol{\phi}_t\left(\boldsymbol{\mathcal{X}}\right) \quad \text{and} \quad \mathbf{x} = \boldsymbol{\psi}_t\left(\boldsymbol{\mathcal{X}}\right) , \tag{5.28}$$

where $\mathbf{X}$ and $\mathbf{x}$ are connected via the physical deformation mapping

$$\mathbf{x} = \boldsymbol{\varphi}_t\left(\mathbf{X}\right) . \tag{5.29}$$

Now, the physical motion shall be reparametrized and expressed in terms of $\tilde{\boldsymbol{\phi}}_t$ and $\tilde{\boldsymbol{\psi}}_t$. The mappings of the reference point $\boldsymbol{\mathcal{X}}$ now read

$$\tilde{\mathbf{X}} = \tilde{\boldsymbol{\phi}}_t\left(\boldsymbol{\mathcal{X}}\right) \quad \text{and} \quad \tilde{\mathbf{x}} = \tilde{\boldsymbol{\psi}}_t\left(\boldsymbol{\mathcal{X}}\right) , \tag{5.30}$$

where $\tilde{\mathbf{X}} \neq \mathbf{X} \in \Omega_{0,t}$ is a different material point of the material domain and $\tilde{\mathbf{x}} \neq \mathbf{x} \in \Omega_{t,t}$ is a different spatial point in the spatial domain. Since the deformation remains constant, they are still related by

$$\tilde{\mathbf{x}} = \boldsymbol{\varphi}_t\left(\tilde{\mathbf{X}}\right) . \tag{5.31}$$

Let $\tilde{\boldsymbol{\mathcal{X}}} \in \Omega$ be the reference point such that

$$\boldsymbol{\phi}_t\left(\tilde{\boldsymbol{\mathcal{X}}}\right) = \tilde{\boldsymbol{\phi}}_t\left(\boldsymbol{\mathcal{X}}\right) = \tilde{\mathbf{X}} \tag{5.32}$$

and

$$\boldsymbol{\psi}_t\left(\tilde{\boldsymbol{\mathcal{X}}}\right) = \tilde{\boldsymbol{\psi}}_t\left(\boldsymbol{\mathcal{X}}\right) = \tilde{\mathbf{x}} \tag{5.33}$$

holds. As only unique mappings are considered here, the reference point $\tilde{\boldsymbol{\mathcal{X}}}$ is defined. It is supposed that, for a given deformation state, one of the two alternative mappings $\tilde{\boldsymbol{\phi}}_t$ or $\tilde{\boldsymbol{\psi}}_t$ is known. This allows the evaluation $\tilde{\boldsymbol{\mathcal{X}}}$ from either equation (5.32) or (5.33) and, with insertion into the remaining one, the determination of $\tilde{\boldsymbol{\phi}}_t$ or $\tilde{\boldsymbol{\psi}}_t$, respectively.

The above derivation contains the evaluation of the alternative reference point $\tilde{\boldsymbol{\mathcal{X}}}$ for a given reference point $\boldsymbol{\mathcal{X}}$. From literature, this relation is known as the advection map

$$\boldsymbol{\chi}_t : \Omega \to \Omega \tag{5.34}$$

defined by

$$\tilde{\boldsymbol{\mathcal{X}}} = \boldsymbol{\chi}_t\left(\boldsymbol{\mathcal{X}}, t\right) . \tag{5.35}$$

The evaluation of the advection map in the finite element discretized problem is stated in Section 5.5.4.

Consideration of wear

Within this work, the ALE kinematics above are used to model surface evolution due to wear. It is obtained by choosing a new spatial mapping $\tilde{\boldsymbol{\psi}}_t$ in order to take the material loss at the contact boundary into account. This results also in adapted material and spatial domains, which are denoted as $\tilde{\Omega}_{0,t} \subset \Omega_{0,t}$ and $\tilde{\Omega}_{t,t} \subset \Omega_{t,t}$, respectively. In order to determine the according material mapping $\tilde{\boldsymbol{\phi}}_t$ with the advection map from above, the physical deformation state of this remaining domain is assumed to be fixed. Accordingly, equation (5.27) is only valid for the remaining domain $\tilde{\Omega}_{0,t}$ as

$$\boldsymbol{\varphi}_t|_{\tilde{\Omega}_{0,t}} = \boldsymbol{\psi}_t \circ \boldsymbol{\phi}_t^{-1} = \tilde{\boldsymbol{\psi}}_t \circ \tilde{\boldsymbol{\phi}}_t^{\,-1} \,. \tag{5.36}$$

The evaluation of $\tilde{\boldsymbol{\mathcal{X}}}$ occurs from equation (5.33) and, with insertion into (5.32), one obtains the demanded alternative material mapping $\tilde{\boldsymbol{\phi}}_t$.

Material time derivatives

As shown, in ALE descriptions, material and spatial fields are expressed as functions of the ALE coordinates $\boldsymbol{\mathcal{X}}$ and time t. Accordingly, material or total time derivatives must be obtained by the chain rule. This is similar to equation (2.6), where the acceleration field of a motion in an EULERian description is derived. It leads to the typical convective terms. In case of the velocity, they represent the difference between the material and mesh velocities.

In this work however, only quasistatic problems are treated and the topic of material time derivatives in ALE descriptions is not considered further. It is referred to the contributions of BELYTSCHKO [9], LINDER [89], HUERTA and CASADEI [60], and WALL [134] instead.

5.5.3 Solution algorithm

The algorithm for the solution of the frictional contact problem treating wear with modeling contact surface evolution is presented in the following. As material is only removed from the slave contact surface within this study, the following equations are related to this side.

For the simulations carried out within this work, the reference configuration of the slave body $\Omega^{(1)}$ is equal to the material configuration $\Omega^{(1)}_{0,t=0}$ at $t = 0$. As the slave body is assumed to be undeformed at this stage, it is equal to the spatial configuration $\Omega_{t,t=0}$ at this point, too. This can also be expressed as

$$\boldsymbol{\mathcal{X}}^{(1)} = \mathbf{X}^{(1)} = \mathbf{x}^{(1)} \quad \text{for} \quad t = 0 \tag{5.37}$$

or

$$\mathbf{u}^{(1)}_{\boldsymbol{\phi}} = \mathbf{u}^{(1)}_{\boldsymbol{\psi}} = 0 \quad \text{for} \quad t = 0 \,. \tag{5.38}$$

Considered is a time interval stepping from t_{n-1} to t_n. It is assumed that the material displacement field $\mathbf{u}^{(1)}_{\boldsymbol{\phi}}\,(t_{n-1})$ and the spatial displacement field $\mathbf{u}^{(1)}_{\boldsymbol{\psi}}\,(t_{n-1})$ at t_{n-1} are known. The algorithm aims for the solution of $\mathbf{u}^{(1)}_{\boldsymbol{\phi}}\,(t_n)$ and $\mathbf{u}^{(1)}_{\boldsymbol{\psi}}\,(t_n)$ at t_n. It is presented in the following.

Algorithm 4

1. Solve the finite deformation frictional contact problem for $\mathbf{u}^{(1)}_{\boldsymbol{\psi}}\,(t_n)$ with holding the material displacements constant ($\mathbf{u}^{(1)}_{\boldsymbol{\phi}}\,(t_{n-1}) = \text{const.}$). This is tantamount to a LAGRANGEan step

as described in Chapter 4. Of course, the solution also contains the LAGRANGE multipliers $\boldsymbol{\lambda}(t_n)$.

2. Evaluate the additional wear height Δw within the time step according to equation (5.4) from the results obtained in 1.

3. Determine the new spatial displacements $\tilde{\mathbf{u}}_{\boldsymbol{\psi}}^{(1)}(t_n)$ according to the additional wear height evaluated in 2. The respective material displacements $\tilde{\mathbf{u}}_{\boldsymbol{\phi}}^{(1)}(t_n)$ are evaluated according to equations (5.32) and (5.33) for fixing the physical deformation. This is called the EULERian phase.

4. Replace the material and spatial displacement fields as

$$\mathbf{u}_{\boldsymbol{\phi}}^{(1)}(t_n) = \tilde{\mathbf{u}}_{\boldsymbol{\phi}}^{(1)}(t_n) \quad \text{and} \quad \mathbf{u}_{\boldsymbol{\psi}}^{(1)}(t_n) = \tilde{\mathbf{u}}_{\boldsymbol{\psi}}^{(1)}(t_n)\,, \tag{5.39}$$

set $t_{n-1} := t_n$ and continue with 1. for the next time step.

In general, the solution of an ALE described problem within a staggered scheme has clear advantages. With splitting the underlying equations into material and convective effects, they become less intricate and allow for the application of well known and robust algorithms. Here, this concerns especially the usage of the LAGRANGEan formalism for the solution of the physical problem with almost no modification. It also contains a not increasing system size due to the serial determination of material and spatial displacements.

5.5.4 Finite element implementation

As the above equations are only discretized temporally so far, this section now treats their spatial discretizations.

Geometry and displacement interpolation

The geometry approximation of the reference domain $\Omega^{(1)h}$ within the ALE formulation is realized as it is done for the reference domain $\Omega_0^{(1)h}$ within the LAGRANGE formulation in Chapter 3.4.1. The interpolated form is denoted as $\boldsymbol{\mathcal{X}}^{(1)h}$, the approach is developed for linearly interpolated 4-node quadrilateral elements in the 2D case. Following an isoparametric concept, the material and spatial displacements are approximated in the same way and lead to their discrete counterparts $\mathbf{u}_{\boldsymbol{\phi}}^{(1)h}$ and $\mathbf{u}_{\boldsymbol{\psi}}^{(1)h}$. Consequently, the respective discrete domains $\Omega_{0,t}^{(1)h}$ and $\Omega_{t,t}^{(1)h}$ are parametrized as

$$\mathbf{X}^{(1)h} = \boldsymbol{\mathcal{X}}^{(1)h} + \mathbf{u}_{\boldsymbol{\phi}}^{(1)h} \quad \text{and} \quad \mathbf{x}^{(1)h} = \boldsymbol{\mathcal{X}}^{(1)h} + \mathbf{u}_{\boldsymbol{\psi}}^{(1)h}\,. \tag{5.40}$$

New spatial displacements due to wear

This section treats the evaluation of the new spatial displacement field $\tilde{\mathbf{u}}_{\boldsymbol{\psi}}^{(1)h}(t_n)$. It corresponds to the first part of the EULERian phase (Algorithm 4, 3.) of the discrete setting.

The weighted wear increment $\Delta\tilde{w}_j$ of a slave node $j \in \mathcal{S}$ is evaluated from equation (5.11) similar to the internal state variable approach. However, this is an integral quantity rather than

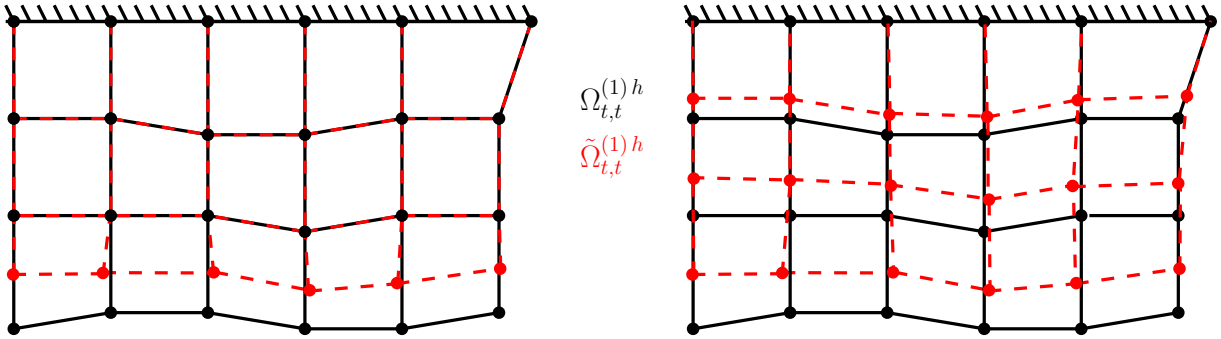

Figure 5.11: Relocation of nodes in the spatial configuration: Only for nodes of the slave contact surface (left) or, in order to be not limited to one element row, for nodes of the slave contact surface plus remaining nodes within the domain (right).

a real physical measure. Consequently, it cannot be used directly for modeling the material loss considered here without modifications. Nevertheless, it is the basis for the derivation of the non-weighted discrete nodal value Δw_j. Of course, Δw_j could be obtained form (5.4) evaluated at node j. From this, it would be a real physical value, but without considering the spatial distribution of solution variables between nodes. It rather would resemble a node-to-segment approach than an integral mortar treatment of interface constraints. It is therefore not applied within this work. Accordingly, Δw_j is obtained from $\Delta \tilde{w}_j$ by removing the weighting as

$$\Delta w_j = \frac{\Delta \tilde{w}_j}{D_{jj}} \,. \tag{5.41}$$

The new spatial postions $\tilde{\mathbf{x}}_j^{(1)}$ of slave nodes $j \in \mathcal{S}$ are then obtained from the nodal wear increment Δw_j and the averaged outward unit normal $\mathbf{n}_j$ from equation (3.51) as

$$\tilde{\mathbf{x}}_j^{(1)} = \mathbf{x}_j^{(1)} - \Delta w_j \, \mathbf{n}_j \,. \tag{5.42}$$

The relocation of only slave contact nodes is visualized in Figure 5.11 on the left hand side. It is limited to the removal of one element row with the risk of degenerated elements with ongoing amount of wear.

In order to avoid this, not only slave contact nodes are repositioned, but also further ones within the domain. This is given schematically on the right hand side of Figure 5.11. For the evaluation of the new locations of these further nodes, there exist various possibilities in literature. Among them, there is the LAPLACEan smoothing as described in LÖHNER and YANG [90] or pseudo-structure approaches using elastic springs, see BATINA [6]. Within this work, a continuous pseudo-structure approach as given in JOHNSON and TEZDUYAR [67] is applied. Basis is the solution of a linear elastic problem with only DIRICHLET conditions. At the contact interface, the prescribed displacements are the displacements determined from wear. The remaining boundaries are adapted to the structural problem itself.

New material displacements, advection mapping

In this section, the construction of the advection map within the finite element discretized problem is considered. It needs to provide the values for the quantities of interest after reorganizing

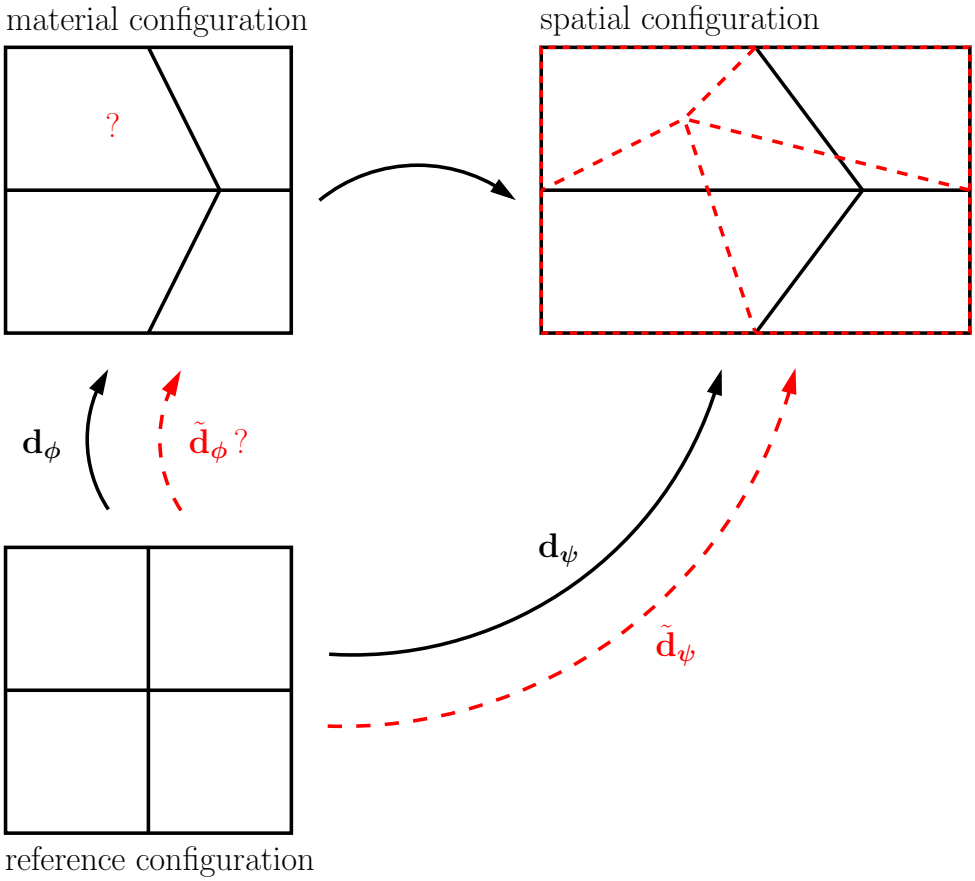

Figure 5.12: Nodal material and spatial displacements $\mathbf{d}_\phi$ and $\mathbf{d}_\psi$ represent a physical deformation state. Given are the new spatial displacements $\tilde{\mathbf{d}}_\psi$, wanted are the corresponding material displacements $\tilde{\mathbf{d}}_\phi$ holding this state.

the mesh in the spatial configuration due to wear. These are the nodal material displacements $\tilde{\mathbf{d}}_\phi^{(1)}$ as counterpart to the new nodal spatial displacements $\tilde{\mathbf{d}}_\psi^{(1)}$. Further quantities are discussed at the end of this section. The construction of the advection map is obtained by tracking of material particles, it corresponds to the second part of the EULERian phase (Algorithm 4, 3.) in the discrete setting.

Starting point for the derivation is a deformation state represented by a known discrete material and spatial displacement field. Both are expressed in terms of the respective nodal displacement vectors $\mathbf{d}_\phi^{(1)}$ and $\mathbf{d}_\psi^{(1)}$ and the interpolation presented above. At this stage, new nodal spatial displacements $\tilde{\mathbf{d}}_\psi^{(1)}$ are given due to the subtraction of wear considered in this work. However, in general, any other reason could be thought of. Figure 5.12 illustrates such a general situation. There and for the further derivation, the superscript (1) for the slave domain is omitted. Wanted are the corresponding material displacements $\tilde{\mathbf{d}}_\phi$ keeping the given physical deformation state.

In the following, a single node j is considered. Its new spatial displacement vector after repositioning is denoted as $\tilde{\mathbf{d}}_{\psi j}$. The determination of $\tilde{\boldsymbol{\chi}}_j$ according to equation (5.33) requires firstly the identification of the "old" finite element in which the considered node will be after reposi-

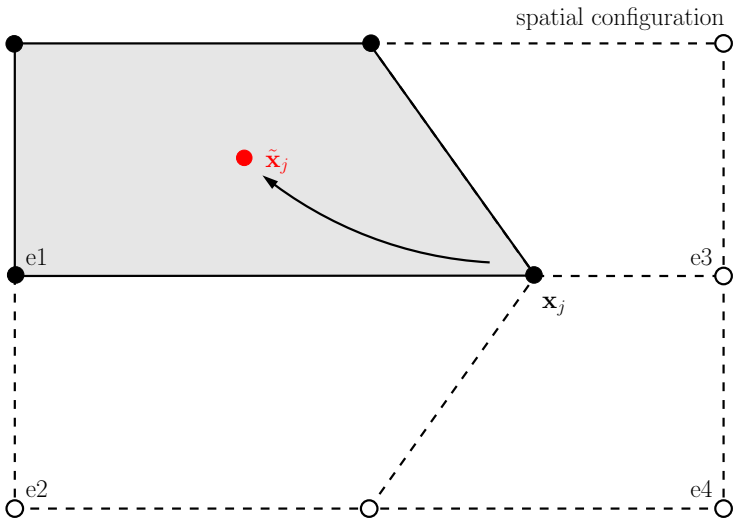

Figure 5.13: Repositioning of node j in the spatial configuration. The determination of the advection map requires the identification of the element where the node will be and its exact postion in element coordinates.

tioning. In the example in Figure 5.12, this is the element on the top left for the node in the middle. Secondly, the element coordinates $\tilde{\boldsymbol{\xi}}_j$ within this element associated with $\tilde{\boldsymbol{\mathcal{X}}}_j$ have to be identified. The problem is extracted in Figure 5.13. The solution within this work combines both steps. It is assumed that mesh changes due to wear are small and the wanted element is adjacent to the node. Based on this, the element coordinates $\tilde{\boldsymbol{\xi}}_j$ of $\tilde{\boldsymbol{\mathcal{X}}}_j$ are evaluated for one adjacent element after another. This is performed until the obtained solution is within the parameter space of the regarded element, i.e. $\tilde{\xi}_j \in [-1..1]$ and $\tilde{\eta}_j \in [-1..1]$.

Equation (5.33) is nonlinear in terms of $\tilde{\boldsymbol{\xi}}$. Therefore, it is written in residual form in the already discrete setting as

$$\mathbf{r}\left(\tilde{\boldsymbol{\xi}}_j\right) := \sum_{i=1}^{n_{ele}} N_i\left(\tilde{\boldsymbol{\xi}}_j\right) \mathbf{x}_i - \tilde{\mathbf{x}}_j = \mathbf{0} \tag{5.43}$$

and solved with a NEWTON scheme towards $\tilde{\boldsymbol{\xi}}_j$. The scalar n_{ele} is the number of nodes of the respective element.

From this, the corresponding material displacement field $\tilde{\mathbf{u}}_{\boldsymbol{\phi}}$ can be evaluated from equation (5.32). In the discrete setting and rewritten in terms of the desired material displacement vector, it reads

$$\tilde{\mathbf{d}}_{\boldsymbol{\phi}j} = \mathbf{N}\left(\tilde{\boldsymbol{\xi}}_j\right) \cdot \left(\mathbf{X}^{ele} - \boldsymbol{\mathcal{X}}^{ele}\right) \ , \tag{5.44}$$

where $\mathbf{N}\left(\tilde{\boldsymbol{\xi}}_j\right)$ is the matrix of shape functions evaluated at $\tilde{\boldsymbol{\xi}}_j$ and the vectors $\boldsymbol{\mathcal{X}}^{ele}$ and $\mathbf{X}^{ele}$ contain the reference and material positions of the nodes of the considered element.

As solely quasistatic problems are considered within this work, the evaluation of velocities and accelerations of the new mesh can be omitted. However, as treating frictional contact problems, the mortar matrices have to be considered. This is because, for the determination of the current slip increment, their values of the former time step are used, see (3.84). They could have changed through modifying the mesh in the EULERian phase. However, since relocation of contact surface

nodes is small and towards the outward unit normal vector, these changes are insignificant and can be neglected. However, this could easily be overcome with an additional mortar projection after the EULERian phase.

Implementation - extended element formulation

Concerning the implementation of structural finite elements, modifications are necessary stepping from a LAGRANGEan formulation to the described ALE formulation resolved with a fractional-step strategy as described above. However, changes are relatively small and the total LAGRANGE framework can be applied to a great extent.

Additional to the spatial displacements, also the material displacements have to be included. And additional to the spatial deformation gradient in (5.25), the material one has to be evaluated according to (5.24). From those, the composed deformation gradient representing the physical motion is obtained from equation (5.26). Strains as well as corresponding internal forces are evaluated from this measure. Depending on the code structure, it may be sufficient to only replace the deformation gradient in the total LAGRANGE setting with the composed one in (5.26). Using the fractional-step strategy, material displacements are held constant for the LAGRANGEan step and consequently do not require linearizations with respect to them.

Within this work, contact surface evolution with an ALE strategy is implemented in BACI for 2D nonlinear bilinear wall elements. The extension to higher-order interpolation and 3D elements would be straightforward.

5.6 Examples

Within this section, three numerical examples are given to clarify the presented approach for contact surface evolution and demonstrate its accuracy. This is shown gradually starting from an example without contact going to a fully nonlinear frictional contact simulation with alternating stick-slip conditions. All simulations are carried out in BACI and are subjected, if not specified otherwise, to the assumptions made in Section 4.6.

5.6.1 Arbitrary mesh movement on rectangle

With this first example, the possibility of arbitrary mesh movement independent of the deformation is demonstrated. For this, the square in Figure 5.14 on the left is considered. It is modelled with a compressible Neo-HOOKEan material law ($E = 10000$, $\nu = 0.0$) and plane strain assumption. As load, the right boundary of the square is subjected to a prescribed horizontal displacement $d = 0.5$. The square is originally discretized as given on the right of Figure 5.14. It is reference-, material-, and spatial domain at $t = 0$.

Applying the entire load within one quasistatic time step, the spatial configuration visualized in Figure 5.15 on the top left is obtained. It shows a linearly increasing deformation in x-direction leading to a constant stress state within the whole domain. Now, to a general reason, the spatial discretization is changed arbitrarily. This is realized with moving the node in the middle by $d_H = 0.375$ and $d_V = 0$ in a first step and further to $d_H = -0.25$ and $d_V = 0.25$ in a second step. This leads to the configurations on the top right and bottom left. It can be seen clearly

that the deformation state and the corresponding stress distribution in the entire domain does not change. This is also valid for moving the middle node back to the initial position ($d_H = 0.0$, $d_V = 0.0$) and reposition the middle node in the bottom row by $d_V = 0.25$. This is close to the wear problem, where boundary nodes are relocated. The corresponding result is given on the bottom right of Figure 5.15.

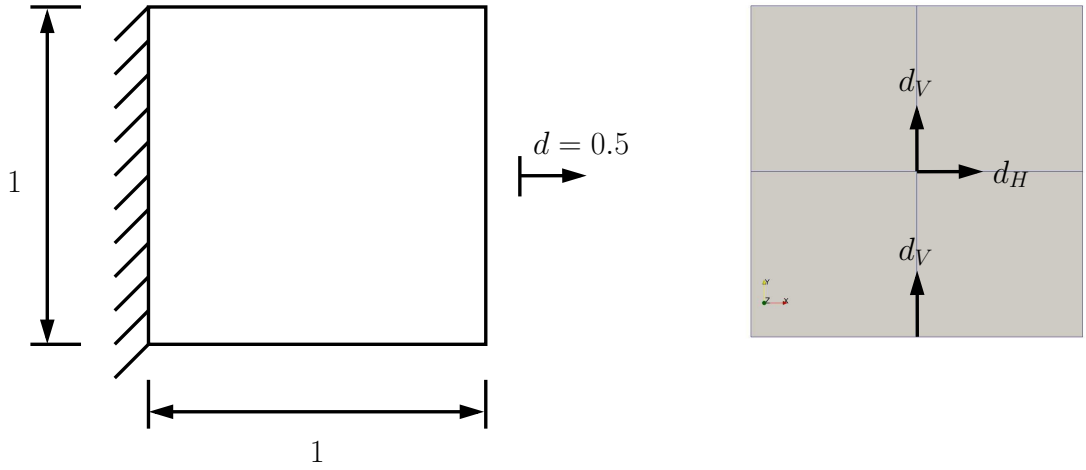

Figure 5.14: Arbitrary mesh movement on rectangle example, problem setup and finite element discretization.

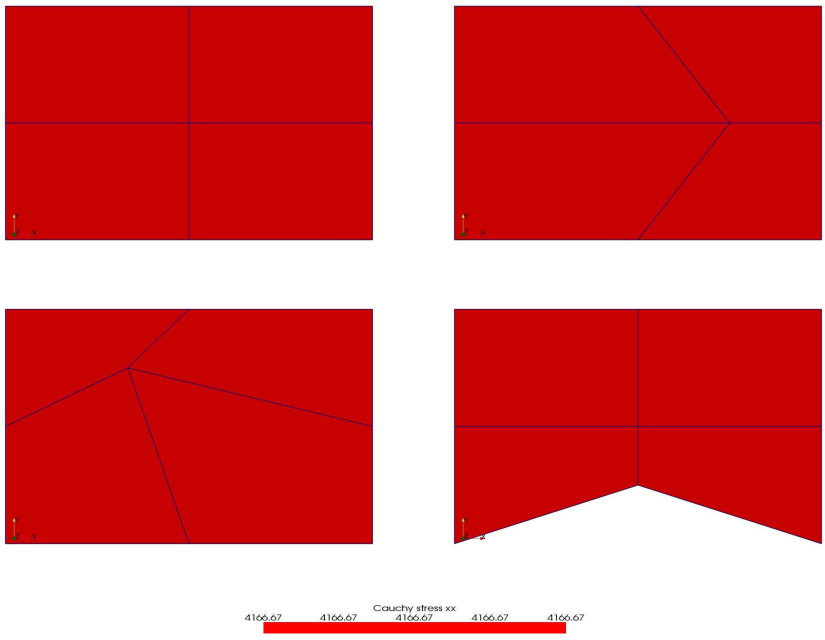

Figure 5.15: Arbitrary mesh movement for given physical deformation.

In this example, the repositioning in the spatial configuration was carried out only for single nodes. Their new locations did not influence the positions of the adjacent or other nodes. This corresponds the approach visualized on the left of Figure 5.11.

5.6.2 Surface evolution

The second example demonstrates the potential wider influence of relocation of nodes as schematically sketched on the right of Figure 5.11. Again, a simple example is chosen to clarify the approach. The square on the left of Figure 5.16 is fixed at the upper end and subjected to a distributed vertical load $p = 0.3$ at the bottom. St. VENANT-KIRCHHOFF's material law is applied ($E = 10$, $\nu = 0.0$) and the thickness of the 2D model is 1. The discretization is shown on the right, as before, it represents the congruence of reference-, material-, and spatial domain at $t = 0$.

The loading is carried out with one quasistatic time step. This leads to the deformed configuration shown on the left of Figure 5.17. Occurring displacements are linear in y-direction and the resultant stress field is constant. Starting from this deformed state, the three nodes on the bottom of the square are relocated within two steps. The respective prescribed displacements in vertical direction are $d_V = 0.07$ and $d_V = 0.21$ for the first and second step, respectively. In contrast to the example above, further nodes are relocated. As explained, their new positions are determined solving a linear elastic problem with respective boundary conditions. The results of these two steps are plotted in the middle and right of Figure 5.17. There, the spatial configurations are reduced by a prescribed movement of the lower boundary. It clearly can be seen that also the nodes of the middle row are relocated in order to keep optimal element sizes within the body. Of course, as requested, the stress in the remaining domain stays constant.

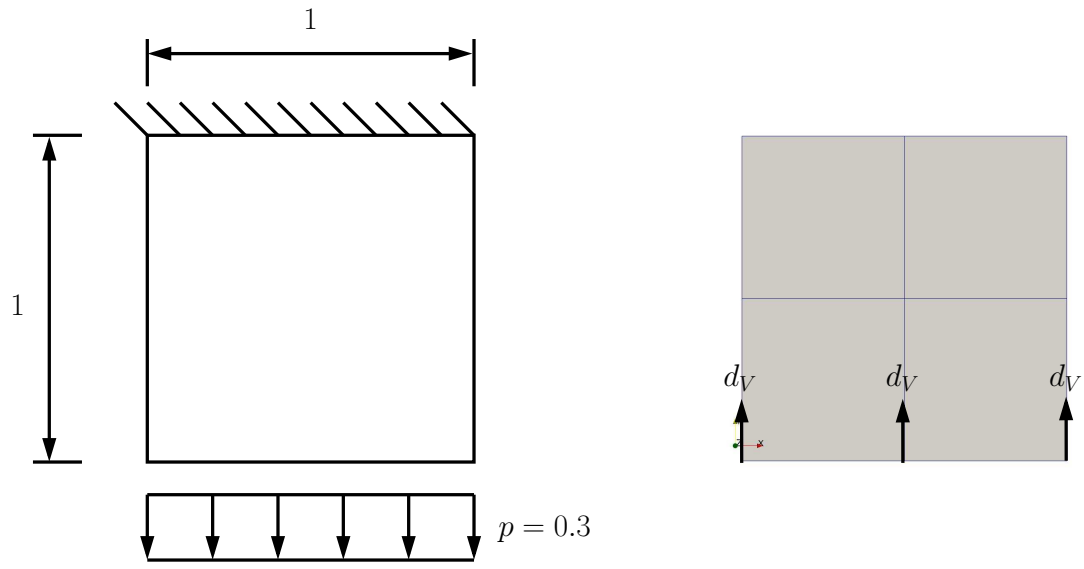

Figure 5.16: Surface evolution example, problem setup and finite element discretization.

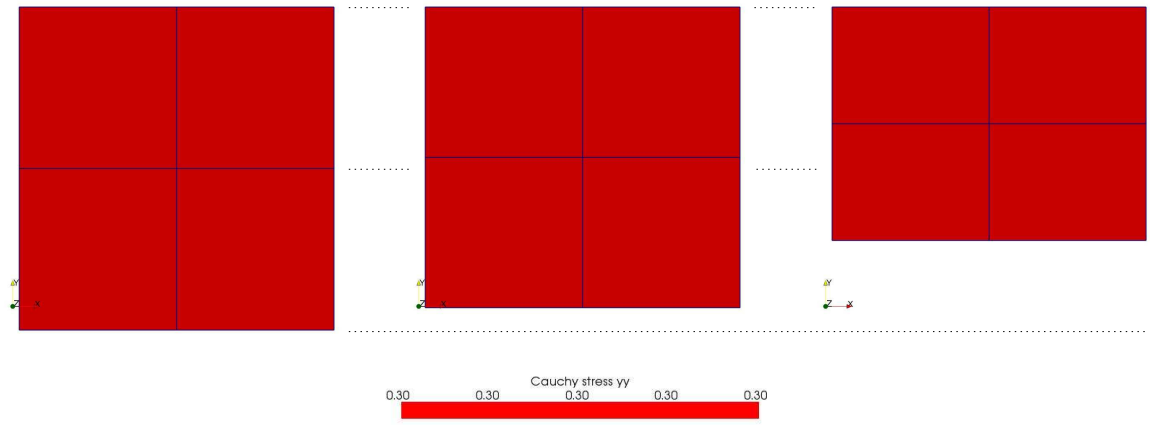

Figure 5.17: Relocation of boundary nodes plus further nodes within the domain.

5.6.3 Oscillating block on cylinder

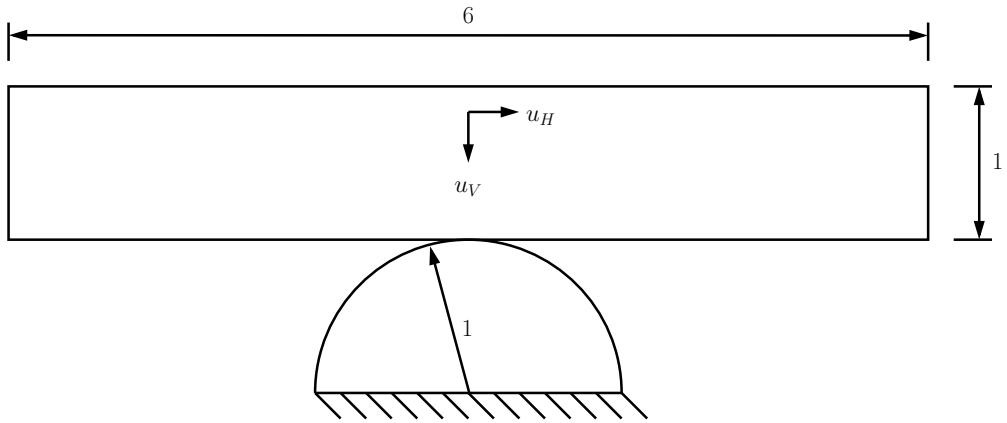

Figure 5.18: Oscillating block on cylinder contact problem with wear.

The third example finally presents a frictional contact simulation with treating a significant amount of wear. The setup of the 2D problem is presented in Figure 5.18. The half of a cylinder is fixed at its lower end and is assumed to be rigid. The block $(E = 100, \nu = 0.3)$ is subjected to DIRICHLET conditions u_H and u_V at its upper end: For $0 \leq t \leq 1$, the block is pressed onto the cylinder by the prescribed vertical displacement $u_V = 0.3\,t$. After that, for $1 \leq t \leq 51$, this value is kept constant and sinusoidal horizontal displacements u_H are applied. The amplitude is determined to 1.0, one phase of this motion requires 10.0 time units. In sum, five runs are performed. After that, for $51 \leq t \leq 53$, the block is removed from the cylinder up to a value of $u_{V\text{end}} = -0.3$. Between the two bodies, frictional contact with $\mu = 0.1$ takes place. Material is supposed to be removed from the slave contact surface of the block, the wear coefficient of the applied ARCHARD's law of wear is assumed to be $k_w = 0.001$. The discretization is shown in Figure 5.19, the simulation is run quasistatically with 530 pseudo-time increments of $\Delta t = 0.1$.

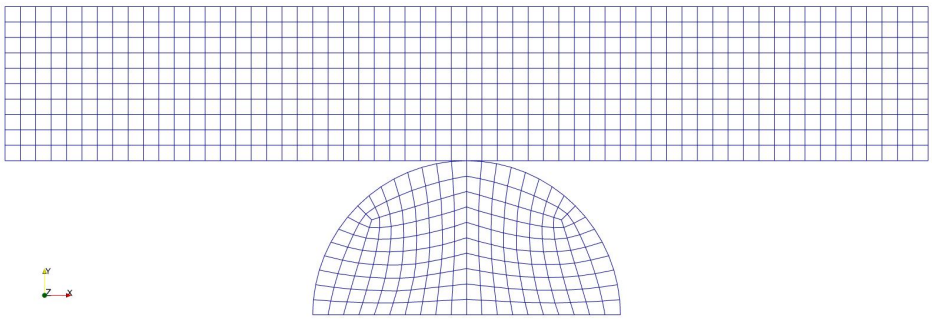

Figure 5.19: Discretization of oscillating block on cylinder contact problem with wear.

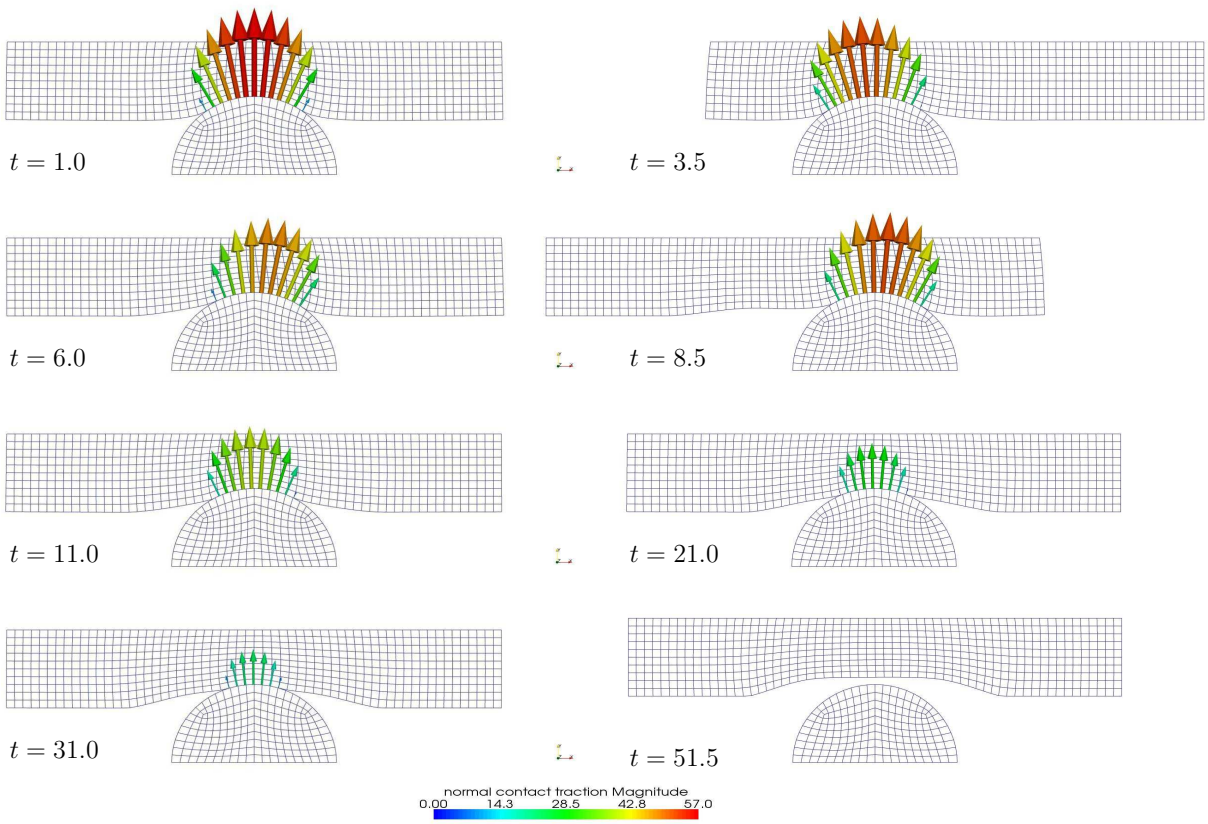

Figure 5.20: Deformed configurations for the oscillating block on cylinder example. After intrusion $(t = 1.0)$, during horizontal oscillation of block $(t = 1.0 - t = 31.0)$ and after removing the block from cylinder $(t = 51.5)$. The arrows represent the normal contact tractions.

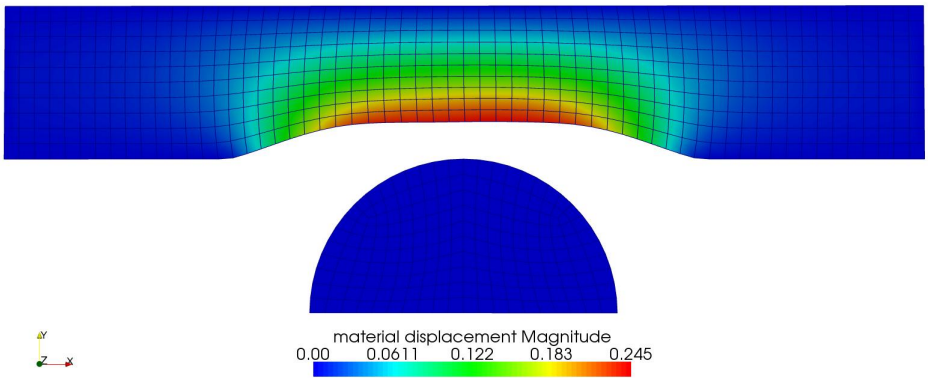

Figure 5.21: Changed material configuration after removing block from cylinder. Relocation of nodes within the whole slave domain due to new nodal positions at the contact interface from wear.

As result, the deformed configurations at different stages are presented in Figure 5.20. There, also the normal contact tractions are visualized. It can be clearly seen that, with ongoing time, material is removed and consequently, the normal contact tractions decrease due to the prescribed constant vertical displacements u_V. When the block is removed in the last subfigure, the remaining body is stress free and worn material can be identified easily. Having a closer look at this stage in Figure 5.21, it can be seen that approximately the height of two element rows has been worn away. However, because of relocating the mesh within the whole body due to new nodal positions at the contact interface, the proposed approach masters this challenge without any problems.

6 Fully coupled thermomechanical contact problem

This chapter extends the finite deformation frictional contact problem towards thermomechanical contact. This implies the addition of a thermal field to the purely mechanical problem treated so far. With that, a fully coupled multiphysics problem is obtained. Coupling effects resulting from contact are heat conduction over contacting surfaces or, very illustrative, production of heat due to frictional dissipation.

Section 6.1 contains the problem formulation within the continuous setting. Focus is especially on the interface equations. Subsequently, the weak form and finite element discretization are treated in Sections 6.2 and 6.3 and the problem is solved with a partitioned approach in Section 6.4. An outlook to monolithic solution schemes is given in Section 6.5 before numerical examples demonstrate the accuracy and efficiency of the proposed methods.

6.1 Problem formulation

The governing equations of the fully coupled thermomechanical contact problem mainly consist of four parts: The balance of linear momentum, the balance of energy and the entropy inequality, the mechanical contact constraints, and the laws of thermodynamics at the contact interface. The fundamental equations in this list are already known from Section 2.1, where basic continuum mechanics for solids have been presented. As the purely mechanical problem has extensively been considered in Chapters 2 - 4, the focus of the further derivation is mainly put on the additional thermal and thermal-structure coupling terms.

Starting point is the frictional contact problem presented in Section 2.2. In addition to the displacements $\mathbf{u}^{(i)}$ of each body i, $i = 1, 2$, also the scalar temperature fields $\theta^{(i)}$, $i = 1, 2$, serve as primary unknowns. The boundaries $\delta\Omega_0^{(i)}$ now include the boundaries $\Gamma_\theta^{(i)}$ and $\Gamma_q^{(i)}$, where temperature (DIRICHLET) and heat flux (NEUMANN) conditions are applied. Their counterparts in the spatial configuration are denoted as $\gamma_\theta^{(i)}$ and $\gamma_q^{(i)}$. The sets $\Gamma_\theta^{(i)}$ and $\Gamma_q^{(i)}$ are allowed to overlap with boundaries carrying structural boundary conditions, but are assumed to not overlap with each other or with the contact boundary $\Gamma_c^{(i)}$. This reads

$$\begin{aligned} &\partial\Omega_0^{(i)} = \Gamma_\theta^{(i)} \cup \Gamma_q^{(i)} \cup \Gamma_c^{(i)} \,, \\ &\Gamma_\theta^{(i)} \cap \Gamma_q^{(i)} = \Gamma_\theta^{(i)} \cap \Gamma_c^{(i)} = \Gamma_q^{(i)} \cap \Gamma_c^{(i)} = \emptyset \end{aligned} \tag{6.1}$$

in addition to (2.44).

Displacement and temperature fields have to be determined with respect to the above mentioned four sets of equations, which are presented in the following. This leads to the boundary value problem of the fully coupled thermomechanical contact problem.

6.1.1 Balance of linear momentum

The local equations considering the balance of linear momentum are equal to those of the purely mechanical problem. These are equations (2.70) - (2.72) representing the local linear momentum balance within the bodies, the NEUMANN boundary conditions, and the linear momentum balance at the contact interface.

6.1.2 Energy balance, entropy inequality

The basic principles of local energy balance and entropy inequality in CLAUSIUS-PLANCK form are stated in (2.33) and (2.36). According to the derivation in SIMO et al. [124], mathematical reformulation leads to the temperature evolution equation within a body i as

$$c^{(i)}\dot{\theta}^{(i)} = \left[\mathcal{D}_{int}^{(i)} - \mathcal{H}^{(i)}\right] - \operatorname{Div}\mathbf{Q}^{(i)} + \rho_0\hat{r}^{(i)} \quad \text{in } \Omega_0^{(i)} \,, \tag{6.2}$$

$$\mathbf{Q}^{(i)} = -k_\theta^{(i)} \operatorname{Grad}\theta^{(i)} \,, \quad i = 1, 2. \tag{6.3}$$

Here, in each of the bodies, $c^{(i)}$ denotes the heat capacity, $\mathcal{D}_{int}^{(i)}$ the mechanical dissipation, and $\mathcal{H}^{(i)}$ the heating from the JOULE effect. FOURIER's law of heat conduction (6.3) relates the heat flux $\mathbf{Q}^{(i)}$ to the temperature gradient via the thermal conductivity $k_\theta^{(i)}$. Since the focus of this work is on contact, a detailled derivation of equations (6.2) and (6.3) is omitted. The reader is referred to the contribution of SIMO et al. [124] instead. In the following, equation (6.2) is also denoted as energy balance equation for the ease of use.

Further balance equations are those at the NEUMANN and the contact boundary as

$$\mathbf{Q}^{(i)}\,\mathbf{N}^{(i)} = \hat{q}_0^{(i)} \quad \text{on } \Gamma_q^{(i)} \,, \tag{6.4}$$

$$\mathbf{Q}^{(i)}\,\mathbf{N}^{(i)} = q_{c,0}^{(i)} \quad \text{on } \Gamma_c^{(i)} \,, \quad i = 1, 2 \,, \tag{6.5}$$

where $\hat{q}_0^{(i)}$ represents a prescribed heat flux and $q_{c,0}^{(i)}$ is the heat flux at the contact boundary. The DIRICHLET condition reads

$$\theta^{(i)} = \hat{\theta}^{(i)} \quad \text{on } \Gamma_\theta^{(i)} \,, \quad i = 1, 2 \,. \tag{6.6}$$

6.1.3 Mechanical contact constraints

In some cases, there exist dependencies of the contact conditions on the temperature at the contact interface. An example for this would be a temperature dependent friction coefficient. In this work however, such effects are neglected. Consequently, the applied mechanical contact conditions in the thermomechanical contact setting are identical to those of Chapter 2, i.e. (2.59) - (2.61) and (2.63) - (2.66).

6.1.4 Laws of thermodynamics at the contact interface

From the first law of thermodynamics, the local form of the energy balance equation for the contact interface is obtained as

$$\dot{e}_c = q_c^{(1)} + q_c^{(2)} + \mathbf{t}_\tau \cdot \mathbf{v}_{\tau,rel} \quad \text{on } \gamma_c^{(1)} \,, \tag{6.7}$$

where e_c is the surface density of the internal energy on the contact surface. The spatial heat flux $q_c^{(i)}$ out of the contact surface of body i is evaluated similar to (6.5) as

$$q_c^{(i)} = \mathbf{q}^{(i)} \cdot \mathbf{n}^{(i)} \ , \quad i = 1, 2 \ . \tag{6.8}$$

For the derivation of (6.7), the reader is referred to LAURSEN [83] or OANCEA and LAURSEN [101]. It has to be pointed out that, for using the outward unit normal vector $\mathbf{n}^{(1)}$ on the slave side for the determination of $q_c^{(2)}$, this term enters equation (6.7) with the minus sign as in OANCEA and LAURSEN [101]. In words, the interface law (6.7) postulates that the sum of the heat flux into the slave body, the heat flux into the master body, which are both negative for the above definition (6.8), and the heat supply from friction per unit time is equal to the change of stored energy at the interface.

Besides the first law of thermodynamics above, also the second one has to be considered. In combination with the formulation of interface free energy and dissipation functions in LAURSEN [83] or OANCEA and LAURSEN [101], dependencies of the heat fluxes on the temperatures at the contact interface arise. They read

$$q_c^{(i)} = \alpha_c^{(i)} \left(p_n\right) \left(\theta^{(i)} - \theta_c\right) \ , \quad i = 1, 2 \ , \tag{6.9}$$

where $\theta^{(i)}$ is the temperature of body i as the contact interface is approached and θ_c is the contact interface temperature. The scalar $\alpha_c^{(i)}(p_n)$ is the contact heat transfer parameter of the contact surface at body i. It depends on the contact normal pressure p_n and is evaluated according to a constant or linear model as

$$\alpha_c^{(i)} = \begin{cases} 0 & \text{for } \ p_n = 0 \quad \text{(no contact)} \\ \bar{\alpha}_c^{(i)} & \text{for } \ p_n < 0 \quad \text{(contact)} \end{cases} \tag{6.10}$$

and

$$\alpha_c^{(i)} = \begin{cases} 0 & \text{for } \ p_n = 0 \quad \text{(no contact)} \\ -\bar{\alpha}_c^{(i)} p_n & \text{for } \ p_n < 0 \quad \text{(contact)} \end{cases} \ , \tag{6.11}$$

where $\bar{\alpha}_c^{(i)}$ is the original heat transfer parameter. Both equations guarantee that no heat flux appears between the two bodies in the case of no contact. For contact, there is, in (6.10) a constant and, in (6.11), a linear dependency on the normal contact pressure. The latter models the approach of two rough surfaces in contact, see WRIGGERS [144]. From the micromechanical point of view, with growing contact pressure, more and larger contact areas are produced. These so-called spots then allow a more easy conductance of heat. Here, both models are applied.

Within the work at hand, the heat capacity of the interface itself and, consequently, $\dot{e}_c$ in (6.7) is going to be neglected. In this particular case, the contact interface temperature θ_c can be eliminated algebraically and the surface heat fluxes (6.9) are expressed as

$$q_c^{(1)} = \beta_c \left(\theta^{(1)} - \theta^{(2)}\right) - \delta_c \left(\mathbf{t}_\tau \cdot \mathbf{v}_{\tau,rel}\right) \quad \text{and} \tag{6.12}$$

$$q_c^{(2)} = -\beta_c \left(\theta^{(1)} - \theta^{(2)}\right) - (1 - \delta_c) \left(\mathbf{t}_\tau \cdot \mathbf{v}_{\tau,rel}\right) \ . \tag{6.13}$$

Here, the parameters β_c and δ_c are evaluated as

$$\beta_c = \frac{\alpha_c^{(1)} \alpha_c^{(2)}}{\alpha_c^{(1)} + \alpha_c^{(2)}} \quad \text{and} \quad \delta_c = \frac{\alpha_c^{(1)}}{\alpha_c^{(1)} + \alpha_c^{(2)}} \ . \tag{6.14}$$

And, directly from (6.7), one obtains

$$q_c^{(2)} = -q_c^{(1)} - \mathbf{t}_\tau \cdot \mathbf{v}_{\tau,rel} \ . \tag{6.15}$$

6.1.5 Boundary value problem of thermomechanical contact

The boundary value problem of the finite deformation thermomechanical contact problem is summarized from Sections 6.1.1 - 6.1.4. As already for the purely mechanical setting in Section 2.3, the derivation is presented for quasistatic analysis neglecting terms containing the time derivation of primary variables. Furthermore, also dissipation within the bodies is not considered further.

The problem is solved for the displacement fields $\mathbf{u}^{(i)}$, $i = 1, 2$, and the temperature fields $\theta^{(i)}$, $i = 1, 2$, by fulfilling the following equations. They all have been already mentioned before, but are briefly summarized here in order to obtain a clear overview on the coupled problem.

The local governing equations in each body are

$$\mathrm{Div}\, \mathbf{P}^{(i)} + \hat{\mathbf{b}}_0^{(i)} = \mathbf{0} \quad \text{and} \tag{6.16}$$

$$-\mathrm{Div}\, \mathbf{Q}^{(i)} + \rho_0\, \hat{r}^{(i)} = 0 \quad \text{in } \Omega_0^{(i)} \ , \quad i = 1, 2 \ . \tag{6.17}$$

The boundary conditions and equilibrium equations at the contact interface read

$$\mathbf{P}^{(i)}\, \mathbf{N}^{(i)} = \hat{\mathbf{t}}_0^{(i)} \quad \text{on } \Gamma_\sigma^{(i)} \ , \tag{6.18}$$

$$\mathbf{P}^{(i)}\, \mathbf{N}^{(i)} = \mathbf{t}_{c,0}^{(i)} \quad \text{on } \Gamma_c^{(i)} \ , \tag{6.19}$$

$$\mathbf{u}^{(i)} = \hat{\mathbf{u}}^{(i)} \quad \text{on } \Gamma_u^{(i)} \ , \tag{6.20}$$

$$\mathbf{Q}^{(i)}\, \mathbf{N}^{(i)} = \hat{q}_0^{(i)} \quad \text{on } \Gamma_q^{(i)} \ , \tag{6.21}$$

$$\mathbf{Q}^{(i)}\, \mathbf{N}^{(i)} = q_{c,0}^{(i)} \quad \text{on } \Gamma_c^{(i)} \ , \tag{6.22}$$

$$\theta^{(i)} = \hat{\theta}^{(i)} \quad \text{on } \Gamma_\theta^{(i)} \ , \quad i = 1, 2 \ . \tag{6.23}$$

As explained, the contact constraints are those of the purely mechanical problem, namely (2.59) - (2.61) and (2.63) - (2.66). And the laws of thermodynamics at the contact interface are represented entirely by the reformulated terms (6.12) and (6.15). They are used for further derivation. The governing equations are completed with the definition of a temperature dependent constitutive behavior as generally expressed in (2.43) and FOURIER's law of heat conduction (6.3).

6.2 Weak form

This section presents the weak form of the thermomechanical contact problem. As the linear momentum equations and the mechanical contact constraints have exactly the same structure as those of Sections 3.3.1 and 3.3.2, only the additional governing equations are considered in detail. These are the energy balance equation and the laws of thermodynamics at the contact interface.

6.2.1 Energy balance equations

In order to formulate the weak form, solution and weighting function spaces have to be defined. For the purely mechanical problem, this is already done with the definitions (3.5) and (3.6). For the thermomechanical problem considered now, there are, additionally, the solution function space $\mathcal{T}^{(i)}$ for the temperatures $\theta^{(i)}$ and the weighting functions space $\mathcal{C}^{(i)}$ for the accompanying test functions $v^{(i)}$. They are defined for each subdomain $\Omega_0^{(i)}$ as

$$\mathcal{T}^{(i)} := \left\{ \theta^{(i)} \in H^1\left(\Omega_0^{(i)}\right) \mid \theta^{(i)} = \hat{\theta}^{(i)} \ \text{ on } \Gamma_\theta^{(i)} \right\} , \tag{6.24}$$

$$\mathcal{C}^{(i)} := \left\{ v^{(i)} \in H^1\left(\Omega_0^{(i)}\right) \mid v^{(i)} = 0 \ \text{ on } \Gamma_\theta^{(i)} \right\} . \tag{6.25}$$

The method of weighted residuals is applied to the equilibrium equations, i.e. the temperature evolution equation (6.17), the thermal NEUMANN boundary condition (6.21), and equation (6.22) at the contact interface. By testing these expressions with the functions $v^{(i)} \in \mathcal{C}^{(i)}$ and integrating over the whole domain $\Omega_0^{(i)}$ of each body i, one obtains

$$\begin{aligned} &\int_{\Omega_0^{(i)}} \left[\operatorname{Div}\left(\mathbf{Q}^{(i)}\right) - \rho_0 \, \hat{r}^{(i)} \right] v^{(i)} \, \mathrm{d}\Omega_0^{(i)} \; + \int_{\Gamma_q^{(i)}} \left[\hat{q}_0^{(i)} - \mathbf{Q}^{(i)} \cdot \mathbf{N}^{(i)} \right] v^{(i)} \, \mathrm{d}\Gamma_q^{(i)} \\ &+ \int_{\Gamma_c^{(i)}} \left[q_{c,0}^{(i)} - \mathbf{Q}^{(i)} \cdot \mathbf{N}^{(i)} \right] v^{(i)} \, \mathrm{d}\Gamma_c^{(i)} = 0 \, . \end{aligned} \tag{6.26}$$

Identifying the arbitrary test functions $v^{(i)}$ as virtual temperatures $\delta\theta^{(i)}$, applying integration by parts and subsequently GAUSS' divergence theorem, the following integral equation for each body i is obtained:

$$\begin{aligned} G_\theta^{(i)}(\mathbf{u}^{(i)}, \theta^{(i)}, \delta\theta^{(i)}) = &\int_{\Omega_0^{(i)}} \mathbf{Q}^{(i)} \left(\operatorname{Grad} \delta\theta^{(i)} \right) \, \mathrm{d}\Omega_0^{(i)} + \int_{\Omega_0^{(i)}} \rho_0 \, \hat{r}^{(i)} \, \delta\theta^{(i)} \, \mathrm{d}\Omega_0^{(i)} \\ &- \int_{\Gamma_q^{(i)}} \hat{q}_0^{(i)} \, \delta\theta^{(i)} \, \mathrm{d}\Gamma_q^{(i)} \\ &- \int_{\Gamma_c^{(i)}} q_{c,0}^{(i)} \, \delta\theta^{(i)} \, \mathrm{d}\Gamma_c^{(i)} = 0 \quad \forall \, \delta\theta^{(i)} \in \mathcal{C}^{(i)} \, . \end{aligned} \tag{6.27}$$

Here, the first three terms represent the internal and external thermal contributions $G_\theta^{int,ext(i)}$. They are seen to balance the contributions of the heat flux across the contact interface $G_\theta^{c(i)}$ acting on $\Gamma_c^{(i)}$ of the respective body i.

Similar to the purely mechanical problem, the further derivation is only performed for $G_\theta^{c(i)}$ stemming from the contact interface. Transformed to the current configuration and stated for the entire system, these contributions can be written as

$$G_\theta^c\left(\mathbf{u}^{(i)}, \theta^{(i)}, \delta\theta^{(i)}\right) = -\sum_{i=1}^{2} \int_{\gamma_c^{(i)}} q_c^{(i)} \, \delta\theta^{(i)} \, \mathrm{d}\gamma \, . \tag{6.28}$$

Using (6.15), where the heat flux on the master side $q_c^{(2)}$ is expressed in terms of the heat flux on the slave side $q_c^{(1)}$ and the mechanical dissipation $\mathbf{t}_\tau \cdot \mathbf{v}_{\tau,rel}$, equation (6.28) can be rewritten as

an integral over the slave surface only

$$G_\theta^c\left(\mathbf{u},\theta,\delta\theta\right) = -\int_{\gamma_c^{(1)}} q_c^{(1)}\left(\delta\theta^{(1)} - \left(\delta\theta^{(2)}\circ P\right)\right) - \left(\mathbf{t}_\tau\cdot\mathbf{v}_{\tau,rel}\right)\left(\delta\theta^{(2)}\circ P\right)\,\mathrm{d}\gamma\,, \tag{6.29}$$

where P is the projection operator presented in Section 2.2.1. Dual LAGRANGE multipliers are introduced for the thermal field, too. These additional unknowns defined on the slave contact surface are identified as the negative heat flux there, i.e.

$$\lambda_\theta = -q_c^{(1)}. \tag{6.30}$$

They are specified to be in the dual trace space $\mathcal{M}$ similar to $\boldsymbol{\mathcal{M}}$ in Section 3.3.1. For a more mathematical background, the interested reader is referred to HÜEBER and WOHLMUTH [58] and WOHLMUTH [140]. The final version of the contact integral reads

$$G_\theta^c\left(\mathbf{u},\boldsymbol{\lambda},\theta,\lambda_\theta,\delta\theta\right) = \int_{\gamma_c^{(1)}} \lambda_\theta\left(\delta\theta^{(1)} - \left(\delta\theta^{(2)}\circ P\right)\right) + \left|\boldsymbol{\lambda}_\tau\cdot\mathbf{v}_{\tau,rel}\right|\left(\delta\theta^{(2)}\circ P\right)\,\mathrm{d}\gamma\,. \tag{6.31}$$

With this, also the weak form of the energy balance equation (6.27) can be written finally for the entire system as

$$G_\theta = G_\theta^{int,ext} + G_\theta^c\,. \tag{6.32}$$

6.2.2 Laws of thermodynamics at the contact interface

So far, equation (6.12) from the laws of thermodynamics at the contact interface has not been used. It is of ROBIN-type relating the temperature $\theta^{(i)}$ to the heat flux on the slave side $q_c^{(1)}$. It can be seen as remaining interface condition which is, as already started within the derivation of the weak energy balance in the previous section, enforced with a LAGRANGE multiplier. For this, condition (6.12) is multiplied with the arbitrary test function $\delta\lambda_\theta$ and is integrated over the slave contact surface resulting in

$$\int_{\gamma_c^{(1)}} \delta\lambda_\theta\,\left[\lambda_\theta - \beta_c\,\left(\theta^{(1)} - \left(\theta^{(2)}\circ P\right)\right) + \delta_c\,\left|\boldsymbol{\lambda}_\tau\cdot\mathbf{v}_{\tau,rel}\right|\right]\,\mathrm{d}\gamma_c = 0 \quad \forall\,\delta\lambda_\theta\in\mathcal{M}\,. \tag{6.33}$$

This equation is added to the weak form of the energy balance equation.

6.2.3 Summarized weak form

Altogether, the mixed variational form of the fully coupled thermomechanical contact problem for finite deformations is for the solution of $\mathbf{u}^{(i)}\in\boldsymbol{\mathcal{U}}^{(i)}$, $\boldsymbol{\lambda}\in\boldsymbol{\mathcal{M}}(\boldsymbol{\lambda})$, $\theta^{(i)}\in\mathcal{T}^{(i)}$, and $\lambda_\theta\in\mathcal{M}$. It is composed of the weakly expressed equations as the balance of linear momentum (3.23), the mechanical contact constraints (3.24) and (3.25), the balance of energy (6.32), and the thermal interface condition (6.33). They must hold for the given test functions.

Remark: Thermal equations without LAGRANGE multipliers

To the enforcement of the thermal interface condition with a LAGRANGE multiplier above, there exists an alternative approach. It does not necessitate the introduction of the additional unknowns λ_θ identified as the negative heat flux on the slave side $q_c^{(1)}$. This is because of the value of $q_c^{(1)}$ can directly be determined in terms of the primary variables $\theta^{(i)}$ according to (6.12). Thus, with insertion of (6.12) into (6.29), the contribution from the heat flux across the contact interface to the weak energy balance equation can be expressed alternatively as

$$G_{2,\theta}^{c}\left(\mathbf{u},\theta,\delta\theta\right) = -\int_{\gamma_c^{(1)}} \beta_c \left(\theta^{(1)} - \left(\theta^{(2)} \circ P\right)\right)\left(\delta\theta^{(1)} - \left(\delta\theta^{(2)} \circ P\right)\right) - \left(\delta_c\,\delta\theta^{(1)} + (1-\delta_c)\left(\delta\theta^{2} \circ P\right)\right)\left(\mathbf{t}_\tau \cdot \mathbf{v}_{\tau,rel}\right)\,\mathrm{d}\gamma\ . \tag{6.34}$$

It already contains the thermal interface condition (6.12) that consequently does not have to be enforced with a LAGRANGE multiplier.

This at a first look more obvious weak problem statement is, for example, used in LAURSEN [83] or OANCEA and LAURSEN [101] in the context of node-to-segment contact surface discretization. However, within the applied mortar framework used here, extensions are necessary. This is due to equation (6.34), which also requires the integration of the product of two functions defined on the master surface, namely $\theta^{(2)}$ and $\delta\theta^{(2)}$. As this has to be performed for the active contact surface within the applied active set strategy, this information, at hand on the slave contact surface so far, has to be transformed to the master contact surface.

Within this work, both alternatives with and without LAGRANGE multipliers have been implemented. Due to the advantage of being able to use the tried and tested framework of mechanical contact, focus and subsequent derivation is on the variant with LAGRANGE multipliers as performed in HÜEBER and WOHLMUTH [58], too.

6.3 Finite element discretization

This section addresses the finite element discretization of equations (6.32) and (6.33). They represent the additional terms when considering thermomechanical contact problems instead of purely mechanical ones. Shape functions are introduced and inserted into the above equations. This leads to the spatially discretized setting of the problem.

6.3.1 Shape functions

The usage of shape functions for the thermal field is very similar to the one for the mechanical field in 3.4.1. Therefore, the section is kept very short.

Temperature field

The underlying geometry of the temperature field is assumed to be identical to the one of the structural field. Furthermore, as solution space for the temperature, the finite dimensional discrete counterpart is defined as subset $\mathcal{T}^{(i)h} \subset \mathcal{T}^{(i)}$ of the continuous one. This work is restricted to 8-node hexahedral elements in the three dimensional setting. Subsequently, the discretization

of the contact surface results in 4-node quadrilateral elements. Following the isoparametric concept, the same interpolation is applied for both geometry and temperature field. This also brings the same shape functions for the displacement and the temperature field.

Slave and master surfaces are of special interest. There, the discrete form of the temperature field $\theta^{(i)}$ reads

$$\theta^{(1)h}|_{\Gamma_c^{(1)h}} = \sum_{k=1}^{n_{sl}} N_k^{(1)}(\xi^{(1)}, \eta^{(1)})\, \theta_k^{(1)} \ , \tag{6.35}$$

$$\theta^{(2)h}|_{\Gamma_c^{(2)h}} = \sum_{l=1}^{n_m} N_l^{(2)}(\xi^{(2)}, \eta^{(2)})\, \theta_l^{(2)} \ . \tag{6.36}$$

The interpolation is carried out with the standard shape functions $N_k^{(1)}$ and $N_l^{(2)}$ on the respective contact surface. The scalars $\theta_k^{(1)}$ and $\theta_l^{(2)}$ denote the nodal temperatures.

Weighting function for energy balance equation

According to the BUBNOV-GALERKIN method, the test function $\delta\theta^{(i)}$ is interpolated the same way as the temperature field $\theta^{(i)}$ in $\Omega_0^{(i)}$, $i = 1, 2$. The according discrete weighting space is the restriction of (6.25) to a finite dimensional subset $\mathcal{C}^{(i)h} \subset \mathcal{C}^{(i)}$. The interpolations on the slave and master surface are then be written as

$$\delta\theta^{(1)h}|_{\Gamma_c^{(1)h}} = \sum_{k=1}^{n_{sl}} N_k^{(1)}(\xi^{(1)}, \eta^{(1)})\, \delta\theta_k^{(1)} \ , \tag{6.37}$$

$$\delta\theta^{(2)h}|_{\Gamma_c^{(2)h}} = \sum_{l=1}^{n_m} N_l^{(2)}(\xi^{(2)}, \eta^{(2)})\, \delta\theta_l^{(2)} \ , \tag{6.38}$$

where $\delta\theta_k^{(1)}$ and $\delta\theta_l^{(2)}$ are the discrete nodal weighting values.

Thermal LAGRANGE multiplier field, weighting function for thermal interface condition

The interpolation of the thermal LAGRANGE multiplier field is carried out with the already used dual shape functions proposed by WOHLMUTH [139, 140] and presented Section 3.4.1. With that, the discrete form $\lambda_\theta^h \in \mathcal{M}^h$ is given as

$$\lambda_\theta^h = \sum_{j=1}^{n_{sl}} \Phi_j(\xi^{(1)}, \eta^{(1)})\, z_{\theta j} \ , \tag{6.39}$$

where $z_{\theta j}$ are the nodal thermal LAGRANGE multipliers. The weighting function field $\delta\lambda_\theta \in \mathcal{M}^h$ is interpolated with the same dual shape functions Φ_j as

$$\delta\lambda_\theta^h = \sum_{j=1}^{n_{sl}} \Phi_j(\xi^{(1)}, \eta^{(1)})\, \delta z_{\theta j} \ . \tag{6.40}$$

Here, $\delta z_{\theta j}$ are the discrete nodal weighting values.

6.3.2 Discrete energy balance equation

Substituting the discrete form of the field variables from Section 6.3.1 into (6.31), one obtains the expression

$$\begin{aligned}
&G_\theta^c\left(\mathbf{u},\boldsymbol{\lambda},\theta,\lambda_\theta,\delta\theta\right)\\
&\approx G_\theta^{c\,h}\left(\mathbf{u}^h,\boldsymbol{\lambda}^h,\theta^h,\lambda_\theta^h,\delta\theta^h\right)\\
&=\int_{\gamma_c^{(1)h}}\lambda_\theta^h\left(\delta\theta^{(1)h}-\left(\delta\theta^{(2)h}\circ P^h\right)\right)+\left|\boldsymbol{\lambda}_\tau^{h\,\mathrm{T}}\,\mathbf{v}_{\tau,rel}^h\right|\left(\delta\theta^{(2)h}\circ P^h\right)\,\mathrm{d}\gamma\\
&=\sum_{j=1}^{n_{sl}}\left[\sum_{k=1}^{n_{sl}}\delta\theta_k^{(1)}\int_{\gamma_c^{(1)h}}\Phi_j N_k^{(1)}\mathrm{d}\gamma-\sum_{l=1}^{n_m}\delta\theta_l^{(2)}\int_{\gamma_c^{(1)h}}\Phi_j\left(N_l^{(2)}\circ P^h\right)\mathrm{d}\gamma\right]\,z_{\theta j}\\
&\quad+\sum_{l=1}^{n_m}\int_{\gamma_c^{(1)h}}\left(N_l^{(2)}\circ P^h\right)\left|\boldsymbol{\lambda}_\tau^{h\,\mathrm{T}}\,\mathbf{v}_{\tau,rel}^h\right|\,\mathrm{d}\gamma\,\delta\theta_l^{(2)}\;.
\end{aligned}\tag{6.41}$$

It is the discrete contribution from contact to the energy balance equation and contains the same coupling integrals as the contact virtual work in Section 3.4.2. From this, it can be rewritten in terms of the global mortar matrices $\mathbf{D}$ and $\mathbf{M}$ as

$$G_\theta^{c\,h}\left(\mathbf{u}^h,\boldsymbol{\lambda}^h,\theta^h,\lambda_\theta^h,\delta\theta^h\right)=\delta\boldsymbol{\theta}^{(1)\mathrm{T}}\,\mathbf{D}^{\mathrm{T}}\,\mathbf{z}_\theta-\delta\boldsymbol{\theta}^{(2)\mathrm{T}}\,\left[\mathbf{M}^{\mathrm{T}}\,\mathbf{z}_\theta+\mathbf{f}^D\right]\;.\tag{6.42}$$

Here, $\mathbf{z}_\theta$ denotes the vector of all discrete nodal thermal LAGRANGE multipliers and $\delta\boldsymbol{\theta}^{(1)}$ and $\delta\boldsymbol{\theta}^{(2)}$ are the vectors of all discrete nodal test function values on the slave and master side. Having a scalar thermal field at hand, the global mortar matrices are reduced accordingly in dimension leading to $\mathbf{D}\in\mathbb{R}^{n_{sl}\times n_{sl}}$ and $\mathbf{M}\in\mathbb{R}^{n_{sl}\times n_m}$. Finally, the vector $\mathbf{f}^D\in\mathbb{R}^{n_m}$ contains all nodal integrals

$$f_{m,l}^D=\int_{\gamma_c^{(1)h}}\left(N_l^{(2)}\circ P^h\right)\left|\boldsymbol{\lambda}_\tau^{h\,\mathrm{T}}\,\mathbf{v}_{\tau,rel}^h\right|\,\mathrm{d}\gamma\,,\quad l=1,...,n_m\;,\tag{6.43}$$

which represent the mechanical dissipation evaluated for nodes on the master side $l\in\mathcal{M}$. They are evaluated with GAUSS integration similar to equation (5.11). Also in this case, the usage of the nodal weighted tangential relative slip increment is desirable.

Dividing all finite element nodes of $\Omega_0=\Omega_0^{(1)}\cup\Omega_0^{(2)}$ into the sets of slave nodes $\mathcal{S}$, master nodes $\mathcal{M}$ and remaining nodes $\mathcal{N}$, the global temperature vector $\boldsymbol{\theta}$ is sorted accordingly to $\boldsymbol{\theta}=(\boldsymbol{\theta}_\mathcal{N},\boldsymbol{\theta}_\mathcal{M},\boldsymbol{\theta}_\mathcal{S})^{\mathrm{T}}$. Assuming arbitrary test functions $\delta\boldsymbol{\theta}^{(1)}$ and $\delta\boldsymbol{\theta}^{(2)}$, the discrete contribution from contact to the energy balance equation can be arranged as

$$\mathbf{f}_\theta^c=\begin{bmatrix}\mathbf{0} & -\mathbf{M} & \mathbf{D}\end{bmatrix}^{\mathrm{T}}\,\mathbf{z}_\theta+\begin{bmatrix}\mathbf{0} & \mathbf{f}^D & \mathbf{0}\end{bmatrix}^{\mathrm{T}}\;.\tag{6.44}$$

Hence, the discrete counterpart of the weak energy balance equation (6.32) finally reads

$$\mathbf{f}_\theta^{int}(\mathbf{d},\boldsymbol{\theta})+\mathbf{f}_\theta^c(\mathbf{d},\mathbf{z},\boldsymbol{\theta},\mathbf{z}_\theta)=\mathbf{f}_\theta^{ext}\;.\tag{6.45}$$

6.3.3 Discrete thermal contact condition

The discrete thermal contact condition is obtained by insertion of the interpolated fields into equation (6.33). This applies to the temperature $\theta^{(i)h}$, the thermal LAGRANGE multiplier λ_θ^h, the

test function $\delta\theta^h$, as well as the displacements $\mathbf{u}^{(i)h}$ and the mechanical LAGRANGE multiplier $\boldsymbol{\lambda}^h$. It leads to

$$\begin{aligned}
&\int_{\gamma_c^{(1)}} \delta\lambda_\theta \left[\lambda_\theta - \beta_c \left(\theta^{(1)} - \left(\theta^{(2)} \circ P\right)\right) + \delta_c \left|\boldsymbol{\lambda}_\tau \cdot \mathbf{v}_{\tau,rel}\right|\right] \mathrm{d}\gamma_c \\
&\approx \int_{\gamma_c^{(1)h}} \delta\lambda_\theta^h \left[\lambda_\theta^h - \beta_c \left(\theta^{(1)h} - \left(\theta^{(2)h} \circ P^h\right)\right) + \delta_c \left|\boldsymbol{\lambda}_\tau^{h\,\mathrm{T}} \mathbf{v}_{\tau,rel}^h\right|\right] \mathrm{d}\gamma_c \\
&= \sum_{j=1}^{n_{sl}} \delta z_{\theta j} \Bigg[\sum_{i=1}^{n_{sl}} \int_{\gamma_c^{(1)h}} \Phi_j \Phi_i \,\mathrm{d}\gamma\, z_{\theta i} \\
&\quad - \beta_c \Bigg[\sum_{k=1}^{n_{sl}} \int_{\gamma_c^{(1)h}} \Phi_j N_k^{(1)} \,\mathrm{d}\gamma\, \theta_i^{(1)} - \sum_{l=1}^{n_m} \int_{\gamma_c^{(1)h}} \Phi_j \left(N_l^{(2)} \circ P^h\right) \mathrm{d}\gamma\, \theta_k^{(2)} \Bigg] \\
&\quad + \delta_c \int_{\gamma_c^{(1)h}} \Phi_j \left|\boldsymbol{\lambda}_\tau^{h\,\mathrm{T}} \mathbf{v}_{\tau,rel}^h\right| \mathrm{d}\gamma \Bigg] = 0 \quad \forall\, \delta\lambda_\theta^h \in \mathcal{M}^h \,. \qquad (6.46)
\end{aligned}$$

Assuming arbitrary discrete test function values, equation (6.46) results in a nodal condition. For each slave node $j \in \mathcal{S}$, one obtains

$$\sum_{i=1}^{n_{sl}} B_{ji}\, z_{\theta i} \; - \beta_c \left(D_{jj}\, \theta_j^{(1)} - \sum_{l=1}^{n_m} M_{jl}\, \theta_l^{(2)} \right) + \delta_c\, f_{s,j}^D = 0 \,. \qquad (6.47)$$

Here, the entries D_{jj} and M_{jl} are the well known mortar coupling terms. The expression B_{ji} is evaluated as

$$B_{ji} = \int_{\gamma_c^{(1)^h}} \Phi_j \Phi_i \mathrm{d}\gamma \,, \quad j = 1, ..., n_{sl} \,, \quad i = 1, ..., n_{sl} \,, \qquad (6.48)$$

and $f_{s,j}^D$, the mechanical dissipation assigned to a slave node $j \in \mathcal{S}$, i.e.

$$f_{s,j}^D = \int_{\gamma_c^{(1)h}} \Phi_j \left|\boldsymbol{\lambda}_\tau^{h\,\mathrm{T}} \mathbf{v}_{\tau,rel}^h\right| \mathrm{d}\gamma \,, \quad j = 1, ..., n_{sl} \,. \qquad (6.49)$$

It is evaluated in the same way as (6.43).

In order to obtain decoupled nodal conditions in (6.47), a lumping technique is applied in HÜEBER and WOHLMUTH [58]. In the work at hand, a similar approach is done. The sum $\sum_{i=1}^{n_sl} B_{ji}$ is approximated by the mortar term D_{jj}. Consequently, equation (6.47) reads for a slave node $j \in \mathcal{S}$

$$r_{\theta j}^{cond} = D_{jj}\, z_{\theta j} \; - \beta_c \left(D_{jj}\, \theta_j^{(1)} - \sum_{l=1}^{n_m} M_{jl}\, \theta_l^{(2)} \right) + \delta_c\, f_{s,j}^D = 0 \qquad (6.50)$$

in its final form.

Remark: Lumping of thermal contact condition

It is mentioned that the described lumping of the thermal contact condition above does not necessarily have to be performed. For the intended easy elimination of the thermal LAGRANGE

multiplier, it is sufficient to have a diagonal structure of the mortar matrix $\mathbf{D}$ in the energy balance equation. From this, also equation (6.47) could be used and has been implemented within this work. But, as experienced differences in results are negligible and lumping is successfully used in HÜEBER and WOHLMUTH [58] for small deformations, focus lies on (6.50) within the further course of this work.

6.3.4 Summarized discrete form

The summarized discrete form of the thermomechanical contact problem is for the solution of $\mathbf{u}^{(i)h} \in \mathcal{U}^{(i)h}$, $\boldsymbol{\lambda}^h \in \boldsymbol{\mathcal{M}}^h(\boldsymbol{\lambda}^h)$, $\theta^{(i)h} \in \mathcal{T}^{(i)h}$ and $\lambda_\theta^h \in \mathcal{M}^h$. It is composed of the linear momentum equation (3.50), the energy balance equation (6.45), and the mechanical and thermal contact constraints (3.63) - (3.65), (3.72) - (3.75), and (6.50).

6.4 Partitioned solution scheme

For multiphysics problems in general, there exist various solution approaches. In FELIPPA et al. [25] and WALL [134], they are divided into monolithic, partitioned and field elimination schemes. Within this work, especially the partitioned approach is used for the solution of the thermomechanical contact problem stated in Section 6.3.4. This is mainly due to the advantage of its inherent modularity, which allows a separate usage of the tried and tested single field solvers. But additional, an outlook to the application of a monolithic solution scheme is given.

The partitioned approach requires the repeated solution of mechanical and thermal fields. For the treatment of the mechanical field, the semi-smooth NEWTON method described in Chapter 4 is applied. The only difference to the purely mechanical problem is the temperature dependent material. It changes the bulk equations within the bodies, but contact contributions itself are not affected by the thermal field. Consequently, focus here is on the solution of the thermal field.

6.4.1 NEWTON algorithm for thermal field

For the solution of the thermal problem within the partitioned scheme, the mechanical field variables as the nodal displacements $\mathbf{d}$ and the nodal LAGRANGE multipliers $\mathbf{z}$ are held constant. This is also true for the contact sets where especially the active node set $\mathcal{A}$ and the set of slipping nodes $\mathcal{S}l$ are relevant for the thermal problem. The remaining equations for the solution of the nodal temperatures $\boldsymbol{\theta}$ and the nodal thermal LAGRANGE multipliers $\mathbf{z}_\theta$ are the discrete expressions (6.45) and (6.50). In order to apply a NEWTON scheme, they are written in residual form as

$$\begin{aligned} \mathbf{r}_\theta = \mathbf{f}_\theta^{int}(\boldsymbol{\theta}) + \mathbf{f}_\theta^{c}(\boldsymbol{\theta}, \mathbf{z}_\theta) - \mathbf{f}_\theta^{ext} = \mathbf{0} \ , \\ r_{\theta j}^{cond}(\boldsymbol{\theta}, z_{\theta j}) = 0 \qquad \forall\, j \in \mathcal{S} \ . \end{aligned} \tag{6.51}$$

For the current iterate k, the linearizations of these equations at $(\boldsymbol{\theta}^k, \mathbf{z}_\theta^k)$ read

$$\Delta \mathbf{r}_\theta^k \left(\boldsymbol{\theta}^k, \mathbf{z}_\theta^k\right) = -\mathbf{r}_\theta^k \ , \tag{6.52}$$

$$\Delta r_{\theta j}^{cond,k} \left(\boldsymbol{\theta}^k, z_{\theta j}^k\right) = -r_{\theta j}^{cond,k} \qquad \forall\, j \in \mathcal{S} \ . \tag{6.53}$$

Here, for the thermal problem, the quantities $\Delta(\cdot)$ denote the directional derivatives given by

$$\Delta\left(\cdot\right) = \frac{\partial\left(\cdot\right)}{\partial\boldsymbol{\theta}}\Delta\boldsymbol{\theta} + \frac{\partial\left(\cdot\right)}{\partial\mathbf{z}_\theta}\Delta\mathbf{z}_\theta \ . \tag{6.54}$$

The NEWTON iteration contains the solution of the linear system of equations (6.52) and (6.53) for the increments $(\Delta\boldsymbol{\theta}^k, \Delta\mathbf{z}_\theta^k)$ and the subsequent update for the new iterate $\left(\boldsymbol{\theta}^{k+1}, \boldsymbol{z_\theta}^{k+1}\right)$ as

$$\left(\boldsymbol{\theta}^{k+1}, \mathbf{z}_\theta^{k+1}\right) = \left(\boldsymbol{\theta}^k, \mathbf{z}_\theta^k\right) + \left(\Delta\boldsymbol{\theta}^k, \Delta\mathbf{z}_\theta^k\right) \ . \tag{6.55}$$

It has to be pointed out that the thermal contact problem considered within this partitioned approach depends linearly on the nodal temperatures $\boldsymbol{\theta}$ and LAGRANGE multipliers $\mathbf{z}_\theta$. Therefore, a NEWTON scheme for its solution has not to be used necessarily. It is chosen nevertheless to have a similar framework to the purely mechanical problem and a good starting point for the nonlinear monolithic approach. Here, consequently, the residual vanishes after only one NEWTON step.

6.4.2 Linearization and algebraic representation

In this section, the linearizations of equations (6.52) and (6.53), their assembly into global matrices, and the formulation of the linear system of equations to be solved is presented.

Energy balance equation

The evaluation of $\Delta\mathbf{r}_\theta^k$ needs the linearization of the different parts of the energy balance equation, i.e. the internal contribution $\mathbf{f}_\theta^{int}(\boldsymbol{\theta})$ and the contribution from contact $\mathbf{f}^c(\boldsymbol{\theta}, \mathbf{z}_\theta)$. The first one, the bulk response, is independent of contact and therefore not discussed within this work. Its treatment can be found for example in SIMO and MIEHE [126], the respective stiffness is denoted as $\mathbf{K}^\theta$. The linearization of the second one can be expressed in already global matrices. For the current iterate k, it reads

$$\Delta\mathbf{f}_\theta^{c,k} = \left(\mathbf{0}, \ -\mathbf{M}^{\mathrm{T}}\,\Delta\mathbf{z}_\theta^k, \ \mathbf{D}^{\mathrm{T}}\,\Delta\mathbf{z}_\theta^k\right)^{\mathrm{T}} \ . \tag{6.56}$$

For the further treatment of this equation, the thermal LAGRANGE multiplier increment $\Delta\mathbf{z}_\theta^k$ is replaced by $\mathbf{z}_\theta^{k+1} - \mathbf{z}_\theta^k$.

Thermal contact condition

Concerning the thermal contact condition, the linearized equation (6.53) for the current iterate k results in

$$\Delta r_{\theta j}^{cond,k} = D_{jj}^k\,\Delta z_{\theta j}^k \ - \beta_c\left(D_{jj}^k\,\Delta\theta_j^{(1)k} - \sum_{l=1}^{n_m} M_{jl}^k\,\Delta\theta_l^{(2)k}\right) = -r_{\theta j}^{cond,k} \qquad \forall\, j \in \mathcal{A}_k \ . \tag{6.57}$$

As before, the equation is reformulated in terms of $\mathbf{z}_\theta^{k+1}$. The assembly of (6.57) for all active contact nodes $j \in \mathcal{A}$ reads

$$\mathop{\mathsf{A}}_{j=1}^{n^a}\left(\Delta r_{\theta j}^{cond,k} + r_{\theta j}^{cond,k}\right) \ = \ \mathbf{U}_{\mathcal{A}_k}\,\Delta\boldsymbol{\theta}_{\mathcal{S}}^k + \mathbf{V}_{\mathcal{A}_k}\,\Delta\boldsymbol{\theta}_{\mathcal{M}}^k + \mathbf{W}_{\mathcal{A}_k}\,\mathbf{z}_{\theta\mathcal{A}}^{k+1} + \mathbf{r}_{\theta\mathcal{A}}^{cond} \ . \tag{6.58}$$

Here, the matrices $\mathbf{U}_{\mathcal{A}_k} \in \mathbb{R}^{n^a \times n^{sl}}$, $\mathbf{V}_{\mathcal{A}_k} \in \mathbb{R}^{n^a \times n^m}$ and $\mathbf{W}_{\mathcal{A}_k} \in \mathbb{R}^{n^a \times n^a}$ are the assembled forms of all linearizations and the vector $\mathbf{r}_{\theta\mathcal{A}}^{cond} \in \mathbb{R}^{n^a}$ represents the right hand side.

System of equations

Finally, with the assembled matrices above, the linear system representing equations (6.52) and (6.53) can be written. The iteration index k is dropped and the stiffness $\mathbf{K}^\theta$ is shortened to $\mathbf{K}$ for the ease of notation:

$$\begin{bmatrix} \mathbf{K}_{\mathcal{N}\mathcal{N}} & \mathbf{K}_{\mathcal{N}\mathcal{M}} & \mathbf{K}_{\mathcal{N}\mathcal{I}} & \mathbf{K}_{\mathcal{N}\mathcal{A}} & \mathbf{0} \\ \mathbf{K}_{\mathcal{M}\mathcal{N}} & \mathbf{K}_{\mathcal{M}\mathcal{M}} & \mathbf{K}_{\mathcal{M}\mathcal{I}} & \mathbf{K}_{\mathcal{M}\mathcal{A}} & -\mathbf{M}_{\mathcal{A}}^{\mathrm{T}} \\ \mathbf{K}_{\mathcal{I}\mathcal{N}} & \mathbf{K}_{\mathcal{I}\mathcal{M}} & \mathbf{K}_{\mathcal{I}\mathcal{I}} & \mathbf{K}_{\mathcal{I}\mathcal{A}} & \mathbf{0} \\ \mathbf{K}_{\mathcal{A}\mathcal{N}} & \mathbf{K}_{\mathcal{A}\mathcal{M}} & \mathbf{K}_{\mathcal{A}\mathcal{I}} & \mathbf{K}_{\mathcal{A}\mathcal{A}} & \mathbf{D}_{\mathcal{A}}^{\mathrm{T}} \\ \mathbf{0} & \mathbf{V}_{\mathcal{A}} & \mathbf{U}_{\mathcal{A}\mathcal{I}} & \mathbf{U}_{\mathcal{A}\mathcal{A}} & \mathbf{W}_{\mathcal{A}} \end{bmatrix} \cdot \begin{bmatrix} \Delta\boldsymbol{\theta}_{\mathcal{N}} \\ \Delta\boldsymbol{\theta}_{\mathcal{M}} \\ \Delta\boldsymbol{\theta}_{\mathcal{I}} \\ \Delta\boldsymbol{\theta}_{\mathcal{A}} \\ \mathbf{z}_{\theta\mathcal{A}} \end{bmatrix} = - \begin{bmatrix} \mathbf{r}_{\theta\mathcal{N}} \\ \mathbf{r}_{\theta\mathcal{M}} + \mathbf{f}^D \\ \mathbf{r}_{\theta\mathcal{I}} \\ \mathbf{r}_{\theta\mathcal{A}} \\ \mathbf{r}_{\theta\mathcal{A}}^{cond} \end{bmatrix} \tag{6.59}$$

The first four rows represent the linearized energy balance equation (6.52) where $\mathcal{I}$ stands for the inactive node set. The fifth row is the algebraic form of the linearized thermal contact condition (6.53) for nodes of the active contact set $\mathcal{A}$.

The system (6.59) contains temperature degrees of freedom $\Delta\boldsymbol{\theta}^k$ and thermal LAGRANGE multipliers $\boldsymbol{z}_\theta^{k+1}$ and is therefore of increased size. But similar to the purely mechanical system in Section 4.5, the LAGRANGE multipliers can easily be eliminated due to the diagonality of the matrix $\mathbf{D}$. From the fourth line in (6.59), they can be expressed as

$$\mathbf{z}_{\theta\mathcal{A}} = \mathbf{D}^{-\mathrm{T}} \left(-\mathbf{r}_{\theta\mathcal{A}} - \mathbf{K}_{\mathcal{A}\mathcal{N}} \Delta\boldsymbol{\theta}_{\mathcal{N}} - \mathbf{K}_{\mathcal{A}\mathcal{M}} \Delta\mathbf{d}_{\mathcal{M}} - \mathbf{K}_{\mathcal{A}\mathcal{S}} \Delta\boldsymbol{\theta}_{\mathcal{S}} \right) . \tag{6.60}$$

With insertion of (6.60) into (6.59), a reduced system with only temperature degrees of freedom is obtained:

$$\begin{bmatrix} \mathbf{K}_{\mathcal{N}\mathcal{N}} & \mathbf{K}_{\mathcal{N}\mathcal{M}} & \mathbf{K}_{\mathcal{N}\mathcal{I}} & \mathbf{K}_{\mathcal{N}\mathcal{A}} \\ \mathbf{K}_{\mathcal{M}\mathcal{N}} + \hat{\mathbf{M}}_{\mathcal{A}}^{\mathrm{T}} \mathbf{K}_{\mathcal{A}\mathcal{N}} & \mathbf{K}_{\mathcal{M}\mathcal{M}} + \hat{\mathbf{M}}_{\mathcal{A}}^{\mathrm{T}} \mathbf{K}_{\mathcal{A}\mathcal{M}} & \mathbf{K}_{\mathcal{M}\mathcal{I}} + \hat{\mathbf{M}}_{\mathcal{A}}^{\mathrm{T}} \mathbf{K}_{\mathcal{A}\mathcal{I}} & \mathbf{K}_{\mathcal{M}\mathcal{A}} + \hat{\mathbf{M}}_{\mathcal{A}}^{\mathrm{T}} \mathbf{K}_{\mathcal{A}\mathcal{A}} \\ \mathbf{K}_{\mathcal{I}\mathcal{N}} & \mathbf{K}_{\mathcal{I}\mathcal{M}} & \mathbf{K}_{\mathcal{I}\mathcal{I}} & \mathbf{K}_{\mathcal{I}\mathcal{A}} \\ \mathbf{W}_{\mathcal{A}} \mathbf{D}_{\mathcal{A}}^{-\mathrm{T}} \mathbf{K}_{\mathcal{A}\mathcal{N}} & \mathbf{W}_{\mathcal{A}} \mathbf{D}_{\mathcal{A}}^{-\mathrm{T}} \mathbf{K}_{\mathcal{A}\mathcal{M}} - \mathbf{V}_{\mathcal{A}} & \mathbf{W}_{\mathcal{A}} \mathbf{D}_{\mathcal{A}}^{-\mathrm{T}} \mathbf{K}_{\mathcal{A}\mathcal{I}} - \mathbf{U}_{\mathcal{A}\mathcal{I}} & \mathbf{W}_{\mathcal{A}} \mathbf{D}_{\mathcal{A}}^{-\mathrm{T}} \mathbf{K}_{\mathcal{A}\mathcal{S}} - \mathbf{U}_{\mathcal{A}\mathcal{A}} \end{bmatrix} \cdot \begin{bmatrix} \Delta\boldsymbol{\theta}_{\mathcal{N}} \\ \Delta\boldsymbol{\theta}_{\mathcal{M}} \\ \Delta\boldsymbol{\theta}_{\mathcal{I}} \\ \Delta\boldsymbol{\theta}_{\mathcal{A}} \end{bmatrix} = - \begin{bmatrix} \mathbf{r}_{\theta\mathcal{N}} \\ \mathbf{r}_{\theta\mathcal{M}} + \mathbf{f}^D + \hat{\mathbf{M}}_{\mathcal{A}}^{\mathrm{T}} \mathbf{r}_{\theta\mathcal{A}} \\ \mathbf{r}_{\theta\mathcal{I}} \\ \mathbf{W}_{\mathcal{A}} \mathbf{D}_{\mathcal{A}}^{-\mathrm{T}} \mathbf{r}_{\theta\mathcal{A}} - \boldsymbol{r}_{\theta\mathcal{A}}^{cond} \end{bmatrix} , \tag{6.61}$$

where it has been made use of definition (4.42). For the solution of this final system, standard direct or iterative solution techniques can be applied.

6.4.3 Partitioned solution scheme

Partitioned solution schemes can be divided into two groups. Strongly coupled ones are characterized by achieving the entire solution of the problem within every time step. It is reached by iterating between the single fields as long as all governing equations are fulfilled. With this, the solution equals the one of the monolithic approach, see for example the discussions in KÜTTLER

and WALL [77] or WALL [134] for fluid-structure interaction problems. This kind of partitioned approach is also denoted as iterative staggered scheme. In contrast, weakly coupled or one way staggered schemes solve the single fields only once in each time step. This is mostly done sequentially and coupling information is passed from one field to the other although that one is going on in time. Consequently, in general, the governing equations are not fulfilled exactly at the end of a time step.

Throughout this work, an iterative staggered scheme for the partitioned solution is applied. Within one time step, it is implemented as given in the following. The iteration index k used in the algorithm is not to be mixed up with that of the NEWTON algorithm.

Algorithm 5

1. Set $k = 0$ and initialize the solution $(\mathbf{d}^0, \mathbf{z}^0, \boldsymbol{\theta}^0, \mathbf{z}_\theta^0)$ and the contact sets $\mathcal{I}_0$, $\mathcal{S}t_0$ and $\mathcal{S}l_0$.
2. Find $\mathbf{d}^{k+1}$, $\mathbf{z}^{k+1}$, $\mathcal{I}_{k+1}$, $\mathcal{S}t_{k+1}$ and $\mathcal{S}l_{k+1}$ with the solution of the nonlinear mechanical contact problem (equation (4.5) plus temperature dependent material behavior). Nodal temperatures $\boldsymbol{\theta}^k$ and thermal LAGRANGE multipliers $\mathbf{z}_\theta^k$ are hold constant.
3. Find $\boldsymbol{\theta}^{k+1}$ and $\mathbf{z}_\theta^{k+1}$ with the solution of the thermal contact problem stated in (6.51). Nodal displacements $\mathbf{d}^{k+1}$, LAGRANGE multipliers $\mathbf{z}^{k+1}$, and the contact sets $\mathcal{I}_{k+1}$, $\mathcal{S}t_{k+1}$ and $\mathcal{S}l_{k+1}$ are hold constant.
4. If $\mathcal{I}_{k+1} = \mathcal{I}_k$, $\mathcal{S}t_{k+1} = \mathcal{S}t_k$, $\mathcal{S}l_{k+1} = \mathcal{S}l_k$, $\|\mathbf{d}^{k+1} - \mathbf{d}^k\| \leq \epsilon_u$, and $\|\boldsymbol{\theta}^{k+1} - \boldsymbol{\theta}^k\| \leq \epsilon_\theta$, then stop, else set $k := k + 1$ and repeat from 2.

Here, ϵ_u and ϵ_θ denote tolerances of choice.

For validating purposes within the work presented here, the original full coupling of the mechanical and thermal field is sometimes reduced. In this regard, it is assumed that the material law is not dependent on the temperature in a few examples. Consequently, the mechanical solution is not influenced by the thermal one and the iterative staggered algorithm above converges after only one iteration. These cases however are marked clearly.

6.5 Outlook to monolithic solution scheme

Monolithic solution schemes are characterized by the simultaneous solution of both fields, in which all dependencies are considered through coupling terms.

Here, an outlook to the treatment of thermomechanical contact problems with a monolithic scheme is given. It is an extension of the problem without contact addressed in DANOWSKI et al. [19]. The contact related terms are newly formulated for finite deformations and contain a consistent linearization. Basis is the work of HÜEBER and WOHLMUTH [58], where this has been carried out in the context of small deformations. The section is titled with "outlook" as the derivation is kept short and some coupling effects are neglected. First, the formulation is for frictionless contact, which results in the absence of frictional dissipation and therefore no heating of the thermal field. Second, the heat flux over the contact surface is only modelled constantly according to (6.10). However, except from these restrictions, the monolithic scheme is applied consistently to the thermomechanical contact problem.

6.5.1 Semi-smooth NEWTON method for fully coupled problem

The fully coupled thermomechanical contact problem in residual form is presented. Dependencies on primary unknowns are given in brackets:

$$\begin{aligned}
\mathbf{r} = \mathbf{f}^{int}(\mathbf{d},\boldsymbol{\theta}) + \mathbf{f}^{c}(\mathbf{d},\mathbf{z}) - \mathbf{f}^{ext} &= \mathbf{0} \ , \\
\mathbf{r}_\theta = \mathbf{f}_\theta^{int}(\mathbf{d},\boldsymbol{\theta}) + \mathbf{f}_\theta^{c}(\mathbf{d},\boldsymbol{\theta},\mathbf{z}_\theta) - \mathbf{f}_\theta^{ext} &= \mathbf{0} \ , \\
C_{nj}\left(\mathbf{d},\mathbf{z}_j\right) &= 0 \qquad \forall\, j \in \mathcal{S} \ , \\
\mathbf{C}_{\tau j}\left(\mathbf{d},\mathbf{z}_j\right) &= \mathbf{0} \qquad \forall\, j \in \mathcal{S} \ , \\
r_{\theta j}^{cond}(\mathbf{d},\boldsymbol{\theta},z_{\theta j}) &= 0 \qquad \forall\, j \in \mathcal{S} \ .
\end{aligned} \tag{6.62}$$

For the current iterate k, the linearizations of these equations at $(\mathbf{d}^k, \mathbf{z}^k, \boldsymbol{\theta}^k, \mathbf{z}_\theta^k)$ read

$$\Delta\mathbf{r}\left(\mathbf{d}^k,\boldsymbol{\theta}^k\mathbf{z}^k\right) = -\mathbf{r}^k \ , \tag{6.63}$$

$$\Delta\mathbf{r}_\theta\left(\mathbf{d}^k,\boldsymbol{\theta}^k,\mathbf{z}_\theta^k\right) = -\mathbf{r}_\theta^k \ , \tag{6.64}$$

$$\Delta C_{nj}\left(\mathbf{d}^k,\mathbf{z}_j^k\right) = -C_{nj}^k \qquad \forall\, j \in \mathcal{S} \ , \tag{6.65}$$

$$\Delta\mathbf{C}_{\tau j}\left(\mathbf{d}^k,\mathbf{z}_j^k\right) = -\mathbf{C}_{\tau j}^k \qquad \forall\, j \in \mathcal{S} \ , \tag{6.66}$$

$$\Delta r_{\theta j}^{cond}\left(\mathbf{d}^k,\boldsymbol{\theta}^k,z_{\theta j}^k\right) = -r_{\theta j}^{cond,k} \qquad \forall\, j \in \mathcal{S} \ . \tag{6.67}$$

Here, the derivatives $\Delta(\cdot)$ have to be evaluated with respect to all primary unknowns as

$$\Delta\left(\cdot\right) = \frac{\partial\left(\cdot\right)}{\partial\mathbf{d}}\Delta\mathbf{d} + \frac{\partial\left(\cdot\right)}{\partial\mathbf{z}}\Delta\mathbf{z} + \frac{\partial\left(\cdot\right)}{\partial\boldsymbol{\theta}}\Delta\boldsymbol{\theta} + \frac{\partial\left(\cdot\right)}{\partial\mathbf{z}_\theta}\Delta\mathbf{z}_\theta \ . \tag{6.68}$$

The linear system of equations (6.63) - (6.67) is solved for the solution increments $(\Delta\mathbf{d}^k, \Delta\mathbf{z}^k, \Delta\boldsymbol{\theta}^k, \Delta\mathbf{z}_\theta^k)$, the update towards the new iterate $(\mathbf{d}^{k+1}, \mathbf{z}^{k+1}, \boldsymbol{\theta}^{k+1}, \mathbf{z}_\theta^{k+1})$ takes place as in (4.10) and (6.55).

6.5.2 Linearization and algebraic representation

The evaluation of necessary linearizations in equations (6.63) - (6.67) is presented in this section. Since the focus is on contact, it is not performed for bulk equations (6.63) and (6.64) leading to the stiffness contributions $\mathbf{K}^{uu}$, $\mathbf{K}^{u\theta}$, $\mathbf{K}^{\theta u}$, and $\mathbf{K}^{\theta\theta}$. Here, it is carried out for contact related terms only and, furthermore, only for expressions that differ from those in the sections before. In this regard, a closer look is given to $\mathbf{f}_\theta(\mathbf{d},\boldsymbol{\theta},\mathbf{z})$ and $r_{\theta j}^{cond}(\mathbf{d},\boldsymbol{\theta},z_{\theta j})$, which are the contact contribution to the energy balance equation in (6.64) and the thermal contact condition in (6.67). Here, in contrast to the partitioned approach above, the solution variables $\mathbf{d}$ and $\mathbf{z}$ are not held constant and directional derivatives with regard to these unknowns have to be considered, too. On the other hand, the contact virtual work $\mathbf{f}^c(\mathbf{d},\mathbf{z})$ and the mechanical contact constraints $C_{nj}\left(\mathbf{d},\mathbf{z}_j\right)$ and $\mathbf{C}_{\tau j}\left(\mathbf{d},\mathbf{z}_j\right)$ in (6.63), (6.65), and (6.66) are not influenced by the temperature $\boldsymbol{\theta}$ or the thermal LAGRANGE multipliers $\mathbf{z}_\theta$. From this, their linearizations are equal to those of Section 4.3 and thus are not discussed further.

Contribution to energy balance equation from contact

For the current iterate k, the linearization of the contribution to the energy balance equation from contact in (6.64) reads

$$\Delta \mathbf{f}_{\theta}^{c,k} = \begin{pmatrix} \mathbf{0} \\ -\Delta \mathbf{M}^{\mathrm{T}}\, \mathbf{z}_{\theta}^{k} - \mathbf{M}^{\mathrm{T}}\, \Delta \mathbf{z}_{\theta}^{k} \\ \Delta \mathbf{D}^{\mathrm{T}}\, \mathbf{z}_{\theta}^{k} + \mathbf{D}^{\mathrm{T}}\, \Delta \mathbf{z}_{\theta}^{k} \end{pmatrix} \tag{6.69}$$

It requires the evaluation of the directional derivatives of the Mortar matrices $\mathbf{D}$ and $\mathbf{M}$. These can be found in POPP et al. [110, 111]. For the further treatment of expression (6.69), the thermal LAGRANGE multiplier increment $\Delta \mathbf{z}_{\theta}^{k}$ is replaced by $\mathbf{z}_{\theta}^{k+1} - \mathbf{z}_{\theta}^{k}$. The directional derivatives of both matrices $\mathbf{D}$ and $\mathbf{M}$ are assembled in $\tilde{\mathbf{E}} \in \mathbb{R}^{(n_{sl}+n_m)\times(3n_{sl}+3n_m)}$ as

$$\left(\mathbf{0},\ \ -\Delta \mathbf{M}^{\mathrm{T}}\, \mathbf{z}_{\theta}^{k},\ \ \Delta \mathbf{D}^{\mathrm{T}}\, \mathbf{z}_{\theta}^{k}\right)^{\mathrm{T}} = \tilde{\mathbf{E}}\, \Delta \mathbf{d}_{\mathcal{SM}}^{k}, \tag{6.70}$$

where they are multiplied with the current LAGRANGE multiplier vector $\mathbf{z}_{\theta}^{k}$. Similar to (4.33), the vector $\Delta \mathbf{d}_{\mathcal{SM}}^{k}$ is a subset of the global displacement vector containing the entries from slave and master nodes $\mathcal{S}$ and $\mathcal{M}$.

Thermal contact condition

The linearized thermal contact condition (6.67) for each slave node $j \in \mathcal{S}$ reads as follows

$$\begin{aligned} \Delta r_{\theta j}^{cond,k} &= \Delta D_{jj}^{k}\, z_{\theta j}^{k} + D_{jj}^{k}\, \Delta z_{\theta j}^{k} \\ &\quad - \beta_c \left(\Delta D_{jj}^{k}\, \theta_{j}^{(1)k} - \sum_{l=1}^{n_m} \Delta M_{jl}^{k}\, \theta_{l}^{(2)k} + D_{jj}^{k}\, \Delta \theta_{j}^{(1)k} - \sum_{l=1}^{n_m} M_{jl}^{k}\, \Delta \theta_{l}^{(2)k} \right) \\ &= -r_{\theta j}^{cond,k} \qquad \forall\, j \in \mathcal{S}_k \ . \end{aligned} \tag{6.71}$$

Again, the equation is reformulated in terms of $\mathbf{z}_{\theta}^{k+1}$. Obtaining zero entries for inactive nodes $j \in \mathcal{I}$, the assembly of (6.67) is performed for active nodes $j \in \mathcal{A}$ only. It reads

$$\mathop{\mathsf{A}}_{j=1}^{n^a} \left(\Delta r_{\theta j}^{cond,k} + r_{\theta j}^{cond,k} \right) = \mathbf{Q}_{\mathcal{A}_k}\, \Delta \mathbf{d}_{\mathcal{SM}}^{k} + \mathbf{R}_{\mathcal{A}_k}\, \Delta \boldsymbol{\theta}_{\mathcal{SM}}^{k} + \mathbf{W}_{\mathcal{A}_k}\, \mathbf{z}_{\theta\mathcal{A}}^{k+1} + \mathbf{r}_{\theta\mathcal{A}}^{cond} \ . \tag{6.72}$$

Here, the matrices $\mathbf{Q}_{\mathcal{A}_k} \in \mathbb{R}^{n^a \times 3(n^{sl}+n^m)}$, $\mathbf{R}_{\mathcal{A}_k} \in \mathbb{R}^{n^a \times (n^{sl}+n^m)}$ and $\mathbf{W}_{\mathcal{A}_k} \in \mathbb{R}^{n^a \times n^a}$ are the assembled forms of all linearizations, the vector $\mathbf{r}_{\theta\mathcal{A}}^{cond} \in \mathbb{R}^{n^a}$ denotes the right hand side.

System of equations

The final linear system representing equations (6.63) - (6.67) can be written in terms of the displacement increments $\Delta \mathbf{d}$, the LAGRANGE multipliers $\mathbf{z}$, the temperature increments $\Delta \boldsymbol{\theta}$, and the thermal LAGRANGE multipliers $\mathbf{z}_{\theta}$. The blocks are written in compact form and the

iteration index k is dropped for the ease of notation:

$$\begin{bmatrix} \mathbf{K}_{\mathcal{N}}^{uu} & \mathbf{0} & \mathbf{K}_{\mathcal{N}}^{u\theta} & \mathbf{0} \\ \tilde{\mathbf{K}}_{\mathcal{M}}^{uu} & -\mathbf{M}_{\mathcal{A}}^{\mathrm{T}} & \mathbf{K}_{\mathcal{M}}^{u\theta} & \mathbf{0} \\ \tilde{\mathbf{K}}_{\mathcal{I}}^{uu} & \mathbf{0} & \mathbf{K}_{\mathcal{I}}^{u\theta} & \mathbf{0} \\ \tilde{\mathbf{K}}_{\mathcal{A}}^{uu} & \mathbf{D}_{\mathcal{A}}^{\mathrm{T}} & \mathbf{K}_{\mathcal{A}}^{u\theta} & \mathbf{0} \\ \mathbf{S}_{\mathcal{A}} & \mathbf{0} & \mathbf{0} & \mathbf{0} \\ \mathbf{F}_{\mathcal{A}} & \mathbf{T}_{\mathcal{A}} & \mathbf{0} & \mathbf{0} \\ \mathbf{K}_{\mathcal{N}}^{\theta u} & \mathbf{0} & \mathbf{K}_{\mathcal{N}}^{\theta\theta} & \mathbf{0} \\ \tilde{\mathbf{K}}_{\mathcal{M}}^{\theta u} & \mathbf{0} & \mathbf{K}_{\mathcal{M}}^{\theta\theta} & -\mathbf{M}_{\mathcal{A}}^{\mathrm{T}} \\ \tilde{\mathbf{K}}_{\mathcal{I}}^{\theta u} & \mathbf{0} & \mathbf{K}_{\mathcal{I}}^{\theta\theta} & \mathbf{0} \\ \tilde{\mathbf{K}}_{\mathcal{A}}^{\theta u} & \mathbf{0} & \mathbf{K}_{\mathcal{A}}^{\theta\theta} & \mathbf{D}_{\mathcal{A}}^{\mathrm{T}} \\ \mathbf{Q}_{\mathcal{A}} & \mathbf{0} & \mathbf{R}_{\mathcal{A}} & \mathbf{W}_{\mathcal{A}} \end{bmatrix} \cdot \begin{bmatrix} \Delta\mathbf{d} \\ \mathbf{z}_{\mathcal{A}} \\ \Delta\boldsymbol{\theta} \\ \mathbf{z}_{\theta\mathcal{A}} \end{bmatrix} = - \begin{bmatrix} \mathbf{r}_{\mathcal{N}} \\ \mathbf{r}_{\mathcal{M}} \\ \mathbf{r}_{\mathcal{I}} \\ \mathbf{r}_{\mathcal{A}} \\ \tilde{\mathbf{g}}_{\mathcal{A}} \\ \mathbf{0} \\ \mathbf{r}_{\theta\mathcal{N}} \\ \mathbf{r}_{\theta\mathcal{M}} \\ \mathbf{r}_{\theta\mathcal{I}} \\ \mathbf{r}_{\theta\mathcal{A}} \\ \mathbf{r}_{\theta\mathcal{A}}^{cond} \end{bmatrix} \tag{6.73}$$

The first four rows represent the linearized force equilibrium (6.63). Here, the blocks with the tilde symbol $\tilde{(\cdot)}$ imply the sum of the respective part of the stiffness matrix $\mathbf{K}^{uu}$ and linearization entries $\tilde{\mathbf{C}}$ from the contact force vector given in (4.33). For example, $\tilde{\mathbf{K}}_{\mathcal{M}}^{uu} = \mathbf{K}_{\mathcal{M}}^{uu} + \tilde{\mathbf{C}}_{\mathcal{M}}$ is the block associated with the master nodes $\mathcal{M}$. The mechanical normal contact condition (6.65) is placed in the fifth row, where the matrix $\mathbf{S}_{\mathcal{A}} \in \mathbb{R}^{n^a \times 3(n^{sl}+n^m)}$ contains all linearization entries from $\tilde{\mathbf{S}}_{\mathcal{A}}$ and $\tilde{\mathbf{M}}_{\mathcal{A}}$ in (4.34). The mechanical tangential contact condition enters the system in the sixth row. As stated above, the frictionless case with $\mathbf{z}_{\tau j} = \mathbf{0}$ for active nodes $j \in \mathcal{A}$ is considered here. Its linearization leads to the matrices $\mathbf{F}_{\mathcal{A}} \in \mathbb{R}^{2n^a \times 3n^{sl}}$ and $\mathbf{T}_{\mathcal{A}} \in \mathbb{R}^{2n^a \times 3n^a}$ containing the derivatives with respect to $\mathbf{d}$ and $\mathbf{z}$. The particular assembly of this subcase of frictional contact can be found in POPP et al. [111]. The energy balance equation is represented in rows seven to ten. Similar to above, blocks marked with the tilde symbol contain the respective part of the stiffness matrix $\mathbf{K}^{\theta u}$ and linearization entries $\tilde{\mathbf{E}}$ from equation (6.70). For example, the master node block reads $\tilde{\mathbf{K}}_{\mathcal{M}}^{\theta u} = \mathbf{K}_{\mathcal{M}}^{\theta u} + \tilde{\mathbf{E}}_{\mathcal{M}}$. And the thermal contact condition is placed in the eleventh row. The zero constraints for inactive nodes $j \in \mathcal{I}$ are not included in the above system of equations.

For the coupled system of equation considered here, structural and thermal LAGRANGE multipliers can easily be expressed in terms of displacement and temperature increments. This reads

$$\mathbf{z}_{\mathcal{A}} = \mathbf{D}^{-\mathrm{T}} \left(-\mathbf{r}_{\mathcal{A}} - \tilde{\mathbf{K}}_{\mathcal{A}}^{uu} \Delta\mathbf{d} - \tilde{\mathbf{K}}_{\mathcal{A}}^{u\theta} \Delta\boldsymbol{\theta} \right) \quad \text{and} \tag{6.74}$$

$$\mathbf{z}_{\theta\mathcal{A}} = \mathbf{D}^{-\mathrm{T}} \left(-\mathbf{r}_{\theta\mathcal{A}} - \tilde{\mathbf{K}}_{\mathcal{A}}^{\theta u} \Delta\mathbf{d} - \tilde{\mathbf{K}}_{\mathcal{A}}^{\theta\theta} \Delta\boldsymbol{\theta} \right) . \tag{6.75}$$

As before, this is achieved cheaply due to the diagonality of the mortar matrix $\mathbf{D}$. Inserting (6.74) and (6.75) into (6.73), one obtains the final system written in terms of displacement and

temperature increments only:

$$\begin{bmatrix} \mathbf{K}_{\mathcal{N}}^{uu} & \mathbf{K}_{\mathcal{N}}^{u\theta} \\ \tilde{\mathbf{K}}_{\mathcal{M}}^{uu} + \hat{\mathbf{M}}_{\mathcal{A}}^{\mathrm{T}} \tilde{\mathbf{K}}_{\mathcal{A}}^{uu} & \mathbf{K}_{\mathcal{M}}^{u\theta} + \hat{\mathbf{M}}_{\mathcal{A}}^{\mathrm{T}} \tilde{\mathbf{K}}_{\mathcal{A}}^{u\theta} \\ \tilde{\mathbf{K}}_{\mathcal{I}}^{uu} & \mathbf{K}_{\mathcal{I}}^{u\theta} \\ \mathbf{S}_{\mathcal{A}} & \mathbf{0} \\ \mathbf{T}_{\mathcal{A}} \mathbf{D}_{\mathcal{A}}^{\mathrm{T}} \tilde{\mathbf{K}}_{\mathcal{A}}^{uu} - \mathbf{F}_{\mathcal{A}} & \mathbf{T}_{\mathcal{A}} \mathbf{D}_{\mathcal{A}}^{\mathrm{T}} \tilde{\mathbf{K}}_{\mathcal{A}}^{u\theta} \\ \mathbf{K}_{\mathcal{N}}^{\theta u} & \mathbf{K}_{\mathcal{N}}^{\theta\theta} \\ \tilde{\mathbf{K}}_{\mathcal{M}}^{\theta u} + \hat{\mathbf{M}}_{\mathcal{A}}^{\mathrm{T}} \tilde{\mathbf{K}}_{\mathcal{A}}^{u\theta} & \mathbf{K}_{\mathcal{M}}^{\theta\theta} + \hat{\mathbf{M}}_{\mathcal{A}}^{\mathrm{T}} \tilde{\mathbf{K}}_{\mathcal{A}}^{\theta\theta} \\ \tilde{\mathbf{K}}_{\mathcal{I}}^{\theta u} & \mathbf{K}_{\mathcal{I}}^{\theta\theta} \\ \mathbf{W}_{\mathcal{A}} \mathbf{D}_{\mathcal{A}}^{\mathrm{T}} \tilde{\mathbf{K}}^{\theta u} - \mathbf{Q}_{\mathcal{A}} & \mathbf{W}_{\mathcal{A}} \mathbf{D}_{\mathcal{A}}^{\mathrm{T}} \tilde{\mathbf{K}}^{\theta\theta} - \mathbf{R}_{\mathcal{A}} \end{bmatrix} \cdot \begin{bmatrix} \Delta \mathbf{d} \\ \Delta \boldsymbol{\theta} \end{bmatrix} = - \begin{bmatrix} \mathbf{r}_{\mathcal{N}} \\ \mathbf{r}_{\mathcal{M}} + \hat{\mathbf{M}}_{\mathcal{A}}^{\mathrm{T}} \mathbf{r}_{\mathcal{A}} \\ \mathbf{r}_{\mathcal{I}} \\ \tilde{\mathbf{g}}_{\mathcal{A}} \\ \mathbf{T}_{\mathcal{A}} \mathbf{D}_{\mathcal{A}}^{\mathrm{T}} \mathbf{r}_{\mathcal{A}} \\ \mathbf{r}_{\theta\mathcal{N}} \\ \mathbf{r}_{\theta\mathcal{M}} + \hat{\mathbf{M}}_{\mathcal{A}}^{\mathrm{T}} \mathbf{r}_{\theta\mathcal{A}} \\ \mathbf{r}_{\theta\mathcal{I}} \\ \mathbf{W}_{\mathcal{A}} \mathbf{D}_{\mathcal{A}}^{\mathrm{T}} \mathbf{r}_{\theta\mathcal{A}} - \mathbf{r}_{\theta\mathcal{A}}^{cond} \end{bmatrix} \tag{6.76}$$

The system can be solved with standard or iterative solution techniques. In a post postprocessing step, the LAGRANGE multipliers are recovered from equations (6.74) and (6.75).

6.6 Examples

Considering thermomechanical contact problems, four examples are presented in this section. As solution schemes, the partitioned as well as the monolithic approach are applied. Accuracy and efficiency of the simulations performed in BACI are demonstrated. Assumptions are the same as in Section 4.6, occurring differences are specified.

6.6.1 Heat conduction over non matching grids

The first example presents the pressure dependent heat conduction over non-matching grids. Accuracy of numerical results is demonstrated by comparison with the analytical solution.

The two cubes in Figure 6.1 are modelled with St. VENANT-KIRCHHOFF's material law ($E = 400$, $\nu = 0.0$), the thermal conductivity is assumed to be $k_{\theta}^{(i)} = 52$. For the heat conduction over the contact surface, the pressure dependent linear model (6.11) with $\bar{\alpha}_c^{(i)} = 100$ is used. A temperature of 40 is applied to the bottom surface of the lower cube and of 20 to the top surface of the upper cube. There, additionally, a vertical displacement of $w = 0.15$ is prescribed. It is performed with 15 pseudo load steps in a quasistatic simulation.

As solution scheme, the partitioned approach is applied. In order to be able to compare with the analytical solution, effects are separated by neglecting the influence of the thermal field on the structural deformation. This results in a temperature independent material behavior and the partitioned approach converges after one solution of each field within a time step.

Figure 6.2 shows deformed configurations at different stages. When the two bodies come into contact, heat flux over the contact surface occurs. It is the same as in the bodies resulting from adjusted temperature gradients there. With growing contact pressure, the heat flux in the entire system increases and temperatures adapt accordingly.

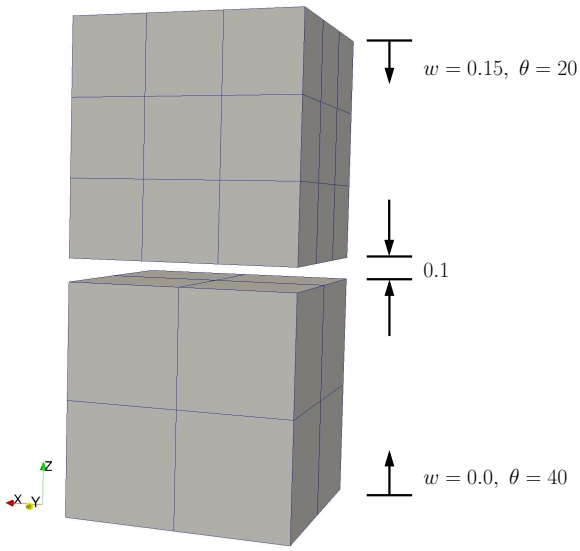

Figure 6.1: Heat conduction over non matching grids, setup and finite element discretization.

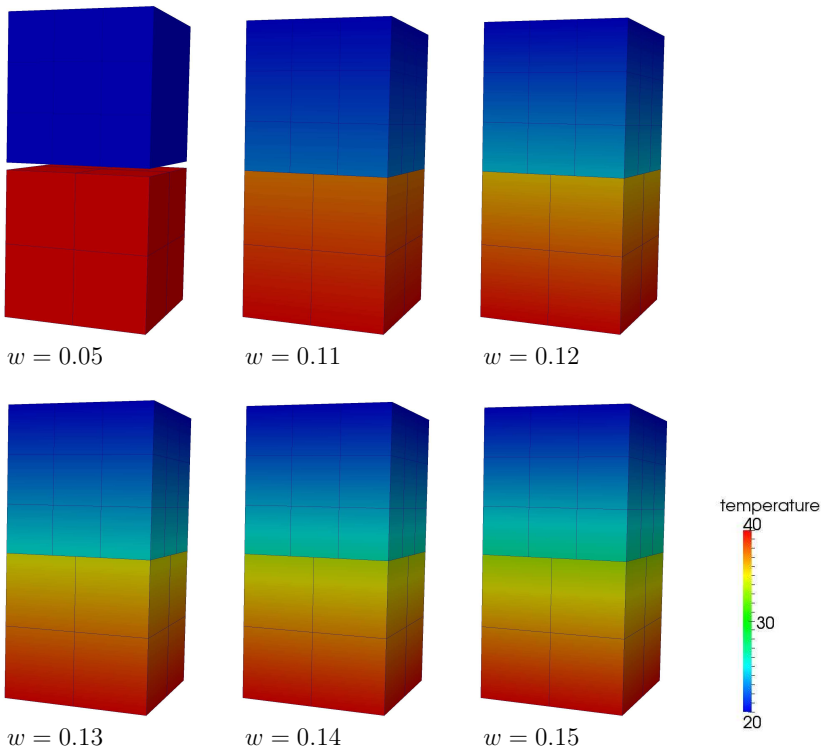

Figure 6.2: Heat conduction over non matching grids, temperature distribution at different deformed stages.

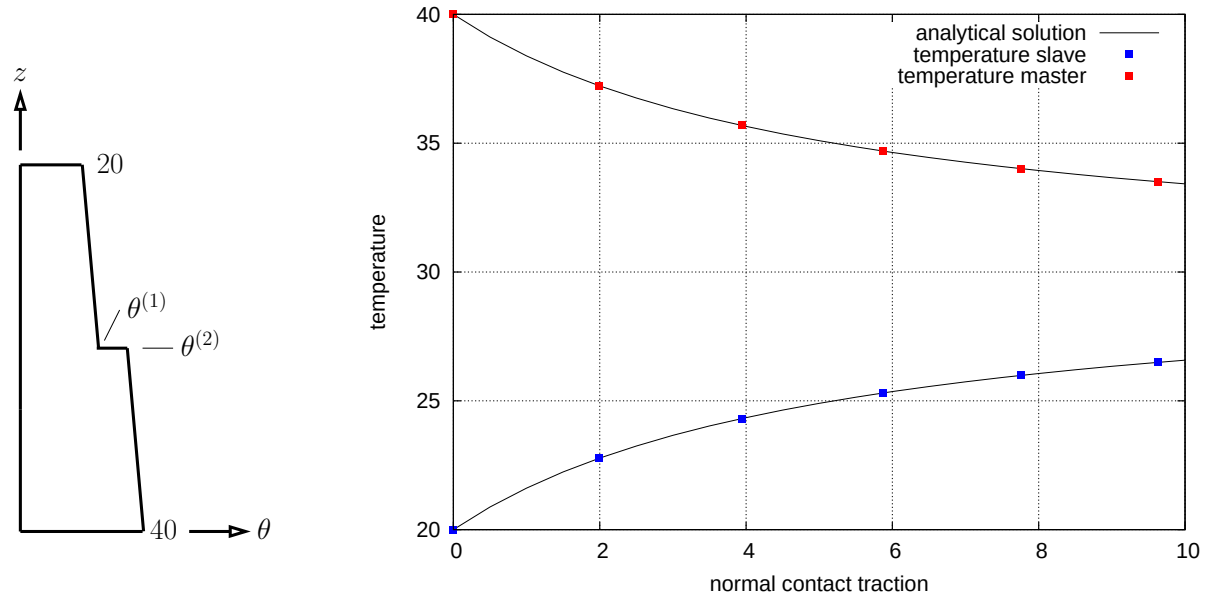

Figure 6.3: Heat conduction over non matching grids. Temperature distribution along a vertical axis through the entire system (left) and contact interface temperatures for changing contact pressure, comparison with analytical solution (right).

The temperature distribution along a vertical axis through the system is presented schematically on the left of Figure 6.3. The values at the contact interface, $\theta^{(1)}$ and $\theta^{(2)}$, depend on the normal contact pressure which is increasing with ongoing simulation. This numerically obtained relationship is plotted on the right of Figure 6.3 for five different stages. It is compared with the analytical solution, which can be evaluated for identical materials and equal heat transfer coefficients of both bodies. According to OANCEA and LAURSEN [101] and WRIGGERS and MIEHE [146], the analytical solution reads

$$\theta^{(1)} = \frac{40\,\eta + 20\,(1+\eta)}{1+2\,\eta}\,, \quad \theta^{(2)} = \frac{20\,\eta + 40\,(1+\eta)}{1+2\,\eta}\,, \quad \eta = \bar{\alpha}_c\,\frac{p_n}{2k}\,. \tag{6.77}$$

The agreement with the analytical solution is perfect as can be seen in Figure 6.3. Also the conduction of the heat flux over the non-matching contact interface is reproduced exactly due to using the mortar method.

6.6.2 Rotating disc

This example is dominated by frictional heating. It is constructed such that the amount of mechanical dissipation transferred to thermal energy can be determined analytically and the accuracy of capturing this basic phenomenon can be demonstrated.

The 3D problem setup is presented in Figure 6.4. It is made up of a block and a disc, both modelled with St. VENANT-KIRCHHOFF's material law ($E = 400000$, $\nu = 0.3$). The thermal conductivity and heat capacity are determined as $k_\theta^{(i)} = 52$ and $c^{(i)} = 4.2$ in each body. Frictional contact with $\mu = 0.35$ is assumed between block and disc. The heat transfer parameters of the

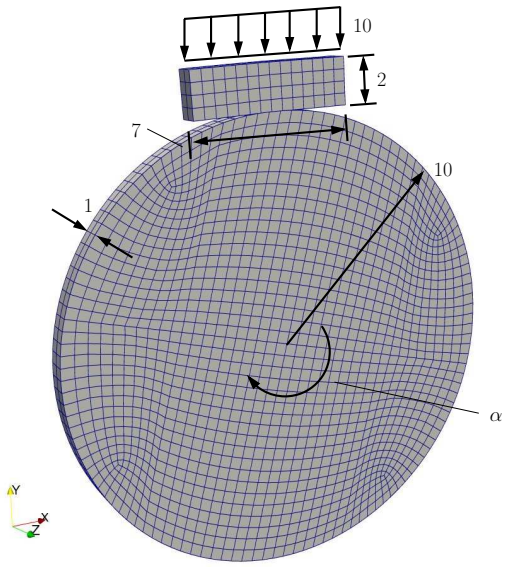

Figure 6.4: Rotating disc contact problem, problem setup and finite element discretization.

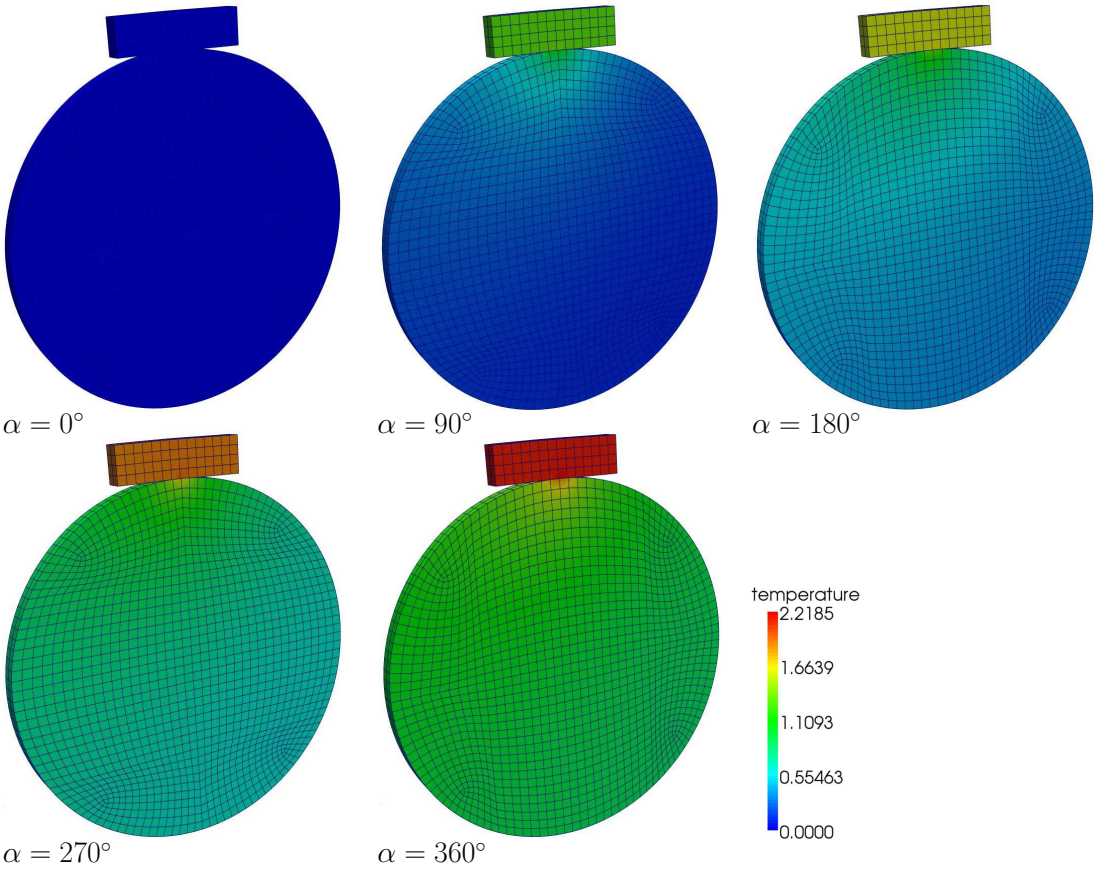

Figure 6.5: Rotating disc contact problem, temperature distribution for different rotation angles.

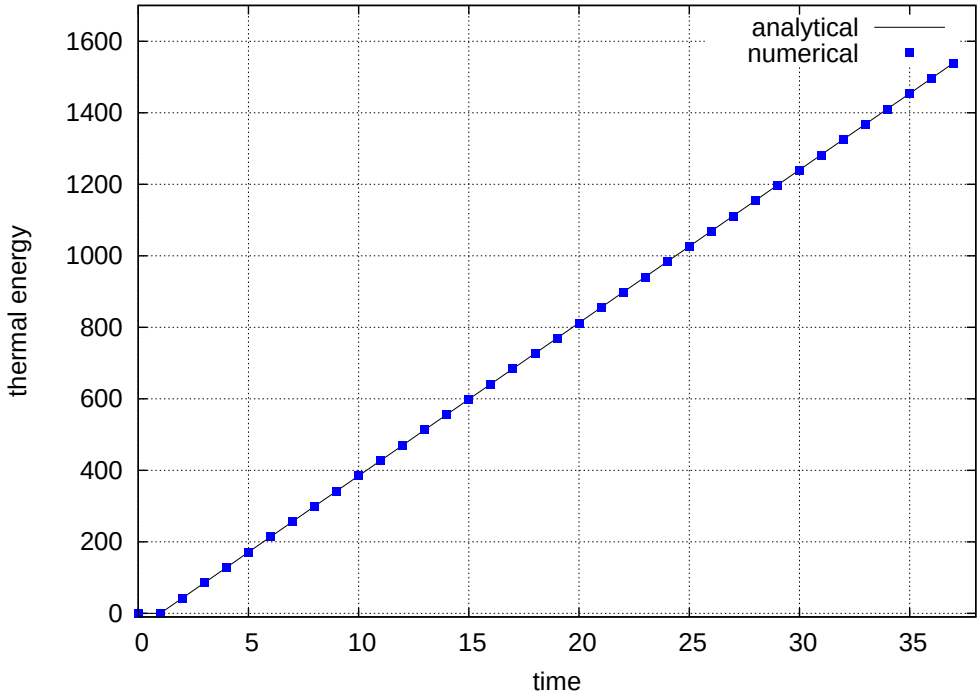

Figure 6.6: Rotating disc contact problem, thermal energy evolution in both bodies. Comparison of numerical results with analytical solution.

slave and master surfaces are determined to $\bar{\alpha}_c^{(i)} = 100$ using the model defined in (6.10). The loading of the problem is split into two parts: First, for $0 \leq t \leq 1$, the block is pressed onto the disc. Then, with holding the vertical pressure constant, the disc is rotated up to an angle of $\alpha_{\text{max}} = 360$ within $1 \leq t \leq 37$. The simulation is realized with a time step size of $\Delta t = 0.1$, the structural field is treated quasistatic, the thermal field resolved with the one-step-theta time discretization scheme ($\theta = 0.5$). The solution approach and mutual relationships are exactly those of example 6.6.1.

As result, in Figure 6.5, the temperature distribution for different rotation angles α is presented. It can clearly be seen that, with ongoing time t, the bodies are heated up due to mechanical dissipation transferred to thermal energy. Assuming rigid bodies, the analytical evolution of this quantity can be determined easily. For the numerical simulation, this assumption is approximated with high values of the YOUNG's moduli E in the bodies. Figure 6.6 shows the comparison of numerical results and analytical solution. A very good agreement can be observed which proves quantitatively the correct modeling of mechanical dissipation depending on slip increment and contact traction and its entire transformation to energy of the thermal field.

6.6.3 Temperature balancing blocks

This example is treated with the monolithic solution scheme. It demonstrates the high efficiency of the algorithm achieved from consistent linearization.

The setup is presented in Figure 6.7. Two blocks of different size are modelled with a geometrically linear element formulation and St. VENANT-KIRCHHOFF's material law ($E = 400$, $\nu =$

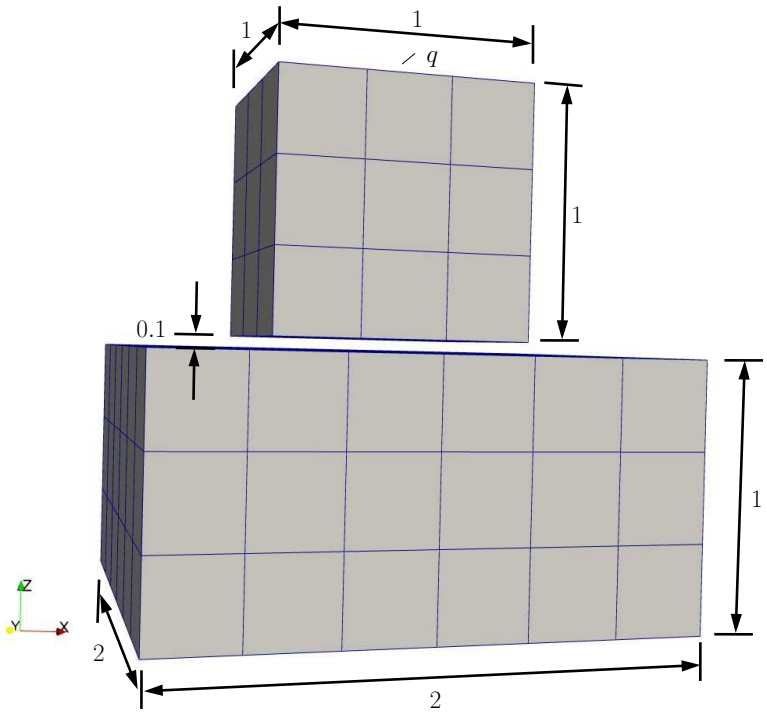

Figure 6.7: Temperature balancing blocks, problem setup and finite element discretization.

0.0). Thermal conductivity, heat capacity, and coefficient of thermal expansion are assumed to be $k_\theta^{(i)} = 5.2$, $c^{(i)} = 42$, and $\alpha_T = 0.0001$ in each body. The smaller block is fixed at its upper surface and the bigger one at its lower surface. In their initial states, the temperature in the whole system is 0 and the potential contact surfaces are placed with a distance of 0.1. Frictionless contact can take place, the thermal heat transfer parameters are both determined to $\bar{\alpha}_c^{(i)} = 1 \cdot 10^6$ using the constant model (6.10). This setup is loaded with a prescribed heat flux $q = 10000$ at the upper surface of the small body. It is hold constant at this value for the period $0 \leq t \leq 4$ and subsequently set to 0 for the remaining time $4 \leq t \leq 20$. The simulation is performed with a time step size of $\Delta t = 1$ using the one-step-theta method ($\theta = 0.5$) for time integration.

As results, deformed configurations at different stages are visualized in Figure 6.8. They are color coded by temperature distribution. It can clearly be seen that, during the first phase of energy supply, the upper block expands and, from there, comes into contact with the lower one. Then, the heating stops but the transfer of heat flux over the contact surface continues towards temperature balancing within the blocks.

The excellent performance of the applied algorithm is demonstrated in Table 6.1. It shows the evolution of the total residual for the challenging time step starting from $t = 2$. Within the time increment Δt, all remaining slave nodes come into contact. It can clearly be seen that, after this change in the active contact set, the residual is reduced quadratically. This is due to the consistent linearization of all displacement, temperature, and LAGRANGE multiplier dependent terms.

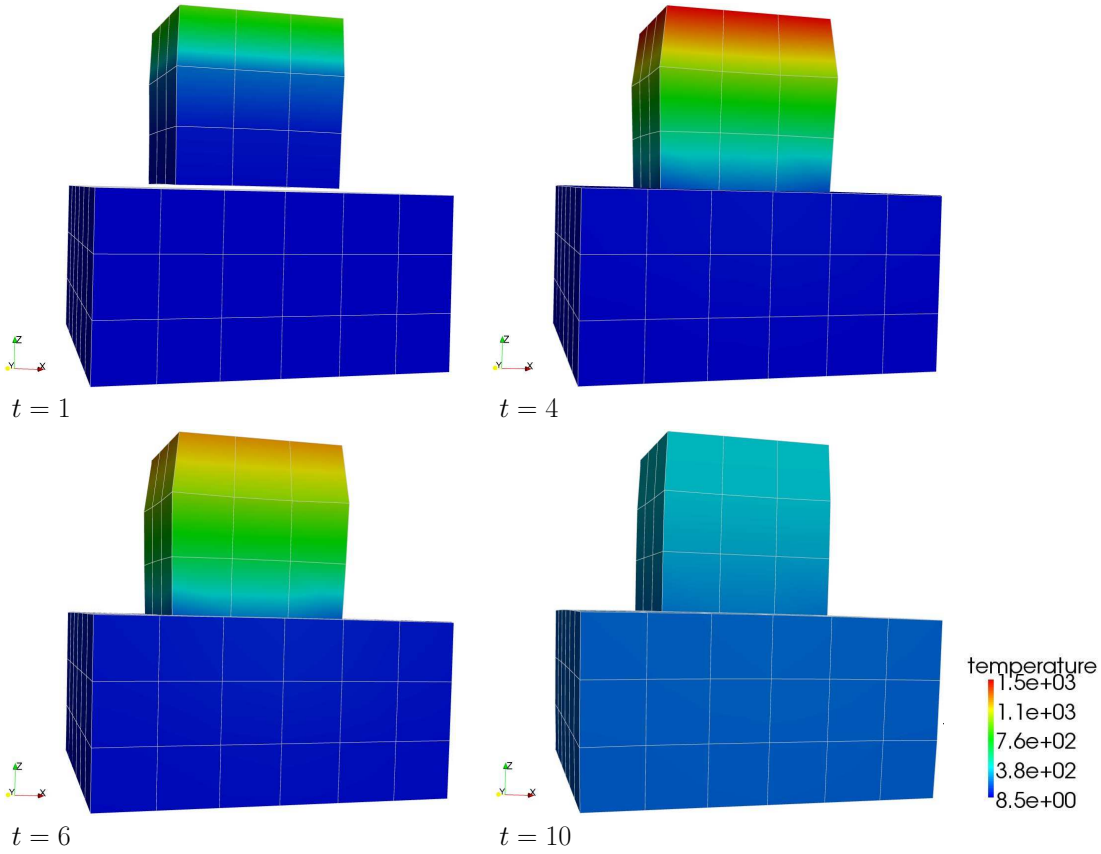

Figure 6.8: Temperature balancing blocks, deformed configurations and temperature distribution at different stages.

	First step with all nodes in contact
1	1.57e+03
2	5.15e+07 (*)
3	1.25e+06
4	1.45e+03
5	1.61e+01
6	4.05e−04
7	3.87e−08
Σ	7

(*) = change in active set

Table 6.1: Convergence behavior of the fully linearized monolithic solution scheme for the first step with all nodes in contact.

6.6.4 Block between plates

In this last example, all coupling terms of the described thermomechanical contact problem are considered. It demonstrates the suitability of the proposed solution algorithm to challenging problems with even extensive interactions of structural and thermal field.

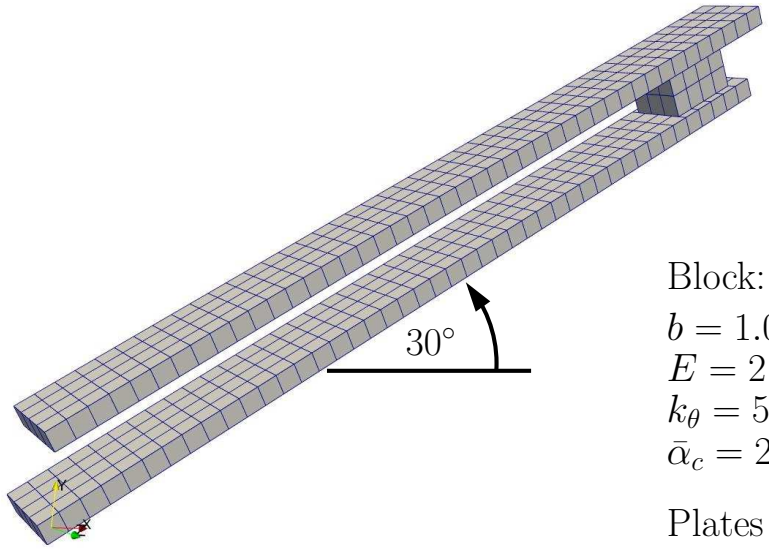

Block:
$b = 1.0,\ h = 0.6,\ t = 0.75$
$E = 21000,\ \nu = 0.0,\ \rho = 0.0078$
$k_\theta = 520000,\ c = 4.2,\ \alpha_T = 0.01$
$\bar{\alpha}_c = 2000,$ constant model

Plates (fixed):
$b = 11.0,\ h = 0.25,\ t = 1.0$
$k_\theta = 52,\ c = 4200$
$\bar{\alpha}_c = 200,$ constant model

Figure 6.9: Block between plates, problem setup and finite element discretization.

As shown in Figure 6.9, a block lies on a fixed inclined plate. With a normal inner distance of 0.60174, as second fixed plate is placed. From this, in its initial configuration, the block is not in contact with the upper plate. Frictional contact with $\mu = 0.2$ is assumed for both contact surface pairings, the initial temperature is 0 and St. VENANT-KIRCHHOFF's material law is applied. Additional parameters and measures are given in Figure 6.9. The system is loaded with a body force of 9.81 in negative y-direction.

The partitioned approach is used for solution. Here, the structural field is resolved with a generalized-alpha time integration scheme ($\alpha_f = 0.0,\ \alpha_m = 0.333,\ \beta = 0.444,\ \gamma = 0.833$) and the thermal one with the one-step-theta method ($\theta = 0.5$). The convergence criterion for both fields is assumed to be $\epsilon_u = \epsilon_\theta = 1 \cdot 10^{-6}$. The time step size is chosen to be $\Delta t = 2.5 \cdot 10^{-3}$.

Figure 6.10 shows configurations after $s = 10,\ 20, \ldots, 120$ steps. It can be observed that, because of the body force, the block starts frictional sliding ($s = 10 - 70$), which leads to heating and thermal expansion. Resulting from this, the sliding block comes into contact with the upper plate and gets stuck ($s = 80$). At this state, heat flows into both plates, the block cools, shrinks, looses contact with the upper plate and starts sliding again ($s = 90 - 120$).

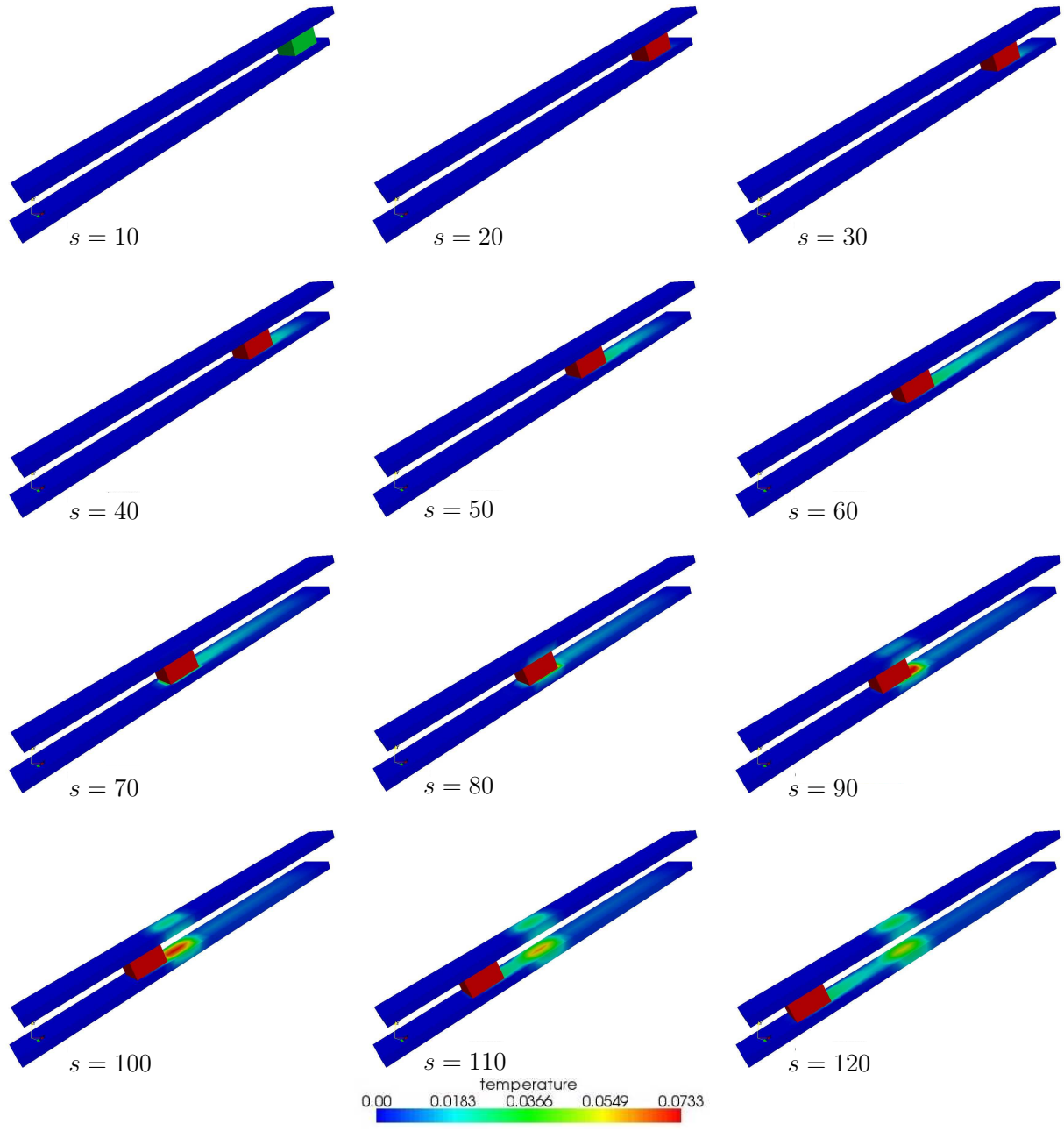

Figure 6.10: Block between plates, temperatures at deformed stages at steps $10, 20, \ldots, 120$. Frictional sliding with heating and thermal expansion $(s = 10 - 70)$, stuck due contact with the upper plate $(s = 80)$, cooling and shrinking and sliding again $(s = 90 - 120)$.

7 Conclusion and outlook

7.1 Conclusion

In this thesis, a 3D finite deformation frictional contact formulation is presented. As friction model, COULOMB's law is applied. The mortar method is chosen for contact surface discretization to overcome problems from node-to-segment approaches. It represents a weak formulation of contact constraints which yields a perfect quality of contact stresses, even for non-matching meshes. For constraint enforcement, the dual LAGRANGE multiplier method is used. It implies that no regularization of contact conditions is needed and allows, due to choosing them from a dual space, for an efficient elimination of these additional unknowns from the global system of equations. The tangential relative velocity, which is an essential quantity for finite sliding, is formulated in terms of the change of the mortar projection in order to obtain a frame indifferent rate measure. The solution is realized with a semi-smooth NEWTON method. Thus, all nonlinearities are treated within one single iterative scheme which leads to a highly efficient solution algorithm when combined with consistent linearization. The accuracy and robustness of the proposed formulation are demonstrated in four numerical examples. Here, comparisons of numerical results with analytical solutions show very good agreement. Convergence behavior of the semi-smooth NEWTON method in the context of finite deformations is also tested: The active set as well as the stick and the slip sets are efficiently located within only a few steps and quadratic convergence is obtained in the limit.

Additionally, this thesis contains the extension of the developed mortar contact formulation towards wear. On the one hand, it is performed using an internal state variable approach. Here, the distance between contacting bodies is increased by a so-called wear-gap. Two 2D numerical examples demonstrate that the proposed method captures wear effects qualitatively and quantitatively in an excellent manner. As the internal state variable approach is mainly suitable for a small amount of wear, on the other hand, it is modelled with contact surface evolution using an ALE approach resolved with a fractional-step strategy. It results in a LAGRANGEan step followed by an EULERian one where the mesh is adjusted due to wear. Here, the LAGRANGEan frictional contact formulation can be used with almost no modifications. It allows significant wear volumes as demonstrated in the third example considering this method.

In the last part of this work, a 3D fully coupled thermomechanical contact formulation is presented as an extension to the developed purely mechanical one. For the thermal field, the mortar method and dual LAGRANGE multipliers are also used for contact surface discretization and enforcement of constraints. This transfers the accompanying advantages, which are the correct heat flux transfer over non-matching meshes and the easy elimination of LAGRANGE multipliers. Coupling effects are resolved with a partitioned scheme and for frictionless contact, also with a monolithic scheme. Due to consistent linearization of all contact related terms, an excellent convergence behavior of the applied semi-smooth NEWTON method is obtained. Four numeri-

cal examples are presented. They demonstrate the accuracy of contact heat conduction and of frictional dissipation transferred to thermal energy when using the proposed methods. They also show the quadratic residual decrease of the monolithic approach and the stable capturing even of strongly coupled nonlinear phenomena in challenging problems.

7.2 Outlook

There are several issues that will require further consideration in the future.

As stated in Chapter 4, the algorithmic parameters c_n and c_t, introduced with the complementarity functions, do not influence the accuracy of results. But their choice may have consequences on the convergence behavior of the semi-smooth NEWTON method, especially for frictional contact problems with complicated alternating stick and slip regions. Although treated in several convergence studies, see LIEBERTSEDER [88], there is, except from the assumptions in Section 4.6.2, still no clear rule for their optimal determination. Here, future work could be worthwhile.

The evaluation of the weighted wear increment (5.11) and the mechanical dissipations in equations (6.43) and (6.49) are based on the tangential relative velocity defined in (2.57), which might not transform in an objective way. Additionally, this represents a little inconsistency as the frictional contact conditions are formulated in terms of expression (3.84), which is derived especially to obtain frame indifference, see Section 3.4.5. To overcome both, it would be worth striving for using the objective tangential relative slip increment (3.84) for the evaluation of the above given wear and thermomechanical quantities. However, as explained, this is not straightforward and would require additional approximations concerning the distribution of normal contact tractions, see Section 5.3.2. This is the reason why these alternative formulations have not yet been implemented, but only expressed exemplarily for the wear problem in equation (5.15). Future work should have a closer look at this topic.

The wear formulation using an internal state variable approach is derived and implemented for 3D, but only 2D examples are tested and consequently presented within this work. This should be extended for 3D. The ALE approach resolved with a fractional-step strategy is formulated and implemented only for 2D linearly interpolated elements. Quadratic interpolation and the extension to 3D are of course desirable.

The monolithic solution scheme for finite deformation thermomechanical contact problems is realized for frictionless contact and a constant model for the heat transfer over the contact surface. Enhancing it towards a linear model and frictional contact brings significant more dependencies of structural and thermal fields into the problem formulation. Its implementation is straightforward and requires extensive linearizations. It should also be considered in future work.

Bibliography

[1] C. AGELET DE SARACIBAR, M. CHIUMENTI, *On the numerical modeling of frictional wear phenomena*, Computer Methods in Applied Mechanics and Engineering **177** (1999) 401–426.

[2] P. ALART, A. CURNIER, *A mixed formulation for frictional contact problems prone to Newton like solution methods*, Computer Methods in Applied Mechanics and Engineering **92** (1991) 353–375.

[3] D. ALDHAM, J. WARBURTON, R.E. PENDLEBURY, *The unlubricated fretting wear of mild steel in air*, Wear **106** (1985) 177–201.

[4] J.F. ARCHARD, *Contact and rubbing of flat surfaces*, Journal of Applied Physics **24** (1953) 981–988.

[5] F. ARMERO, E. LOVE, *An arbitrary Lagrangian-Eulerian finite element method for finite strain plasticity*, International Journal for Numerical Methods in Engineering **57** (2003) 471–508.

[6] J.T. BATINA, *Unsteady Euler algorithm with unstructured dynamic mesh for complex-aircraft aerodynamic analysis*, AIAA Journal **29** (1991) 327–333.

[7] F.B. BELGACEM, *The Mortar finite element method with Lagrange multipliers*, Numerische Mathematik **84** (1999) 173–197.

[8] F.B. BELGACEM, P. HILD, P. LABORDE, *The mortar finite element method for contact problems*, Mathematical and Computer Modelling **28** (1998) 263–271.

[9] T. BELYTSCHKO, W.K. LIU, B. MORAN, *Nonlinear finite elements for continua and structures*, Wiley, 2000.

[10] D.J. BENSON, J.O. HALLQUIST, *A single surface contact algorithm for the post-buckling analysis of shell structures*, Computer Methods in Applied Mechanics and Engineering **78** (1990) 141–163.

[11] C. BERNARDI, Y. MADAY, A.T. PATERA, *A new nonconforming approach to domain decomposition: the mortar element method*, Nonlinear partial differential equations and their applications (1994) 13–51.

[12] S. BRUNSSEN, F. SCHMID, M. SCHÄFER, B.I. WOHLMUTH, *A fast and robust iterative solver for nonlinear contact problems using a primal-dual active set strategy and algebraic multigrid*, International Journal for Numerical Methods in Engineering **69** (2007) 524–543.

[13] T. BUCHNER, *Analyse der Tangentialbedingungen im reibungsbehafteten Finite-Element Kontakt*, Semesterarbeit, Institute for Computational Mechanics, Technische Universität München (2009).

[14] V. CHAWLA, T.A. LAURSEN, *Energy consistent algorithms for frictional contact problems*, International Journal for Numerical Methods in Engineering **42** (1998) 799–827.

[15] P.W. CHRISTENSEN, *A semi-smooth Newton method for elasto-plastic contact problems*, International Journal of Solids and Structures **39** (2002) 2323 – 2341.

[16] P.W. CHRISTENSEN, A. KLARBRING, J.S. PANG, N. STRÖMBERG, *Formulation and comparison of algorithms for frictional contact problems*, International Journal for Numerical Methods in Engineering **42** (1998) 145–173.

[17] M. CRISFIELD, *Non-linear finite element analysis of solids and structures*, vol. 2 advanced topics, Wiley, 1997.

[18] M. CRISFIELD, *Non-linear finite element analysis of solids and structures*, vol. 1, Wiley, 1998.

[19] C. DANOWSKI, V. GRAVEMEIER, L. YOSHIHARA, W.A. WALL, *A monolithic computational approach to thermo-structure interaction*, in preparation.

[20] L. DE LORENZIS, I. TEMIZER, P. WRIGGERS, G. ZAVARISE, *A large deformation frictional contact formulation using NURBS-based isogeometric analysis*, International Journal for Numerical Methods in Engineering **87** (2011) 1278 – 1300.

[21] H.B. DHIA, M. TORKHANI, *Modeling and computation of fretting wear of structures under sharp contact*, International Journal for Numerical Methods in Engineering (2011) 61–83.

[22] T. DICKOPF, R. KRAUSE, *Efficient simulation of multi-body contact problems on complex geometries: A flexible decomposition approach using constrained minimization*, International Journal for Numerical Methods in Engineering **77** (2009) 1834–1862.

[23] J. DING, S.B. LEEN, I.R. MCCOLL, *The effect of slip regime on fretting wear-induced stress evolution*, International Journal of Fatigue **26** (2004) 521 – 531.

[24] T. ERHART, W.A. WALL, E. RAMM, *Robust adaptive remeshing strategy for large deformation, transient impact simulations*, International Journal for Numerical Methods in Engineering **65** (2006) 2139–2166.

[25] C.A. FELIPPA, K.C. PARK, C. FARHAT, *Partitioned analysis of coupled mechanical systems*, Computer Methods in Applied Mechanics and Engineering **190** (2001) 3247–3270.

[26] B.A. FINLAYSON, *The method of weighted residuals and variational principles with application in fluid mechanics, heat and mass transfer*, vol. 87, Academic Press, 1972.

[27] K.A. FISCHER, P. WRIGGERS, *Frictionless 2D contact formulations for finite deformations based on the mortar method*, Computational Mechanics **36** (2005) 226–244.

[28] K.A. FISCHER, P. WRIGGERS, *Mortar based frictional contact formulation for higher order interpolations using the moving friction cone*, Computer Methods in Applied Mechanics and Engineering **195** (2006) 5020–5036.

[29] B. FLEMISCH, B.I. WOHLMUTH, *Stable Lagrange multipliers for quadrilateral meshes of curved interfaces in 3D*, Computer Methods in Applied Mechanics and Engineering **196** (2007) 1589–1602.

[30] J. FOLEY, *Computer Graphics: Principles and Practice*, Addison-Wesley, 1997.

[31] D. FRANKE, A. DÜSTER, V. NÜBEL, E. RANK, *A comparison of the h-, p-, hp-, and rp-version of the FEM for the solution of the 2d Hertzian contact problem*, Computational Mechanics **45** (2010) 513–522.

[32] D. FRANKE, A. DÜSTER, E. RANK, *Computational contact mechanics based on the rp-version of the finite element method*, International Journal of Computational Methods **8** (2011) 493–512.

[33] M. FRENZEL, *Advanced structural finite element modeling of arterial walls for patient-specific geometries*, Ph.D. thesis, Technische Universität München (2009).

[34] M.W. GEE, *Effiziente Lösungsstrategien in der nichtlinearen Schalenmechanik*, Ph.D. thesis, Universität Stuttgart (2004).

[35] M. GITTERLE, A. POPP, M.W. GEE, W.A. WALL, *Finite deformation frictional mortar contact using a semi-smooth Newton method with consistent linearization*, International Journal for Numerical Methods in Engineering **84** (2010) 543–571.

[36] C. HAGER, S. HÜEBER, B.I. WOHLMUTH, *A stable energy-conserving approach for frictional contact problems based on quadrature formulas*, International Journal for Numerical Methods in Engineering **73** (2008) 205–225.

[37] J. HALLQUIST, G. GOUDREAU, D. BENSON, *Sliding interfaces with contact-impact in large-scale Lagrangian computations*, Computer Methods in Applied Mechanics and Engineering **51** (1985) 107–137.

[38] G. HANSEN, *A Jacobian-free Newton Krylov method for mortar-discretized thermomechanical contact problems*, Journal of Computational Physics **230** (2011) 6546–6562.

[39] S. HARTMANN, *Kontaktanalyse dünnwandiger Strukturen bei großen Deformationen*, Ph.D. thesis, Universität Stuttgart (2007).

[40] S. HARTMANN, S. BRUNSSEN, E. RAMM, B.I. WOHLMUTH, *Unilateral non-linear dynamic contact of thin-walled structures using a primal-dual active set strategy*, International Journal for Numerical Methods in Engineering **70** (2007) 883–912.

[41] S. HARTMANN, J. OLIVER, R. WEYLER, J.C. CANTE, J.A. HERNANDEZ, *A contact domain method for large deformation frictional contact problems. Part 2: Numerical aspects*, Computer Methods in Applied Mechanics and Engineering **198** (2009) 2607–2631.

[42] S. HARTMANN, R. WEYLER, J.C. OLIVER, J. HERNANDEZ, *A 3D frictionless contact domain method for large deformation problems*, Computer Modeling in Engineering and Sciences **55** (2012) 211 – 269.

[43] P. HEINTZ, P. HANSBO, *Stabilized Lagrange multiplier methods for bilateral elastic contact with friction*, Computer Methods in Applied Mechanics and Engineering **195** (2006) 4323–4333.

[44] C. HESCH, *Mechanische Integratoren für Kontaktvorgänge deformierbarer Körper unter grossen Verzerrungen*, Ph.D. thesis, Universität Siegen (2008).

[45] C. HESCH, P. BETSCH, *A mortar method for energy-momentum conserving schemes in frictionless dynamic contact problems*, International Journal for Numerical Methods in Engineering **77** (2009) 1468–1500.

[46] C. HESCH, P. BETSCH, *Transient three-dimensional domain decomposition problems: Frame-indifferent mortar constraints and conserving integration*, International Journal for Numerical Methods in Engineering **82** (2010) 329–358.

[47] C. HESCH, P. BETSCH, *Energy-momentum consistent algorithms for dynamic thermomechanical problems - Application to mortar domain decomposition problems*, International Journal for Numerical Methods in Engineering **86** (2011) 1277–1302.

[48] C. HESCH, P. BETSCH, *Transient 3d contact problems - NTS method: mixed methods and conserving integration*, Computational Mechanics **48** (2011) 437–449.

[49] C. HESCH, P. BETSCH, *Transient three-dimensional contact problems: mortar method. Mixed methods and conserving integration*, Computational Mechanics **48** (2011) 461–475.

[50] M.R. HESTENES, *Multiplier and gradient methods*, Journal of Optimization Theory and Applications **4** (1969) 303–320.

[51] D. HILLS, D. NOWELL, *Mechanics of Fretting Fatigue*, Kluwer Academic Publishers, 1994.

[52] M. HINTERMÜLLER, K. ITO, K. KUNISCH, *The primal-dual active set strategy as a semismooth Newton method*, SIAM Journal on Optimization **13** (2002) 865–888.

[53] G.A. HOLZAPFEL, *Nonlinear solid mechanics - a continuum approach for engineering*, Wiley, 2000.

[54] S. HÜEBER, *Discretization techniques and efficient algorithms for contact problems*, Ph.D. thesis, Universität Stuttgart (2008).

[55] S. HÜEBER, A. MATEI, B.I. WOHLMUTH, *Efficient algorithms for problems with friction*, SIAM Journal on Scientific Computing **29** (2007) 70–92.

[56] S. HÜEBER, G. STADLER, B.I. WOHLMUTH, *A primal-dual active set algorithm for three-dimensional contact problems with Coulomb friction*, SIAM Journal on Scientific Computing **30** (2008) 572–596.

[57] S. HÜEBER, B.I. WOHLMUTH, *A primal-dual active set strategy for non-linear multibody contact problems*, Computer Methods in Applied Mechanics and Engineering **194** (2005) 3147–3166.

[58] S. HÜEBER, B.I. WOHLMUTH, *Thermo-mechanical contact problems on non-matching meshes*, Computer Methods in Applied Mechanics and Engineering **198** (2009) 1338 – 1350.

[59] S. HÜEBER, B.I. WOHLMUTH, *Equilibration techniques for solving contact problems with coulomb friction*, Computer Methods in Applied Mechanics and Engineering **205 - 208** (2012) 29–45.

[60] A. HUERTA, F. CASADEI, *New ALE applications in non-linear fast-transient solid dynamics*, Engineering Computations **11** (1994) 317 – 345.

[61] T.J.R. HUGHES, *The finite element method: linear static and dynamic finite analysis*, Dover Publications, 1987.

[62] P.L. HURRICKS, *The mechanism of fretting wear - a review*, Wear **15** (1970) 389–409.

[63] P. IREMAN, A. KLARBRING, N. STRÖMBERG, *Finite element algorithms for thermoelastic wear problems*, European Journal of Mechanics - A/Solids **21** (2002) 423 – 440.

[64] P. IREMAN, A. KLARBRING, N. STRÖMBERG, *A model of damage coupled to wear*, International Journal of Solids and Structures **40** (2003) 2957–2974.

[65] O. JIN, S. MALL, *Influence of contact configuration on fretting fatigue behavior of Ti-6Al-4V under independent pad displacement condition*, International Journal of Fatigue **24** (2002) 1243 – 1253.

[66] O. JIN, S. MALL, *Effects of slip on fretting behavior: experiments and analyses*, Wear **256** (2004) 671 – 684.

[67] A.A. JOHNSON, T.E. TEZDUYAR, *Mesh update strategies in parallel finite element computations of flow problems with moving boundaries and interfaces*, Computer Methods in Applied Mechanics and Engineering **119** (1994) 73–94.

[68] K. JOHNSON, *Contact Mechanics*, Cambridge University Press, 1985.

[69] F. JOURDAN, *Numerical wear modeling in dynamics and large strains: Application to knee joint prostheses*, Wear **261** (2006) 283–292.

[70] N. KIKUCHI, J.T. ODEN, *Contact problems in elasticity: A study of variational inequalities and finite element methods*, Society for Industrial and Applied Mathematics (SIAM), 1988.

[71] T. KIM, J. DOLBOW, T.A. LAURSEN, *A mortared finite element method for frictional contact on arbitrary interfaces*, Computational Mechanics **39** (2007) 223–235.

[72] D.E. KIOUSIS, T.C. GASSER, G.A. HOLZAPFEL, *Smooth contact strategies with emphasis on the modeling of balloon angioplasty with stenting*, International Journal for Numerical Methods in Engineering **75** (2008) 826–855.

[73] A. KONYUKHOV, K. SCHWEIZERHOF, *Covariant description for frictional contact problems*, Computational Mechanics **35** (2005) 190–213.

[74] A. KONYUKHOV, K. SCHWEIZERHOF, *On the solvability of closest point projection procedures in contact analysis: Analysis and solution strategy for surfaces of arbitrary geometry*, Computer Methods in Applied Mechanics and Engineering **197** (2008) 3045–3056.

[75] A. KONYUKHOV, K. SCHWEIZERHOF, *Incorporation of contact for high-order finite elements in covariant form*, Computer Methods in Applied Mechanics and Engineering **198** (2009) 1213–1223.

[76] T. KOZIARA, N. BICANIC, *Semismooth Newton method for frictional contact between pseudo-rigid bodies*, Computer Methods in Applied Mechanics and Engineering **197** (2008) 2763–2777.

[77] U. KÜTTLER, W.A. WALL, *Fixed-point fluid-structure interaction solvers with dynamic relaxation*, Computational Mechanics **43** (2008) 61–72.

[78] B.P. LAMICHHANE, R.P. STEVENSON, B.I. WOHLMUTH, *Higher order mortar finite element methods in 3D with dual Lagrange multiplier bases*, Numerische Mathematik **102** (2005) 93–121.

[79] B.P. LAMICHHANE, B.I. WOHLMUTH, *Higher order dual Lagrange multiplier spaces for mortar finite element discretizations*, Calcolo **39** (2002) 219–237.

[80] B.P. LAMICHHANE, B.I. WOHLMUTH, *Biorthogonal bases with local support and approximation properties*, Mathematics of Computation **76** (2007) 233–249.

[81] T.A. LAURSEN, *Formulation and treatment of frictional contact problems using finite elements*, Ph.D. thesis, Stanford University (1992).

[82] T.A. LAURSEN, *On the development of thermodynamically consistent algorithms for thermomechanical frictional contact*, Computer Methods in Applied Mechanics and Engineering **177** (1999) 273 – 287.

[83] T.A. LAURSEN, *Computational contact and impact mechanics*, Springer, 2002.

[84] T.A. LAURSEN, M.A. PUSO, J. SANDERS, *Mortar contact formulations for deformable-deformable contact: past contributions and new extensions for enriched and embedded interface formulations*, Computer Methods in Applied Mechanics and Engineering **205 - 208** (2012) 3 – 15.

[85] T.A. LAURSEN, J.C. SIMO, *A continuum-based finite element formulation for the implicit solution of multibody, large deformation-frictional contact problems*, International Journal for Numerical Methods in Engineering **36** (1993) 3451–3485.

[86] J. LENGIEWICZ, J. KORELC, S. STUPKIEWICZ, *Automation of finite element formulations for large deformation contact problems*, International Journal for Numerical Methods in Engineering **85** (2011) 1252–1279.

[87] J. LENGIEWICZ, S. STUPKIEWICZ, *Continuum framework for finite element modelling of finite wear*, Computer Methods in Applied Mechanics and Engineering **205 - 208** (2012) 178–188.

[88] J. LIEBERTSEDER, *Convergence behavior in contact simulation depending on two algorithmic parameters*, Technical report, Institute for Computational Mechanics, Technische Universität München (2011).

[89] C. LINDER, *An arbitrary Lagrangian-Eulerian finite element formulation for dynamics and finite strain plasticity models*, Master's thesis, Universität Stuttgart (2003).

[90] R. LÖHNER, C. YANG, *Improved ALE mesh velocities for moving bodies*, Communications in Numerical Methods in Engineering **12** (1996) 599–608.

[91] M. LONG, H. RACK, *Titanium alloys in total joint replacements - materials science perspective*, Biomaterials **19** (1998) 1621–1639.

[92] J.J. MADGE, S.B. LEEN, I.R. MCCOLL, P.H. SHIPWAY, *Contact-evolution based prediction of fretting fatigue life: Effect of slip amplitude*, Wear **262** (2007) 1159–1170.

[93] J.J. MADGE, S.B. LEEN, P.H. SHIPWAY, *The critical role of fretting wear in the analysis of fretting fatigue*, Wear **263** (2007) 542–551.

[94] I.R. MCCOLL, J. DING, S.B. LEEN, *Finite element simulation and experimental validation of fretting wear*, Wear **256** (2004) 1114 – 1127.

[95] T.W. MCDEVITT, T.A. LAURSEN, *A mortar-finite element formulation for frictional contact problems*, International Journal for Numerical Methods in Engineering **48** (2000) 1525–1547.

[96] H.C. MENG, K.C. LUDEMA, *Wear models and predictive equations: their form and content*, Wear **181 - 183, Part 2** (1995) 443 – 457.

[97] J.F. MOLINARI, M. ORTIZ, R. RADOVITZKY, E.A. REPETTO, *Finite-element modeling of dry sliding wear in metals*, Engineering Computations **18** (2001) 592 – 610.

[98] Z. MRÓZ, S. STUPKIEWICZ, *An anisotropic friction and wear model*, International Journal of Solids and Structures **31** (1994) 1113 – 1131.

[99] R. NEUGEBAUER, T. ALTAN, M. GEIGER, M. KLEINER, A. STERZING, *Sheet metal forming at elevated temperatures*, CIRP Annals - Manufacturing Technology **55** (2006) 793–816.

[100] J. NITSCHE, *Über ein Variationsprinzip zur Lösung von Dirichlet-Problemen bei Verwendung von Teilräumen, die keinen Randbedingungen unterworfen sind*, Abhandlungen aus dem Mathematischen Seminar der Universiät Hamburg **36** (1971) 9–15.

[101] V.G. OANCEA, T.A. LAURSEN, *A finite element formulation of thermomechanical rate-dependent frictional sliding*, International Journal for Numerical Methods in Engineering **40** (1997) 4275–4311.

[102] J. OLIVER, S. HARTMANN, J. CANTE, R. WEYLER, J.A. HERNANDEZ, *A contact domain method for large deformation frictional contact problems. Part 1: Theoretical basis*, Computer Methods in Applied Mechanics and Engineering **198** (2009) 2591–2606.

[103] M. ÖQVIST, *Numerical simulations of mild wear using updated geometry with different step size approaches*, Wear **249** (2001) 6–11.

[104] P. PÕDRA, S. ANDERSSON, *Simulating sliding wear with finite element method*, Tribology International **32** (1999) 71–81.

[105] V. PADMANABHAN, T.A. LAURSEN, *A framework for development of surface smoothing procedures in large deformation frictional contact analysis*, Finite Elements in Analysis and Design **37** (2001) 173–198.

[106] P. PAPADOPOULOS, R.L. TAYLOR, *A mixed formulation for the finite element solution of contact problems*, Computer Methods in Applied Mechanics and Engineering **94** (1992) 373–389.

[107] C. PAULIN, S. FOUVRY, C. MEUNIER, *Finite element modelling of fretting wear surface evolution: Application to a Ti-6A1-4V contact*, Wear **264** (2008) 26–36.

[108] G. PIETRZAK, A. CURNIER, *Large deformation frictional contact mechanics: continuum formulation and augmented Lagrangian treatment*, Computer Methods in Applied Mechanics and Engineering **177** (1999) 351–381.

[109] V.L. POPOV, *Contact mechanics and friction, pysical principles and applications*, Springer, 2010.

[110] A. POPP, M.W. GEE, W.A. WALL, *A finite deformation mortar contact formulation using a primal-dual active set strategy*, International Journal for Numerical Methods in Engineering **79** (2009) 1354–1391.

[111] A. POPP, M. GITTERLE, M.W. GEE, W.A. WALL, *A dual mortar approach for 3D finite deformation contact with consistent linearization*, International Journal for Numerical Methods in Engineering **83** (2010) 1428–1465.

[112] A. POPP, B.I. WOHLMUTH, M.W. GEE, W.A. WALL, *Dual quadratic mortar finite element methods for 3D finite deformation contact*, SIAM Journal on Scientific Computing **in press**.

[113] M.J.D. POWELL, *A method for nonlinear constraints in minimization problems*, Optimization (1969) 283–298.

[114] M.A. PUSO, *A 3D mortar method for solid mechanics*, International Journal for Numerical Methods in Engineering **59** (2004) 315–336.

[115] M.A. PUSO, T.A. LAURSEN, *A 3D contact smoothing method using Gregory patches*, International Journal for Numerical Methods in Engineering **54** (2002) 1161–1194.

[116] M.A. PUSO, T.A. LAURSEN, *A mortar segment-to-segment contact method for large deformation solid mechanics*, Computer Methods in Applied Mechanics and Engineering **193** (2004) 601–629.

[117] M.A. PUSO, T.A. LAURSEN, *A mortar segment-to-segment frictional contact method for large deformations*, Computer Methods in Applied Mechanics and Engineering **193** (2004) 4891–4913.

[118] M.A. PUSO, T.A. LAURSEN, J. SOLBERG, *A segment-to-segment mortar contact method for quadratic elements and large deformations*, Computer Methods in Applied Mechanics and Engineering **197** (2008) 555–566.

[119] L. QI, J. SUN, *A nonsmooth version of Newton's method*, Mathematical Programming **58** (1993) 353–367.

[120] E. RABINOWICZ, *Friction and wear of materials*, 2nd ed., Wiley, 1995.

[121] A. RODRÍGUEZ-FERRAN, F. CASADEI, A. HUERTA, *ALE stress update for transient and quasistatic processes*, International Journal for Numerical Methods in Engineering **43** (1998) 241–262.

[122] A. RODRÍGUEZ-FERRAN, A. PÉREZ-FOGUET, A. HUERTA, *Arbitrary Lagrangian - Eulerian (ALE) formulation for hyperelastoplasticity*, International Journal for Numerical Methods in Engineering **53** (2002) 1831–1851.

[123] L. SALLES, L. BLANC, F. THOUVEREZ, A.M. GOUSKOV, *Dynamic analysis of fretting-wear in friction contact interfaces*, Journal of Engineering for Gas Turbines and Power **132** (2010) 1513 – 1524.

[124] J.C. SIMO, J.E. MARSDEN, P.S. KRISHNAPRASAD, *The Hamiltonian structure of nonlinear elasticity: The material and convective representations of solids, rods, and plates*, Archive for Rational Mechanics and Analysis **104** (1988) 125–183.

[125] J.C. SIMO, C. MIEHE, *Associative coupled thermoplasticity at finite strains: Formulation, numerical analysis and implementation*, Computer Methods in Applied Mechanics and Engineering **98** (1992) 41–104.

[126] J.C. SIMO, N. TARNOW, *The discrete energy-momentum method. Conserving algorithms for nonlinear elastodynamics*, Zeitschrift für Angewandte Mathematik und Physik (ZAMP) **43** (1992) 757–792.

[127] K.N. SMITH, P. WATSON, T.H. TOPPER, *A stress-strain function for the fatigue of metals*, Journal of Materials **4** (1970) 767–778.

[128] N. STRÖMBERG, *An augmented Lagrangian method for fretting problems*, European Journal of Mechanics - A/Solids **16** (1997) 573 – 593.

[129] N. STRÖMBERG, *A Newton method for three-dimensional fretting problems*, International Journal of Solids and Structures **36** (1999) 2075 – 2090.

[130] N. STRÖMBERG, *A method for structural dynamic contact problems with friction and wear*, International Journal for Numerical Methods in Engineering **58** (2003) 2371–2385.

[131] N. STRÖMBERG, L. JOHANSSON, A. KLARBRING, *Derivation and analysis of a generalized standard model for contact, friction and wear*, International Journal of Solids and Structures **33** (1996) 1817 – 1836.

[132] M. TUR, F. FUENMAYOR, P. WRIGGERS, *A mortar-based frictional contact formulation for large deformations using Lagrange multipliers*, Computer Methods in Applied Mechanics and Engineering **198** (2009) 2860–2873.

[133] O. VINGSBO, S. SÖDERBERG, *On fretting maps*, Wear **126** (1988) 131 – 147.

[134] W.A. WALL, *Fluid-Struktur-Interaktion mit stabilisierten Finiten Elementen*, Ph.D. thesis, Universität Stuttgart (1999).

[135] W.A. WALL, M.W. GEE, *Baci - a multiphysics simulation environment*, Technical report, Institute for Computational Mechanics, Technische Universität München (2009).

[136] R.B. WATERHOUSE, *Fretting fatigue*, International Materials Reviews **37** (1992) 77–98.

[137] R. WEYLER, J.C. OLIVER, T. SAIN, J.C. CANTE, *On the contact domain method: a comparison of penalty and Lagrange multiplier implementation*, Computer Methods in Applied Mechanics and Engineering **205 - 208** (2012) 68 – 82.

[138] K. WICHMANN, *Verschleiß in reibungsbehafteter Mortar-Formulierung unter Verwendung eines semi-smooth Newton*, Semesterarbeit, Institute for Computational Mechanics, Technische Universität München (2010).

[139] B.I. WOHLMUTH, *A mortar finite element method using dual spaces for the Lagrange multiplier*, SIAM Journal on Numerical Analysis **38** (2000) 989–1012.

[140] B.I. WOHLMUTH, *Discretization methods and iterative solvers based on domain decomposition*, Springer, 2001.

[141] B.I. WOHLMUTH, *Variationally consistent discretization schemes and numerical algorithms for contact problems*, Acta Numerica **20** (2011) 569–734.

[142] B.I. WOHLMUTH, R.H. KRAUSE, *Monotone multigrid methods on nonmatching grids for nonlinear multibody contact problems*, SIAM Journal on Scientific Computing **25** (2003) 324–347.

[143] B.I. WOHLMUTH, A. POPP, M.W. GEE, W.A. WALL, *An abstract framework for a priori estimates for contact problems in 3D with quadratic finite elements*, Computational Mechanics **49** (2012) 735 – 747.

[144] P. WRIGGERS, *Computational contact mechanics*, Wiley, 2002.

[145] P. WRIGGERS, *Nonlinear finite element methods*, Springer, 2008.

[146] P. WRIGGERS, C. MIEHE, *Contact constraints within coupled thermomechanical analysis–a finite element model*, Computer Methods in Applied Mechanics and Engineering **113** (1994) 301 – 319.

[147] P. WRIGGERS, T. VU VAN, E. STEIN, *Finite element formulation of large deformation impact-contact problems with friction*, Computers & Structures **37** (1990) 319–331.

[148] B. YANG, T. LAURSEN, *A contact searching algorithm including bounding volume trees applied to finite sliding mortar formulations*, Computational Mechanics **41** (2008) 189–205.

[149] B. YANG, T.A. LAURSEN, *A large deformation mortar formulation of self contact with finite sliding*, Computer Methods in Applied Mechanics and Engineering **197** (2008) 756–772.

[150] B. YANG, T.A. LAURSEN, X. MENG, *Two dimensional mortar contact methods for large deformation frictional sliding*, International Journal for Numerical Methods in Engineering **62** (2005) 1183–1225.

[151] G. ZAVARISE, P. WRIGGERS, B.A. SCHREFLER, *On augmented Lagrangian algorithms for thermomechanical contact problems with friction*, International Journal for Numerical Methods in Engineering **38** (1995) 2929–2949.

[152] G. ZAVARISE, P. WRIGGERS, B.A. SCHREFLER, *A method for solving contact problems*, International Journal for Numerical Methods in Engineering **42** (1998) 473–498.